

Behaviour of low porosity microcracked thermal barrier coatings under thermal loading

Citation for published version (APA):

Koolloos, M. F. J. (2001). *Behaviour of low porosity microcracked thermal barrier coatings under thermal loading*. [Phd Thesis 1 (Research TU/e / Graduation TU/e), Mechanical Engineering]. Technische Universiteit Eindhoven. <https://doi.org/10.6100/IR542266>

DOI:

[10.6100/IR542266](https://doi.org/10.6100/IR542266)

Document status and date:

Published: 01/01/2001

Document Version:

Publisher's PDF, also known as Version of Record (includes final page, issue and volume numbers)

Please check the document version of this publication:

- A submitted manuscript is the version of the article upon submission and before peer-review. There can be important differences between the submitted version and the official published version of record. People interested in the research are advised to contact the author for the final version of the publication, or visit the DOI to the publisher's website.
- The final author version and the galley proof are versions of the publication after peer review.
- The final published version features the final layout of the paper including the volume, issue and page numbers.

[Link to publication](#)

General rights

Copyright and moral rights for the publications made accessible in the public portal are retained by the authors and/or other copyright owners and it is a condition of accessing publications that users recognise and abide by the legal requirements associated with these rights.

- Users may download and print one copy of any publication from the public portal for the purpose of private study or research.
- You may not further distribute the material or use it for any profit-making activity or commercial gain
- You may freely distribute the URL identifying the publication in the public portal.

If the publication is distributed under the terms of Article 25fa of the Dutch Copyright Act, indicated by the "Taverne" license above, please follow below link for the End User Agreement:

www.tue.nl/taverne

Take down policy

If you believe that this document breaches copyright please contact us at:

openaccess@tue.nl

providing details and we will investigate your claim.

**Behaviour of Low Porosity Microcracked Thermal
Barrier Coatings under Thermal Loading**

M.F.J. Koolloos

CIP-DATA LIBRARY TECHNISCHE UNIVERSITEIT EINDHOVEN

Koolloos, Martijn F.J

Behaviour of low porosity microcracked thermal barrier coatings under thermal loading / by Martijn F.J. Koolloos. – Eindhoven: Technische Universiteit Eindhoven, 2001.

Proefschrift. – ISBN 90-386-2712-2

NUGI 841

Subject headings: thermal barrier coatings (TBC) / failure mechanisms /burner rig test / furnace test / thermal barrier coating properties /residual stresses / finite element modelling

Copyright © 2001 by M.F.J. Koolloos

Druk: UNIVERSITEITSDRUKKERIJ TU EINDHOVEN

Behaviour of Low Porosity Microcracked Thermal Barrier Coatings under Thermal Loading

PROEFSCHRIFT

ter verkrijging van de graad van doctor aan de
Technische Universiteit Eindhoven, op gezag van de
Rector Magnificus, prof.dr. M. Rem, voor een
commissie aangewezen door het College voor
Promoties in het openbaar te verdedigen
op dinsdag 20 maart 2001 om 16.00 uur

door

Martijn Frans Jan Koolloos

geboren te Heerenveen

Dit proefschrift is goedgekeurd door de promotoren:

prof.dr.ir. M.J.W. Schouten

en

prof.dr. R. Metselaar

Copromotor:

dr.ir. J.M. Houben

CONTENTS

Summary.....	v
Samenvatting.....	vii
1. Introduction	1
1.1 Gas turbine development.....	1
1.2 Thermal Barrier Coatings.....	3
1.3 Purpose and scope of this thesis.....	6
2. Plasma Spraying of TBCs: Experimental Details	7
2.1 Introduction.....	7
2.2 Plasma spray process (APS).....	9
2.2.1 The plasma torch	9
2.2.2 Peripheral equipment	10
2.2.3 Plasma spray parameters	12
2.2.4 Plasma stability	13
2.3 Optimisation of plasma spray parameters – an engineering approach	14
2.3.1 Introduction.....	14
2.3.2 Deposition efficiency.....	14
2.4 Spraying the coatings.....	16
2.4.1 Materials and spraying conditions	16
2.4.2 Thick TBCs and bond coat preoxidation.....	18
2.5 Microstructural investigations	21
2.5.1 Top coat surface	21
2.5.2 Preparation method	21
2.5.3 Microstructures.....	22
2.5.4 Porosity and flexibility.....	25
3. Thermal Testing of TBCs	27
3.1 Introduction.....	27
3.2 Experimental	29
3.2.1 Thermal test equipment.....	29
3.2.2 Test conditions	31
3.2.3 Specimens and number of tests	33
3.3 Temperature profile during burner rig testing	34
3.3.1 Through-thickness gradient.....	34
3.3.2 Radial temperature profile	34
3.4 Number of cycles to failure.....	35
3.4.1 Furnace tests.....	36
3.4.2 Burner rig tests.....	37

3.5	Failure modes and microstructural changes	38
3.5.1	Furnace tests.....	40
3.5.2	Burner rig tests.....	42
3.5.3	Microstructural changes	46
3.6	Discussion.....	47
3.6.1	Furnace tests.....	47
3.6.2	Burner rig tests.....	48
3.6.3	Comparison of test methods	49
3.6.4	Preoxidation	50
3.6.5	The importance of microcracks	51
3.7	Conclusions	51
4.	Coating Properties	53
4.1	Introduction.....	53
4.2	Hardness	53
4.2.1	Introduction.....	53
4.2.2	Experimental	54
4.2.3	Results and discussion.....	54
4.3	Erosion resistance	57
4.3.1	Introduction.....	57
4.3.2	Experimental	57
4.3.3	Results and discussion.....	58
4.4	Adhesion strength.....	59
4.4.1	Introduction.....	59
4.4.2	Experimental	60
4.4.3	Results and discussion.....	61
4.5	Phase analysis	62
4.5.1	Introduction.....	62
4.5.2	Experimental	63
4.5.3	Results and discussion.....	64
4.6	Bond coat composition	65
4.6.1	Introduction.....	65
4.6.2	Experimental	65
4.6.3	Results and discussion.....	65
4.7	Conclusions	68
5.	Measurement of Residual Stresses.....	69
5.1	Introduction.....	69
5.2	Experimental procedures	71
5.2.1	X-ray diffraction.....	71
5.2.2	Hole-drilling method	72
5.2.3	Specimens	74
5.3	Preliminary measurements.....	75
5.4	Main measurements.....	76

5.4.1	Introduction.....	76
5.4.2	Results	77
5.4.3	Discussion.....	80
5.5	Experimental problems	84
5.6	Conclusions	88
6.	Modelling of Thermal Stresses	89
6.1	Introduction.....	89
6.2	Modelling methodology.....	90
6.2.1	Analysis procedure	91
6.2.2	Geometry and mesh generation	91
6.2.3	Global analysis	92
6.2.4	Local analysis	93
6.2.5	Material properties.....	96
6.3	Boundary and thermal loading conditions.....	97
6.3.1	Furnace simulation.....	97
6.3.2	Burner rig simulation.....	98
6.4	Furnace global analysis	102
6.4.1	Temperature	102
6.4.2	In-plane stresses.....	102
6.4.3	Shear and normal stresses	103
6.5	Furnace local analysis	105
6.5.1	Comparison with global analysis.....	105
6.5.2	Stresses at centre of disc	105
6.5.3	Stresses near free edge	106
6.6	Discussion of furnace simulation.....	108
6.6.1	Global analysis	108
6.6.2	Local analysis	109
6.6.3	Summary.....	110
6.7	Thermal shock global analysis.....	110
6.7.1	Temperature	110
6.7.2	In-plane stresses.....	112
6.7.3	Shear and normal stresses	114
6.8	Thermal shock local analysis	115
6.8.1	Parametric study.....	115
6.8.2	Stresses near flame edge.....	116
6.9	Thermal cycling global analysis	118
6.9.1	Temperature	118
6.9.2	In-plane stresses.....	119
6.9.3	Shear and normal stresses	122
6.10	Discussion of burner rig simulations.....	123
6.10.1	Thermal analysis.....	123
6.10.2	Global in-plane stresses	124
6.10.3	Global shear and normal stresses.....	125

6.10.4 Local stresses	126
6.10.5 Final remarks about local stress distribution	126
6.11 Conclusions	127
Appendix 6A Bond coat roughness	129
Appendix 6B Effect of oxide layer on temperature profile	131
Appendix 6C Creep of a coated bar	132
Appendix 6D Heat transfer coefficient for free convection	133
Appendix 6E Heat transfer coefficient for impinging jet	134
7. Discussion	137
7.1 Introduction	137
7.2 Furnace testing	137
7.2.1 Residual stresses	137
7.2.2 Failure modes	138
7.2.3 Effect of top coat thickness and test temperature	140
7.3 Burner rig testing	141
7.3.1 Temperature profile	141
7.3.2 Failure by delamination	141
7.3.3 Other failure modes	143
7.4 Effect of preoxidation	144
7.5 A remark about top coat thickness	146
7.6 Fracture mechanics	146
7.7 Use and further development of the present model	148
8. Conclusions and Recommendations	149
8.1 General conclusions	149
8.2 Detailed conclusions	150
8.3 Recommendations	154
References	155
Acknowledgements	165
Curriculum Vitae	167

SUMMARY

Thermal Barrier Coatings (TBCs) are applied to the hot components of gas turbines in order to allow higher turbine entry temperatures (which increases the thermal efficiency of the gas turbine) or to achieve lower base metal temperatures. A TBC consists of a heat-resistant ceramic top coat and a metallic bond coat. The bond coat's main purpose is to attach the top coat to the substrate, but the bond coat also prevents or delays oxidation of the substrate. Unfortunately, a major life-limiting weakness of TBCs is oxidation of the bond coat itself; the other major problem is their susceptibility to damage by thermally-induced stresses. The mechanisms of damage and ultimate failure of TBCs are still not entirely understood. The objective of the present work, reported in this thesis, has been to use a combination of experiments and theoretical modelling to improve the understanding of TBC damage accumulation and failure.

Several TBCs were applied by Air Plasma Spraying (APS) to Hastelloy X substrates with NiCrAlY bond coats. The main process variables were the top coat thickness and the bond coat condition (as-sprayed or preoxidised) before applying the top coat. The secondary process variables were optimisation of the spraying parameters and comparison of 'mild' and 'excessively energetic' plasma spraying conditions.

The TBCs were subjected to three types of thermal tests: isothermal furnace tests, short cycle (thermal shock) burner rig tests, and long cycle burner rig tests. The results were the number of thermal cycles to failure and a phenomenological description of failure as function of the type of test, the top coat thickness, and bond coat condition before applying the top coat. It was concluded that failure of a TBC under realistic testing conditions must be due to an interaction between thermal stresses and bond coat oxidation. However, empirical testing, no matter how realistic, is insufficient for understanding the failure mechanisms. Thus the changes in the TBC systems, including bond coat oxidation, should be investigated, and also the stresses that develop during thermal testing should be quantitatively predicted.

Several properties were determined for both the as-sprayed and thermally tested TBCs. There was evidence that sintering occurred during isothermal heating of the TBCs, and this resulted in microstructural changes. In general, sintering meant that the porosity decreased and sealing of flaws occurred. In consequence the micro-hardness, erosion resistance and bond strength increased. Despite the high temperature of some heat treatments no detrimental phase transformations were

observed. However, aluminium depletion of the bond coat did occur during isothermal heating.

Residual stresses in as-sprayed and thermally tested coatings were measured and related to the thermal history of the TBCs. The stresses were measured using the hole-drilling method. Despite the difficulties involved in this technique some trends were observed. However, the differences in life and failure mechanisms for thin and thick TBCs during furnace testing and burner rig testing could not be explained from the in-plane residual stresses in the as-sprayed state.

The theoretical modelling used the Finite Element Method (FEM) to simulate the three types of thermal testing. The so-called global-local approach was used. First, overall temperature and stress distributions in the TBCs were obtained as functions of the type of test. These global analyses provided useful information about the locations of highly stressed areas. Next, the interesting areas were subjected to local and more refined FEM modelling. The local model provided additional information about the effects of bond coat roughness and the presence of an interface oxidation layer, especially with respect to the shear and normal stresses near and at the top coat / bond coat interface. Interface roughness resulted in small variations of the local solution shear and normal stresses around the global solution; and an oxide layer between the top coat and bond coat reversed the sign of the normal stresses and increased the shear and normal stresses considerably.

In conclusion, it was shown that the model presented in this thesis provides information about the stress distributions that is useful for understanding the experimentally observed failure mechanisms. High normal and/or shear stresses (a) near the intersection of the top coat / bond coat interface and a free edge, or (b) in the flame area close to the interface roughness peaks, caused the top coat to delaminate. It is worth noting that a local analysis was not always required to understand failure.

Furthermore it was shown and explained that bond coat preoxidation has a beneficial effect for test methods with long heating cycles, and thick TBCs exhibited excellent thermal strain tolerance. However, where actual gas turbine components have free edges the thickness of TBCs will have to be limited.

SAMENVATTING

Thermal Barrier Coatings (TBCs) worden aangebracht op onderdelen in de hoge temperatuur sectie van een gasturbine. Het doel van een TBC is het beschermen van een component tegen hoge gastemperaturen. Het effect is dat de temperatuur van de onderliggende component lager wordt of dat de toegestane maximale gastemperatuur omhoog kan (waardoor het thermisch rendement van de gasturbine toeneemt). TBCs bestaan uit een warmtewerende, keramische toplaag en een metallische hechtlaag. Deze hechtlaag zorgt voor de hechting van de toplaag aan het substraat en beschermt het substraatmateriaal tegen oxidatie. Het grote probleem bij TBCs is de beperkte levensduur tijdens thermische belasting vanwege hoge thermische spanningen en oxidatie van de hechtlaag. De faalmechanismen zijn tot op heden nog steeds niet geheel doorgrond. Het doel van het onderzoek beschreven in dit proefschrift is om met een gecombineerde experimentele en modelmatige aanpak het faalmechanisme van TBCs nader te verklaren.

Verschillende TBCs zijn door middel van Atmosferisch Plasma Spuiten (APS) aangebracht op Hastelloy-X substraten met NiCrAlY hechtlagen. De belangrijkste systeemvariabelen zijn de toplaagdikte en voorbehandeling (preoxidatie) van de hechtlaag. Daarnaast zijn de procesparameters van het plasma spuiten geoptimaliseerd en zijn milde en hoog-energetische plasma-spuitcondities met elkaar vergeleken.

De TBCs zijn tijdens een uitgebreid proevenprogramma op drie verschillende manieren getest: cyclisch isothermische ovenproeven, korte cyclus *burner rig* proeven (*thermal shock*) en lange cyclus *burner rig* proeven. De resultaten van deze proeven zijn beschreven in termen van het aantal cycli tot falen en een fenomenologische beschrijving van het faalmechanisme, beide als functie van de testmethode, toplaagdikte en voorbehandeling van de hechtlaag. Hieruit is geconcludeerd dat het falen van TBCs in een realistische omgeving wordt veroorzaakt door een combinatie van thermische spanningen en oxidatie van de hechtlaag. Het bleek echter ook dat empirische testen niet voldoende zijn om de waargenomen faalmechanismen te verklaren. Vandaar dat de veranderingen in de TBCs, inclusief oxidatie van de hechtlaag, onderzocht moeten worden. Bovendien was het nodig om de spanningen die ontstaan tijdens de thermische testen te voorspellen middels een numeriek model.

Van zowel de *as-sprayed* als de thermisch geteste TBCs zijn de relevante eigenschappen bepaald. Het blijkt dat tijdens een warmtebehandeling de microstructuur van de toplaag verandert door sintereffecten. Dit uit zich door een afname in de porositeit en het gedeeltelijk verdwijnen van kleine scheurtjes. Als een gevolg

hiervan nemen de hardheid, erosieweerstand en hechtsterkte van de toplaag toe. Ondanks de hoge temperaturen van enkele warmtebehandelingen zijn er geen ongunstige fasetransformaties waargenomen. Wel is gebleken dat er door een langdurige warmtebehandeling aluminium verarming van de hechtlaag optreedt.

De restspanningen in de *as-sprayed* en de thermisch geteste TBCs zijn gemeten en in verband gebracht met de thermische geschiedenis van de TBCs. De spanningen zijn gemeten met de *hole-drilling* methode. Ondanks enige experimentele problemen, welke inherent zijn aan het gebruik van deze techniek, kunnen er trends worden waargenomen. De geobserveerde verschillen in levensduur en faalmechanisme kunnen echter niet verklaard worden aan de hand van de restspanningen in de *as-sprayed* TBCs.

De Eindige Elementen Methode (EEM) is gebruikt om een numeriek model te ontwikkelen waarmee de drie testmethodes gesimuleerd zijn. Dit model maakt gebruik van de zogenaamde *global-local approach* waarbij eerst op globale schaal het temperatuur- en spanningsprofiel bepaald wordt, als functie van het type test. Aan de hand van deze globale analyses zijn de gebieden met hoge thermische spanningen gelokaliseerd. Vervolgens zijn op lokale schaal de interessante gebieden geanalyseerd met een fijner model. Het lokale model verschaft extra informatie over het effect van de ruwheid van de hechtlaag en de aanwezigheid van een grensvlak oxidatielaag, met name wat betreft de normaal- en schuifspanningen op en bij het grensvlak tussen toplaag en hechtlaag. Het blijkt dat de ruwheid van de hechtlaag resulteert in een variatie van de normaal- en schuifspanningen rond de globale oplossing, en dat een oxidatielaag tussen de toplaag en de hechtlaag het teken van de normaalspanningen omkeert en zorgt voor een aanzienlijke toename van de normaal- en schuifspanningen.

Concluderend kan worden gesteld dat de resultaten van het model gepresenteerd in dit proefschrift bruikbaar zijn om de experimenteel waargenomen faalmechanismen te verklaren. Hoge normaal- en/of schuifspanningen bij de grensvlakruwheidspieken (a) ter plaatse van het snijpunt van het grensvlak tussen toplaag en hechtlaag en de vrije rand, of (b) in het gebied dat verhit wordt door een vlam, veroorzaken delaminatie van de toplaag. Opgemerkt dient te worden dat een lokale analyse niet altijd vereist is om het faalmechanisme te begrijpen.

Tenslotte is aangetoond en verklaard dat preoxidatie van de hechtlaag een gunstig effect heeft op de levensduur voor testmethodes met lange cycli, en dat de dikke TBCs onderzocht in dit proefschrift zeer goed thermische rekken kunnen verdragen. Indien een gasturbine onderdeel echter een vrije rand heeft, is de toplaagdikte gelimiteerd.

1 INTRODUCTION

1.1 Gas turbine development

The thermal efficiency of gas turbine engines is largely determined by the turbine entry temperature (TET): a higher TET results in higher efficiency. Consequently, the development of ever more efficient gas turbines has been paced by developments in high-temperature – high-strength materials, protective and heat resistant coatings, and component cooling, see figure 1.1 (Williams, 1994; Miller, 1997; Goward, 1998; Wigren and Pejryd, 1998; Stringer, 1999).

Alloy development. To allow for metal temperature increases, alloys were developed with improved strength capability at higher temperatures. The sequence of material systems followed a path from heat resisting steels and wrought Ni-Cr alloys in the nineteen-fifties to conventionally cast Ni-based superalloys in the nineteen-sixties and -seventies to the directionally solidified and single crystal alloys in the nineteen-eighties and -nineties. However, the strength improvements were realised at the expense of less resistance to oxidation and hot corrosion. Therefore protective metallic surface coatings were developed. The earliest coatings were diffusion coatings to increase the aluminium content of the component surface. More recently, overlay MCrAlY coatings (where M = Ni, Co or NiCo) were developed.

Air Cooling. A large part of the gain in TET over the last three decades has been achieved by cooling hot section components with bleed air from the compressor. Although using compressor air to cool the engine involves some efficiency loss, the total efficiency is increased owing to the increase in TET. Since air cooling needs complex internal channels and thin walled blades, it requires more sophisticated structural design and casting techniques of airfoils.

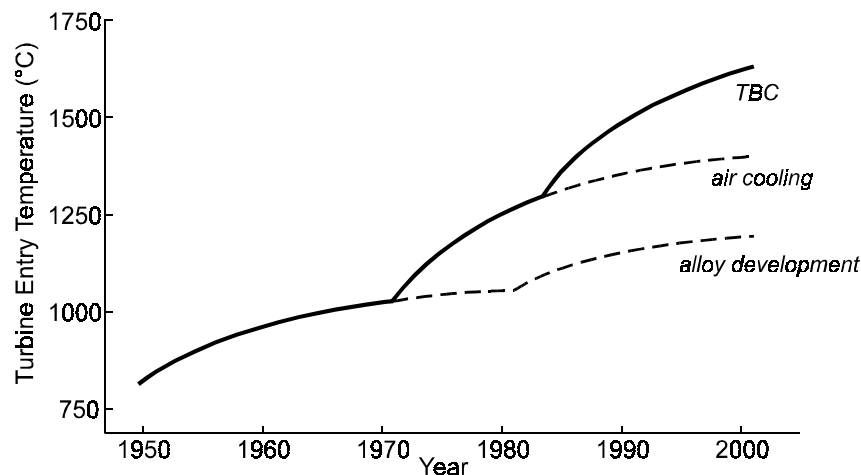


Figure 1.1 Turbine Entry Temperature (TET) development over the past 50 years. The upward kink in the alloy development curve around 1980 is due to the introduction of directionally solidified and single crystal alloys. TBC = Thermal Barrier Coating.

Thermal Barrier Coatings. The most recent increase in TET has been obtained by the use of Thermal Barrier Coatings (TBCs) on cooled hot section components. A TBC is actually a coating system consisting of a ceramic top coat applied to a metallic bond coat. This bond coat provides oxidation resistance and adherence of the top coat to the substrate. As the name implies, TBCs possess a low thermal conductivity resulting in a significant temperature drop across the coating. A TBC can be used in three ways (Stringer, 1999):

- The TET is kept constant and the cooling air flow is kept constant, resulting in reduced metal temperature and hence improved life.
- The TET is kept constant and the cooling air flow is reduced, resulting in increased efficiency.
- The TET is increased and the metal temperature allowed to be the same as without a TBC, resulting in increased efficiency.

The most important issue concerning the way TBCs are used is their limited service life compared to the component design life requirements. In the first two ways listed above the TBC is used as an *add-on*: the engine components will not fail after TBC loss. The third way is called *prime reliant*: if the TBC is lost the components will rapidly suffer severe damage. Thus to achieve application of TBCs in a prime reliant mode it is necessary to do research aimed at TBC life improvement and failure prevention.

The present work, reported in this thesis, aims to contribute to a better description and understanding of TBC failure mechanisms. However, before arriving at the purpose and scope of the thesis TBCs will be discussed in more detail.

1.2 Thermal Barrier Coatings

Of the possible thermal barrier materials, partially stabilised zirconia (ZrO_2) is currently favoured. Pure zirconia has a cubic structure at temperatures above 2400°C , a tetragonal structure at temperatures between 1100°C and 2400°C , and a monoclinic structure below 1100°C . The tetragonal to monoclinic transformation is diffusionless (martensitic) and is accompanied by a volume increase of about 5%, resulting in compressive stresses and a very brittle, cracked material, which makes pure zirconia unsuitable for TBCs. In order to suppress this transformation, ZrO_2 can be alloyed with stabilising oxides like MgO , CaO , CeO_2 or Y_2O_3 (Claussen *et al.*, 1984; Brandon and Taylor, 1991; Ibégazène *et al.*, 1993).

The earliest example of the use of TBCs for aerospace applications was around 1970, when an Air Plasma Sprayed (APS) magnesia-stabilised zirconia was applied to combustion chamber walls with a NiCr or NiAl bond coat. Extensive research, notably at NASA and the Original Equipment Manufacturers (OEMs) resulted in the currently applied 6-8 wt% Y_2O_3 -partially stabilised ZrO_2 (PSZ) on MCrAlY bond coats. This TBC, still applied by APS, could be used for more highly thermally loaded parts like vane airfoils and vane platforms, see *e.g.* Meier and Gupta (1994) or Miller (1997). The Y_2O_3 - ZrO_2 system will be discussed in detail in section 4.5.

However, the need for higher operating temperatures logically led to the need to apply TBCs on the most highly loaded gas turbine components, namely the rotating blade airfoils and platforms. This resulted in development of electron beam-physical vapour deposited (EB-PVD) TBCs (Strangman, 1982). Owing to their aerodynamically smooth surfaces and excellent strain tolerance and adhesion, EB-PVD TBCs offer significant benefits over APS TBCs for use on blade airfoils, despite the higher costs and their higher thermal conductivity. However, for vanes and combustion chamber walls APS TBCs still perform adequately, and because of their relatively low production costs they are still preferable to EB-PVD TBCs (Meier and Gupta, 1994; Kaysser *et al.*, 1998; Morrell and Rickerby, 1998).

The present research concerns air plasma sprayed TBCs. In the following subsections the processing and failure of APS TBCs will be concisely discussed.

The plasma spray process

Plasma spray deposition is based on melting and accelerating small particles by a plasma. The plasma is generated in a plasma torch where a mixture of two or more of the gases Ar, H_2 , He or N_2 is ionised by an electric arc discharge. The ionised gas heats up to over 15000 K, expands enormously, and leaves the anode exit with high

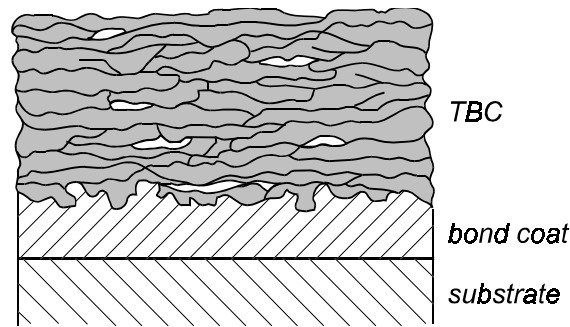


Figure 1.2 Typical microstructure of APS TBC (schematic)

velocity, ranging from 100 to 800 m/s (Fauchais et al, 1989). The powder particles, which can vary in size from 5–200 μm , are injected in the plasma just outside the anode, where the ions and electrons of the plasma recombine. There the particles are heated to a semi-plastic or even molten state and accelerated towards the workpiece to be coated. The particle velocities vary between 80 to 300 m/s depending on the plasma properties and particle size (Fauchais *et al.*, 1989; Diessen, 1998). Upon impact the particles flatten and solidify, producing a coating with a lamellar, porous microstructure, see figure 1.2 (McPherson, 1981; Houben, 1988; Dykhuizen, 1994). The plasma spray process and equipment used during the present research will be described in more detail in section 2.2.

Bond coat

The MCrAlY bond coat is deposited by air, low pressure or vacuum plasma spraying (APS, LPPS or VPS). More recently, High Velocity Oxygen Fuel (HVOF) has been used for the bond coat. The bond coat is required to improve top coat adhesion by mechanical interlocking (see the irregular top coat / bond coat interface in figure 1.2), and to prevent or delay oxidation of the substrate material by forming a dense oxide layer that acts as a oxygen diffusion barrier.

Failure of TBCs

As mentioned in section 1.1, the main obstacle to the use of TBCs in the prime reliant mode is the limited service life. Failure occurs by top coat delamination as a result of cracking in the top coat parallel and adjacent to, but not coincident with, the irregular top coat / bond coat interface (Miller and Lowell, 1982; Chang *et al.*, 1987a; DeMasi *et al.*, 1990), see figure 1.3. Though the failure mechanisms of TBCs are still not entirely understood, bond coat oxidation and thermal expansion mismatch stresses are generally believed to be the main causes of failure (Miller and Lowell, 1982; Wu *et al.*, 1989; DeMasi *et al.*, 1990; Nissley, 1997).

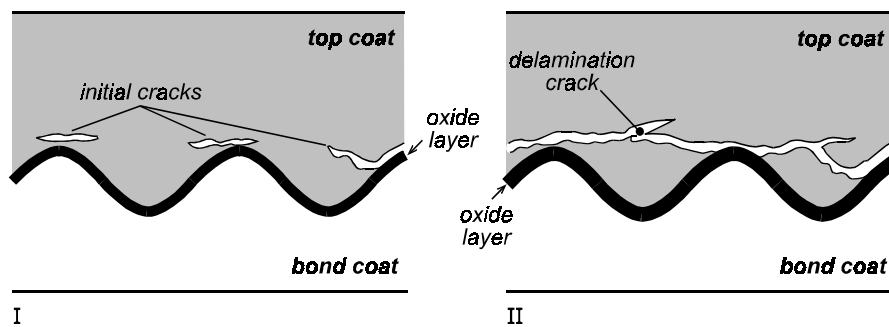


Figure 1.3 Schematic representation of delamination sequence in plasma sprayed TBCs during thermal loading. Cracks are formed at or near the top coat / bond coat interface peaks and grow parallel to the interface. Delamination occurs upon link-up. Note that the oxide layer for case II is thicker than for case I, owing to longer high temperature exposure.

Bond coat oxidation can be reduced by (1) lowering the interface temperature or (2) including an oxygen diffusion barrier between the top coat and the bond coat.

1. An obvious way to decrease the interface temperature is to apply a thicker top coat. However, the thermal stresses in the top coat are then higher and in some cases the top coat delaminates even during the spraying process. Wigren *et al.* (1996b) and Bengtsson *et al.* (1998) showed that thick TBCs could be sprayed provided that a network of segmentation cracks is present. Also, Verbeek (1992) suggested that his spraying technology enabled thick TBCs to be sprayed, owing to a dense network of microcracks. Both TBC systems showed high thermal shock resistance, owing to cracks giving the top coat a high flexibility.
2. An oxygen diffusion barrier, generally Al_2O_3 , can be achieved by bond coat preoxidation (Lih *et al.*, 1991), by use of a Chemical Vapour Deposited (CVD) Al_2O_3 -layer (Sun *et al.*, 1993) or by applying a VPS Al_2O_3 -layer (Tsui and Clyne, 1996). Using an oxygen barrier resulted in longer lives during isothermal heating tests, irrespective of the production method.

It should be mentioned that the oxidation response of the bond coat depends primarily on its composition. However, changing its composition also changes other bond coat properties like coefficient of thermal expansion, creep behaviour and Young's modulus, and these changes can have considerable effects on TBC life (Brindley, 1997).

Thermal expansion mismatch stresses can be mitigated by functionally graded TBCs (Khor *et al.*, 1998; Musil *et al.*, 1995). These coating systems have a graded zone between the top coat and bond coat, whereby the amount of bond coat material decreases gradually towards the top coat and vice versa. Though good results were obtained during isothermal cyclic heating tests (Khor *et al.*, 1998) a graded TBC did not perform better during burner rig tests. The reason was oxidation of bond coat material close to the exposed top coat surface (DeMasi *et al.*, 1990; Miller, 1997).

In a recent NASA Tech Brief (Brindley and Miller, 1998) a metal/ceramic bond coat was considered to lower the thermal expansion mismatch between the top coat and bond coat. The upper part of the bond coat incorporated a fine dispersion of particulate second phase (Al_2O_3) in an MCrAlY matrix. Preliminary tests showed that using a bond coat with only 5 percent alumina doubled TBC life.

1.3 Purpose and scope of this thesis

The purpose of this thesis is to better describe and understand the failure mechanisms of APS TBCs. Although much research has been done, it usually falls into one of two categories: (a) experiments and description of failure modes, or (b) modelling and prediction of TBC failure. The present work aims at a combined approach whereby experiments are designed and used to support and validate modelling.

This approach requires an extensive test programme, in which different kinds of thermal loads are applied to TBCs of various thicknesses and with or without oxygen barriers at the top coat / bond coat interface. These experiments are intended to provide correlations between the effects of thermal loads on TBC properties, the failure modes, and the number of thermal load cycles to failure. Subsequently the tests are simulated by Finite Element Modelling, using input parameters obtained from the experiments. (It must be noted here that purely analytical modelling is unfeasible except for drastically simplified situations.)

The scope of this thesis is as follows. Firstly, the TBCs used to investigate the failure mechanisms are based on the TBC system developed by Verbeek (1992). Chapter 2 describes further modification of these TBCs and the experimental details of the TBC production. Chapter 3 presents the failure modes and lives of TBCs under different thermal loads, and chapter 4 compares the properties of the as-sprayed and thermally loaded TBCs. Chapter 5 describes the measurements of residual stresses in TBCs before and after thermal loading. Chapter 6 gives the formulation and results of a numerical model that simulates the different thermal loads applied to the TBCs as presented in chapter 3. Chapter 7 pools the experimental and modelling results in order to provide explanations of the observed failure modes. Chapter 8 ends the thesis with conclusions and recommendations.

2 PLASMA SPRAYING OF TBCs: EXPERIMENTAL DETAILS

2.1 Introduction

Coating structure and quality are determined mainly by the temperature, velocity and size (distribution) of the incident particles (McPherson, 1981; Houben, 1988; Fauchais *et al.*, 1989; Vardelle *et al.*, 1993; Lugscheider *et al.*, 1996). The particles should be molten before impact and have velocities sufficient to enable spreading out and flowing into the irregularities of the previously deposited material.

The particle temperature depends on the plasma temperature, the heat transfer of the plasma to the particles, the heat conduction in the particles and the dwell time of the particles in the plasma. The particle velocity depends on the plasma velocity and viscosity, the size, geometry and density of the particles, and the dwell time of the particles in the plasma. The particle size (distribution) is determined by the powder stock material. The particle size affects the microstructure and also the particles' velocities and temperatures. Moreover, a wider variation in the particle size distribution causes larger variations in particle velocity and temperature.

The above mentioned plasma properties (temperature, velocity, viscosity) depend on the plasma parameters, which are commonly expressed in terms of arc current, primary gas flow (Ar) and secondary gas flow (He or H₂)¹. The correlation between plasma parameters and particle properties is complex owing to the many interactions that occur. Moreover, secondary factors like *constriction* (decrease of

¹ H₂ was used as secondary gas in the present work. It should be mentioned that for a systematic parameter study it is more convenient to express the gas flow parameters by two independent parameters: total gas flow (ϕ), and fraction of secondary gas (%H₂) These parameters will be used in this thesis.

plasma flame diameter, resulting in a change in temperature distribution) and the *pumping effect* (plasma mixing with ambient air when it leaves the anode, resulting in temperature drops) affect the plasma properties significantly. On the whole, the effect of the plasma parameters can be summarised qualitatively as follows (Fauchais *et al.*, 1989; Verbeek, 1992; Vardelle *et al.*, 1993; Diessen, 1998):

- An increase in arc current results in increased plasma power. The particle velocity increases proportionally, while the plasma length increases slightly. The dwell time (t_{dw}) in the plasma is shorter, but since the plasma enthalpy is higher the particle temperature will increase.
- An increase in gas flow results in increased plasma velocity and hence particle velocity. Owing to the pumping effect the plasma temperature and plasma length decrease. The dwell time (t_{dw}) is shorter but owing to constriction the plasma enthalpy is higher. The net result is that the particle temperature increases slightly.
- An increase in hydrogen content results in an increased plasma velocity and hence particle velocity. Although the dwell time (t_{dw}) is shorter, the particle temperature increases owing to an increase in heat conduction of the plasma.

It must be mentioned that the final coating quality depends not only on the particle properties during consolidation, but also on the residual stresses in the coating, which are controlled by the substrate temperature. Substrate cooling during spraying results in residual tensile stresses (see also chapter 5 of this thesis), which increase life during thermal cycling despite the lower bond strength of the top coat (Watson and Levine, 1984; Steffens *et al.*, 1991; Verbeek, 1992; Bartuli *et al.*, 1995).

Since the interactions between plasma spray parameters, plasma properties and particle properties are qualitatively known, the question arises whether these relations can be quantified. Houben (1980) showed that to obtain a well-heated particle the following condition must be fulfilled:

$$t_{dw} \geq t_{hs} \geq t_{ha} \quad (2.1)$$

where t_{dw} is the dwell time, which includes the particle velocity implicitly; t_{hs} is the heat supply time, which is the time needed to heat up a particle to a certain temperature; and t_{ha} is the heat absorption time, which is the time needed by a particle to reach a uniform temperature. Equation 2.1 can be rewritten in terms of relevant *plasma parameters* like viscosity, conductivity, temperature, and velocity; and *particle parameters* like diameter, density, diffusivity and conductivity (Houben, 1980).

For poorly conducting ceramic materials the heat absorption time is usually larger than the heat supply time. This results in an overheated outer shell of the particle and a relatively cold core. To obtain well-heated ceramic particles it is therefore desirable to increase the heat supply time and particle dwell time. This can be achieved by using a long plasma with a low velocity (but high enough to accelerate the particles adequately), and a low heating power (but high enough to melt the ceramic material).

Verbeek (1992) developed a plasma spray technology that largely fulfilled the conditions of Eq 2.1 for ZrO_2 - Y_2O_3 particles. His TBC parameters resulted in low porosity microcracked top coats, which had both a high thermal shock resistance *and* a high erosion resistance. However, as will be shown in this chapter, it was found that the “Verbeek parameters” were too aggressive (excessive energy input) and it was therefore considered desirable to optimise the parameters before spraying the TBCs to be tested in the present work.

In this chapter an efficient optimisation approach is used to find suitable plasma spray parameters for ZrO_2 - Y_2O_3 . First, section 2.2 describes the plasma spray equipment for the present investigation. Section 2.3 presents the optimisation process of the plasma spray parameters, and section 2.4 describes the spraying of the TBCs. The chapter ends with presentation of microstructural investigations in section 2.5.

2.2 Plasma spray process (APS)

2.2.1 The plasma torch

The plasma torch used during this project was developed by the Thermal Spraying Group from Eindhoven University of Technology. The torch’s special construction results in a diffuse arc discharge, and hence high electric efficiency and an extended lifetime in comparison with industrial torches.

The plasma torch can be equipped with a standard anode and a 20 mm extended anode (Verbeek, 1992). The standard anode (\varnothing 8mm) is used when metallic coatings are sprayed. Powder injection takes place outside the anode. The extended anode (\varnothing 8mm) is used for spraying ceramic coatings, and powder injection takes place *in* the anode 15 mm before the nozzle exit. In comparison with the standard anode the plasma length using an extended anode is increased from about 50 to 70 mm, where the exact length depends on the spraying parameters. The plasma is also hotter, since no pumping effect takes place for the first 20 mm. Moreover, the particle

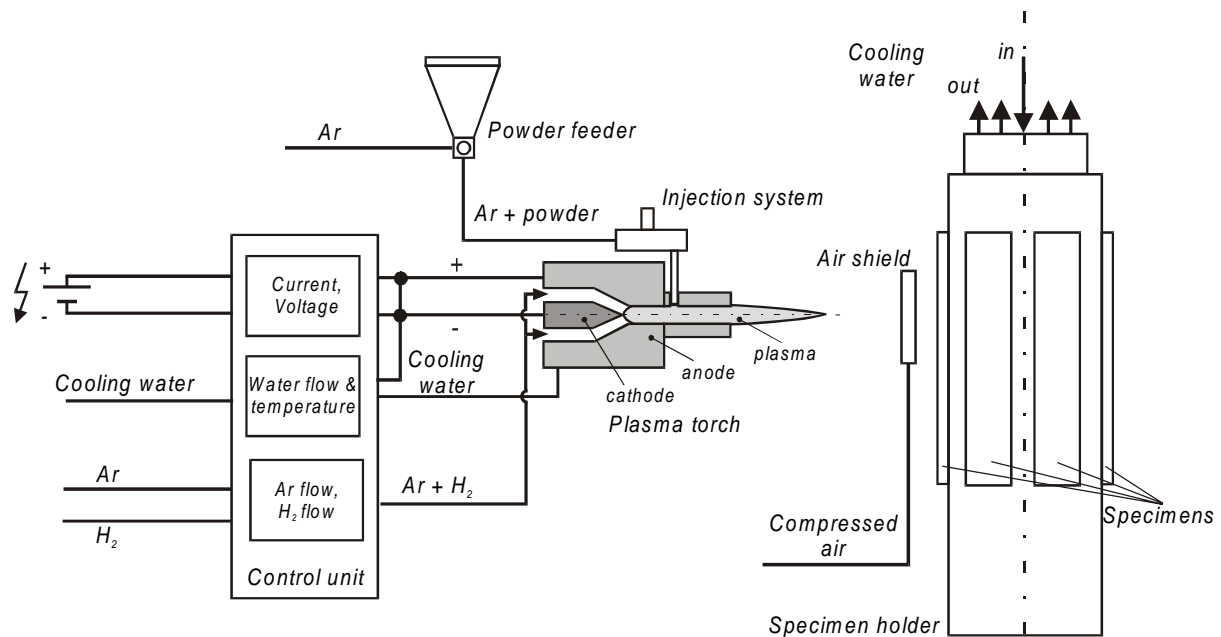


Figure 2.1 Schematic of plasma spray system with extended anode. Not to scale.

bundle of an extended anode is narrower, with a spraying spot of about 15 mm at 100 mm from the nozzle exit. This means that the variations in particle velocities and temperatures are smaller. All these differences due to an extended anode result in increased particle temperatures and velocities, thereby more easily fulfilling Eq. 2.1 for ceramic particles.

2.2.2 Peripheral equipment

Figure 2.1 shows the plasma spray set-up schematically (torch equipped with extended anode) and figure 2.2 shows a detailed photographic view of the plasma torch and specimen holder. The components additional to the plasma torch will be described in this section.

Supply and control units

A 100 kW power supply unit and a gas supply unit enable generating the plasma. In addition, a cooling unit is required for cooling the anode, cathode and high current wires. The gas flows and current are set with a control unit, which also monitors the cooling water flow and temperature and the arc voltage.

Powder feeding

The powder feeding equipment (Metco MFP) provides a constant particle mass flow, about 45 g/min for the present investigation. Dosing is accomplished by a hopper,

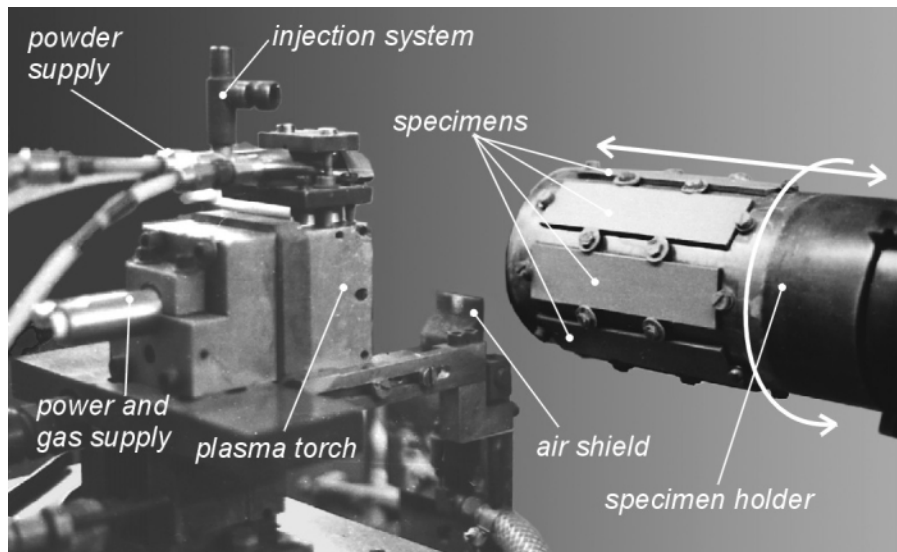


Figure 2.2 Overview of plasma spray set-up for the production of TBCs. The arrows indicate the directions of movement of the specimen holder (traverse and rotational).

and transport takes place by a carrier gas (Ar). A major drawback of the as-supplied equipment is that the required carrier gas flow for particle transport results in a too high particle injection velocity. This causes the spray jet and plasma to be non-concentric. To avoid this Houben (1976) developed an injection method, with centre-line injection of the particles, leading to rotational symmetry of spray jet and plasma. This method allows the carrier gas flow to fulfil its transport function prior to injection, but the gas flow is reduced at the beginning of injection.

Air shield

An air shield is placed between the plasma torch and the substrate at 10 mm from the substrate surface. The air shield's purpose is to avoid excessive heating of the substrate by the plasma gases and to remove very light particles and vaporised powder from the particle bundle. The air shield consists of a 1 mm thick and 30 mm wide fast airflow travelling perpendicular to the particle bundle. Owing to the high velocity and relatively large mass of the spraying particles, the influence of the air shield on their trajectory and temperature is negligible.

The effect of the air shield can be determined by measuring the heat flow of the plasma to the substrate with and without an air shield. This was done by heating a piece of Armco iron ($\text{Ø}30 \times 10$ mm) with the plasma flame at a distance of 100 mm from the anode nozzle exit. The iron piece was placed behind a water-cooled mask containing a hole of $\text{Ø}25$ mm. The iron's temperature was measured with a thermocouple spot-welded on the surface opposite the heated surface. Since the Biot number was smaller than 0.1, the iron could be considered to behave according to the lumped

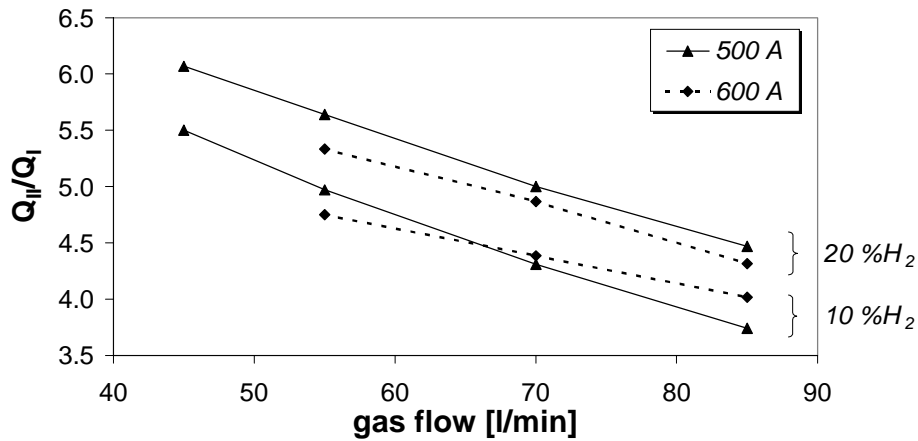


Figure 2.3 The ratio of the heat flow without (Q_{II}) and with (Q_I) an air shield as a function of the gas flow for 500 A and 600 A and for 10% H_2 and 20% H_2

capacitance method, which means that temperature gradients within the solid are negligible (Incropera and De Witt, 1990). Hence the heat flow can be determined from the measured initial heating rate:

$$Q_{\text{plasma}} = mc_p \left(\frac{\partial T}{\partial t} \right)_{t \downarrow 0} \quad [\text{J/s}] \quad (2.2)$$

where m is the mass and c_p is the specific heat of the Armco iron piece ($55.44 \cdot 10^{-3}$ kg and 447 J/kg K respectively). Figure 2.3 shows the ratio of the heat flows without and with an air shield. It is seen that the air shield reduces the heat flow by a factor of 4-6, depending on the spraying parameters.

Specimen holder

A hollow cylindrical specimen holder is used for spraying the TBCs. It contains eight rectangular holes on which 125×30 mm strips can be mounted. Cooling water flows on the inside of the specimen holder, resulting in *direct* cooling of the substrate rear sides. Leakage-free operation is ensured by a rubber sealing ring and pressing the strips on the sealing ring, by means of small-headed bolts and washers. The specimen holder can rotate at up to 300 rpm, and can move on a sliding carriage along the spraying direction, see figure 2.2.

2.2.3 Plasma spray parameters

Verbeek (1992) sprayed TBCs using the plasma spray parameters in table 2.1. Spraying of the top coats was done with the air shield and with substrate cooling. These conditions resulted in the low porosity microcracked top coats mentioned in section 2.1.

Table 2.1 Spray parameters used by Verbeek (1992)

I [A]	Ar [l/min]	H ₂ [l/min]		φ [l/min]	% H ₂
600	70	8	⇒	78	10,2
600	70	15	⇒	85	17,7

For the present investigation the top coat plasma gas parameters covered more variations, and are given in table 2.2. Each of the gas combinations could be sprayed with either 500A or 600A.

Table 2.2 Spray parameter matrix used during present investigation. The numbers in italics give the argon / hydrogen gas flows, adding up to the total gas flows, φ.

φ [l/min]	%H ₂			
	10	15	20	25
45	<i>40.50/4.50</i>	<i>38.25/6.75</i>	<i>36.00/9.00</i>	<i>33.75/11.25</i>
55	<i>49.50/5.50</i>	<i>46.75/8.25</i>	<i>44.00/11.00</i>	<i>41.25/13.75</i>
70	<i>63.00/7.00</i>	<i>59.50/10.50</i>	<i>56.00/14.00</i>	<i>52.50/17.50</i>
85	<i>76.50/8.50</i>	<i>72.25/12.75</i>	<i>68.00/17.00</i>	<i>63.75/21.25</i>

2.2.4 Plasma stability

During parametric studies and actual spraying of the TBCs it was found that the behaviour of the plasma torch was sometimes unreliable. This means the reproducibility of some of the studies or the deposition characteristics were not as high as desired. In detail, although the arc current, gas flow and gas composition were relatively constant (within 1% deviation), the plasma characteristics varied. It would appear that the arc voltage varied owing to small fluctuations in parameters that affect the arc discharge, e.g. wear of the cathode, position of discharge in anode, and cooling of the anode and cathode. Also, the powder injection was manually adjusted for each spraying session, and this could have facilitated small deviations from centreline injection. Possibly of most importance is cathode wear, which during a large number of starts can result in considerable differences in plasma behaviour between the first and last starts. In any event, one should be aware of these variations and recognise that plasma properties, and consequently particle properties and coating characteristics, can be specified and obtained only within a certain probability rather than precisely.

2.3 Optimisation of plasma spray parameters – an engineering approach

2.3.1 Introduction

To avoid an extensive parametric study of the relation between plasma spray parameters, particle properties, and coating quality (see section 2.1) most coating manufacturers use the following empirical rule (Te Raa, 1996):

The larger the percentage of spraying material that is actually assimilated in the coating, the better the spraying parameters.

In other words: the spraying parameters, and hence the coating quality can be optimised by the so-called *deposition efficiency*. This is an indirect parameter, substituting for the particle velocity and temperature. Since the relationship between plasma spray parameters and particle properties is known qualitatively (see section 2.1) the deposition efficiency is controllable and will be used here to optimise the Verbeek parameters.

2.3.2 Deposition efficiency

First some pilot measurements were carried out for gas flows from 55 to 85 l/min, 10 to 25 % H₂, and an arc current of 600A. The mass increase of a Hastelloy-X strip with bond coat and top coat was measured after one torch passage. The powder feed rate and specimen movement were kept constant, and centreline powder injection was set for all measurements. The following observations were made:

- The deposition efficiency decreased dramatically when the gas flow was increased from 55 to 85 l/min.
- For constant gas flow the deposition efficiency showed a maximum at 15 to 20 %H₂. This effect was more pronounced for higher gas flows.

It was concluded that deposition efficiency increased as the spraying conditions became “milder”, and that an optimum had not yet been reached. Apparently, the spray parameters during the pilot measurements resulted in an aggressive “excessive energy input” plasma: the heating power and/or velocity were too high to fulfil equation 2.1 for ZrO₂-Y₂O₃ particles. A possible explanation for the low deposition efficiency at high gas flows is that the high velocity particles rebound from impact.

Based on these pilot measurements, it was decided to perform the main deposition efficiency studies with ‘milder’ plasma conditions: a gas flow, ϕ , of 45 and 55 l/min, a hydrogen content ranging from 10 to 25% H₂, and an arc current, I , of

500A and 600A. The measurements were done with a water cooled steel tube having a diameter of 102 mm, which is the same as that of the specimen holder used for spraying the TBCs (see section 2.2.2). The tube was provided with a NiCrAlY bond coat. The test conditions are presented in table 2.3. Materials specifications are given in section 2.4.1, table 2.4.

Table 2.3 Deposition efficiency test conditions: these are in addition to the spraying parameters

rotational speed [rpm]	traverse speed [mm/s]	powder feed rate [g/min]	spraying distance [mm]
200	25	45	100

Figure 2.4 shows the results of the deposition efficiency studies. The seven above the horizontal line were done six months before the five below the line. The difference in deposition efficiency between the two measurements with $\varphi=45$, $\%H_2=15$ and $I=500A$ on either side of the line (59.9% vs. 56.8%) illustrates clearly the unreliable behaviour of the plasma, as mentioned in section 2.2.4. In order to compare the results of the two measurement sets, the results below the line were up-scaled to get agreement between the two [$\varphi=45$, $\%H_2=15$, $I=500A$] measurements:

$$DE_{scaled} = \frac{59.9}{56.8} DE_{measured} \quad (2.3)$$

where DE is the deposition efficiency. The up-scaling is indicated by the light grey bands added to the dark grey ones. The following observations can be made from figure 2.4:

- The deposition efficiency increased when the plasma spray conditions became milder (except the result for $\varphi=45$, $\%H_2=15$ and $I=600A$). The Verbeek parameters resulted in a relatively low DE .
- The use of an air shield resulted in a higher deposition efficiency. This effect is not understood, but is considered beneficial.
- Substrate cooling did not affect the deposition efficiency.
- For $\varphi=45$ l/min the deposition efficiency increased with increasing hydrogen content of the gas, but the difference in DE for $\%H_2=20$ and $\%H_2=25$ was small.

It was concluded that the parameter setting $\varphi=45$ l/min, $\%H_2=20$ and $I=500A$ was the best choice for spraying TBCs. This is based on the following considerations:

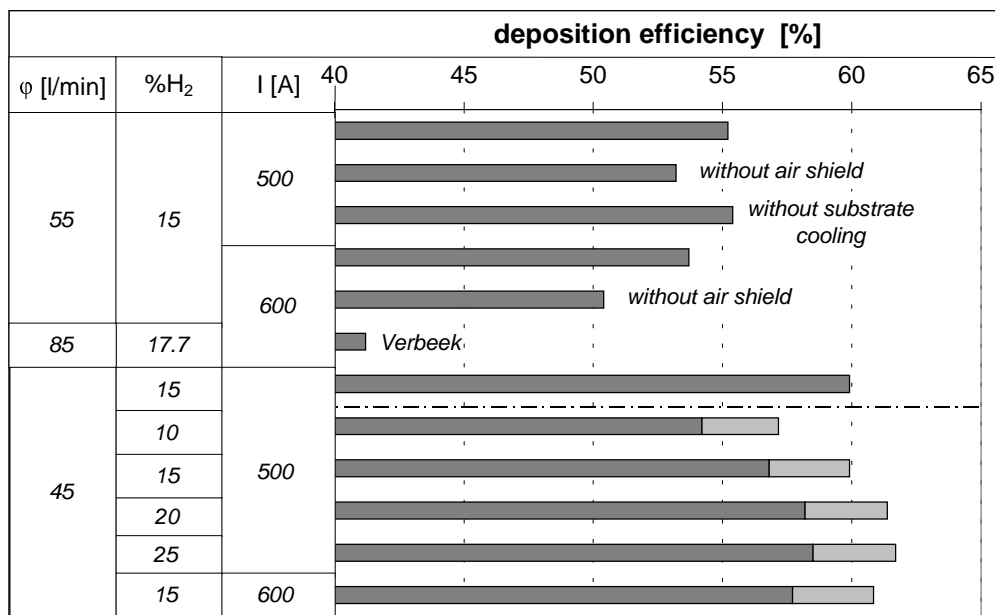


Figure 2.4 Results of deposition efficiency measurements. The measurements above the dashed/dotted line were done 6 months before the measurements below the line. The results below the line are up-scaled to get agreement between the two [45/15/500]-measurements: the light grey bands denote the up-scaling

- Deposition efficiency was highest for $\varphi=45$ l/min.
- The plasma with $\varphi=45$ l/min and $I=600$ A was very unstable and hence unsuitable for coating deposition.
- The cathode wear increased with increasing %H₂, and this makes 20%H₂ more suitable than 25%H₂.

2.4 Spraying the coatings

2.4.1 Materials and spraying conditions

The coatings were applied to Hastelloy-X² substrate strips. The strips were 125 mm long by 30 mm wide and had a thickness of 3.25 mm. After grit blasting, eight strips were mounted on the specimen holder (see section 2.2.2), and provided with a 0.1 mm thick NiCrAlY bond coat. The top coat was then applied. Table 2.4 gives the powder specifications for the bond coat and top coat. The ZrO₂-7.9Y₂O₃ powder is illustrated in figure 2.5: its size is fairly uniform (21-45 μ m) although the particles are angular.

² Hastelloy-X is a nickel-based superalloy (Ni-22Cr-18Fe-9Mo-1.5Co-0.6W) that combines a high-temperature strength with excellent oxidation resistance. It has wide use in gas turbine engines for combustion zone components such as transition ducts and combustion chambers.

Table 2.4 Powder specification for bond coat and top coat

Coating	Composition*	Brand name	Size (μm)	Manufacturing	Morphology
bond coat	Ni-22Cr-10Al-1.0Y	Amperit 413.6	45-90	gas atomised	spherical
top coat	ZrO ₂ -7.9Y ₂ O ₃	Amperit 825.1	21-45	fused & crushed	angular

* in wt%

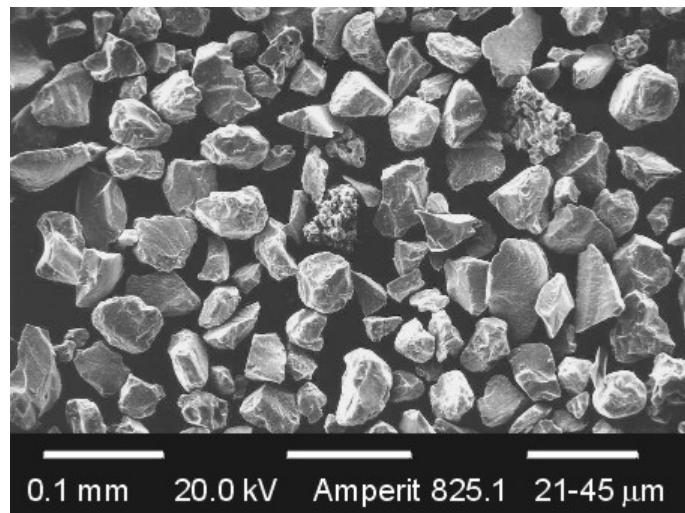
**Figure 2.5** ZrO₂-7.9wt%Y₂O₃ powder

Table 2.5 gives the spraying parameters for the bond coat and top coat. The specimen designation that will be used in this thesis is given in the second row of table 2.5. The arc voltage (U) is the average value for each set of I, ϕ , and %H₂. The plasma enthalpy is defined as the total electric power input ($I \times U$) minus the cooling water losses, divided by the gas mass flow. Though the deposition efficiency was highest for ‘mild’ spraying conditions ($\phi=45$ l/min, %H₂=20, I=500 A), some TBCs were deliberately sprayed with an ‘excessive energy’ plasma to study the differences between these two top coats. The rotational speed and traverse speed for the ‘mild’ plasma TBCs were increased to more industrial settings (Te Raa, 1996). Due to the difference in specimen traverse speed, the number of torch passages was 10 for the TBCs sprayed with the excessive energy plasma and 20 ± 1 per 0.3 mm (linear increase with coating thickness) for the TBCs sprayed with the mild plasma. The variation in number of passages is caused by the plasma variations discussed in section 2.2.4.

Table 2.5 Plasma spray parameters for bond coat and top coat. The bond coat was sprayed with a standard anode, and the top coat with an extended anode.

designation	Bond coat		Top coat			
		55/10	55/25	85/10	85/25	45/20
I [A]	500	600	600	600	600	500
ϕ [l/min]	55	55	55	85	85	45
%H ₂	15	10	25	10	25	20
U [V]	59.6	51.4	63.8	60.2	75.3	56.0
Plasma enthalpy (MJ/kg)	11.2	7.2	11.0	6.7	10.5	8.0
torch traverse speed [mm/s]	3	7	7	7	7	15
specimen holder rotation [rpm]	100	100	100	100	100	225

An important point of clarification is needed here. Although the plasma enthalpies of the 55/10 and 85/10 plasmas are *lower* than that of the 45/20 plasma, they are still referred to as excessive energy plasmas. The reasons are as follows:

- The plasma energy increases with increasing gas flow and increasing current for the same %H₂.
- Particle velocity increases with increasing gas flow (Verbeek, 1992; Diessen, 1998), and so a relatively large part of the energy input is converted to kinetic energy rather than thermal energy.
- The higher deposition efficiency using the ‘mild’ plasma conditions indicates that the particle heating is adequate but the particle velocity is not so high that rebounds occur. Thus the particles do not “bomb” already deposited layers.

2.4.2 Thick TBCs and bond coat preoxidation

As mentioned in the introduction to this thesis, there are several possible ways to increase the life of TBCs. The first is to increase the top coat thickness, resulting in a lower bond coat temperature and hence a lower oxidation rate during thermal tests in which the top coat surface is heated (burner rig tests). During the present research TBCs with thicknesses of 0.3, 0.6, 1.0 and 2.0 mm were prepared and tested. All thick TBCs ($d \geq 0.6$ mm) were sprayed using the “mild” plasma conditions.

Another beneficial way to increase TBC life is to provide the bond coat with an oxygen barrier layer. Of the several possible ways to do so (section 1.2), bond coat pre-oxidation looks very promising owing to good results during thermal tests (Lih *et al.*, 1991) and its being relatively easy and inexpensive. In order to choose a preoxidation treatment for the bond coat it was necessary to conduct some initial studies:

- Bond coats were heat treated in a high temperature furnace at 1050°C for 2.5, 5, 10, 25 and 50 hr.
- Cross-sections of each bond coat were embedded and examined by Scanning Electron Microscopy (SEM) using a JEOL 8600 SX. The oxide layer thicknesses were determined from the SEM photographs.
- The phases and elements were determined to reveal the composition of the preoxidised layer. Phase analysis was done by X-ray diffraction, element analysis by electron probe micro analysis. The experimental details of both methods are described in sections 4.5.2 and 4.6.2 respectively. The elemental analysis was also used to examine the influence of preoxidation on the bond coat composition.

The preoxidising treatment of the bond coats resulted in $<1\mu\text{m}$ (2.5 hr), $1.5\pm 0.25\mu\text{m}$ (5 hr), $2.0\pm 0.5\mu\text{m}$ (10 hr), and $2.5\pm 0.5\mu\text{m}$ (25 hr and 50 hr) thick oxide layers. The oxide layer after only 2.5 hr did not cover the entire surface and was hence unusable for a TBC system. After 5 and 10 hr a dense uniformly thick layer had formed, and was adherent to the bond coat. Longer preoxidation treatments resulted in dense oxide layers which were partly cracked or spalled. Moreover, severe internal oxidation of the bond coat occurred. Figure 2.6 shows the oxide layer on bond coats preoxidised for 5 hr and 50 hr, to illustrate these points.

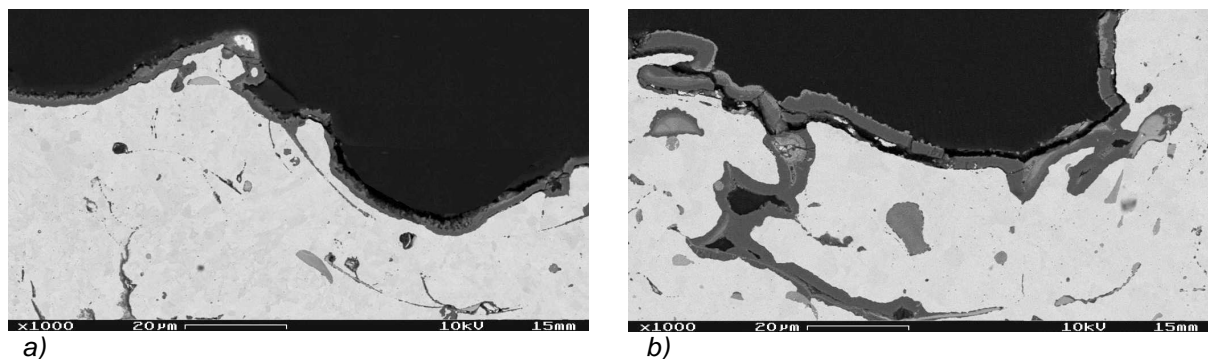


Figure 2.6 Scanning Electron Microscopy (SEM) backscattered electron image of preoxidised bond coat surface. a) 5hr, dense adherent oxide layer. b) 50 hr, dense but partly cracked and spalled oxide layer.

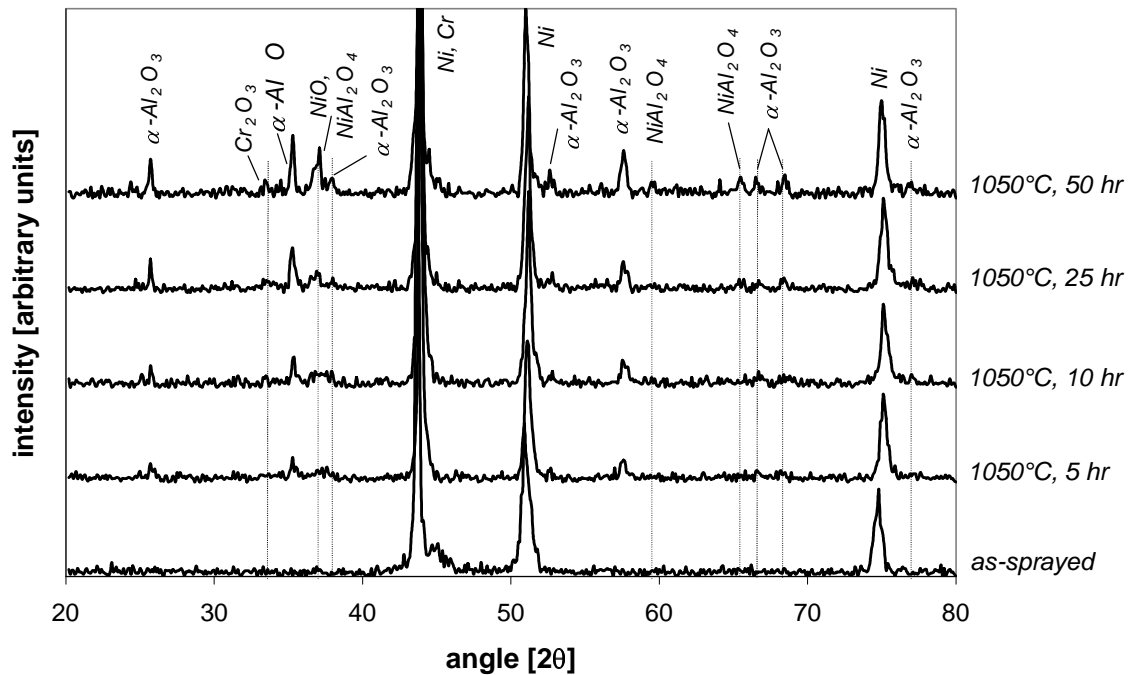


Figure 2.7 Diffraction patterns of as-sprayed and preoxidised bond coats. Preoxidation temperatures and times are indicated on the right-hand side.

Figure 2.7 shows the diffraction patterns of the as-sprayed and preoxidised bond coats (results for 2.5 hr preoxidation time are omitted). For the preoxidation treatments of 5 and 10 hr the oxide layer consisted predominantly of α - Al_2O_3 . Small amounts of other oxides like NiO and spinel type structures (e.g. NiAl_2O_4) were also detected. Preoxidation treatments for 25 and 50 hr resulted in more of these oxides and spinel type structures compared to α - Al_2O_3 , and this change is detrimental to the thermal shock resistance (Wu *et al.*, 1989; Lih *et al.*, 1991; Shillington and Clarke, 1999). N.B.: stress relief in the bond coat due to the heat treatment caused the shifts of the Ni-peaks in the preoxidised specimens (Noyan and Cohen, 1987).

The elemental analysis results support the observation that the oxide layer consisted predominantly of α - Al_2O_3 . Figure 4.11 shows the composition of a bond coat of local thickness 52 μm and preoxidised for 10 hr. At the oxide location a strong increase in Al (from 8 to about 40wt.%) and a decrease in Cr and Ni were observed. The preoxidation heat treatment resulted in a decrease of the bond coat bulk content of Ni and Al, and an increase of Cr. However, the bond coat composition after 5 and 10 hr preoxidation was not dramatically changed (no severe Al-depletion).

It was concluded that preoxidation times of 5 and 10 hr were suitable for further experiments. A 0.3 mm TBC was applied to the bond coats preoxidised for 5 hr, and 0.3 and 0.6 mm TBCs were applied to the bond coats preoxidised for 10 hr.

2.5 Microstructural investigations

2.5.1 Top coat surface

Figure 2.8a shows the top coat surface of a 55/25 specimen. Some individual splats can still be distinguished. Figure 2.8b shows a splat in detail. The hairline cracks are caused by primary cooling stresses, which develop when the deposited particles cool from above the melting temperature to the substrate contact temperature (Kuroda and Clyne, 1991; Verbeek, 1992). The other specimens showed very similar surface morphologies. The top coat surfaces were rather rough, but less so than the underlying bond coat (see Appendix 6A). The roughness was measured on a Mitutoya SurfTest profilometer with a cut-off length of 800 μm and a measurement length of 4 mm. The arithmetic average roughness, R_A , of the surfaces was $4.5 \pm 0.5 \mu\text{m}$ and was independent of the measuring orientation. The TBCs sprayed under 'mild' plasma conditions and those sprayed under 'excessive energy' plasma conditions showed no significant differences in R_A .

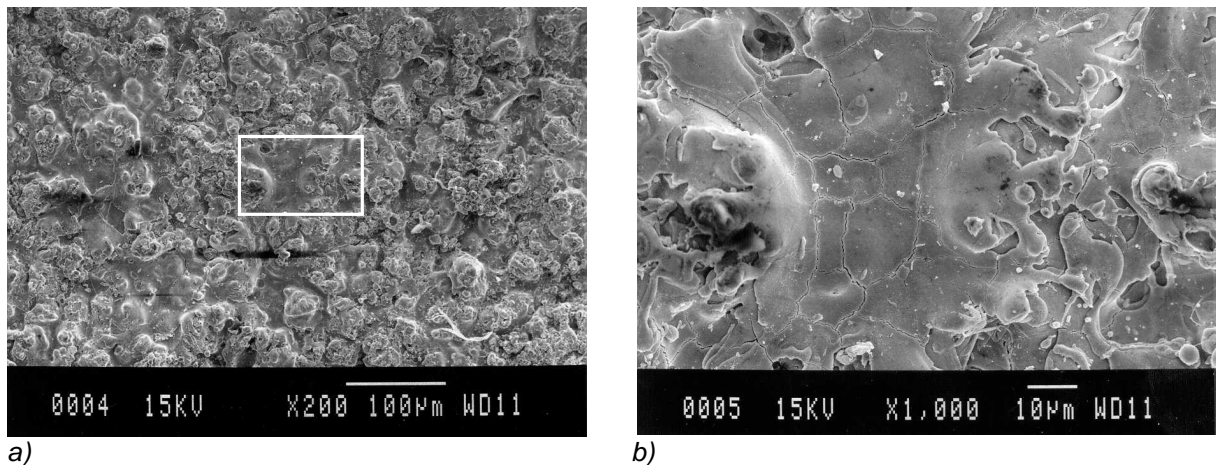


Figure 2.8 Scanning Electron Microscopy (SEM) photograph of top coat surface, 55/25 specimen: b) is a detail of a), showing hairline cracks in a splat

2.5.2 Preparation method

Preparation of TBCs for microscopic examination is a critical process which should be done very carefully, for two reasons. First, cutting with a standard abrasive wheel can cause interface cracks. Second, owing to the brittleness and microcracked porous structure of the top coat, pull-out of small particles easily occurs, resulting not only in a damaged surface but also in a false impression of the porosity (Roode and Beardsley, 1988; Wigren and Pejryd, 1998).

The following preparation procedure was applied. First, samples with appropriate size were cut from the specimen strips with a diamond wire saw (Well 5237). The wire thickness was 0.5 mm and the diamond grain size was 46 μm . The samples were then cold embedded in Technovit 4071. Next, the samples were wet abraded on SiC paper (Struers), successively with 240, 320, 500 and 800 grit. Finally, the samples were polished in five steps on a semi-automatic Struers DAP-V device, see table 2.6.

Table 2.6 Polishing procedure for TBCs

step	cloth	duration (min)	force (N)	polishing medium	lubricant
1	Petrodisk	10	15	6 μm diamond spray*	Lubricant Blue HQ#
2	DP Plan#	5	15	6 μm diamond spray*	Lubricant Blue HQ#
3	Pan W#	5	15	3 μm diamond spray*	Lubricant Blue HQ#
4	DP Dur#	10	15	1 μm diamond spray*	Lubricant Blue HQ#
5	OP Chem#	1	15	OP-S SiO ₂ #	-

= Struers

* = Engis

2.5.3 Microstructures

Figures 2.9 and 2.10 show the microstructures of the 0.3 mm TBCs sprayed with an “excessive energy” plasma ($\phi=85$ l/min, $\%H_2=25$, $I=600A$) and a “mild” plasma ($\phi=45$ l/min, $\%H_2=20$, $I=500A$). Although not obvious from the photographs, both coatings had dense, microcracked structures without large cracks and were similar in these respects³.

Figure 2.11 shows a 1.0 mm TBC. The microstructure is similar to that of the 0.3 mm TBCs. Segmentation cracks — deliberately applied by Wigren and co-workers in thick TBCs to obtain high thermal shock resistance (Wigren *et al.*, 1996b; Bengtsson *et al.*, 1998) — are not present. In the next chapter it will be seen whether the present microcracked thick TBCs possess good thermal shock resistance although they do not have segmentation cracks.

³ Differences in microstructure are mainly caused by differences in level of pull-out, which will be discussed in the next sub-section.

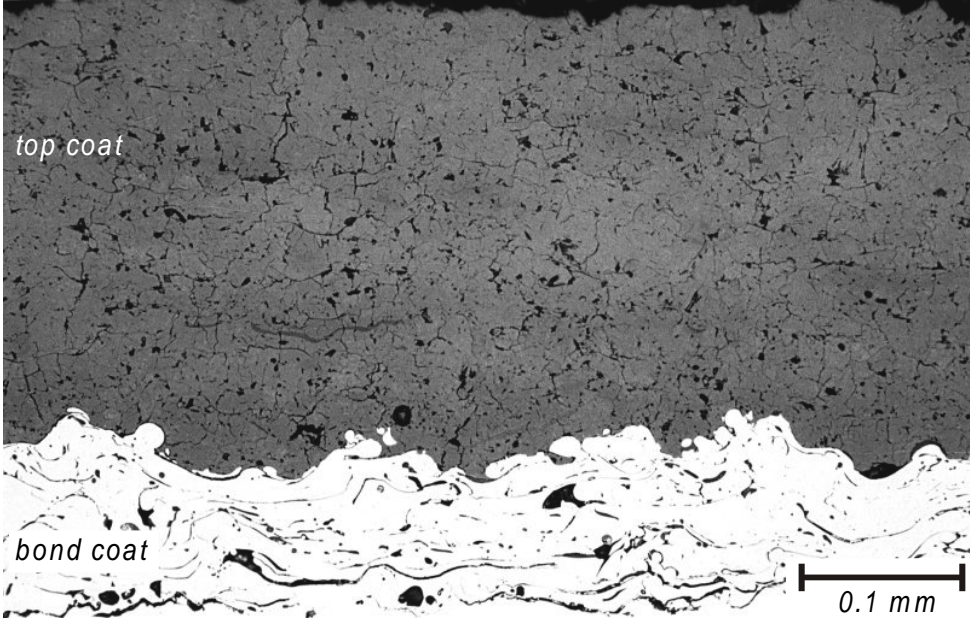


Figure 2.9 Microstructure of TBC sprayed with 'excessive energy' plasma conditions

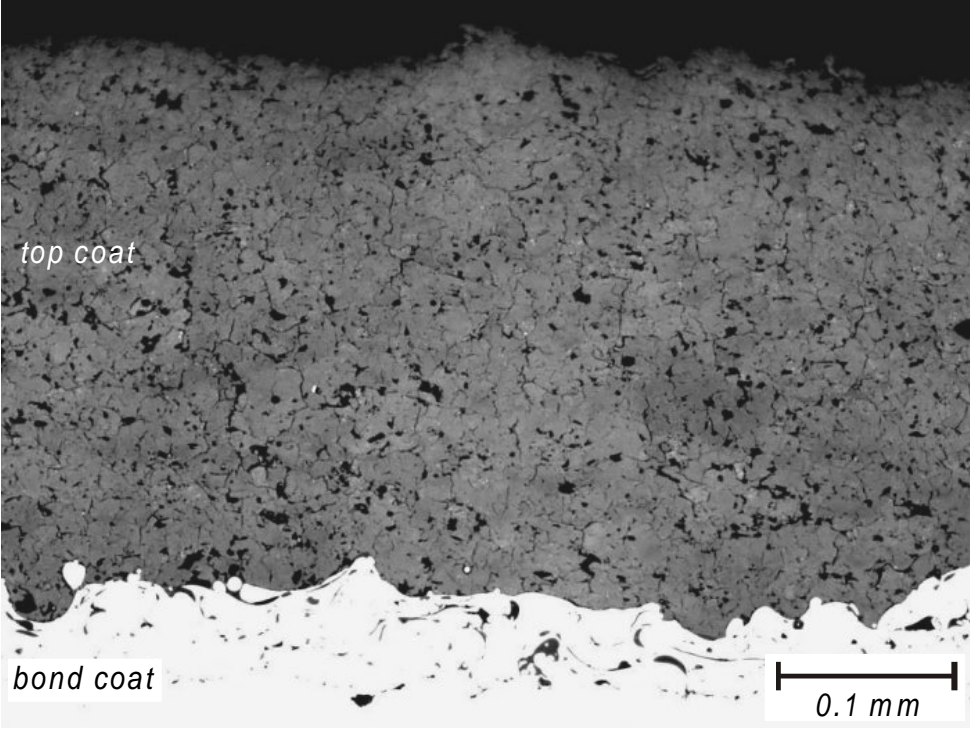


Figure 2.10 Microstructure of TBC sprayed with mild plasma conditions

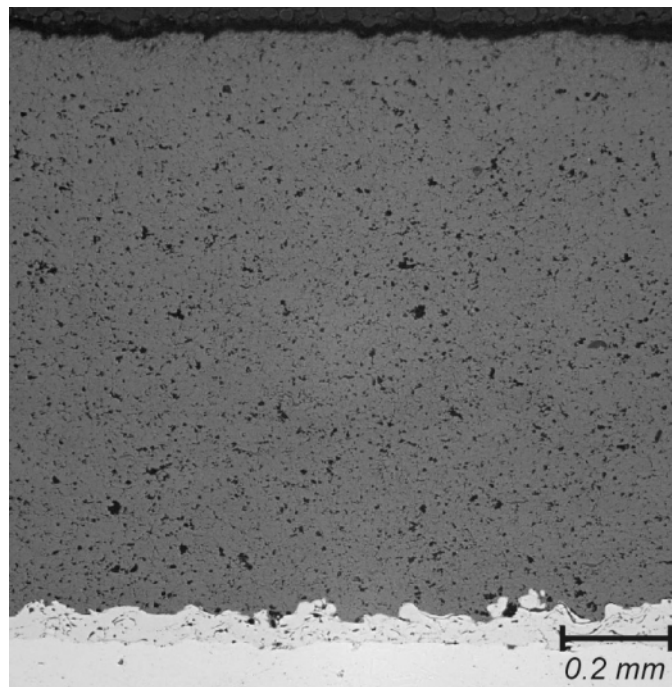


Figure 2.11 Microstructure of 1 mm TBC sprayed with mild plasma conditions

Figure 2.12 shows a 0.6 mm TBC with preoxidised bond coat. The microstructure is similar to that of the 0.3 mm TBCs. The presence of an oxide layer did not result in interfacial cracks. A close examination of the top coat/bond coat interface (not shown here) showed that oxide layer was not damaged by spraying the top coat onto it.

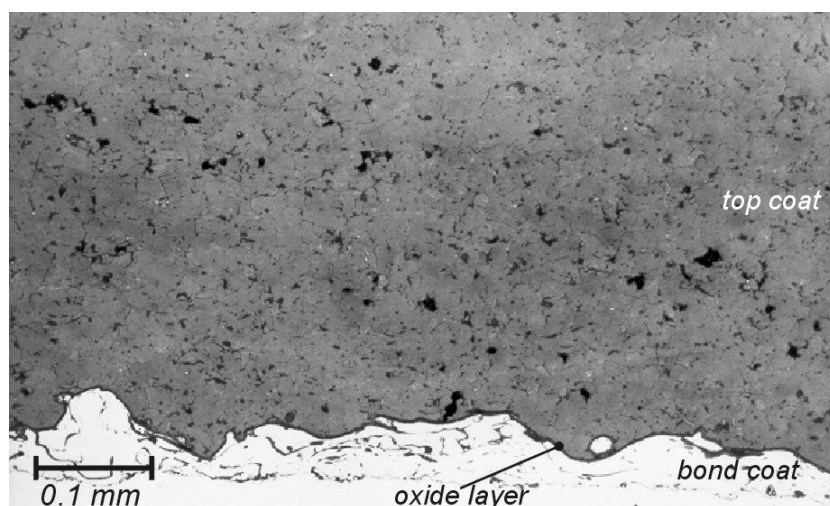


Figure 2.12 Cross-section of 0.6 mm TBC with preoxidised bond coat

For all the microstructures shown here, the observed pores are not necessarily as-sprayed pores. Judging from their angular morphology it is likely that some “pores” are actually particle pull-out. This will be considered in the following sub-section.

2.5.4 Porosity and flexibility

Differences in microstructure owing to different preparation methods find expression in the porosity measured by image analysis, where no distinction can be made between real porosity and particle pull-out. After spraying the “excessive energy” plasma TBCs an ad hoc round-robin was done. Samples of the same TBC coated strip were sent to two other laboratories for preparation. Subsequently both labs measured the porosities of the specimens prepared by themselves and those prepared according to the procedure described in section 2.5.2. Porosity measurements were done using microscopy image analysis.

The preparation procedures used by both laboratories are confidential and cannot be given here in detail. A large difference with the procedure described in section 2.5.2 is that both laboratories (A and B) *vacuum* embedded the specimens. Moreover, lab B applied a 30 min. low-force final polishing step with $\frac{1}{4}$ μm diamond polishing medium.

Figure 2.13 shows the results of the round-robin for 85/10 and 85/25 specimens. The porosity measured by lab A lies between 4% and 6%, the porosity measured by lab B is about 3%. Both the preparation method and the analysis system/operator settings affect the result. Apparently, the preparation procedure described in this chapter, data points AT and BT, results in more particle pull-out than the procedures of the other laboratories, data points AA and BB. The lower porosity measured by lab B may be due to the very long low-force final polishing step, but could also be due to different threshold settings of the porosity image definition by the operator.

Summarising, the round-robin showed that:

- When studying microstructures of TBCs one should be aware of false morphologies, caused by particle pull-out.
- The final result of porosity measurements by image analysis depends not only on the amount of particle pull-out, but also on the settings by the operator.
- The TBCs for the present investigation have a low porosity ($P \approx 3\%$ according to lab B) compared to industrial TBCs ($10\% < P < 25\%$).

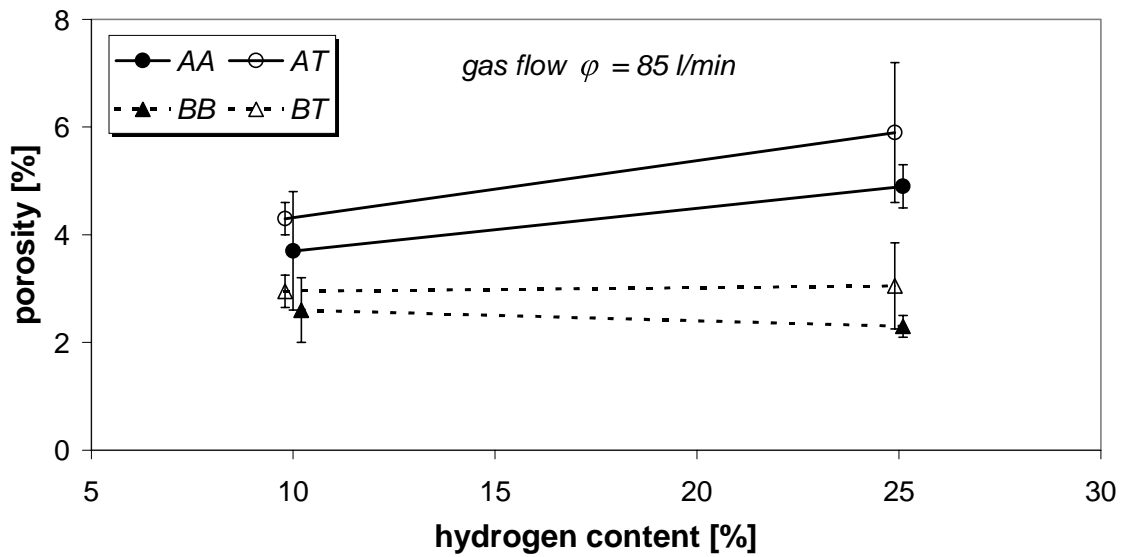


Figure 2.13 Results of round-robin porosity measurements. The first letter of each plot label indicates the laboratory that did the porosity measurement; the second letter indicates the laboratory that prepared the specimens. T=Eindhoven University of Technology. Data points are deliberately shifted aside from 10 and 25% H_2 to show error bars.

Flexibility

TBC flexibility can be assessed from its Young's modulus. The lower the Young's modulus, the more flexible the TBC and the higher its capability to accommodate and withstand thermal stresses. Typical values of a TBC Young's modulus range from 10 to 70 GPa, depending on the level of porosity and/or microcrack density but also on the measuring method and direction (Steffens and Fischer, 1988; Verbeek, 1992; Duan et al, 1997). Although the porosity of the present TBCs is low, the flexibility is expected to be high owing to the deliberate formation of a dense network of microcracks. The Young's moduli of both the "excessive energy" plasma and "mild" plasma TBCs were measured by a three-point-bending test as described by Verbeek (1992). An average Young's modulus of 25 ± 5 GPa was obtained. This value will be used in data reduction for the stress measurements (chapter 5) and for modelling (chapter 6). *It is important to note that for both cases the typical low porosity microcracked microstructure is represented only by this measured value of the Young's modulus.*

3 THERMAL TESTING OF TBCs

3.1 Introduction

The behaviour of TBCs during thermal testing can provide an indication of coating performance in actual gas turbine operation. The number of thermal cycles to failure and the failure mode depend on coating characteristics like top coat thickness, top coat density, top coat / bond coat interface roughness and as-sprayed residual stresses. Also, many thermal loading effects may influence the top coat durability: bond coat oxidation, thermal stresses due to thermal expansion mismatch strains, thermal stresses due to fast temperature changes and steep temperature gradients, phase transformations of the top coat, creep behaviour of both the top coat and bond coat, changes in the Young's modulus of the top coat, sintering of the top coat, top coat embrittlement, and Al-depletion of the bond coat (Miller and Lowell, 1982; Watson and Levine, 1984; Chang *et al.*, 1987a; Wu *et al.*, 1989; DeMasi-Marcin *et al.*, 1990; Thornton *et al.*, 1994; Tsui *et al.*, 1998; Zhu and Miller, 1997; Brindley, 1997; Nissley, 1997; Bengtsson *et al.*, 1998; Rettig *et al.*, 1999; Haynes *et al.*, 2000; Rabiei and Evans, 2000). Moreover, many of these effects may or could interact with each other. In practice, however, there will be a predominant failure mechanism, and this as well as the actual life depend on the TBC system being studied, the method of thermal testing and the severity of the test conditions.

In the literature several methods are described for subjecting coatings to a thermal load. A coated specimen can be placed in a high temperature furnace for isothermal heating cycles (Wu *et al.*, 1989; Joshi and Srivastava, 1993, 1995; Thornton *et al.*, 1994; Tsai and Tsai, 1995; Rabiei and Evans, 2000). In this case, hereafter referred to as furnace testing, the entire specimen is kept at an elevated temperature for a long time, after which the specimen is cooled in a relatively short time, and this

is repeated many times. Another method is burner rig testing, where the top coat surface is heated with a flame. The heating period can be short (McDonald and Hendricks, 1980; Miller and Lowell, 1982; Miller and Berndt, 1984; Taylor *et al.*, 1990; Bengtsson *et al.*, 1998) or long enough to result in a steady state temperature profile in the specimen (McDonald and Hendricks, 1980; Miller and Lowell, 1982, Watson and Levine, 1984). In both cases, heating periods are followed by short cooling periods. Finally, a high heat flux can also be obtained by heating the top coat surface with a laser (Zhu and Miller, 1997; Choules *et al.*, 1998; Rettig *et al.*, 1999). For this method the heating period can be very short (< 1 sec), which makes it suitable for high cycle thermal fatigue testing to simulate *e.g.* the in-cylinder combustion process in a diesel engine.

Burner rig tests differ essentially from furnace tests. During burner rig testing a thermal gradient exists over the specimen thickness, resulting in a relatively low interface temperature. During furnace testing the entire specimen is heated to a certain temperature and in general held at temperature for much longer times, which means that degradation of the bond coat and substrate owing to oxidation and diffusion is more severe. Also, during burner rig tests thermal stresses are mainly induced by steep temperature gradients and fast temperature changes, while during furnace testing the thermal stresses are mainly cooling stresses caused by the large differences in thermal expansion between substrate, bond coat and top coat. Nevertheless, while it is recognised that the behaviour of TBCs during burner rig testing and actual gas turbine use is the true indicator of coating performance, much information regarding the comparative durability of TBC systems can be obtained from furnace thermal cycling (Joshi and Srivastava, 1995).

The purpose of this chapter is to study the behaviour of the TBCs described in the previous chapter using three thermal testing methods: *furnace tests*, short cycle burner rig tests, hereafter referred to as *thermal shock tests*, and long cycle burner rig tests, hereafter referred to as *thermal cycling tests*. The effects of top coat thickness, bond coat preoxidation, cycle lengths and test temperatures are considered. The emphasis in this experiment-based chapter will be on the lives of TBCs and a phenomenological description of the failure modes. Section 3.2 describes the furnaces and burner rig used and the test conditions. Section 3.3 gives the thermal gradients observed during burner rig testing. Section 3.4 gives the number of cycles to failure for all test methods. The observed failure modes and microstructural changes are presented in section 3.5, and the results are discussed in section 3.6. Section 3.7 ends the chapter with conclusions.

3.2 Experimental

Table 3.1 shows an overview of the test programme. Details of the thermal test equipment, test conditions, and specimens are given in subsections 3.2.1 to 3.2.3.

Table 3.1 Survey of thermal test programme. The test temperatures for burner rig tests are the top coat surface temperatures, the cycle lengths include heating and cooling.

top coat thickness [mm]		→	0.3			0.6		1.0	2.0
preoxidation time [hr]		→	0	5	10	0	10	0	0
type of test	T _{test} [°C]	cycle length	number of specimens						
<i>Furnace Testing</i>									
ITC	1137	1 hr	6	1	1	3	2	1	...
NLR	1100	1 hr	3
		2 hr	3
		8 hr	3
		24 hr	3
	1000	1 hr	3
<i>Burner Rig Testing</i>									
thermal shock	1300	1 min	2	...	1	1	...
	1350		2	1	1
	1400		4	1	2
	1475		1	...
thermal cycling	1350	1 hr	1	1	1
	1400		1	...	1	...
	1500		1	1

3.2.1 Thermal test equipment

Furnaces

Two types of furnace tests were done. The first was to investigate the effect of coating thickness and preoxidation. This test was carried out at Interturbine Coating Centre, Lomm, The Netherlands, and will be referred to as the *ITC furnace tests*. The computer controlled furnace test rig is shown schematically in figure 3.1. Sample heating is done with MoSi₂ heating elements, and cooling is by forced convection.

The second type of furnace test was to investigate the effect of cycle length. This test was carried out at the National Aerospace Laboratory NLR, Amsterdam, The Netherlands and will be referred to as the *NLR furnace test*. A photograph of the experimental set-up is given in figure 3.2. It consists of a high temperature furnace with four ceramic tubes that run from the back wall of the furnace to four holes in the furnace door. The samples are placed in v-shaped slides that can be pushed pneumatically in and out of the ceramic tubes. The cycle time for each slide, which can contain five samples, can be programmed separately. Thus four experiments with different cycle times can be done concurrently.

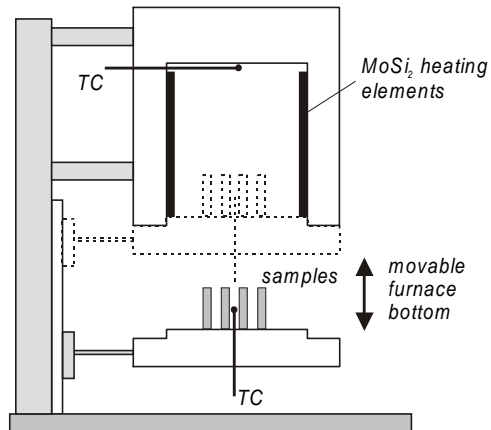


Figure 3.1 Schematic drawing of the ITC furnace (TC = thermocouple)

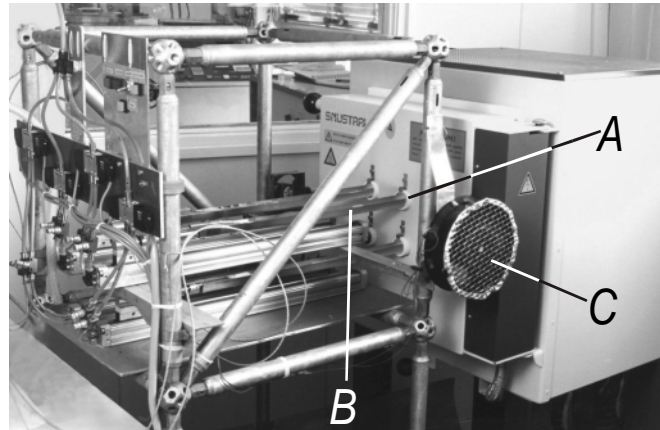


Figure 3.2 NLR furnace test set-up. A: end of ceramic tube through hole in door; B: v-shaped slide; C: air fan

Burner rig

The thermal shock and thermal cycling tests were done with a special burner rig developed to simulate a local thermal load, which occurs for example when a fuel nozzle in a combustion chamber is misaligned. Figure 3.3 shows the burner rig in operation. It consists of an acetylene-oxygen burner and two air jets, one at each side of the burner. Figure 3.4 shows the burner schematically. It produces a flame with a diameter of about 15 mm. At the front of the burner head (1), five small outflow holes (diameter 0.8 mm) are distributed over a 4 mm diameter area. The coupling piece (2) contains a metal gauze insert to enable a homogenous gas mixture and constant outflow. To avoid overheating the burner head a copper cooling pipe (3) is brazed onto its front. Both the burner and air jets are mounted on a computer-controlled trolley. Two specimens (width: 30 mm, length: >80 mm) are clamped in a water-cooled holder in such a way that when one specimen is heated by the burner, the other one is cooled by one of the two air jets.

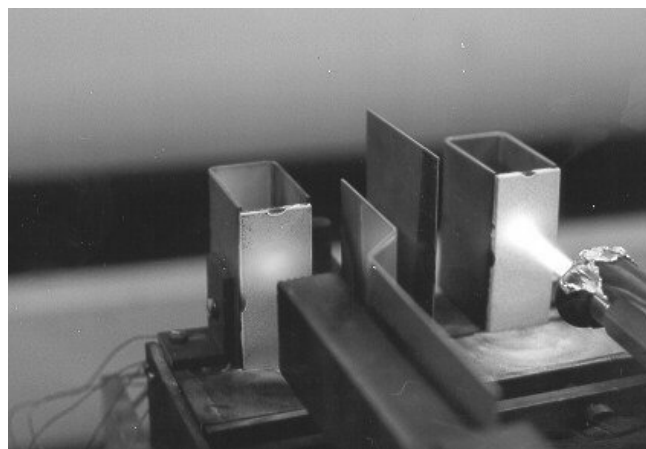


Figure 3.3 The burner rig in operation. The specimen on the right side is being heated, the left side one is being cooled by an air jet.

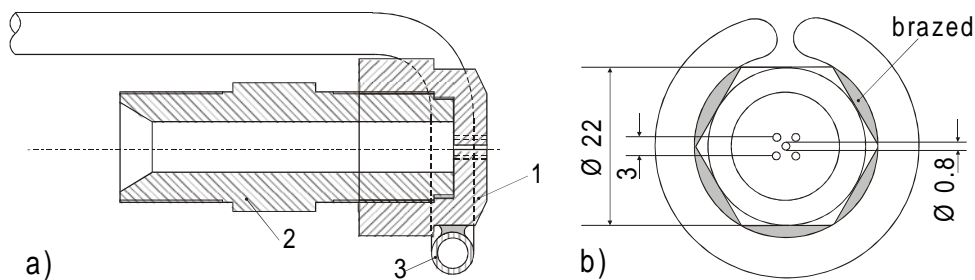


Figure 3.4 The burner head used for the thermal shock and thermal cycling tests: a) composite sketch with 1: copper end piece, 2: brass coupling piece with length of 50 mm, and 3: copper coolant pipe, $\text{Ø}6 \times 4$ mm; b) front view of burner head (dimensions in mm)

The test temperature given in table 3.1 is the top coat surface temperature, T_{surf} , and is measured with an optical pyrometer. The substrate rear side temperature, T_{sub} , is measured at the mid-point of the heated area with a thermocouple. The signal from the thermocouple on the substrate rear side is sent to the computer, where it is used to control the test. The heating and cooling rates and the maximum and minimum temperatures of the top coat surface are controlled by the distance between the specimens and the burner and air jets. Using the same device as during the plasma heat flux measurements (see sub-section 2.2.2), the heat flux from the burner was determined to be about 0.6 W mm^{-2} at a stand-off distance of 45 mm. At that distance the heat flux decreased by approximately 0.12 W mm^{-2} per cm stand-off distance. It must be mentioned that owing to deviations in the gas pressure the heat flux was not constant, resulting in a varying top coat surface temperature. However, this effect was minimised by frequently controlling the gas flow, and the variation of T_{surf} was kept to within $\pm 30^\circ\text{C}$.

Compared to the more conventional burner rig tests, where the entire surface of a specimen is heated (see *e.g.* Verbeek, 1992) the present local thermal load test set-up results in an extra temperature gradient that is parallel to the surface.

3.2.2 Test conditions

Furnace tests

During the *ITC furnace tests* the samples (30×30 mm) were heated to 1137°C . The cycle length was 1 hr, including a 4 min heat-up period and a 6 min cool-down to 200°C . After every 20 cycles the samples were cooled to room temperature and kept there for 4 hr. Any failures of the samples were detectable during each 6 min cooling period, and the samples were thoroughly inspected for signs of failure after a sequence of 20 cycles. The criterion for failure and removal of the *ITC furnace test* samples was 20% delamination of the top coat.

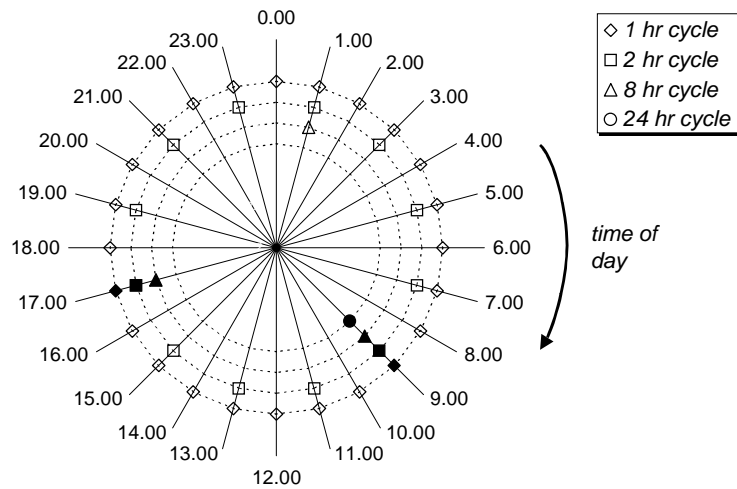


Figure 3.5 Cool-down and inspection schedule for NLR furnace testing. Open symbols: cool-down; closed symbols: cool-down and inspection (once per day for 24 hr cycles, twice per day for shorter cycles).

During the *NLR furnace tests* the samples (20×10 mm) were heated to 1100°C. The cycle lengths were 1, 2, 8 and 24 hr, including a heat-up period of approximately 4 min and a cool-down to room temperature of about 3 min. The samples were inspected thoroughly according to the schedule in figure 3.5. The inspections took no more than 10 minutes. In order to keep the different cycles in phase the four timers were synchronised every 24 hr. Three coated specimens were tested for each cycle time. The criterion for failure and removal of the NLR furnace test samples was 25% top coat delamination. The tests were also stopped if no damage had occurred after 1000 hr. Since the number of cycles between the first visual damage and 25% delamination was rather large, the number of cycles after which the first corner of the specimen delaminated was also recorded. After the tests at 1100°C, a test at 1000°C was run with 1 hr cycles to investigate the effect of temperature. This test was stopped after 25% delamination or 2000 hr, whichever came first.

Burner rig tests

During thermal shock the specimens were heated in 28 s to a maximum T_{surf} . This temperature was varied from 1300°C to 1475°C in order to investigate its effect on the failure mechanism. After the heating period the specimens were cooled over the entire coating surface for 28 s, after which T_{sub} was about 400°C. After each 100 cycles the specimens were cooled to room temperature in order to simulate gas turbine shutdown.

During thermal cycling the test specimens were heated for 60 minutes. A steady state was reached after a short transient period. The steady state surface temperature of the top coat was deliberately increased with increasing coating thickness for the following reason. In actual gas turbine operation the heat input is constant, irrespective of coating thickness. Therefore, owing to the low thermal conductivity of TBCs the surface temperature of thicker top coats will be higher than for thinner top coats. This was readily simulated by keeping the stand-off distance of the burner practically the same for all coating thicknesses (only the 1.0 mm TBC was tested at two temperatures). After the heating period the specimens were cooled for 1 min to about 200°C.

The burner rig tests were stopped if delamination of the top coat occurred in the flame area or in the case of severe bond coat and/or substrate degradation. The tests were also stopped if no damage had occurred after a large number of cycles.

3.2.3 Specimens and number of tests

The tests were done mainly with the specimens coated with the 'mild' plasma (45/20). Some exceptions were made for the 0.3 mm TBCs. These were as follows (spraying parameters and specimens codes are given in chapter 2, table 2.5):

- ITC furnace test: done with TBCs deposited under 'mild' plasma and all 'excessive energy' plasma conditions (55/10, 55/25, 85/10, 85/25);
- Burner rig thermal shock, $T_{\text{surf}}=1300^{\circ}\text{C}$: done with TBCs deposited under 'mild' plasma and one 'excessive energy' plasma condition (55/10)
- Burner rig thermal shock, $T_{\text{surf}}=1400^{\circ}\text{C}$: done only with TBCs deposited under the 'excessive energy' plasma conditions (55/10, 55/25, 85/10, 85/25).

Since thermal testing of TBCs is a very time-consuming process and many different coatings were tested, the number of duplicate experiments was kept small, see table 3.1. Most experiments were repeated twice or more, but when there was an evident trend for any type of experiment then only one sample was tested. This was the case when determining the influence of preoxidation treatment time (5 hr vs. 10 hr) which was evaluated for thermal shock, thermal cycling and furnace tests. It was also the case when the thick coatings did not fail, and for the thermal cycling tests in general.

After all tests the specimens were cross-sectioned and examined microscopically. To prevent any damage by the preparation process the coatings were impregnated with glue, and in some cases a small coupon of stainless steel was glued on the top coat surface to assist its retention.

3.3 Temperature profile during burner rig testing

3.3.1 Through-thickness gradient

The maximum temperature on the substrate rear side during the burner rig tests (T_{sub}) depended on the coating thickness and on whether or not the specimen had reached a steady state (thermal cycling vs. thermal shock). Moreover, owing to microstructural changes and crack forming the substrate temperature changed during testing. Table 3.2 gives the average T_{sub} at the *beginning* of the burner rig tests for various values of T_{surf} . For the thermal shock tests T_{sub} after 30 s is given, and for the thermal cycling tests the steady-state T_{sub} is given. Bond coat preoxidation had no effect on the thermal gradient.

Table 3.2 Maximum substrate temperatures (T_{sub}) and temperature differences between top coat surface and substrate rear side (ΔT) during the beginning of TBC burner rig testing for several top coat thicknesses (d_{tc}) and top coat surface temperatures (T_{surf})

Burner rig tests	d_{tc} [mm]	T_{surf} [°C]	T_{sub} [°C]	ΔT [°C]
Thermal shock (after 30 s)	0.3	1300	1000	300
		1350	1040	310
		1400	1080	320
	0.6	1400	875	525
		1300	750	540
		1475	790	685
Thermal cycling (steady-state)	0.3	1350	1100	250
	0.6	1400	1030	370
	1.0	1400	975	425
		1500	1000	500
	2.0	1500	940	560

Figure 3.6 shows the same data plotted as ΔT versus top coat thickness. It is seen that the temperature difference between the top coat surface and substrate rear side, *i.e.* the thermal barrier effect of the top coat, increased with increasing top coat thickness – as expected – and that this effect was larger during the transient period (thermal shock) than during steady-state (thermal cycling). Furthermore, the thermal barrier effect was larger for higher heat input, *i.e.* higher T_{surf} , for both types of test.

3.3.2 Radial temperature profile

Figure 3.7 shows an example of the radial temperature profile at the substrate rear side after 30 s, measured with thermocouples ($d_{\text{tc}}=0.3$ mm). The top coat surface

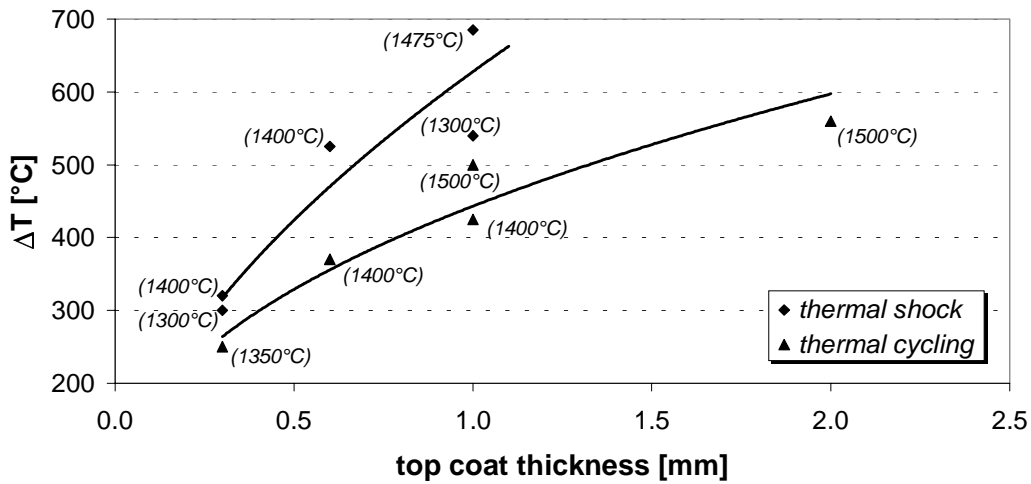


Figure 3.6 Temperature difference between top coat surface and substrate rear side during the beginning of each burner rig test. The values in parentheses are the corresponding top coat surface temperatures, the lines indicate trend differences between the two types of tests (thermal shock and thermal cycling).

temperature was 1300°C. The temperature decrease in the vertical direction (c-f2-e2) is larger than that in the horizontal direction (c-f1-e1), namely 200°C compared to 100°C. This is explicable from the geometry: the distance between location e2 and the specimen top edge is larger than that between location e1 and the specimen side edge, and so there is more material in the vertical direction to act as a heat sink.

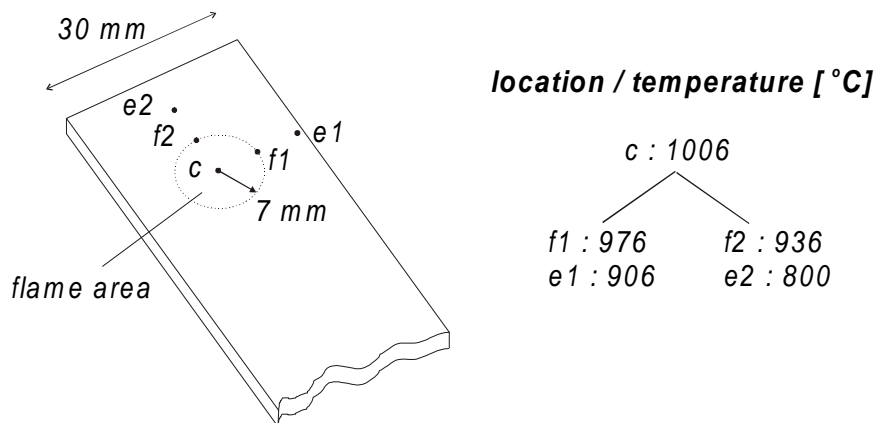


Figure 3.7 Radial temperature profile at substrate rear side 30 s after beginning a burner rig test. $T_{surf}=1300^{\circ}\text{C}$; $d_{tc}=0.3\text{ mm}$

3.4 Number of cycles to failure

This section presents the number of cycles to failure for all tests. For most cases failure is defined as (partial) delamination of the top coat. However, many different failure modes were observed, and these will be treated separately in section 3.5.

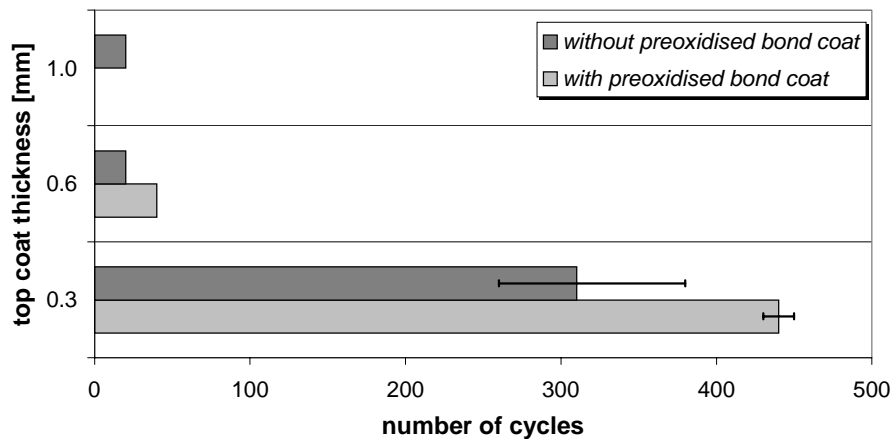


Figure 3.8 Number of cycles to failure during the ITC furnace test for TBCs with and without a preoxidised bond coat. Test temperature is 1137°C

3.4.1 Furnace tests

ITC furnace tests

Figure 3.8 shows the results of the ITC furnace tests. Delamination of the top coat almost always occurred during the 4 hr stay at room temperature after a sequence of 20 cycles. The 0.3 mm TBCs failed on average after 310 cycles. No appreciable effect of the spraying parameters was found. A considerable increase in cycles to failure (440 cycles) was obtained by using a preoxidised bond coat. However, the difference in life between the 5 hr and 10 hr preoxidised specimens was negligible: 450 and 430 cycles respectively.

The number of cycles to failure decreased dramatically with increasing top coat thickness. The 0.6 mm and 1.0 mm coatings failed within the first 20 cycles or during the 4 hr stay at ambient temperature after the first 20 cycles. Of the two 0.6 mm TBCs with a preoxidised bond coat, one failed after 20 cycles, and the other after 40 cycles.

NLR furnace tests

Figure 3.9 shows the results of the NLR furnace tests at 1100°C, whereby the number of cycles to failure and the time to failure are plotted against cycle length. It is seen that longer heating cycles reduce the number of cycles to failure but increase the time to failure: all 1 hr and 2 hr cycle specimens and one 8 hr cycle specimen failed within 1000 hr, but not the 24 hr cycle specimen. Delamination of the first corner, which was observed for all specimens except two of the 24 hr cycle specimens, occurred on average at one-quarter of the total life.

The specimens tested at 1000°C showed delamination at all four corners, beginning at about 1200 cycles, but this was still less than 25% of the area after 2000 cycles.

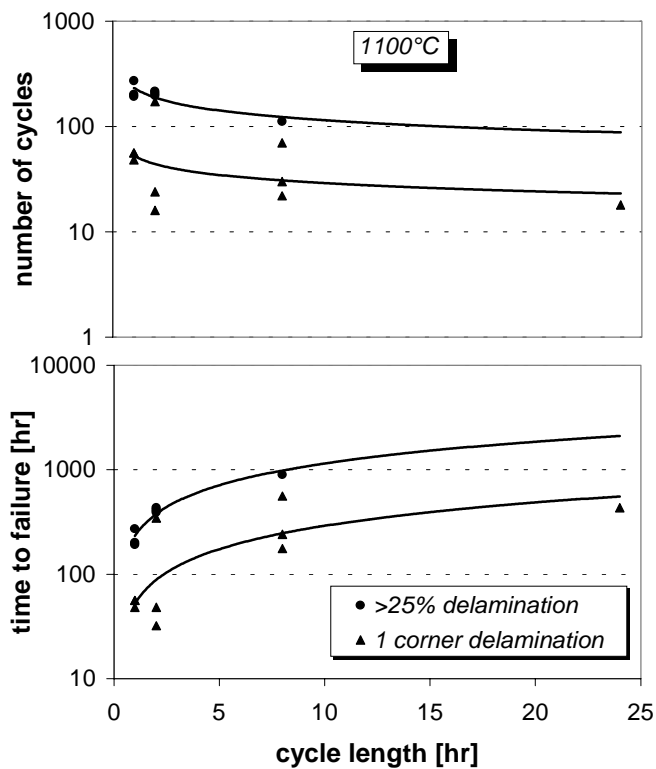


Figure 3.9 Number of cycles to failure and time to failure during the NLR furnace test for 0.3 mm TBCs. Test temperature is 1100°C. The number of cycles and time after which the first corner spalled off are also given. The curves are a power law fit.

3.4.2 Burner rig tests

Thermal shock

Figure 3.10 shows the results of the burner rig thermal shock tests. The number of cycles to failure for the 0.3 mm TBCs decreased greatly with increasing temperature. However, as will be shown in sub-section 3.5.2, the failure mode also changed. Bond coat preoxidation had no significant effect on the number of cycles to failure.

The thick TBCs (0.6 mm and 1.0 mm) without a preoxidised bond coat did not fail – or would not have failed – within 5000 cycles (testing of the 1.0 mm TBC at 1475°C was stopped after 3000 cycles, for reasons given in sub-section 3.6.2). However, specimens with a 0.6 mm top coat *and* a preoxidised bond coat failed after about 2400 cycles when tested with $T_{\text{surf}}=1400^{\circ}\text{C}$.

Thermal cycling

Figure 3.11 shows the results of the burner rig thermal cycling tests. The thin coatings ($T_{\text{surf}}=1350^{\circ}\text{C}$) failed after about 100 cycles, but the specimens with a 0.6 mm and 1 mm top coat tested at $T_{\text{surf}}=1400^{\circ}\text{C}$ did not fail within 250 cycles. Finally, tests of the 1 mm and 2 mm coatings at $T_{\text{surf}}=1500^{\circ}\text{C}$ resulted in failure after 60 and 3 cycles respectively. In sub-section 3.5.2 it will be shown that the failure mode depended on the top coat thickness.

Bond coat preoxidation resulted in an increase in lifetime of about 25% (115 vs. 92 cycles) for the 0.3 mm specimens. The difference in results between 5 hr and 10 hr preoxidation was negligible: delamination occurred after 116 and 115 cycles respectively.

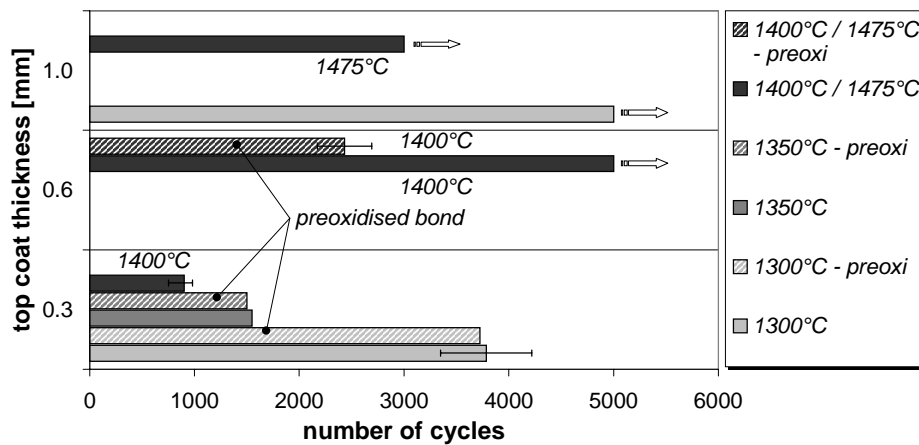


Figure 3.10 Number of cycles to failure during burner rig thermal shock tests as a function of coating thickness and test (top coat surface) temperature. The hatched bars represent the results of the TBCs with a preoxidised bond coat. Error bars indicate the minimum and maximum observed number of cycles, where appropriate.

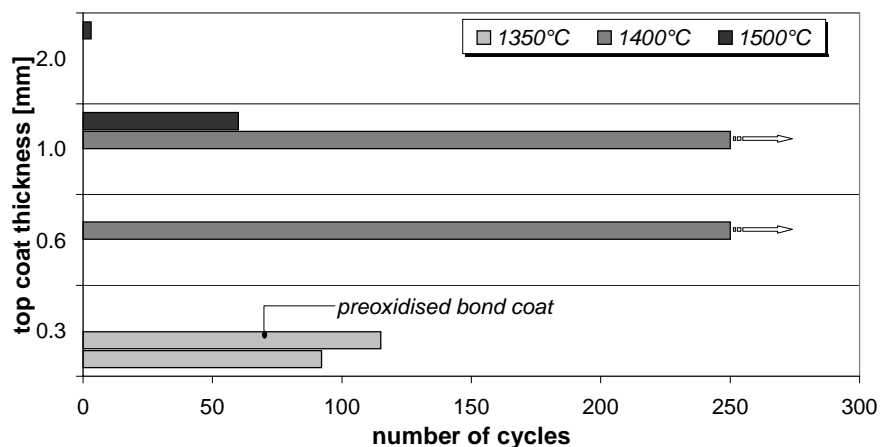


Figure 3.11 Number of cycles to failure during burner rig thermal cycling tests as a function of coating thickness and test (top coat surface) temperature.

3.5 Failure modes and microstructural changes

Tables 3.3 and 3.4 provide an overview of the observed failure modes, which will be described and discussed in the following sub-sections. The codes for the failure modes in table 3.4 and in the text refer to the codes in the second column of table 3.3.

Before discussing the results we define here *remaining* coating as non-delaminated coating material (e.g. the grey material in failure mode TN), and *residual* coating as the coating material still adhering to the bond coat after delamination (e.g. the grey material in failure mode TCD).

Table 3.3 Schematic overview of failure modes. Grey-shaded material represents top coat

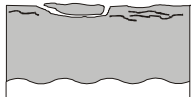


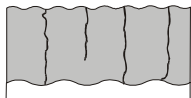
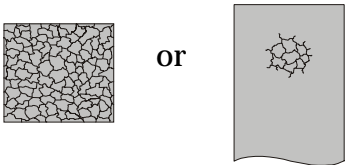
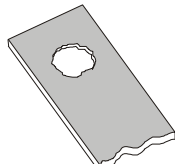
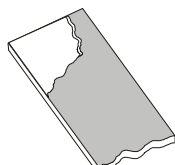
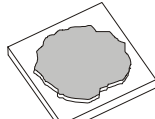


Description of failure mode	Code	Schematic representation
<i>Top coat Surface Spalling</i>	<i>TSS</i>	
<i>Top coat Complete Delamination</i>	<i>TCD</i>	
<i>Top coat Interface Cracking</i>	<i>TIC</i>	
<i>Top coat Vertical Cracking</i>	<i>TVC</i>	
<i>Top coat Segmentation Cracking (furnace test or burner rig)</i>	<i>TSC</i>	
<i>Top coat Flame area Delamination</i>	<i>TFD</i>	
<i>Top coat Edge-to-flame-area Delamination</i>	<i>TED</i>	
<i>Top coat Nibbling-off</i>	<i>TN</i>	
<i>severe Bond coat Degradation (interface oxide layer, internal oxidation, substrate/ bond coat interface carbides and oxides)</i>	<i>BD</i>	
<i>Specimen Bending</i>	<i>SB</i>	

Table 3.4 Observed failure modes for the three thermal tests: d_{tc} =top coat thickness; failure mode codes are explained in table 3.3

Test *	d_{tc} [mm]	T_{test} [°C]	TSS	TCD	TIC	TVC	TSC	TFD	TED	TN	BD	SB
F	0.3 #	**		×	×	×				×	×	
	0.6/1.0 #	**		×			×					
BR-TS	0.3 #	1300		×	×	×		×			×	×
		1350				×						×
		1400	×			×		×				
	0.6	1400			×	×						
	0.6preoxi	1400		×					×			
	1.0	1300; 1475			×	×						
BR-TC	0.3 #	1350		×	×	×		×				
TC	0.6/1.0	1400			×	×	×					
	1.0	1500		×			×		×			
	2.0	1500		×			×		×			

* F = furnace tests, BR-TS = burner rig, thermal shock; BR-TC = burner rig, thermal cycling

** for both the NLR tests at 1100°C and the ITC tests at 1137°C

including the preoxidised specimens

3.5.1 Furnace tests

The 0.3 mm top coats failed in a similar way: first delamination occurred at the corners and free edges, after which the top coat was gradually ‘nibbled off’ (TN), see figure 3.12. The remaining coating showed interface cracking (TIC) and vertical

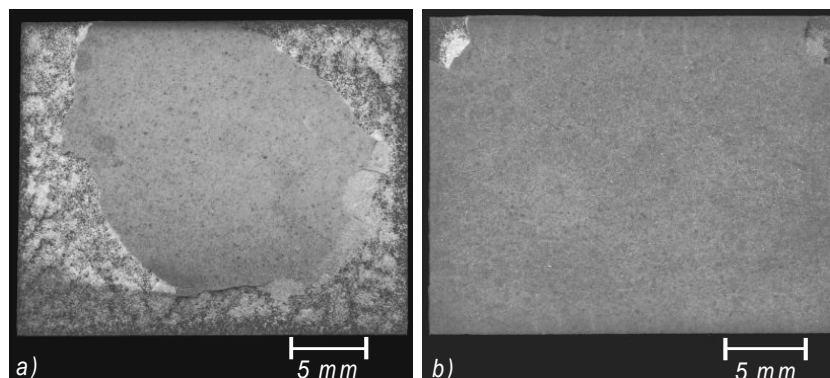


Figure 3.12 Example of top coat ‘nibbling off’ observed during the NLR furnace tests at 1100°C for the 0.3 mm TBCs: a) after 200 1hr cycles; b) after 80 8hr cycles. Comparison of the two shows that thermal cycling is more damaging than cycle length, since the top coat is nearly intact in b)

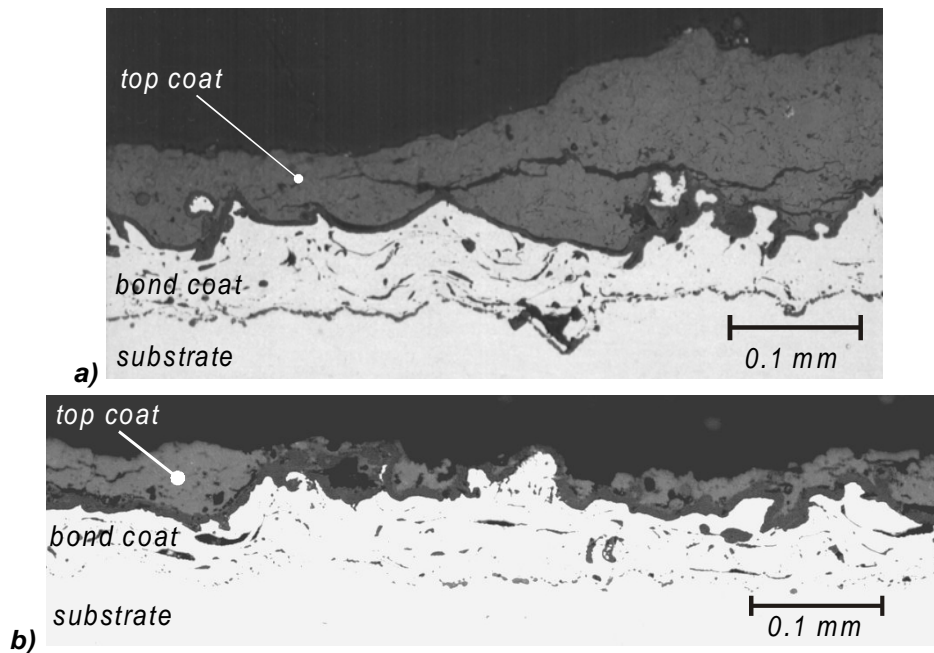


Figure 3.13 Furnace tested 0.3 mm TBC: a) after 90 cycles near edge of remaining top coat material; b) after failure (300 cycles) whereby the top coat is completely delaminated

cracking (TVC). In some cases, the top coat delaminated over the entire specimen area (TCD) before the failure criterion was reached. Figure 3.13 shows cross-sections of the 1 hr cycle specimens: (a) near the edge of the remaining coating after 90 cycles when two corners were delaminated: the interface cracks in the remaining coating are clearly visible; and (b) a part of the specimen where complete delamination had occurred at total life: after complete delamination the crack path runs just above the interface roughness peaks. The TBCs with a preoxidised bond coat and the specimens tested at the other cycle lengths showed a similar crack path after complete delamination to that in figure 3.13 (b). From figure 3.13 it is also seen that severe bond coat degradation (BD) occurred during the furnace tests.

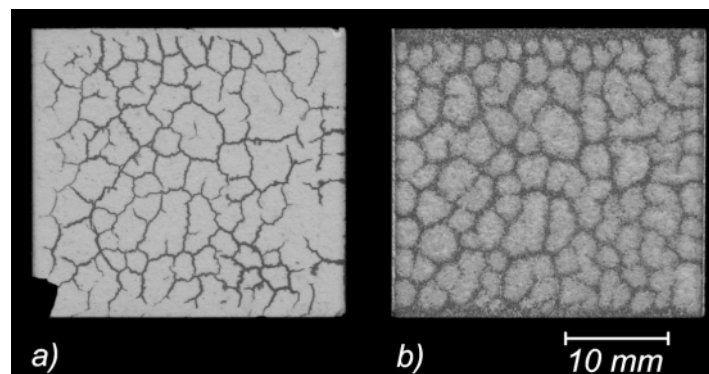


Figure 3.14 Example of segmentation cracking observed from furnace testing of 0.6 mm and 1.0 mm TBCs: a) top surface of entirely delaminated top coat; b) fracture surface at top coat / bond coat interface

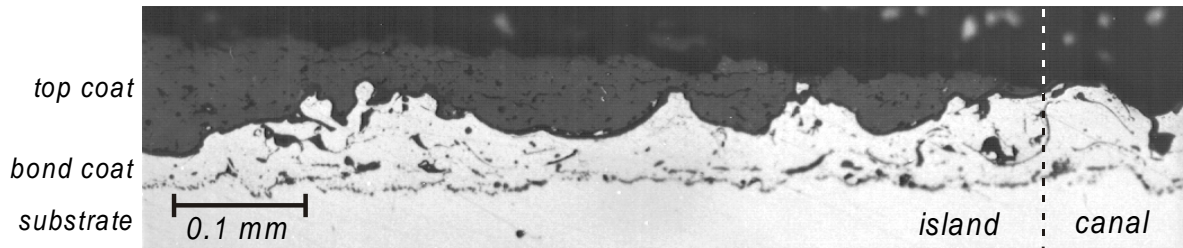


Figure 3.15 Furnace tested 0.6 mm TBC after failure (20 cycles)

The failure mode of the thick (0.6 mm and 1.0 mm) TBCs differed essentially from that of the 0.3 mm TBCs. The entire top coat delaminated (TCD) after a low number of cycles without nibbling-off, and this was preceded by segmentation cracking (TSC). Figure 3.14 shows a typical example of TSC. On the left-hand side the top coat surface crack pattern is revealed by impregnation at the top coat / bond coat interface side with a fluid colorant. On the right-hand side the fracture surface is shown, whereby the residual top coat material appears as small 'islands' with an average diameter of 3 mm. The 'canals' between the islands (bond coat material) correspond to the segmentation crack pattern in the top coat. Figure 3.15 shows a 0.6 mm specimen after top coat delamination. The crack path of the 'canals' (right-hand side of dotted line) was closer to the top coat / bond coat interface than that of the 'islands' (left-hand side of dotted line). Figure 3.16 shows a representative SEM fractograph of a 0.6 mm top coat near the canals. The smooth parts (outlined in black) are the oxidised bond coat, the rough parts are residual top coat material.

3.5.2 Burner rig tests

Thermal shock

The failure modes of the 0.3 mm top coats depended on the test temperature:

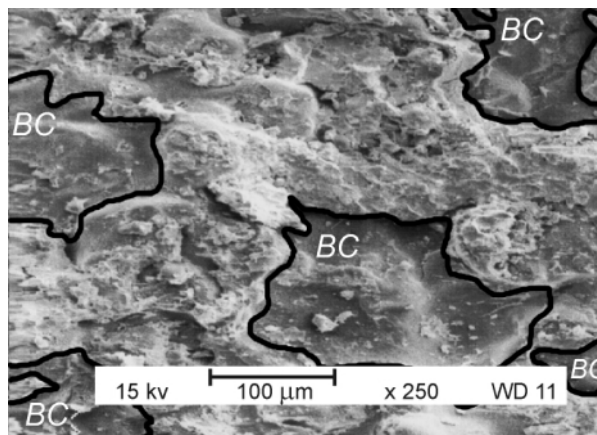


Figure 3.16 SEM fractograph of delaminated 0.6 mm TBC after furnace test. The bond coat material (BC) is outlined in black

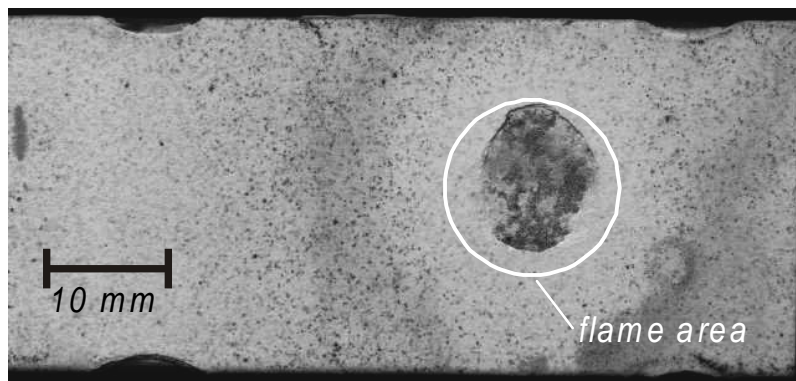


Figure 3.17 Example of top coat flame area delamination after burner rig thermal shock testing of a 0.3 mm TBC

- $T_{\text{surf}}=1300^{\circ}\text{C}$: complete delamination of the top coat in the flame area (TFD / TCD) after a large number of cycles. Figure 3.17 shows an example of flame area delamination. Bond coat oxidation was considerable (BD) and the specimens were slightly bent (SB). The crack path was very similar to that observed for the furnace tested 0.3 mm TBCs (figure 3.13b). Some tests were stopped half-way through the coating life and the specimens were microscopically investigated, see figure 3.18. It is seen that some top coat / bond coat interface cracks (TIC) were already formed, and these interface cracks run from peak to peak (arrowed).
- $T_{\text{surf}}=1350^{\circ}\text{C}$: severe specimen bending (SB) for both the non-preoxidised and preoxidised 0.3 mm TBCs. Figure 3.19 shows the damage after 1500 cycles.

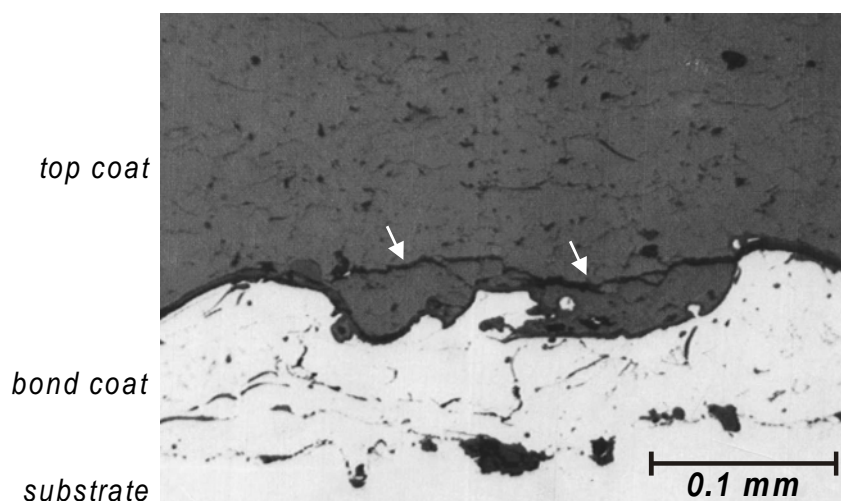


Figure 3.18 Example of top coat / bond coat interface cracking in a 0.3 mm top coat specimen before complete delamination after burner rig thermal shock testing with $T_{\text{surf}}=1300^{\circ}\text{C}$

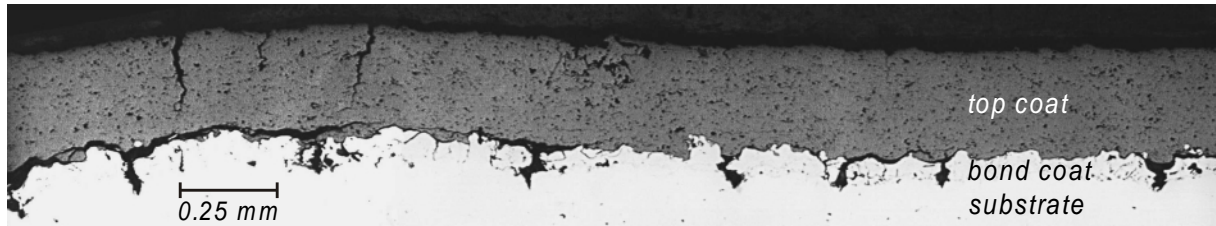


Figure 3.19 TBC damage due to specimen bending and bond coat degradation in 0.3 mm top coat specimen after 1500 burner rig thermal shock cycles with $T_{surf}=1350^{\circ}\text{C}$

- $T_{surf}=1400^{\circ}\text{C}$: top coat surface spalling in the flame area (TFD / TSS) after a small number of cycles. This was observed visually when small particles on the surface lit up very strongly during heating. After stopping the test it was seen that small flakes thinner than the coating thickness had broken off. Several horizontal cracks varying in length from 50 to 300 μm had formed but there were no vertical cracks. At some places near the surface the structure was crumbled: clusters of pores and cracks 200 μm in size expanded the coating, leading to a slight increase in thickness. Figure 3.20 shows an example of this failure mode. On the left, surface spalling is clearly visible. On the right, two examples of crumbling are shown. The bond coat was slightly oxidised. It should be remembered that the 0.3 mm TBCs tested with $T_{surf}=1400^{\circ}\text{C}$ were all sprayed with the ‘excessive energy’ plasma conditions. We will return to this in sub-section 3.6.2.

Outside the flame area, vertical cracking (TVC) had occurred for all test temperatures. An example for a 0.3 mm top coat is given in figure 3.21.

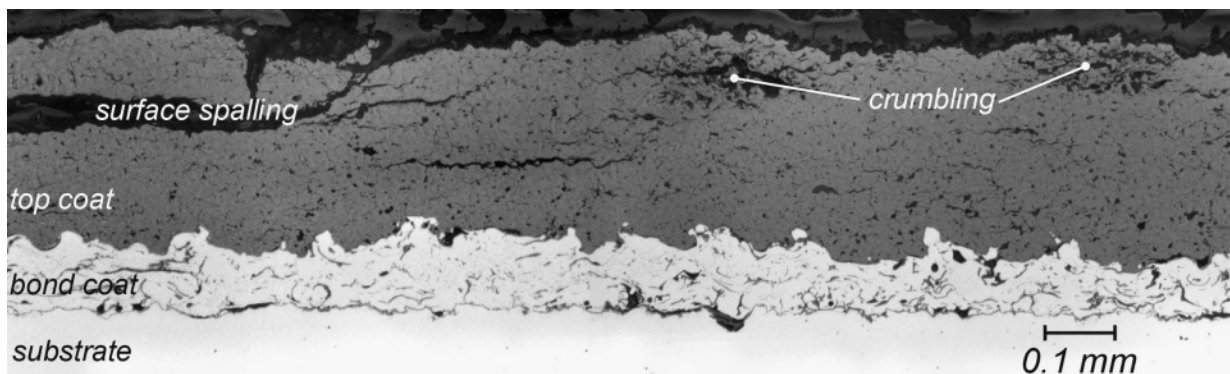


Figure 3.20 Surface spalling and crumbling of a 0.3 mm top coat specimen after 900 burner rig thermal shock cycles with $T_{surf}=1400^{\circ}\text{C}$

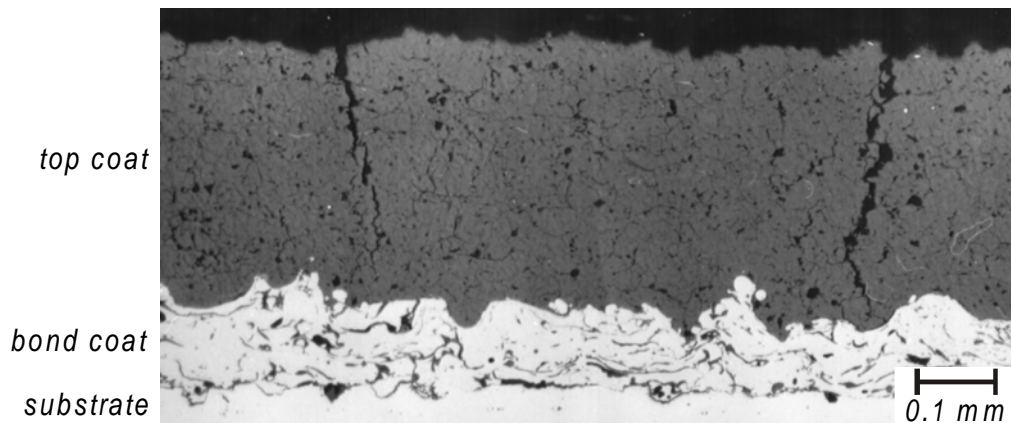


Figure 3.21 Vertical cracks outside the flame area in a 0.3 mm top coat specimen after burner rig thermal shock testing with $T_{surf}=1300^{\circ}\text{C}$

The 0.6 and 1.0 mm thick coatings did not fail but showed some vertical cracks (TVC) both inside and outside the flame area, and a little interface cracking (TIC) in the flame area, see figure 3.22. These cracks were already observed after 200 thermal shock cycles (in specimens for residual stress measurements, see chapter 5). Bond coat oxidation and specimen bending were negligible.

The 0.6 mm specimens *with a preoxidised bond coat* delaminated from the specimen side edge to the flame area over the entire thickness (TED / TCD), see figure 3.23. Bond coat oxidation was far less than for the 0.3 mm top coats. The crack path was similar to that observed for specimens with a 0.6 mm top coat and pre-oxidised bond coats that failed during furnace testing.

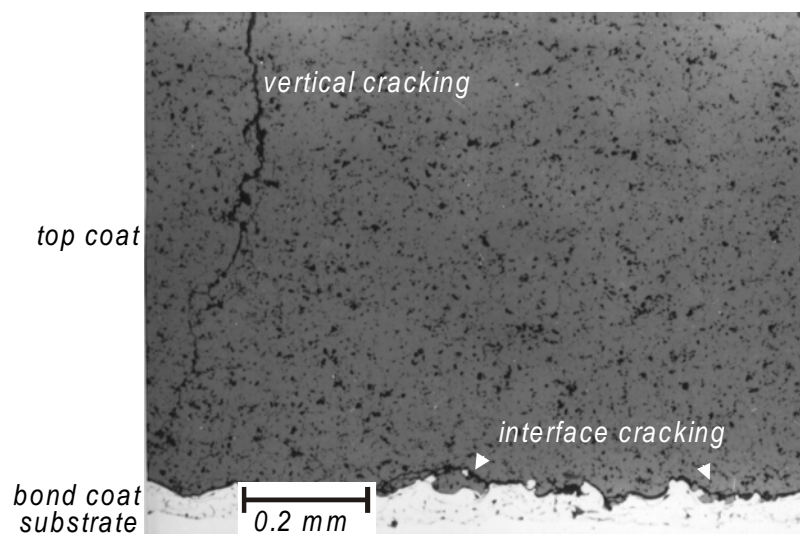


Figure 3.22 Vertical cracks and interface cracking in the flame area in a 1.0 mm top coat specimen after 5000 burner rig thermal shock cycles with $T_{surf}=1300^{\circ}\text{C}$

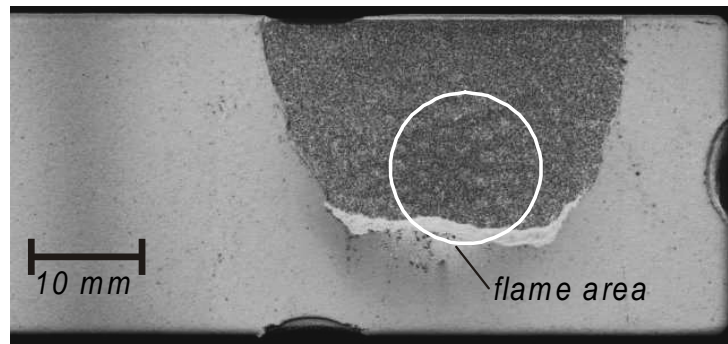


Figure 3.23 Example of top coat edge-to-flame-area delamination in a 0.6 mm top coat specimen with preoxidised bond coat after 2400 burner rig thermal shock cycles with $T_{surf}=1400^{\circ}\text{C}$

Thermal cycling

Failure of the 0.3 mm specimens (both non-preoxidised and preoxidised) occurred by complete delamination in the flame area (TFD / TCD). The crack path was similar to that observed for the failed 0.3 mm specimens during furnace testing and burner rig thermal shock, *i.e.* just above the interface roughness peaks. It can therefore be assumed that delamination was preceded by interface cracking (TIC). The bond coat was more oxidised than during thermal shock, but less than during furnace testing.

The 1.0 mm specimens showed segmentation cracking in the flame area (TSC). The TBC tested at 1400°C did not delaminate and showed no further damage. The TBC test at 1500°C was stopped when the surface temperature of the entire flame area had increased to values far above 1500°C , indicating that the top coat had delaminated. This was confirmed by optical microscopy, which also revealed that edge-to-flame-area delamination had occurred (TED).

The 2.0 mm specimen tested at 1500°C failed after a few cycles by edge-to-flame-area delamination, whereby the top coat delaminated over its entire thickness (TED / TCD). Segmentation cracking was observed in the flame area (TSC). No bond coat oxidation occurred in this short time period.

3.5.3 Microstructural changes

Besides the above-mentioned failure features, some microstructural changes in the top coats had occurred, which are not clearly visible from the microstructural photographs in this chapter. From optical microscopy observations it was seen that the number of microcracks and pores had decreased in the heated parts of the top coat. This densification effect, clearly illustrated in chapter 5, figure 5.11, was not measured directly in terms of porosity but indirectly in terms of hardness and erosion resistance. This will be treated in chapter 4.

3.6 Discussion

Most thermal tests are not standardised, which makes it very difficult to compare the results from different laboratories. This was clearly demonstrated by Haubold *et al.* (1998) who compared the thermal shock resistance of six different TBCs prepared by three different coating manufacturers and tested with three different burner rigs. They found that the (three) burner rig rankings of coating lives did not agree. Therefore, in this section the numbers of cycles to failure obtained during the present programme are compared solely for the present test methods and not with results from the literature.

3.6.1 Furnace tests

Increasing cycle length reduced the cycles to failure but increased the time-based life, as was also found by McDonald and Hendricks (1980). This clearly demonstrates the interaction of thermal fatigue and oxidation with regard to failure. For short cycles the amount of oxidation per cycle is small compared to long cycles, and hence the number of cycles to failure will be larger. However, per unit of time (same degree of oxidation) the number of cycles is highest for short cycles. This means that the contribution of thermal fatigue is larger for short cycles and failure will occur after a relatively short time-based life

The failure modes during furnace testing of thin coatings (TN and TIC) suggest that high shear or normal stresses develop near the free edges of the specimen and just above the top coat / bond coat interface peaks, and that these stresses have a primary contribution to failure. In addition, the severe bond coat degradation (BD) observed for the thin TBCs after long exposure may well enhance failure: in chapter 4 it will be shown that severe bond coat degradation is accompanied by bond coat aluminium-depletion.

Thick coatings performed very poorly during the furnace tests. Failure occurred by segmentation cracking (TSC) followed by complete delamination (TCD) after a short number of cycles. This suggests that high in-plane tensile stresses develop as well as the shear or normal stresses mentioned above.

To better understand these failure mechanisms it is necessary to obtain more information about the thermal stresses that develop during cooling.

3.6.2 Burner rig tests

Temperature profile

The burner rig tests induced three-dimensional temperature profiles in the specimens. The temperature drop over the specimen thickness increased with increasing top coat thickness and increasing heat input. The radial temperature drop at the substrate rear side depended on the amount of material adjacent to the flame area. Owing to the low conductivity of the top coat it would be expected that the radial temperature drop at the top coat surface is much larger than at the substrate rear side.

Thermal shock

The effects of test temperature and top coat thickness during thermal shock can be summarised as follows:

- For $T_{\text{surf}}=1300^{\circ}\text{C}$ the thick coatings did not fail within 5000 cycles, the 0.3 mm TBCs failed on average after 3700 cycles. Failure occurred by complete delamination (TCD). Bond coat oxidation played an important role in failure for the 0.3 mm coatings. The main effect of an increase in top coat thickness is a decrease of the interface temperature, and hence lower oxidation rates, for the same T_{surf} . Moreover, the strain tolerance was increased by vertical cracking. Be that as it may, to better understand the effect of coating thickness and the observed failure mechanisms it is necessary to obtain more information about the thermal stresses that develop during thermal shock.
- For $T_{\text{surf}}=1350^{\circ}\text{C}$ the 0.3 mm coating test was stopped owing to severe degradation of the metallic components. Since this type of damage cannot be regarded as *coating* failure, it will not be discussed further.
- For $T_{\text{surf}}=1400^{\circ}\text{C}$ top coat surface spalling occurred for the 0.3 mm specimens, but not for the thicker coatings, which did not fail¹. Surface spalling was also observed by Miller and Berndt (1984) who attributed it to uneven heating caused by surface roughness, and by Wigren *et al.* (1996b) and Bengtsson *et al.* (1998) who attributed it to poor splat adhesion and hence poor particle melting. During the present test programme surface spalling was observed only for the 0.3 mm TBCs sprayed under the ‘excessive energy’ plasma conditions. The coatings sprayed under the ‘mild’ plasma conditions did not show surface spalling, even when

¹ The 1.0 mm top coat test at 1475°C was done to investigate whether surface spalling (TSS) would occur. When this had not happened after 3000 cycles, and since it was unlikely that complete delamination owing to bond coat oxidation would occur, the test was stopped.

tested with $T_{\text{surf}}=1475^{\circ}\text{C}$.² In sub-section 2.5.1 it was mentioned that no differences in top coat surface roughness were observed between the ‘excessive energy’ and ‘mild’ plasma TBCs. Hence it is unlikely that surface spalling is caused by a rough surface. Therefore, surface spalling of the ‘excessive energy’ plasma TBCs was most probably caused by poor splat adhesion. Apparently, the particles deposited under ‘mild’ plasma conditions had been well heated and adhered better.

Thermal cycling

It appears there is an optimum coating thickness for the thermal cycling tests under constant heat input:

- 0.3 mm top coat at 1350°C : delamination in flame area accompanied by bond coat oxidation.
- 0.6 mm and 1.0 mm top coat at 1400°C : no failure
- 1.0 mm top coat at 1500°C : delamination preceded by segmentation cracking, no oxidation.
- 2.0 mm top coat at 1500°C : complete delamination initiated at specimen side edge, no oxidation.

The results suggest that failure is caused by a combination of oxidation and thermal stresses, and that the dominant process changes with coating thickness. Again, to better understand this interaction it is necessary to obtain more information about the thermal stresses that develop during thermal cycling.

3.6.3 Comparison of test methods

Table 3.5 gives the total times at high temperature before failure occurred for the 0.3 mm TBCs subjected to all three test types. The time-based life was highest in the case of furnace testing with long cycles and lowest in the case of burner rig thermal shock. For the latter the time of the complete heating period is given, which means that the total time at high temperature was even shorter than the 30 hr in table 3.5.

Though the bond coat temperatures for all tests did not exactly agree, the results in table 3.5 indicate that introducing a three-dimensional stress gradient decreases the time-based life considerably. Hence, the discussion in section 3.6.1 on the effect of cycling time during NLR *furnace tests* can be broadened by considering the *burner rig tests* also. The test ranking in table 3.5, proceeding from thermal shock

² Tests of ‘mild’ plasma sprayed TBCs were only for the 1.0 mm TBC, but in chapter 6 it will be shown that the in-plane stresses in the surface region of the 1.0 mm top coat are even higher than those for the 0.3 mm top coat.

down to long-cycle furnace tests, reflects the increasing domination of oxidation with respect to thermal fatigue stresses, *i.e.* one proceeds from mainly cycle-dependent failure to mainly time-dependent failure.

Table 3.5 Time at high temperature for 0.3 mm TBCs under three different types of thermal load

testing method	average number of cycles to failure	heating period	total time [hr]
thermal shock	3800	28 s*	30
thermal cycling	100	1 hr	100
NLR furnace testing	220	1 hr	220
NLR furnace testing	210	2 hr	420
NLR furnace testing	110	8 hr	880

* time of complete heating period.

Once again it must be mentioned that furnace tests are not a true indicator of coating performance, since the hot section components in gas turbines are always heated at the coated side and often cooled at the substrate side. The reason furnace tests are still widely used is that they are easy and provide information on the comparative durability and oxidation behaviour of TBC systems. It is an improvement to do burner rig thermal shock tests, where thick coatings performed very well. Still better, because most generally realistic, is burner rig thermal cycling, where the failure behaviour is intermediate to those of furnace testing and thermal shock.

Effect of spraying parameters

Compared with the 'mild' plasma TBCs, the 'excessive energy' plasma TBCs showed:

- No essential differences in furnace test performance (0.3 mm top coat).
- No difference in burner rig thermal shock performance with $T_{\text{surf}}=1300^{\circ}\text{C}$.
- Failure by surface spalling during burner rig thermal shock test with $T_{\text{surf}}=1400^{\circ}\text{C}$.

3.6.4 Preoxidation

Preoxidation of the bond coat has a beneficial effect for thermal loading with long heating cycles, *i.e.* thermal cycling and furnace testing. This was also found by Lih *et al.* (1991). One beneficial effect is prevention of initial rapid growth of an oxide layer between the bond coat and the top coat, which is known to induce extra stresses (Evans *et al.*, 1983; Freborg *et al.*, 1998; Tsui *et al.*, 1998). However, to better

understand the effect of preoxidation on the life of TBCs, its effect on the adhesion strength and on the thermally induced stresses should be investigated.

3.6.5 *The importance of microcracks*

The present TBCs showed good thermal shock resistance, especially the thick TBCs. This can be attributed to the microcracked coating structure, which is caused by substrate cooling during deposition (see chapter 2 and Verbeek, 1992; Sturlese and Bertamini, 1994). This contrasts with the results of Wigren *et al.* (1996b) and Bengtsson *et al.* (1998) who found poor thermal shock resistance for microcracked top coats but good thermal shock resistance for top coats with a segmentation crack network. They concluded that the optimum TBC contains a low percentage of microcracks. From these contrasting opinions it can be concluded that good thermal shock resistance is not unambiguously correctable to the microcrack density, but that good thermal shock resistance is basically obtained via a low value of the Young's modulus (high flexibility). This can be achieved by omitting substrate cooling during deposition, resulting in segmentation cracking, or by forced substrate cooling during deposition, resulting in a high microcrack density. In fact, there is yet another possibility, because the high thermal shock resistance of thick TBCs observed during the present programme can be attributed to the microcracks as well as the vertical cracks that were formed after only a few cycles.

3.7 Conclusions

Failure of a TBC in a realistic environment must be due to an interaction between thermal stresses and bond coat oxidation. For example, thick TBCs perform excellently during burner rig thermal shock tests and poorly during furnace tests. For the most generally realistic test, burner rig thermal cycling, there seems to be an optimum coating thickness.

Good thermal shock resistance can be obtained from a high microcrack density in the top coat, provided that good particle adhesion exists. This was achieved with the 'mild' spraying conditions during the present research. However, during testing vertical cracking or segmentation cracking occurs (especially in the thick TBCs), which also contributes to good thermal shock resistance.

Thick TBCs always fail by delamination starting from a free edge. This indicates that specimen geometry also plays an important part in the failure mode.

Empirical testing, no matter how realistic, is insufficient for understanding the observed failure mechanisms and the effects of coating thickness and preoxidation on these mechanisms. Thus the changes in the TBC systems, including bond coat oxidation, should be investigated, and the stresses that develop during thermal testing should be quantitatively predicted. These aspects are treated in chapters 4–6, leading to a more definitive discussion of the observed failure mechanisms in chapter 7.

4 COATING PROPERTIES

4.1 Introduction

Coating properties like density, Young's modulus and phase composition, and coating residual stresses determine to a large extent the performance of a TBC during service. Most of the time the properties in the as-sprayed condition are measured. However, as mentioned in the previous chapter, sub-section 3.5.3, some microstructural changes take place when TBCs are heat-treated (furnace and burner rig testing). The main process at high temperatures is densification of the top coat owing to sintering (Eaton and Novak, 1987b; Wesling *et al.*, 1994; Janos *et al.*, 1999; Allen *et al.*, 1999; Thompson and Clyne, 1999), which changes most of the properties. Hence it would be more realistic to determine the properties after heat treatment and use them to characterise a TBC.

In this chapter the room temperature microhardness, erosion resistance, adhesion strength and phase composition of the as-sprayed and heat treated TBCs will be compared. Also, the change of bond coat chemical composition upon heating will be presented. However, the residual stress changes due to heating the top coat will be treated separately in chapter 5.

4.2 Hardness

4.2.1 Introduction

As for all materials, the hardness of a coating is a measure of the resistance to plastic deformation. It is widely recognised that the hardness increases with increasing density, *i.e.* decreasing number of pores and micro-cracks (*e.g.* Janos *et al.*, 1999).

Hence the hardness of the top coat is a measure for the amount of sintering and integrity, and can provide information on the temperature history of the top coat.

4.2.2 Experimental

The microhardness of as-sprayed, isothermally heated (various heating temperatures and times) and thermally shocked TBCs (top coat and bond coat) was measured on polished metallographic sections using a Leitz Durimet IC microhardness tester with a Vicker's diamond indenter and 200 g applied load for 15 sec. The hardness was determined from the average length of the diagonals of each diamond shaped indentation.

4.2.3 Results and discussion

Top coat

Figure 4.1 shows the microhardness of as-sprayed and isothermally heated top coats. The error bars indicate the maximum and minimum microhardness. The large differences between these values are caused by the inhomogeneity of the coatings. The as-sprayed microhardness is given for several specimens (for spraying parameters, see section 2.4) and varied from 600 to 900 HV200. The average value was about 750 HV200 and the effect of spraying parameters on the microhardness was negligible. Janos *et al.* (1999) measured the microhardness for TBCs with porosity levels of 12.9%, 17.8% and 27.3%. If their results are graphically extrapolated to the porosity levels of the TBCs tested here ($P \approx 3\%$, see sub-section 2.5.4) a microhardness of about 750 HV200 is found, which agrees very well with the present results.

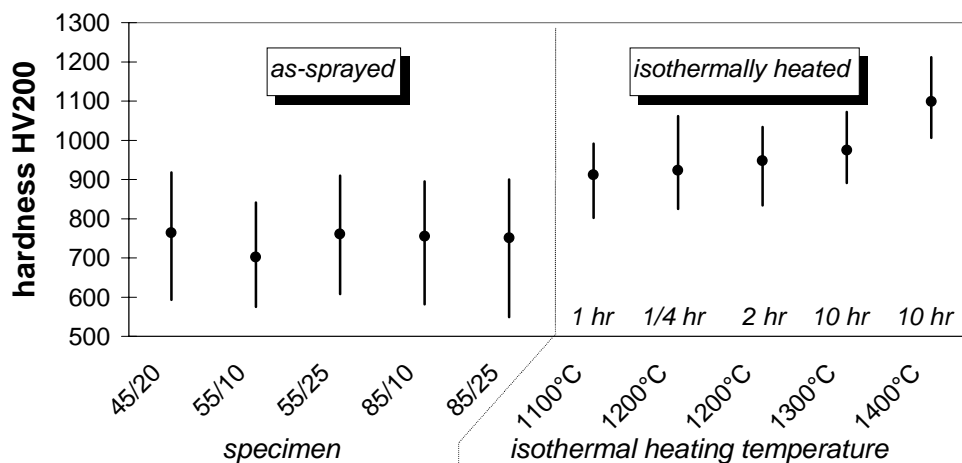


Figure 4.1 Microhardness in kg mm^{-2} of top coat in as-sprayed (several specimens) and isothermally heated (55/25 specimens only) TBCs. The specimen codes refer to the spraying parameters, see section 2.4, table 2.5

The isothermally heated microhardness is measured only for the 55/25 specimens (owing to negligible effect of spraying parameters on microhardness). For temperatures from 1100°C to 1300°C only a slight microhardness increase with increasing temperature was found (900 HV200 at 1100°C, 975 HV200 at 1300°C), and the effect of heating time was also slight. On the other hand, after isothermal heating at 1400°C the microhardness had increased to 1100 HV200. This sharp microhardness increase of the specimen heated at 1400°C is explained by the fact that pronounced sintering of bulk partially yttria-stabilised zirconia occurs above 1350°C (Sato and Shimada, 1984). Sintering below this temperature can be attributed to the “healing” of small defects in the sprayed microstructure, *e.g.* the sealing of micro-cracks (Eaton and Novak, 1987b; Wesling *et al.*, 1994; Thompson and Clyne, 1999; Ilavsky *et al.*, 1999).

The dependency on isothermal heating temperature of the microhardness is similar to that of the room temperature Young’s modulus (Eaton and Novak, 1987b; Allen *et al.*, 1999; Thompson and Clyne, 1999; Siebert *et al.*, 1999). The modulus change was also attributed to sintering effects, and here too a sharp increase above 1300°C was measured.

The microhardness measurements in thermal shock specimens showed more complex results, whereby the values depended on temperature, number of cycles and location. The results are summarised in table 4.1.

Table 4.1 Microhardness of thermal shock specimens in kg mm^{-2} under a load of 200 g

top coat thickness [mm]	T_{surf} [°C]	# cycles	location of hardness indentation	
			flame area	edge of specimen
0.3	1300	4220	968±127	808±117
1.0	1300	5000	976±138	686±36
0.3	1400	750	918±83	
0.6	1410	2690	935±34	
0.6	1425	4870	1046±114	

In the flame area and after a large number of cycles the microhardness was the same as the microhardness of the specimens isothermally heated at the same temperature, see figure 4.1. However, after a small or intermediate number of cycles at 1400°C the microhardness of thermal shock specimens was less, with values similar to those of specimens isothermally heated at 1100-1200°C. This indicates that at 1400°C the amount of sintering during thermal shock testing depends on time.

At the edge of the top coat the microhardness hardly changed. This is because the temperature at that position was too low for sintering.

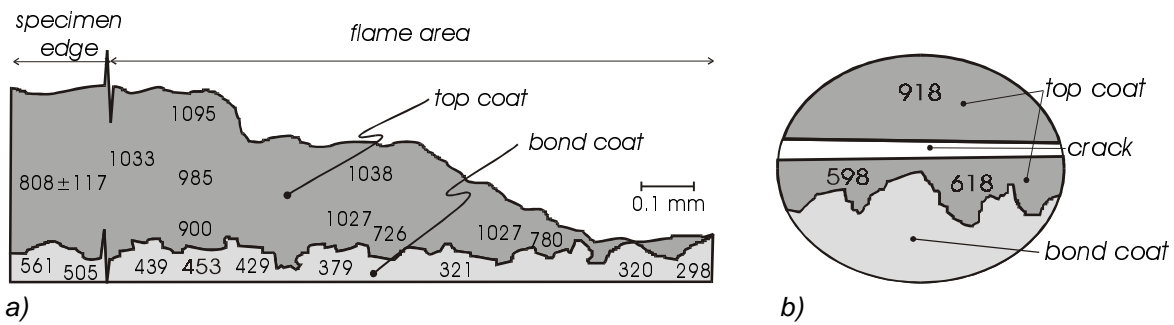


Figure 4.2 Microhardness in kg mm^{-2} in thermal shock specimen ($T_{\text{surf}}=1300^{\circ}\text{C}$) after 4220 cycles; a) near delaminated part; b) above and below delamination crack

Figure 4.2a is an example of the microhardness data corresponding to the thermal shock specimen in the first row of table 4.1. The right-hand part of the figure shows the microhardness at the edge of the flame area after delamination of the top coat. The left-hand part shows the microhardness at the specimen edge. It is seen that local hardness variations can be rather large.

Figure 4.2b shows a special case whereby a delamination crack occurred in the top coat. Above the crack the top coat hardness was normal. However, the hardness of the top coat still adhering to the bond coat had dropped to about 600HV200, which can be attributed to severe micro cracking in this region, see e.g. figure 3.13b.

Bond coat

Bond coat hardness has *no* effect on TBC life (Haynes *et al.*, 1999) but it provides information on the thermal history of the bond coat. The microhardness was 338 ± 30 in the as-sprayed specimens and 212 ± 8 in the isothermally heated ($1300^{\circ}\text{C}/10\text{hr}$) specimens. Unlike the microhardness increase due to sintering of the ceramic top coat, the microhardness of the bond coat dropped upon heating owing to stress relief, coarsening of γ' ($=\text{Ni}_3\text{Al}$, the ordered intermetallic strengthening phase) and/or phase changes (Itoh *et al.*, 1993; Haynes *et al.*, 1999). After thermal shock the bond coat microhardness varied widely, see figure 4.2. At locations where the top coat had not delaminated the bond coat microhardness had *increased* to values of about 440HV200 in and near the flame area, and 530HV200 at the specimen edge. Since the bond coat is constrained by the top coat, this increase in hardness might be due to an increase in residual stresses. At locations where the top coat had delaminated the hardness had *decreased* to values of about 310HV200, which is lower than the as-sprayed microhardness. The reason is that after delamination the bond coat temperature drastically increases and the bond coat is no longer constrained by the top coat, and so stress relief, γ' coarsening and/or phase changes cause the bond coat microhardness to decrease.

4.3 Erosion resistance

4.3.1 Introduction

TBC degradation by erosion occurs mainly on turbine blades and vanes, especially when the (aircraft) engine operates in a sandy environment (*e.g.* desert). High erosion resistance is normally obtained by *decreasing* the porosity. However, high thermal shock resistance is obtained by *increasing* the porosity (Eaton and Novak, 1987a; Taylor *et al.*, 1990; Janos *et al.*, 1999). Therefore gas turbine manufacturers have to compromise, and in general a high thermal shock resistance is given priority.

The present TBC system was developed by Verbeek (1992). He showed that owing to the dense microcracked microstructure the coating combines a high thermal shock resistance with a high erosion resistance. The latter was three to four times as high as that of a conventional coating. However, he conducted the erosion measurements on as-sprayed coatings, while in gas turbines erosion will always occur on heated TBCs. It is known that owing to sintering effects the erosion resistance increases after a heat treatment (Usmani and Sampath, 1996; Janos *et al.*, 1999). Therefore, in this section the influence of isothermal heating (1100°C/1 hr) on the erosion resistance of the present TBC system will be discussed.

4.3.2 Experimental

The erosion experiments were carried out at room temperature, using a modified and unlit flame spray torch to propel the erodent particles. The coating surfaces of 30×25 mm² specimens were grit blasted with alumina particles (200-500µm) with a velocity of 20 m/s. The angle of incidence was 90°, the particle feed rate was 200 g/min and the nozzle-to-specimen distance was 200 mm. The TBCs were eroded for 20 minutes, with the mass and thickness decrease being measured every five minutes.

In the literature the erosion rate is commonly expressed in milligrams of material loss per gram of erodent. However, this can be done only when the particle spray is smaller than the specimen surface. This was not the case in the present experiments, but the goal of the current investigation was to determine the effect of a heat treatment on the erosion resistance rather than to compare it with literature values. For all specimens the thickness decrease was constant over the entire surface and the mass decrease was constant in time. Hence an appropriate measure to express the erosion rate is the mass decrease per unit area per unit time.

4.3.3 Results and discussion

Figure 4.3 shows the erosion rates of several TBC specimens in both the as-sprayed and isothermally heated conditions. For both conditions an increase of gas flow resulted in a decreased erosion rate. Isothermal heating much improved the subsequent erosion resistance, *i.e.* the inverse value of erosion rate, by 70 up to 90%.

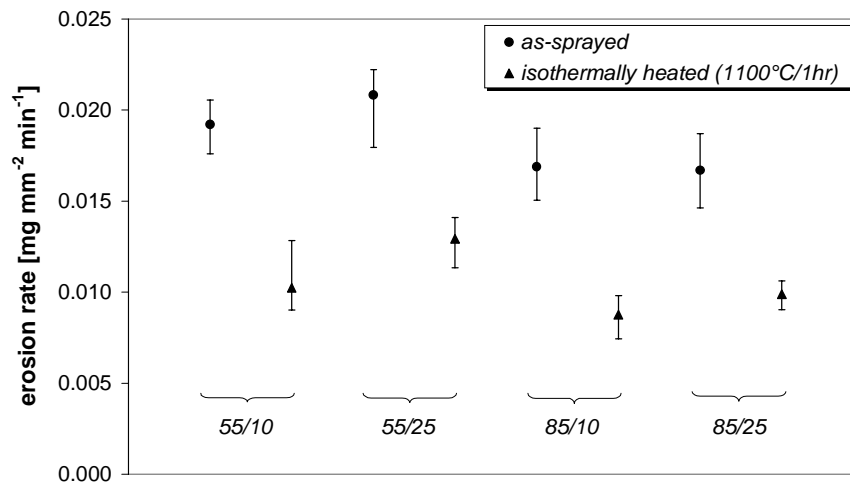


Figure 4.3 Erosion rate for four different TBCs (55/10, 55/25, 85/10, 85/25) in as-sprayed and isothermally heated (1100°C/1hr) state. The specimen codes refer to the spraying parameters, see chapter 2

In section 4.2 it was shown that after isothermal heating at 1100°C the hardness had increased from 750 to 900 HV₂₀₀ owing to sintering. Thus we may attribute the increased erosion resistance to an increase in hardness, as observed by Janos *et al.* (1999) and Taylor *et al.* (1990), and this in turn is related to a decrease in porosity owing to sintering. There is a slight trend of lower erosion rates for coatings sprayed with a higher gas flow (85/10, 85/25), but this cannot be directly related to hardness, see section 4.2.3. To explain these differences extensive microstructural investigations on splat interfaces, involving electron microscopy, should be done: this is beyond the scope of this thesis.

Janos *et al.* (1999) derived a power-law equation to relate the erosion rate V (in milligrams of TBC material loss per gram of erodent) to the top coat hardness H_{tc} :

$$V = 6 \cdot 10^{11} H_{tc}^{-3.82} \quad (4.1)$$

This results in 6.2 mg[TBC]/g[erodent] for the as-sprayed top coats and 3.1 mg[TBC]/g[erodent] for the isothermally heated top coats. This calculated halving of erosion rate is consistent with the measured improved erosion resistance after isothermal heating.

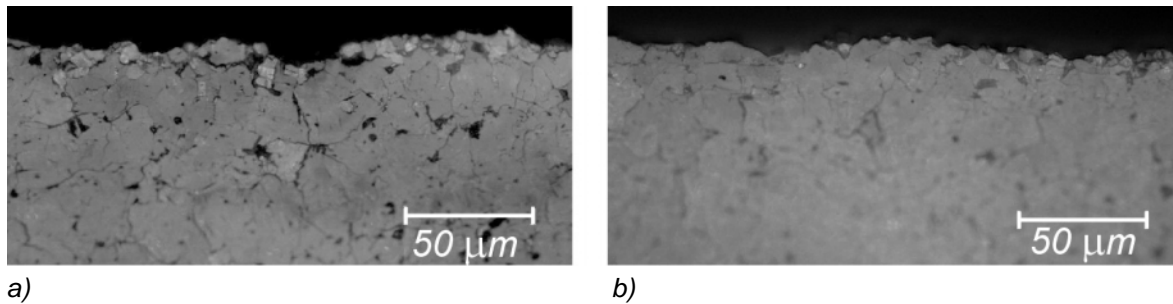


Figure 4.4 Erosion damage of top coat surface in a) as-sprayed; and b) isothermally heated (1100°C/1hr) specimen.

Figure 4.4 shows cross-sections of as-sprayed and isothermally heated specimens after the erosion test. The morphology of the surface layer can provide information about the erosion rate. Eaton and Novak (1987a) distinguished three different types of erosion mechanisms associated with low, moderate and high erosion rates. These are respectively (1) ploughing, where primary impact scars are present at the surface, (2) fracture, where the erodent particles cause fractures to occur in the surface around the impact site, and (3) tunnelling, where pores along the surface are interconnected by fracture. In the present as-sprayed specimen (Fig. 4.4a) the surface layer was fractured to a depth of approximately 20 μm and erosion type 2, associated with moderate erosion rates, applies best. In the isothermally heated specimens (Fig. 4.4b) the surface is characterised by impact scars and cracks were hardly observed. Here erosion type (1) applies best. Hence the observed surface layer morphologies after erosion testing agreed with the measured erosion rates.

4.4 Adhesion strength

4.4.1 Introduction

Coating adherence is accomplished by many mechanisms, of which mechanical interlocking owing to the rough surface of the underlying material is the most important (McPherson, 1981; Sobolev *et al.*, 1997). Another is the co-adherence of the individual splats, which is determined by the degree of flattening at the moment of deposition, and hence by the particle temperature and velocity and substrate temperature (Houben, 1988; Steffens *et al.*, 1991). Recently it was shown with TEM investigations that an amorphous film ranging in thickness from 50-1000 nm is formed at the top coat / bond coat interface. This film is a chemical bond that also affects the adhesion strength of TBCs, but the exact effect is not yet known (Harmsworth and Stevens, 1992; Bartuli *et al.*, 1995).

The objective of this section is to investigate whether coating thickness, bond coat preoxidation and isothermal heating (1050°C/5hr) affect the adhesion strength, and whether the crack path during adhesion testing is the same as in delamination during thermal testing. For this the relatively easy tensile pull-off test is sufficient (Brown *et al.*, 1988; Lin and Berndt, 1994). This test subjects the coating to a uniaxial tensile force.

4.4.2 Experimental

Figure 4.5 shows the test specimen configuration schematically. Small sections with a size of 18×18 mm² were cut from the coated strips with a diamond wire saw and glued onto steel bars using a high strength adhesive (3M HT 2214, bond strength ~70 MPa). To avoid penetration of the adhesive into the porous top coat, the top coat surface was first sealed with Metco AP sealer. The bars were mounted in a 100 kN tensile testing machine with special gripping fixtures to avoid bending. The bond strength tests were performed with a tensile speed of 2 mm min⁻¹. All specimen conditions were tested at least five times.

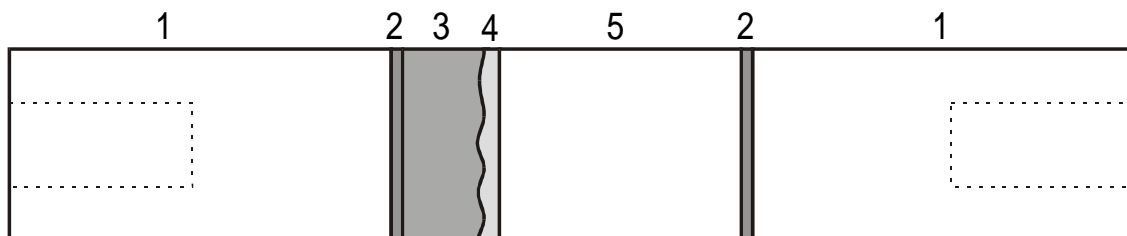


Figure 4.5 Specimen set-up for tensile adhesion test (not to scale). 1) steel bars; 2) adhesive; 3) top coat; 4) bond coat; 5) substrate. The surface of the top coat is sealed before adhesive bonding. The cross-section is square shaped, 18×18 mm, and the dashed lines represent threaded holes for mounting the specimen set-up in the tensile testing machine.

The adhesion strength test described here is similar to the ASTM C633 method (1982), but differs in the specimen preparation for the following reason. The coating for the ASTM standardised test is directly sprayed onto the end of a cylindrical bar that is rotated during the spraying process. Consequently the substrate velocity is zero at the centres of the ends of the bar and maximum at the circumference. This results in varying deposition characteristics over the bar end surface, which may result in varying coating properties and is therefore less definitive.

4.4.3 Results and discussion

Three different failure modes were observed (for locations, see figure 4.5):

- 1) Failure in the glued joint between steel bar and top coat (1/2/3).
- 2) Failure at the top coat / bond coat interface (3/4).
- 3) Combination of the first and second modes.

Failures at the substrate/bond coat interface (4/5) or entirely in the top coat (3) were not observed. The results of the first failure mode will be disregarded. The third failure mode was observed in most of the tests. The adhesion strengths of specimens that failed according to this mode were considered for further interpretation when more than 50% of the failure occurred at the top coat / bond coat interface, *i.e.* failure mode 2.

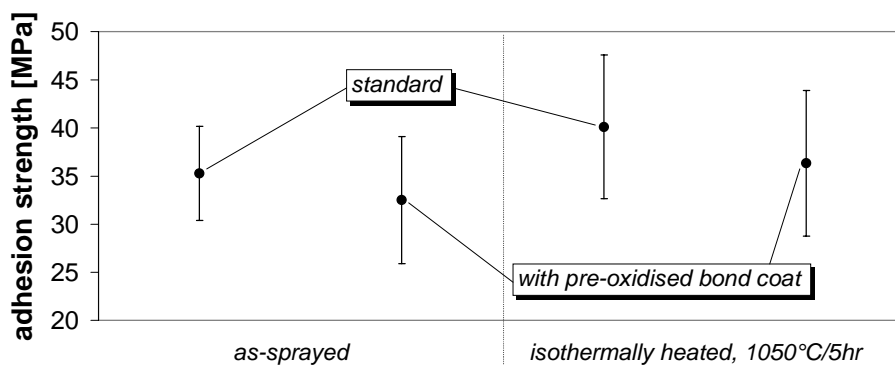


Figure 4.6 Adhesion strengths of 0.3 mm as-sprayed and isothermally heated (1050°C/5hr) TBCs, with and without (standard) a preoxidised bond coat. Error bars indicate standard deviation

Figure 4.6 shows the adhesion strengths of 0.3 mm as-sprayed and isothermally heated top coats. The data show much scatter, which is a recognised drawback of the tensile adhesion test (Ostojic and Berndt, 1988). The average adhesion strengths were somewhat lower than found by Verbeek (1992) for similar TBCs. This indicates that some specimen bending may have occurred inadvertently during tensile testing, thereby causing failure at a lower nominal tensile stress level (Brown *et al.*, 1988). However, the results are sufficient for studying the effect of preoxidation and isothermal heating. It can be concluded that isothermal heating improves the average adhesion strength by 10%, and that for both the as-sprayed and isothermally heated specimens the average adhesion strength drops about 10% if the bond coats are preoxidised. The adhesion strength of the 1.0 mm top coats (not shown in figure 4.6) averaged about 20 MPa. This lower value is because the negative effect of specimen bending on the adhesion strength is larger for thick coatings (Howard *et al.*, 1994).

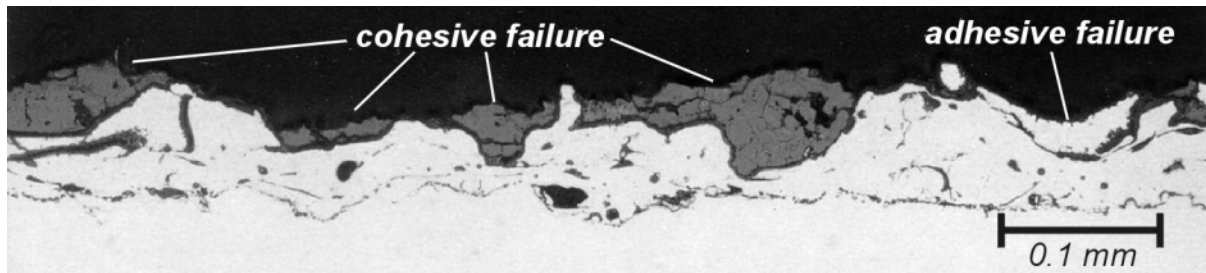


Figure 4.7 Cross-section of isothermally heated (1050°C/5hr) TBC after tensile adhesion testing

Figure 4.7 shows a representative cross-section of a failed specimen. It is seen that the second failure mode is a mixed adhesive/cohesive failure. The crack path during adhesion testing is fairly similar to that observed during the thermal load experiments (chapter 3, section 3.5), indicating the same failure mechanism.

4.5 Phase analysis

4.5.1 Introduction

Pure zirconia (ZrO_2) has a monoclinic structure at room temperature. This structure is formed by a diffusionless martensitic transformation, at about 1100°C, from a tetragonal structure. The transformation is accompanied by a volume increase of about 5%, resulting in compressive stresses and a very brittle, cracked material, which makes pure zirconia unsuitable for TBCs. As mentioned in chapter 1, the martensitic transformation is suppressed by alloying ZrO_2 with stabilising oxides. The best mechanical stability is obtained with 6 to 8 wt% Y_2O_3 (Stecura, 1978; Miller and Berndt, 1984; Claussen *et al.*, 1984; Miller, 1987).

Figure 4.8 shows the low-yttria region of the ZrO_2 - Y_2O_3 phase diagram according to Scott (1975). Owing to the high cooling rates during plasma spraying, a nonequilibrium, non-transformable tetragonal phase (T') is formed directly from the cubic phase (F) by a diffusionless transformation. This phase, which has an yttria content equal to the bulk composition, is stable at room temperature (Miller *et al.*, 1981; Claussen *et al.*, 1984; Lelait *et al.*, 1989). During high temperature exposure, however, the T' phase slowly decomposes into the equilibrium low-yttria tetragonal (T) and high yttria cubic (F) phases, see for example the 1400°C tie line in figure 4.8. This transformation is diffusion controlled, so the amounts of T and F phases and the yttria content in both phases depend on time and temperature. On cooling, the cubic phase can remain cubic or transforms to T', depending on the yttria content. Similarly, the tetragonal phase can remain tetragonal (with a high yttria content,

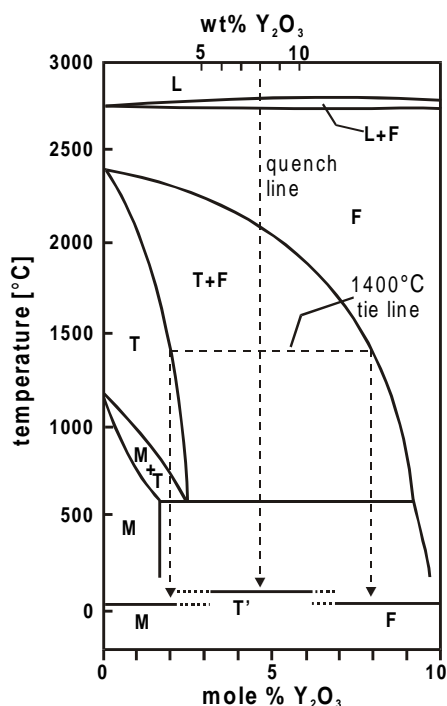


Figure 4.8 Low-yttria region of ZrO_2 - Y_2O_3 phase diagram. Non-equilibrium phases are indicated by horizontal bars. Dashed lines are composition lines after quenching or after isothermal heating at 1400°C . L=liquid, F=cubic, T=transformable tetragonal, M=monoclinic, T'=non-transformable tetragonal. Redrawn from Scott (1975)

hence T') or transforms to M in the case of low yttria content. (Miller *et al.*, 1981; Claussen *et al.*, 1984; Lelait *et al.*, 1989; Brandon and Taylor, 1991; VanValzah and Eaton, 1991; Verbeek, 1992).

It is sometimes claimed that the detrimental T-M martensitic transformation contributes to failure during burner rig testing (Levit *et al.*, 1994; Scardi *et al.*, 1995). The failure mode of the 0.3 mm coatings tested at a surface temperature of 1400°C (crumbled structure and surface spalling, see chapter 3, sub-section 3.5.2) indicate this may be true. In this section the phases present in the thermally shocked coatings are determined to investigate whether failure can be attributed to the T-M martensitic transformation. Since the temperature during burner rig testing decreases strongly through the thickness of the coating, only the top coat surfaces are analysed. If no monoclinic phase is observed there, it can be assumed absent in the bulk of the top coat.

4.5.2 Experimental

Phase analysis was done by X-ray diffraction, using a Rigaku Geiger Flex XRD apparatus with a voltage of 35 kV and a current of 20 mA. Diffraction scans were run from 20° - 80° 2θ , with a scanning speed of 0.12° 2θ min^{-1} (the diffraction scans of the bond coats, see section 2.4, were run with a scanning speed of 2° 2θ min^{-1}). The radiation used was $\text{Cu}_{K\alpha}$ with a wavelength of 1.5405 \AA . Peak identification was done with JCPDS.

4.5.3 Results and discussion

Figure 4.9 shows the diffraction patterns of PSZ powder, an as-sprayed top coat and two thermally shocked top coats, one with 3500 cycles at a maximum surface temperature of 1300°C, the other with 900 cycles at a maximum surface temperature of 1400°C. The latter had failed by surface spalling, see sub-section 3.5.2. The diffraction pattern of the powder is a reference to show the (more or less) equilibrium phase composition of PSZ. The crosses indicate the peaks of the monoclinic phase: in particular the two small peaks on both sides of the (1,1,1) peak at $2\theta=30.3^\circ$ are very characteristic for this phase.

For the as-sprayed top coat the monoclinic peaks were absent, as expected. The observed peaks belong to the nonequilibrium tetragonal (T') and cubic (F) phases, and are labelled at the top of the graph. Both thermally shocked top coats show diffraction patterns very similar to that of the as-sprayed top coat. For the thermally shocked top coats the relative intensities of the T' and F-peaks in the (4,0,0) region at $2\theta=74^\circ$ and in the (3,1,1) region at $2\theta=59^\circ$ are different to that of the as-sprayed top coat. This means that a shift from the nonequilibrium tetragonal (T') phase to the equilibrium cubic (F) phase has occurred (Miller *et al.*, 1981; Verbeek, 1992). Since the peaks in the (4,0,0) region are not easily resolved (Miller *et al.*, 1981), the amounts of phases are not quantitatively determined here.

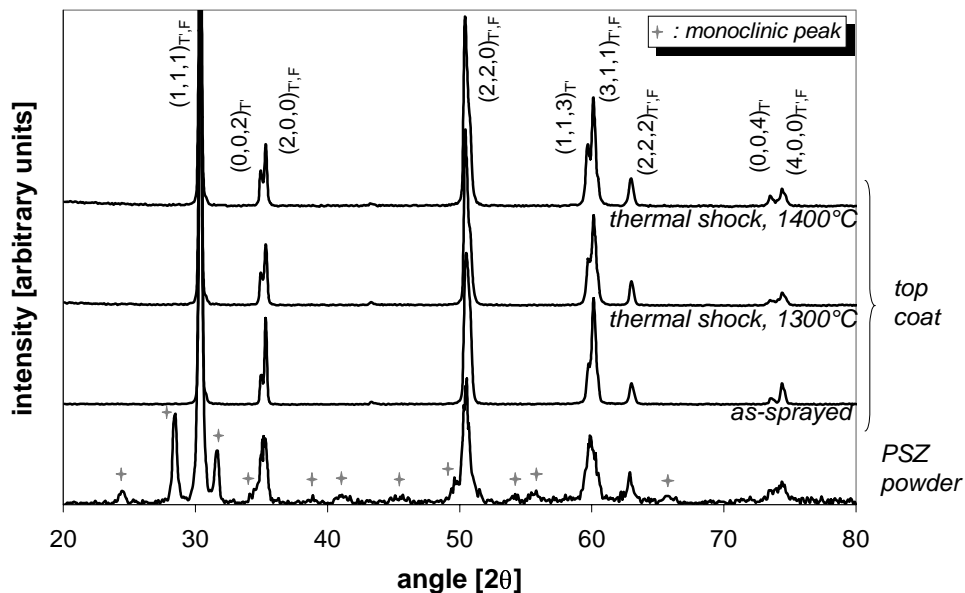


Figure 4.9 X-ray diffraction patterns of PSZ powder material, as-sprayed top coat, and thermally shocked ($T_{surf,max}=1300^\circ\text{C}$ and 1400°C) top coat. Crosses (\diamond) indicate peaks due to the monoclinic phase; $(h,k,l)_{T,F}$ refers to the Miller indices of diffraction planes in the tetragonal or cubic structures

It may be concluded that since the monoclinic phase was not observed in the thermally shocked top coats, failure during thermal shock testing is *not* due to the T→M martensitic transformation.

4.6 Bond coat composition

4.6.1 Introduction

Oxidation of the metallic MCrAlY bond coat has been clearly associated with the delamination of TBCs (conclusions chapter 3; Miller and Lowell, 1982; Haynes *et al.*, 2000). Despite formation of a protective Al₂O₃ layer on the top coat / bond coat interface, high temperature oxidation of the bond coat proceeds during long term exposure. This results in aluminium depletion of the bond coat and fast growth of other oxides (NiO, Cr₂O₃) and spinels (Ni[Cr,Al]₂O₄), which is detrimental to coating life (Wu *et al.*, 1989; Lih *et al.*, 1991; Shillington and Clarke, 1999).

In this section the effect of isothermal heating on the composition of the bond coat is investigated. The changes in composition owing to preoxidation (see chapter 2, sub-section 2.4.2), and furnace testing (see chapter 3, section 3.2) are presented. In the case of furnace testing, the bond coat composition was determined after top coat delamination had occurred.

4.6.2 Experimental

Chemical element analysis was done by electron probe microanalysis, using a JEOL 8600 SX with a voltage of 20 kV. For each measurement a line scan was carried out with a step size of 2 μm, starting in the substrate and ending in the top coat. The elements O and Ni were determined by WDS (Wavelength Dispersive Spectrometry), and the elements Al, Cr, Fe and Mo by EDS (Energy Dispersive Spectrometry).

4.6.3 Results and discussion

Table 4.2 gives the nominal bond coat composition and the average measured bulk composition of the bond coat in the as-sprayed and several preoxidised and furnace tested conditions. The general trends are that the Ni-content decreased with increasing heating time; the Cr-content first decreased upon heating but subsequently increased after long high temperature exposures; the Al-content decreased

with increasing heating time to almost zero after 300 cycles of 1 hr at 1137°C (aluminium depletion); and the Fe- and Mo-contents increased owing to diffusion from the Hastelloy-X substrate. In the following, three conditions will be discussed in more detail: as-sprayed, preoxidised (1050°C/10 hr), and furnace tested (1137°C/300×1 hr).

Table 4.2 Nominal and average measured bulk compositions of NiCrAlY bond coat in various conditions

Condition	Ni	Cr	Al	Fe	Mo
nominal	67	22	10	0	0
as-sprayed	67.9	21.6	8.8	0.4	0.1
preoxidised, 1050°C/5 hr	68.7	20.1	6.4	2.9	0.9
preoxidised, 1050°C/10 hr	67.9	19.5	5.7	4.7	1.6
furnace tested, 1137°C/20×1 hr	60.0	21.9	2.3	10.2	4.4
preoxidised, 1050°C/10 hr + furnace tested, 1137°C/40×1 hr	58.4	22.4	1.5	11.5	5.0
furnace tested, 1137°C/300×1 hr	55.9	23.1	0.9	12.9	5.7

As-sprayed, figure 4.10

In the as-sprayed bond coat the element contents equalled the nominal values, except for Al, which can be attributed to oxidation during the spraying process. The as-sprayed bond coat bulk composition was fairly constant over the thickness, except that some oxides (formed during spraying) were present at 68, 78, and 86 µm.

Preoxidised (1050°C/10 hr), figure 4.11

Preoxidation hardly changed the bulk Ni-content, but at the substrate / bond coat interface the Ni-content of the bond coat started to decrease and that of the substrate to increase, indicating that Ni diffused from the bond coat into the substrate. The Cr- and Al-contents in the bond coat decreased due to oxidation. The Al-content dropped to less than 6 wt%, which, combined with the fact that hardly any Ni and Cr were found in the preoxidation surface layer, indicates that this layer consisted predominantly of Al₂O₃. Also, some Fe and Mo had diffused from the substrate into the bond coat.

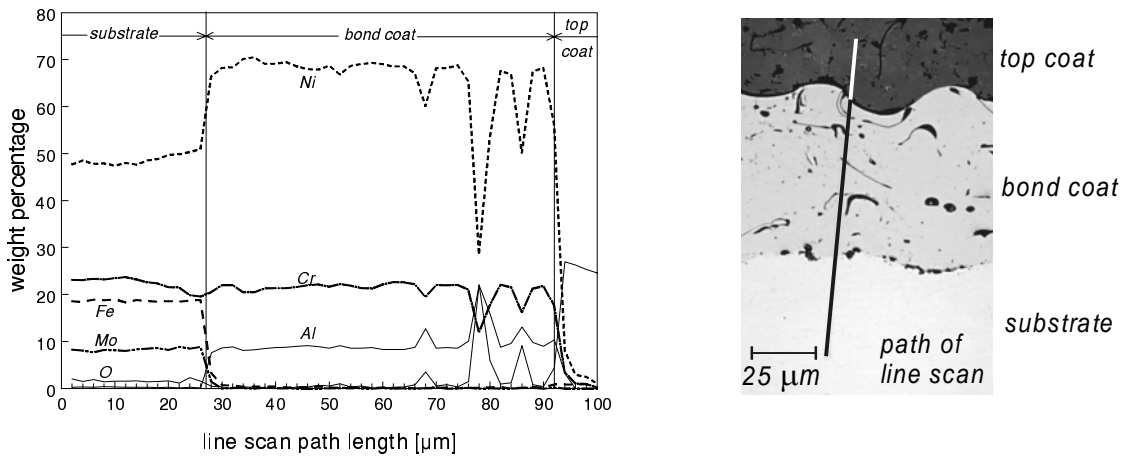


Figure 4.10 Chemical composition of bond coat in as-sprayed TBC. Local thickness is 65 μm . Cross-section on the right shows path of line scan

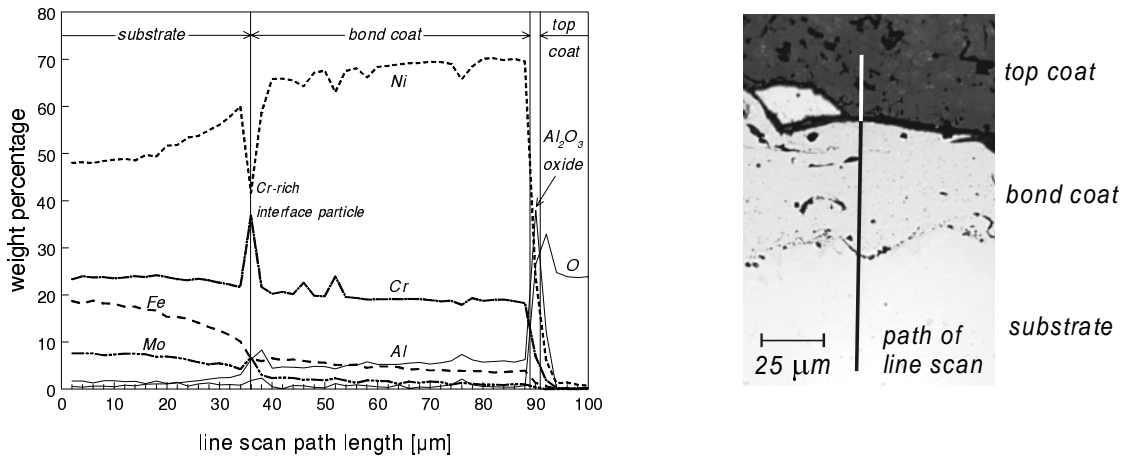


Figure 4.11 Chemical composition of preoxidised (1050°C / 10hr) bond coat. Local thickness is 52 μm . Cross-section on the right shows path of line scan

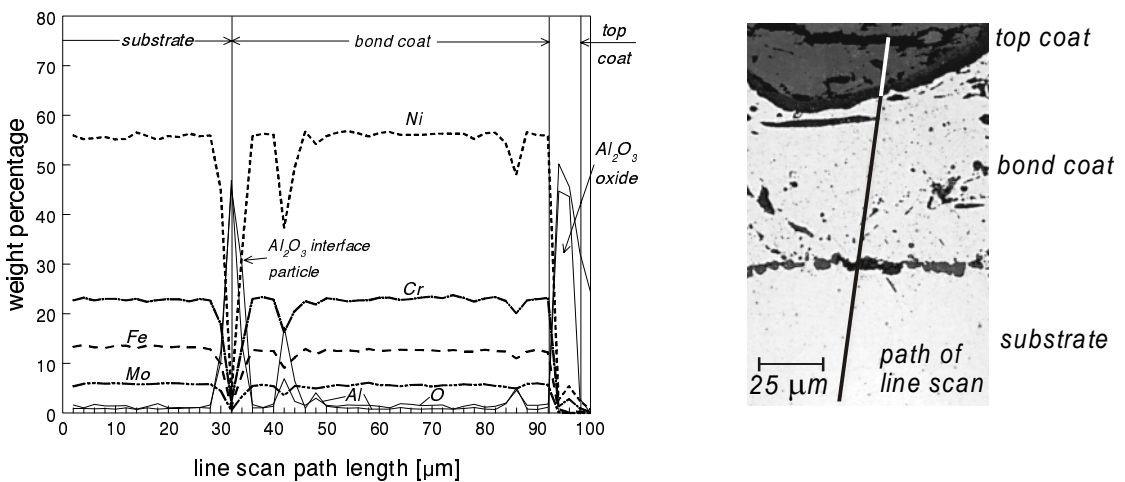


Figure 4.12 Chemical composition of bond coat in furnace tested (300 cycles of 1hr at 1137°C) TBC. Local thickness is 62 μm . Cross-section on the right shows path of line scan

Furnace tested (300 cycles of 1 hr at 1137°C), figure 4.12

After 300 cycles of 1 hr at 1137°C almost complete depletion of Al (less than 1wt%) had occurred. The level of all metallic elements was the same in the substrate near the substrate / bond coat interface, and the bond coat, except for some oxides at the substrate / bond coat interface and at 42, 48 and 86 μm . Some Ni and Cr were present in the oxide layer at the top coat / bond coat interface, probably in the form of $\text{Ni}(\text{Cr},\text{Al})_2\text{O}_4$ spinel.

Substrate / bond coat interface

In general (isothermal) heating results show that an interdiffusion zone developed at the substrate / bond coat interface. Complex particles containing Ni, Cr and Al were precipitated, see figure 4.11, and these particles have been identified as M_{23}C_6 and MC carbides by Lih *et al.* (1991). However, after long term (isothermal) heating alumina was found at the substrate / bond coat interface, figure 4.12. It would appear that interface porosity occurs owing to diffusion across the interface, after which Al_2O_3 is formed on the surfaces of the pores.

4.7 Conclusions

Sintering occurred during isothermal heating of the TBCs and resulted in microstructural changes. In general, the porosity decreased and sealing of flaws occurred. In consequence the microhardness, erosion resistance, and top coat bond strength increased.

Surface spalling of the top coat during burner rig testing with a coating surface temperature of 1400°C is not caused by the tetragonal to monoclinic phase transformation.

Aluminium depletion of the bond coat occurred during furnace testing of TBCs with 0.3 mm thick top coat. It should be further investigated how the formation of oxides other than Al_2O_3 enhances TBC failure.

5 MEASUREMENT OF RESIDUAL STRESSES

5.1 Introduction

Residual stresses in TBCs can be classified into two types: 1) stresses owing to the deposition process and 2) stresses caused by a thermal load (isothermal or thermal cycling).

1. Deposition stresses: these originate from primary cooling (quenching) and secondary cooling effects (Kuroda and Clyne, 1991; Verbeek, 1992; Clyne and Gill, 1996; Bengtsson and Persson, 1997). Quenching stresses arise during solidification of individual splats. Since the splats already adhere to the underlying material, tensile stresses develop upon cooling, and these relax by microcracking. Secondary cooling stresses arise due to differential thermal contraction between the substrate and the deposit, as a result of different coefficients of thermal expansion. These quenching and secondary stress components are superimposed, and so measurement of the residual stresses provides insight into evolution of the coating build-up.

Controlling the coating and hence stress build-up is very important. High stresses during spraying can lead to severe cracking or even delamination, and must therefore be avoided. However, some cracking of the top coat can also be desirable to obtain a low elastic modulus and hence a high thermal shock resistance (Verbeek, 1992; Bengtsson *et al.*, 1998). In this respect the as-sprayed residual stresses are highly significant for the interfacial adhesion and life of a TBC, and it is now widely recognised that tensile stresses are the most favourable (Watson and Levine, 1984; Clyne and Gill, 1996; Wigren *et al.*, 1996b).

2. Thermal load: after isothermal heating or after a few heating cycles (many of which occur during the operation of aircraft and marine gas turbines) the initial

as-sprayed stress state can be completely altered owing to sintering effects (see chapter 4, sections 4.2 and 4.3) and stress relaxation by cracking, plasticity and creep (Jordan and Faber, 1993; Grünling and Mannsmann, 1993; Scardi *et al.*, 1995, 1996; Wigren *et al.*, 1996a). Measurement of residual stresses in TBCs after thermal loading provides some insight into thermal history and damage evolution during service use.

Many techniques are available to measure residual stresses. They can be put into three main categories (Clyne and Gill, 1996): diffraction methods, material removal methods and curvature methods.

- In the first category, diffraction methods, the stresses are determined from the changes in crystal lattice spacing measured by X-ray diffraction (XRD) or neutron diffraction (Noyan and Cohen, 1987). XRD measurements have been used successfully for coatings by many authors (Kingswell *et al.*, 1991; Verbeek, 1992; Lee *et al.*, 1992; Jordan and Faber, 1993; Levit *et al.*, 1994; Scardi *et al.*, 1995, 1996). However, since the penetration depth of X-rays is limited to a few micrometers, only surface stresses can be measured. In contrast, the penetration depth of neutrons can be millimeters and hence proper depth profiling can be achieved. However, this technique is relatively new and as yet only sporadically applied to coatings (Matejcek *et al.*, 1999).
- Stress measurement in coatings by material removal is done by either the hole-drilling method (Pantucek *et al.*, 1991; Hoel *et al.*, 1991; Dolhof *et al.*, 1995) or the layer-removal method (SAE, 1965; Kim *et al.*, 1992; Greving *et al.*, 1994; Wigren *et al.*, 1996a; Bengtsson and Persson, 1997). For both methods the relieved strains due to material removal are measured by strain gauges and converted to the stresses in the removed material.
- The third category involves measuring the specimen curvature that occurs due to residual stresses. This can be done for the substrate/coating system after deposition (Knight and Smith, 1993) or during deposition (Kuroda *et al.*, 1988; Kuroda and Clyne, 1991; Gill and co-workers, summarised in Clyne and Gill, 1996). Another way is to measure the change in curvature of the coating after debonding (Hobbs and Reiter, 1988). The curvature technique results in an average stress value or, provided certain boundary conditions are assumed, a linear approximation of the stress gradient.

High stress gradients can arise in a top coat owing to the coating deposition process and the thermal history. It is therefore essential to measure the through-thickness stress profile. As mentioned above, this can be achieved by neutron diffraction and material removal techniques. Neutron diffraction is relatively new and neutron sources are hardly available (Clyne and Gill, 1996). On the other hand, material removal techniques entail some experimental problems, and so when they are applied it is advisable to validate the measured surface stresses with the more convenient XRD method.

The objective of this chapter is to relate the residual stress state to the thermal history of the TBCs, both in the as-sprayed condition and after isothermal heating or thermal shock. The stresses are measured by the hole-drilling method. It must be mentioned that some effort was undertaken to measure the residual stresses with the layer-removal method. However, with the available equipment it was not possible to obtain reliable results (Koolloos, 1996). It would have taken much time, effort, and trial and error to develop a reliable experimental set-up. Since the residual stress measurements are a small part of the present investigation, it was decided to continue the measurements with the hole-drilling method only.

Section 5.2 describes the two methods used. These are the hole-drilling method and XRD, which was used to validate the surface stress measurements obtained from the hole-drilling method: XRD will be described first. Section 5.3 gives the results of the preliminary validation measurements. Section 5.4 gives the results of the stress measurements with the hole-drilling method, and section 5.5 discusses some of the experimental problems. Section 5.6 ends this chapter with conclusions concerning the residual stress measurements.

5.2 Experimental procedures

5.2.1 X-ray diffraction

For stress measurements using X-ray diffraction (XRD) techniques, the $\sin^2\psi$ method is applied. The method is based on Bragg's law, which states that each crystalline material has a unique set of diffraction angles (Noyan and Cohen, 1987):

$$2d \sin \theta = \lambda \quad (5.1)$$

where d is the lattice plane spacing for a certain set of (hkl) planes, θ the diffraction angle and λ the wavelength of the radiation. From Eq. 5.1 it is clear that for a certain wavelength, the diffraction angle depends entirely on the lattice plane spacing. The

principle of the $\sin^2\psi$ method is that for an elastic body subjected to a plane stress situation the spacing between the lattice planes will change, resulting in a peak shift. By monitoring this peak shift as a function of ψ , the angle between the normal of the coating surface and the normal to the diffracting planes, the lattice strain in direction φ , $\varepsilon_{\varphi,\psi}$, can then be obtained from (Noyan and Cohen, 1987):

$$\varepsilon_{\varphi,\psi} = \frac{d - d_0}{d_0} = \left(\frac{1}{2}S_2\right)_{hkl} (\sigma_1 \cos^2 \varphi + \sigma_2 \sin^2 \varphi) \sin^2 \psi + (S_1)_{hkl} (\sigma_1 + \sigma_2) \quad (5.2)$$

where d_0 is the unstressed lattice spacing and S_1 and $\frac{1}{2}S_2$ are the X-ray elastic constants, which are (hkl) dependent. When d is determined for a range of ψ values the stress σ_φ ($=\sigma_1 \cos^2 \varphi + \sigma_2 \sin^2 \varphi$) can be calculated from the slope of d versus $\sin^2 \psi$ according to:

$$\sigma_\varphi = \left(\frac{1}{2}S_2\right)_{hkl} \frac{1}{d_0} \left(\frac{\partial d}{\partial \sin^2 \psi} \right) \quad (5.3)$$

The unstressed lattice spacing d_0 cannot be determined without a stress-free specimen. However, from Eqs. 5.2 and 5.3 it follows that by taking $d_0 = d_{\psi=0}$ only a very small error in σ_φ (<2%) is made.

The XRD measurements were carried out at Twente University using a Rigaku Strainflex MSF-2M with $\text{CrK}\alpha$ radiation ($\lambda=0.2291$ nm). The analyses were performed on the (331/133) t-ZrO₂ peak ($2\theta \approx 153.5^\circ$) with $\frac{1}{2}S_2 = 7,14 \cdot 10^{-6}$ mm²N⁻¹ (Eigenmann *et al.*, 1989). The irradiated area was 22×5 mm². The specimens were tilted from $\psi=0^\circ$ to $\psi=45^\circ$ ($\sin^2 \psi = 0.5$) in 6 steps for $\varphi=0^\circ$ (longitudinal direction of coated strip) and $\varphi=90^\circ$ (transverse direction of coated strip). The experimental uncertainty for the XRD measurements was about 15%.

5.2.2 Hole-drilling method

The hole-drilling method (ASTM, 1992; Measurements Group, 1993) is a method to evaluate residual stresses near the surface of a specimen by drilling a small hole and measuring the relieved strains in the surrounding material. It is often referred to as a semi-destructive technique, since the small hole does not significantly affect the structural integrity of the specimen. The strains are measured with a three-element strain gauge rosette as shown in figure 5.1. The rosette consists of three radially oriented gauges with their centres at the strain gauge circle with diameter D . The rosette design incorporates centring marks for aligning the drill precisely at the centre of the gauge circle. The diameter of the drilled hole, D_0 , should be related to the diameter of the gauge circle by

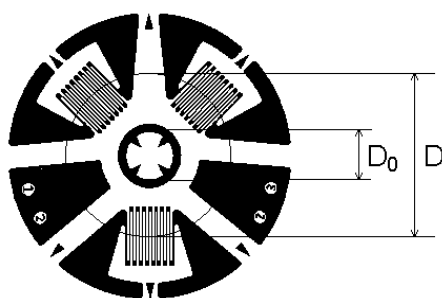


Figure 5.1 Strain gauge rosette for the hole-drilling method

$$0.3 < \frac{D_0}{D} < 0.5 \quad (5.4)$$

The hole is incrementally drilled in order to measure a possibly non-uniform stress profile. Due to a decrease in accuracy with increasing depth (see section 5.5), the hole depth, Z , is limited and should obey the following equation:

$$\frac{Z}{D} \leq 0.25 \quad (5.5)$$

The relieved strains are measured for each increment and converted to the principal stresses by the following formula:

$$\sigma_{\max, \min} = \frac{\varepsilon_1 + \varepsilon_3}{4A} \pm \frac{\sqrt{2}}{4B} \sqrt{(\varepsilon_1 - \varepsilon_2)^2 + (\varepsilon_3 - \varepsilon_2)^2} \quad (5.6)$$

where ε_1 , ε_2 , and ε_3 are the measured strains at gauges 1, 2 and 3 respectively (figure 5.1). A and B are coefficients to be determined from the following equations:

$$\begin{aligned} A &= -\frac{1+\nu}{2E} \bar{a} \\ B &= -\frac{1}{2E} \bar{b} \end{aligned} \quad (5.7)$$

E and ν are the coating Young's modulus and Poisson's ratio respectively. \bar{a} and \bar{b} are dimensionless, material-independent coefficients, which depend on Z , D and D_0 . These coefficients were derived from finite element studies by Schajer (1988).

The stresses $\sigma_{\max, \min}$ according to Eq 5.6 are the so-called equivalent uniform stresses, *i.e.* the uniform stresses within the total hole depth that produce the same total strain relaxation as the actual non-uniform stress distribution. It is more convenient to calculate the average stresses within each hole depth increment, the so called apparent equivalent uniform stresses. This is done separately for σ_{\max} and σ_{\min} as follows (Nickola, 1986):

$$\sigma'_n = \frac{\sigma_n Z_n - \sigma_{n-1} Z_{n-1}}{Z_n - Z_{n-1}} \quad (5.8)$$

where σ'_n is the maximum or minimum apparent equivalent uniform stress in the n^{th} drilling increment, Z_n and Z_{n-1} are the depths of drilling increments n and $n-1$, and σ_n and σ_{n-1} are the equivalent uniform stresses from the surface to depths Z_n and Z_{n-1} .

The general procedure for the hole-drilling method was as follows. The holes were drilled with a high-speed air turbine diamond cutter, using an RS-200 Milling Guide. First the specimen was bonded on a thick steel plate with a quick-setting frangible adhesive. Next the milling guide was adhesive bonded to the same plate via its three supports. Before drilling, a microscope was installed to align the device visually. The first drilling increment was 0.06 mm, followed by steps of 0.04 mm up to a depth corresponding to the total coating thickness.

In more detail, the size of the strain gauge rosette (D), and hence the diameter of the drilled hole (D_0), should be determined by the top coat thickness according to Eq. 5.5. This means that for the TBCs with thicknesses 0.3 and 0.6 mm the strain gauge rosette EA-06-031RE-120 ($D=2.56$ mm, $D_0=0.9$ mm) and for the TBCs with thickness 1.0 mm the strain gauge rosette EA-06-062RE-120 ($D=5.13$ mm, $D_0=1.8$ mm) were used (both rosettes are from Measurements Group). Figure 5.2 shows the drill used for making the 0.9 mm holes. The abrasive head is clearly visible.

After hole drilling the diameters of the holes were measured with an Amsler binocular. Data reduction was performed with the assumption of a top coat Young's modulus of 25 GPa (see section 2.5) and a Poisson's ratio of 0.2 (Clyne and Gill, 1996).

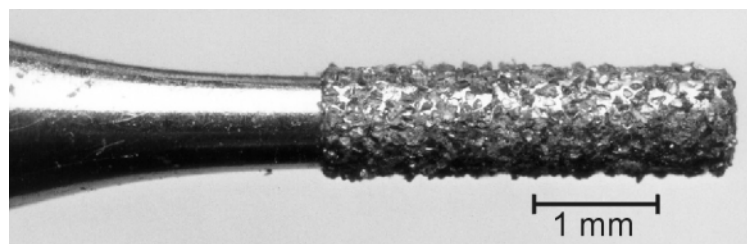


Figure 5.2 Example drill used for the hole-drilling method. Diameter of drill head is 0.9 mm.

5.2.3 Specimens

The preliminary stress measurements were done on the as-sprayed 'excessive energy plasma' specimens. Coupons with dimensions of 30×30 mm were cut from the 125×30 mm strips. This had the consequence that the stresses at the boundaries of the coupons were reduced to zero, causing the stresses in the coupons to diminish (Shadley *et al.*, 1987). However, since the width-thickness ratio of the coupons was

large ($w/t \approx 10$) and the stresses in the top coat would be low, the stress changes involved in the cutting-out step are assumed to be negligible. Moreover, for both methods (XRD and hole-drilling) the measurements take place over a very small area in the centre of each coupon, where the stress state is unlikely to be affected by the cutting-out step.

5.3 Preliminary measurements

Figure 5.3 shows the results of the X-ray diffraction stress measurements for both the longitudinal and cross directions. It can be seen that tensile stresses were low, varying between 50 and 80 MPa. The variation is considerable but close to the experimental uncertainty, except for the 55/25 and 85/25 specimens measured lengthwise. The differences between lengthwise and crosswise measurements are considered insignificant. ψ -splitting, which indicates the presence of shear stresses, as observed by Lee *et al.* (1992), was not found (Koolloos, 1996).

Figure 5.4 shows the average stresses¹ according to the hole-drilling method. As found by XRD, the coatings contain low tensile stresses, which are sometimes even compressive near the surface.

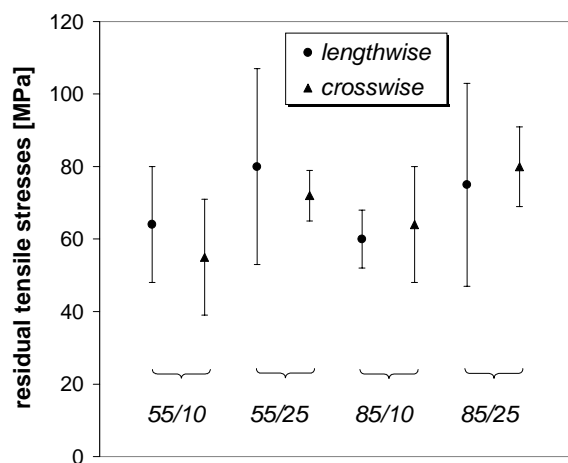


Figure 5.3 Preliminary results of the $\sin^2\psi$ method for 0.3 mm as-sprayed 'excessive energy plasma' specimens (in longitudinal and cross direction of the strip).

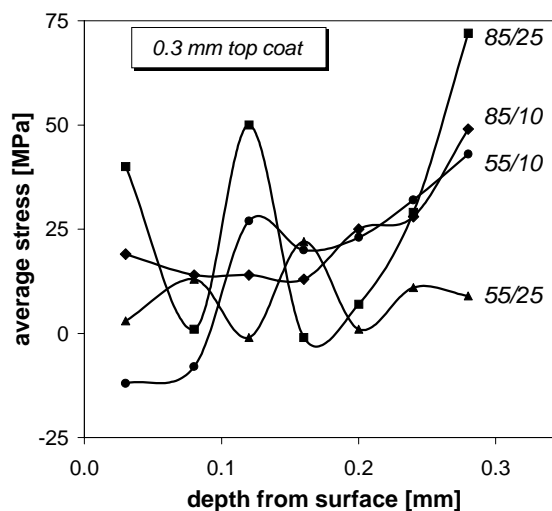


Figure 5.4 Preliminary results of the hole-drilling method for 0.3 mm as-sprayed 'excessive energy plasma' specimens

¹ Since the differences between the maximum and minimum principal stresses were relatively small, only the average stresses, $(\sigma_{\max} + \sigma_{\min})/2$, are shown in figure 5.4.

The results of the X-ray diffraction method and the hole-drilling method show low tensile stresses in as-sprayed TBCs. This agrees with previous observations that cooling during spraying causes primary tension stresses, which relax to low values owing to microcracking (Kingswell *et al.*, 1991; Kuroda and Clyne, 1991; Verbeek, 1992; Scardi *et al.*, 1995, 1996; Clyne and Gill, 1996; Wigren *et al.*, 1996a; Bengtsson and Persson, 1997). Moreover, all coated strips were concave on the coated surfaces, indicating tensile residual stresses in the coating (Knight and Smith, 1993).

The stresses according to the XRD method were higher than those determined with the hole-drilling method, compare figures 5.3 and 5.4. The microcracked structure of TBCs and the different volume scales of the material sampled by both methods can explain this (Kuroda and Clyne, 1991; Pina *et al.*, 1999). The high initial stresses are relaxed by microcracking, after which the stresses in the islands of intact material surrounded by flaws are higher than the average stresses in the microcracked, porous coating. The X-ray diffraction method determines the stresses from the lattice strains in the islands of intact material, while the hole-drilling method determines the average coating stresses since the strain gauge rosette covers a large area of the coating surface.

It must be mentioned that the preliminary measurements obtained with the hole-drilling method were not very accurate, owing to some experimental problems which are described in section 5.5. However, for a comparison with the XRD-method, the results were sufficient to justify the decision to continue with this method. Furthermore, for the measurements described in section 5.4 the experimental conditions and accuracy were improved.

5.4 Main measurements

5.4.1 Introduction

This section describes the effect of top coat thickness, bond coat preoxidation, isothermal heating, and thermal shock on the top coat residual stresses measured with the hole-drilling method. The experimental programme is given in table 5.1. The measurements were carried out on the 45/20 specimens. The top coat thicknesses were 0.3, 0.6 and 1.0 mm.

Table 5.1 Overview of specimens for residual stress measurements

thickness [mm]	preoxida- tion time	as-sprayed	isothermal heating, 5hr		thermal shock (1300°C)	
			1050°C	1250°C	centre	15 mm
0.3	—	×	×	×	×	×
	5 hr	×	×	—	—	—
	10 hr	×	—	—	—	—
0.6	—	×	×	—	×	×
1.0	—	×	×	—	×	x

First the deposition residual stresses were measured. This was done for all coatings, including the 0.3 mm top coats with a pre-oxidized bond coat. Next, the stresses developed after isothermal heating in a furnace were determined. Initially, the heat treatment was chosen to be 1250°C for 5 hr. However, for this condition the thick (0.6 and 1.0 mm) TBCs failed after cooling. Therefore the specimens were isothermally heated at 1050°C for 5 hr, which offered the opportunity to study the effect of isothermal heating temperature for the 0.3 mm top coats. Thirdly, the stresses in the top coat after 200 thermal shock cycles in the burner rig with a maximum surface temperature of 1300°C were measured. This was done in the centre of the area covered by the flame, and 15 mm from this centre, near the edge of the heat affected zone.

The specimens for the measurements on the as-sprayed and isothermally heated TBCs were similar to those described in section 5.2.3 (30×30 mm). The strain gauge rosettes were positioned in the centres of the specimens. The thermally shocked specimens were 30×80 mm² with two strain gauge rosettes (centre flame area and 15 mm off-centre) as mentioned in the previous paragraph. Figure 5.5 is an example, showing the configuration of a thermally shocked 1.0 mm TBC specimen with strain gauge rosettes EA-06-062RE-120 connected to contact wires via a terminal.

5.4.2 Results

Figures 5.6—5.8 give the average residual stresses for each top coat thickness. It is seen that the stresses in the TBCs were almost uniform over the thickness for each coating condition and coating thickness. Therefore, the equivalent uniform stress for the last increment equals the average stress for the entire coating thickness. This provides a good overall picture of the effect of coating condition and coating thickness that is not troubled by scattering, figure 5.9. The results show:

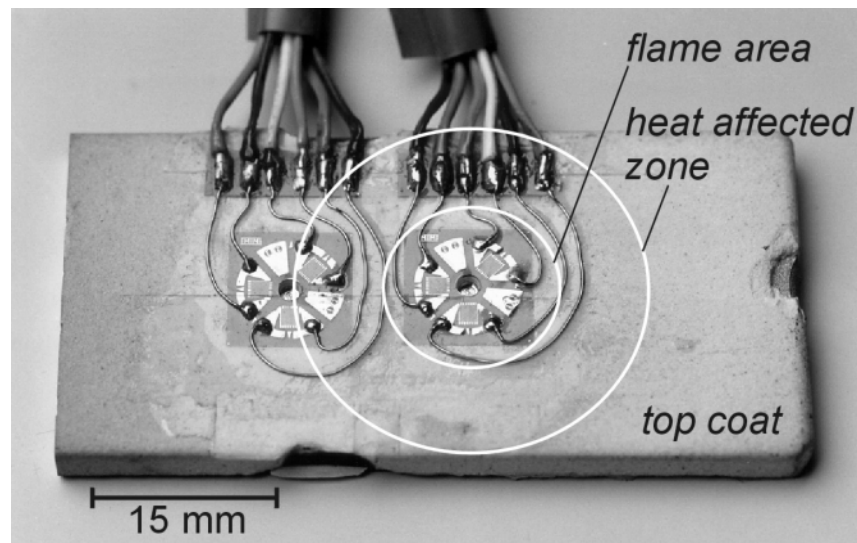


Figure 5.5 Hole-drilling method strain gauge rosettes on thermal shock specimen. Measurements have already been carried out and the holes are visible. The flame area and heat affected zone are indicated.

- Significant differences in residual stresses depending on the coating condition. In general the as-sprayed residual stresses were returned to less tensile or even compressive stresses by isothermal heating and thermal shock.
- The as-sprayed residual stresses were low (ranging from about 0–40 MPa in the tensile regime) and apparently independent of depth within the coatings. The stresses in the 1.0 mm top coat were lower than those in the 0.3 and 0.6 mm top coats.
- After isothermal heating the residual stresses were entirely compressive, increasingly so towards the top coat / bond coat interface. The magnitudes of the stresses decreased with increasing coating thickness. The isothermal heating temperature had only a minor effect on the residual stresses.
- Thermal shock resulted in low residual stresses with the sign depending on location and coating thickness. In the centre of the flame covered area the residual stresses were compressive for the 0.3 mm top coat and tensile for the 0.6 mm and 1.0 mm top coat. At 15 mm off-centre the residual stresses were tensile for the 0.3 mm top coat and compressive for the 0.6 mm and 1.0 mm top coat. The stresses showed no trend with respect to depth within the coatings.

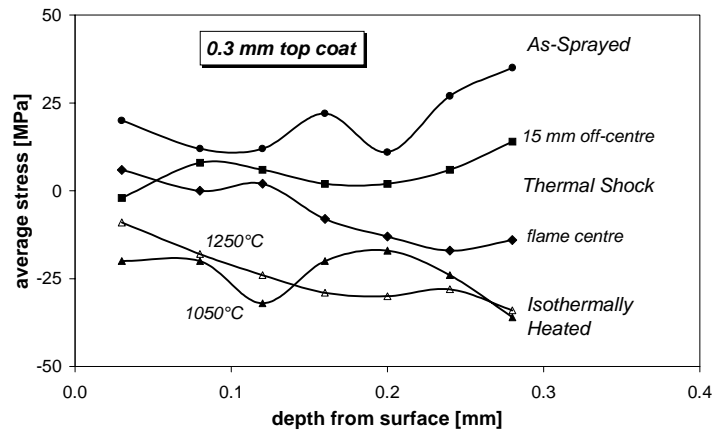


Figure 5.6 Stress profile in 0.3 mm TBC. Stress is given as distance from coating surface in as-sprayed, isothermally heated (1050°C/5hr and 1250°C/5hr) and thermal shock (at centre of flame covered area and 15 mm off-centre) specimens.

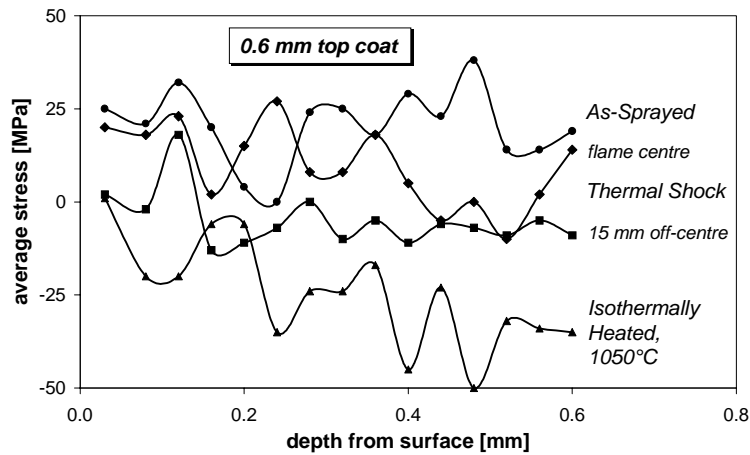


Figure 5.7 Stress profile in 0.6 mm TBC. Stress is given as distance from coating surface in as-sprayed, isothermally heated (1050°C/5hr) and thermal shock (at centre of flame covered area and 15 mm off-centre) specimens.

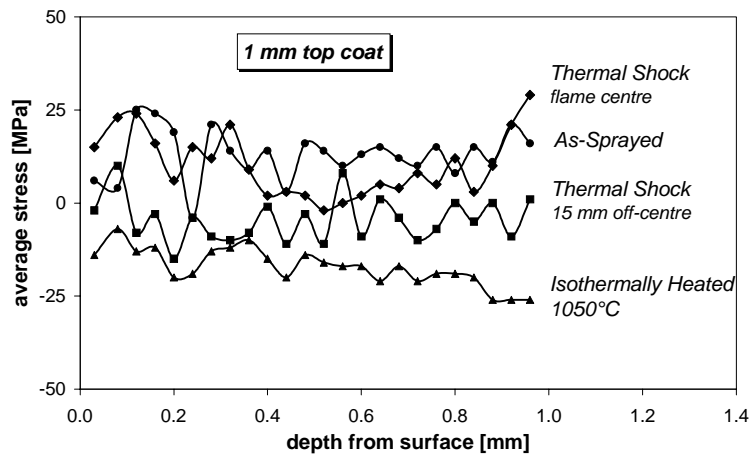


Figure 5.8 Stress profile in 1.0 mm TBC. Stress is given as distance from coating surface in as-sprayed, isothermally heated (1050°C/5hr) and thermal shock (at centre of flame covered area and 15 mm off-centre) specimens.

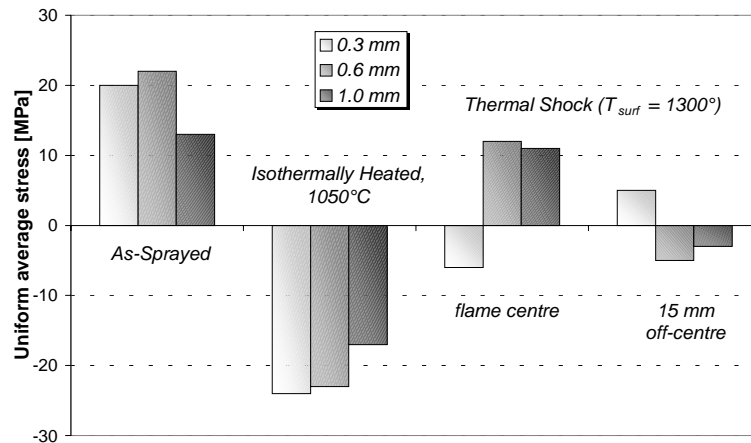


Figure 5.9 Equivalent uniform stresses over entire coating thickness in as-sprayed, isothermally heated (1050°C/5hr) and thermal shock (at centre of flame covered area and 15 mm off-centre) specimens for 0.3 mm, 0.6 mm and 1.0 mm.

Figure 5.10 shows the influence of a preoxidised bond coat on the residual stresses in a 0.3 mm top coat. The effect of the preoxidation time (5 and 10 hr) is shown only for the as-sprayed state. It is seen that bond coat preoxidation did not affect the residual stresses in the top coat, whether measured in the as-sprayed state or after isothermal heating.

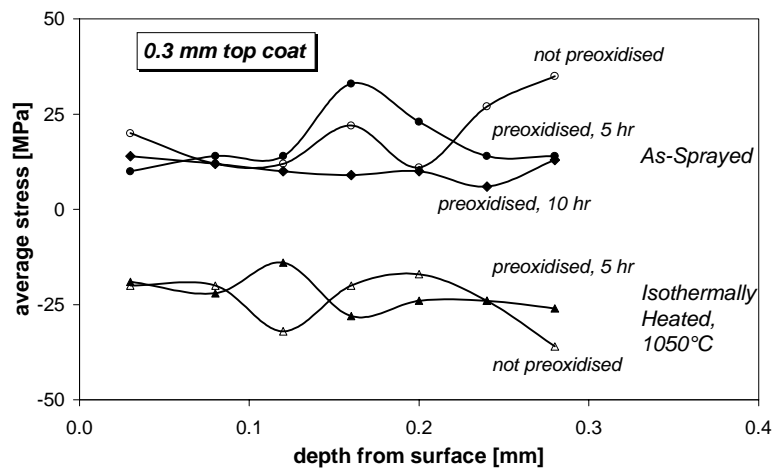


Figure 5.10 Stress profile in 0.3 mm TBC with and without preoxidised bond coat (5hr and 10 hr at 1050°C). Stress is given as distance from coating surface in as-sprayed and isothermally heated (1050°C/5hr) specimens.

5.4.3 Discussion

The scatter in the residual stress data over the coating thickness could be considerable. The variation in stress for the as-sprayed preoxidised specimen (figure 5.10) was only 5 MPa, while the stresses in the as-sprayed 0.6 mm specimen (figure 5.7) varied from 0 to 40 MPa. The scatter can be attributed to experimental errors,

which will be discussed in the next section. It should also be noted that most experiments were done only once, so statistical averaging was not possible. In that light the fairly smooth curves in figure 5.10 are good.

In the following the general effect of coating thickness and coating condition on the residual stresses in the top coat, as shown in figure 5.9, will be discussed in detail.

1. *As-sprayed specimens*

The magnitude of the measured stresses agrees well with other measurements for cooled specimens (see section 5.3) and also predictions for cooled specimens (Takeuchi *et al.*, 1990; Elsing *et al.*, 1990; Verbeek, 1992; Clyne and Gill, 1996; Bengtsson and Persson, 1997). Hence in the as-sprayed condition the residual stresses can be attributed mainly to primary cooling effects.

Though no differences in stress levels were found between the 0.3 and 0.6 mm coatings, the average tensile stresses in the 1.0 mm top coat were lower. This is remarkable since it is widely known that very thick TBCs (>2 mm) can delaminate spontaneously just after deposition, which suggests increasing stresses with thickness. These phenomena can be explained as follows. For a relatively large thickness the heat from the plasma and melting particles is poorly removed and the specimen temperature increases during spraying. Subsequent cooling results in secondary cooling stresses. These are compressive for the case where $CTE_{tc} < CTE_{sub}$, and hence the residual tensile stresses are lowered. At the same time, however, high shear stresses develop at the intersection of the top coat / bond coat interface and the free edges of the specimen. These shear stresses increase with coating thickness and can cause delamination. This will be shown in chapter 6.

2. *Isothermally heated specimens*

Residual compressive stresses were present after isothermal heating for all values of the coating thickness. This can be understood as follows. The coating stresses after heating relax completely within one hour at high temperatures (see Appendix 6C). Hence, since $CTE_{tc} < CTE_{sub}$, compressive stresses develop in the top coat and these increase towards the interface owing to specimen bending. This was also observed by Jordan and Faber (1993), Grünling and Mannsmann (1993) and Scardi *et al.* (1996), who measured the stresses by XRD, and by Wigren *et al.* (1996a) who used the layer-removal method. However, all authors found slightly higher compressive stresses compared to the values reported here. The discrepancy can be attributed to the

differences in techniques, as discussed in section 5.3, and to the fact that owing to sintering the Young's modulus of a heat-treated TBC becomes higher than the as-sprayed Young's modulus (Wesling *et al.* 1994, Rettig *et al.* 1999): this was not taken into account during data reduction in the present work. Also, it is possible that owing to the dense network of microcracks the presently prepared TBC accommodated the thermal stresses better than the others, resulting in lower residual stresses.

The effects of coating thickness and isothermal heating temperature on residual stresses will be compared with model predictions in chapter 7.

Table 5.2 Results of residual stress measurements, microscopic investigations (vertical cracking and densification) and modelling (creep, see chapter 6) for thermal shock specimens and isothermally heated specimens

type of test	top coat thickness	position	stress #	vertical cracking	densification	creep
thermal shock	0.3 mm	centre	-	no	yes, decreases towards edge	no
		15 mm	+	no	no	no
	0.6 mm	centre	+	yes, from surface to bond coat, mutual distance ~0.6 mm	yes, decreases towards edge	no
		15 mm	-	no	yes, in area 2.5 mm around hole	no
	1.0 mm	centre	+	yes, from surface to bond coat, mutual distance 2-3 mm	yes, decreases towards edge	no
		15 mm	-	yes, from surface to mid depth, mutual distance ~3 mm	yes, in area 3 mm around hole	no
isothermal heating	0.3, 0.6, 1.0 mm	entire specimen	-	yes, from surface to bond coat, mutual distance ~3 mm	yes, entire specimen	yes

tensile = +; compressive = -

3. Thermal shock specimens

Figure 5.9 shows that both in the centre of the flame covered area and in the heat affected zone the residual stresses underwent a remarkable reversal in sign as the coating thickness increased. The specimens were microscopically investigated near

the locations of the stress measurements to find an explanation for these results. Table 5.2 summarises the results of the microscopy investigations and the stress measurements, with the results for isothermally heated specimens added for comparison. There are three phenomena to be considered:

1. *Vertical cracks*, which develop only under tensile loads, *i.e.* during heating of the specimens. There are two opposing effects of vertical cracking on the coating stresses. Firstly, vertical cracking lowers the Young's modulus during testing, so the residual stresses after testing will be higher than before testing. Secondly, the tensile stresses developed during heating will be partly relaxed by crack forming, which results in lower stresses after testing than before testing.
2. *Densification*, attributed to sintering, which can occur at temperatures well below normal sintering temperatures (1400°C for ceramic material), see chapter 4. The net effect of densification is that the Young's modulus during the first heating period is lower than that during the last cooling period, so the residual stresses after testing will be lower than before testing. At 15 mm off-centre the densification was observed only in the 0.6 mm and 1 mm top coat, and only in a small area around the drilled hole, see figure 5.11 for an example. Apparently, the heat affected zone in which sintering occurred extended just to the 15 mm off-centre stress measurement location for the thick coatings (see also figure 5.5). It should be noted that sintering was not induced by hole-drilling since 1) it is very unlikely that the temperature during the short drilling increments was drastically increased, and 2) sintering was not observed for the 0.3 mm top coats at 15 mm off-centre.
3. *Creep*, which did not occur for the thermal shock specimens, since the time at high temperature per cycle is too short, see section 6.9.2, figure 6.29b. Therefore, the sign of the residual stresses after cooling is determined by the occurrence of vertical cracking and/or densification.

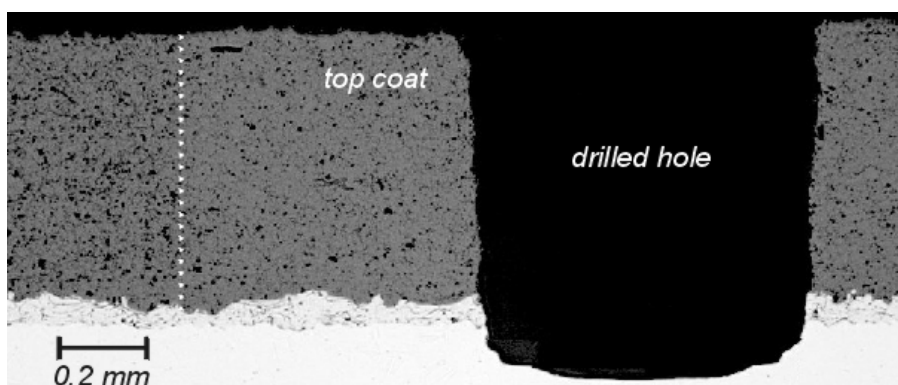


Figure 5.11 Densification of 0.6 mm TBC in the area of the drilled hole, 15 mm off-centre. The microstructure at the right-hand side of the dotted line is denser.

The consequences of the foregoing observations are:

- When neither densification nor vertical cracking take place the TBC behaves elastically and the stresses after testing should be the same (tensile) as in the as-sprayed specimen. However, for the 0.3 mm top coat, 15 mm off-centre, although the stresses are still tensile they are lower than in the as-sprayed state, see figures 5.6 and 5.9. Apparently some stress relaxation and/or increase in Young's modulus occurred at high temperatures. This behaviour will be called the reference case.
- Densification without vertical cracking results in post-test residual stresses that are lower than the residual stresses in the reference case. This explains the compressive stresses in the 0.3 mm top coat, centre location, and the 0.6 mm top coat, 15 mm off-centre, see figures 5.6, 5.7 and 5.9.
- Densification *and* through-thickness vertical cracking result in small changes in post-test residual stresses owing to their opposing contributions, see the 0.6 and 1.0 mm top coats, centre locations in figures 5.7– 5.9. Apparently, the net effect of vertical cracking is an increase in post-test stresses, and since the residual tensile stresses are higher than for the reference case, it may even be concluded that the effect of vertical cracking is stronger than that of densification.

When the cracks run only to mid-depth (1.0 mm top coat, 15 mm off-centre) the Young's modulus during cooling is not as low as for through thickness cracked specimens, and so low compressive stresses develop.

- Note that when creep occurs (isothermally heated specimens) the specimens are stress-free before cooling, and since $CTE_{tc} < CTE_{sub}$ the residual stresses after cooling will *always* be compressive, irrespective of whether densification or vertical cracking takes place.

N.B.: Some authors claim that compressive residual stresses after long term high temperature treatments are partly caused by the tetragonal to monoclinic phase transformation (Levit *et al.*, 1994; Scardi *et al.*, 1995). However, no traces of the monoclinic phase were found in the thermal shock specimens (see chapter 4, section 4.5), and so this possible cause of compressive stresses may be discounted.

5.5 Experimental problems

When interpreting the results of the hole-drilling method it must be kept in mind that numerous experimental errors can affect the results. This is because residual stress measurements with the hole-drilling method involve many variations in

technique and parameters (material removal, depth and diameter determination, strain measurement). Most of these possible errors are discussed in the literature (Schajer and Altus, 1996; Measurements Group, 1993; Sandifer and Bowie, 1978; Ajovalasit, 1979). In this section some experimental problems encountered during the present measurements and their effects on the calculated stresses will be discussed.

Strain measurements

The main source of errors concerns the strain measurements. Firstly, the strains are measured at the specimen surface, remote from the desired stresses except for the first increment. It can be shown that for a particular increment the relieved strains at the surface are caused only partly by the residual stresses in that increment, and that the relative contribution of the stress in an increment to the change in measured strain decreases with distance from the surface (Schajer, 1988; Measurements Group, 1993). Secondly, owing to the strains being small, measurement errors like instrumentation errors, thermally induced strains, and strains induced by the hole drilling process can be significant. In fact, Schajer and Altus (1996) identified these errors as the major error source. They are hard to quantify and hence to correct for. During the measurements the utmost attention is paid to trying to avoid these errors by calibrating the instrumentation, frequent checks for strain drift, keeping the environmental conditions constant (no heat sources like a light in the vicinity of the specimen) and gradually drilling with a low feed. In this context, glueing of the strain gauge rosettes on the specimens must also be mentioned. Strain gauge adhesion can be poor owing to the relatively rough top coat surface, resulting in strain drifting during the measurements. Based on our experiences, a procedure was developed by which good strain gauge adherence was obtained.

Hole eccentricity

A major experimental difficulty was to position the drill precisely in the centre of the strain gauge rosette. Small eccentricities of the hole can result in considerable errors in predicted stress. Sandifer and Bowie (1978) and Ajovalasit (1979) developed methods to correct for hole eccentricity, but the computational techniques are very complex. It is more convenient to make an approximate estimate of the misalignment error. The magnitude of the stress error depends on the relative eccentricity, \bar{e} :

$$\bar{e} = \frac{2e}{D_0} \quad (5.9)$$

where e is the absolute eccentricity. According to Ajovalasit (1979), an eccentricity of 0.08 mm for a strain gauge rosette with $D=2.56$ mm ($\bar{e}=18\%$) results in a maximum stress error of 25%. The same result was found by Sasaki *et al.* (1997), who simulated the hole-drilling method by the indirect fictitious-boundary integral method, in order to verify the accuracy of the measurement procedure.

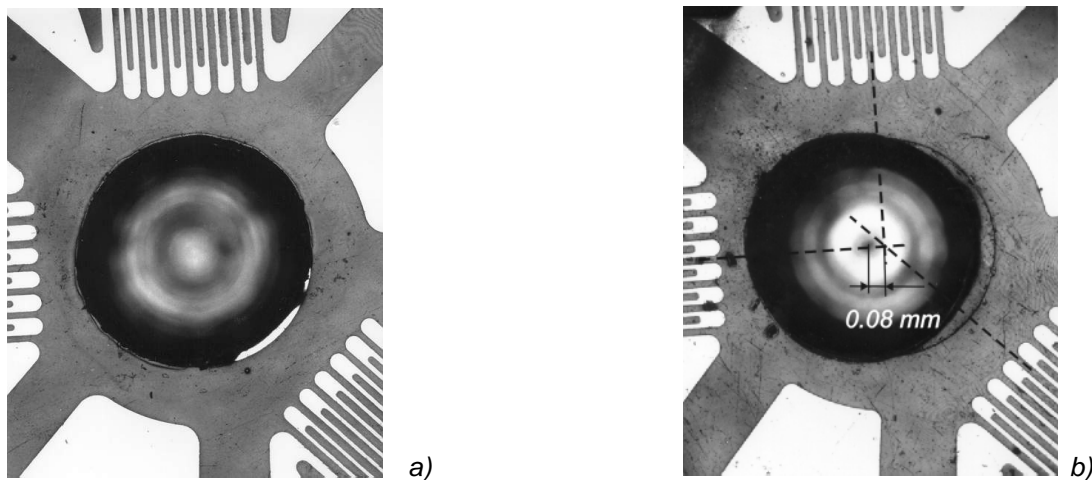


Figure 5.12 Examples of concentric (a) and eccentric (b) holes. The hole diameter is about 1 mm, the eccentricity 0.08 mm.

During the present measurements a relative eccentricity of 18% was taken as the maximum allowable error. Figure 5.12 shows as an example a concentric hole and a hole with an eccentricity of 0.08 mm. It should be noted that although the possibility of large stress errors increases with decreasing strain gauge rosette size (see Eq. 5.9) the smallest possible rosettes were used. This is because both the strain measurement and the determination of \bar{a} and \bar{b} are more accurate for smaller strain gauge rosettes.

Hole diameter and shape

Figure 5.13 shows a blind hole in a 0.3 mm TBC. It is clear that the hole diameter in the top coat is larger than the drill diameter. The widening during drilling is caused by lateral deflection of the drill owing to the porous structure of the coating and by abrasion during material removal. This means that the diameters of the increments *during* drilling are smaller than *after* the entire drilling procedure and that widening increases towards the surface. Since the hole diameter is measured after the drilling procedure an overestimate of the diameter is made. It can be deduced that an overestimate of the hole diameter by 10% results in an underestimate of the residual stresses by about 20%.

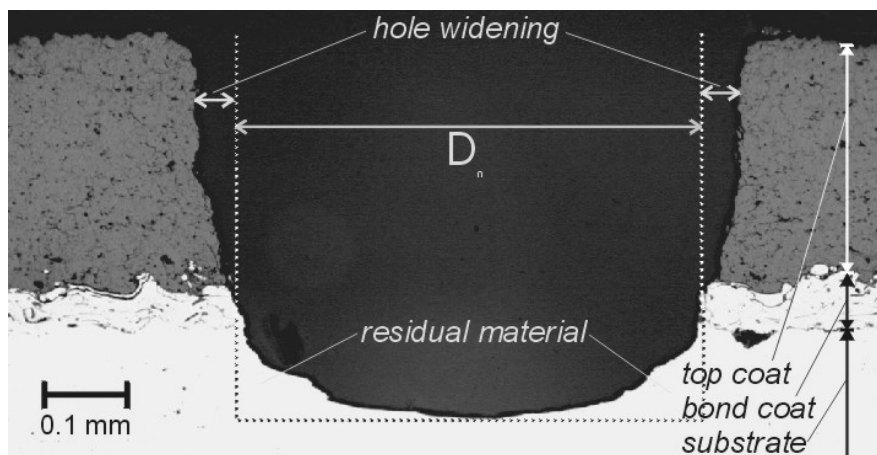


Figure 5.13 Cross-section of drilled 0.3 mm specimen showing hole widening and non-ideal hole shape. The hole diameter is about 1 mm.

Another source of error visible in figure 5.13 is the overall shape of the hole, which is round bottomed and conical. To fulfil the incremental drilling requirements as stipulated in ASTM (1992), a flat-bottomed orthogonal hole shape should be obtained throughout the entire drilling process. The error involved by deviation from this shape is not known.

Hole depth

The hole depth was measured indirectly by the depth indication of the micrometer on the milling guide. Though it increases the possibility of errors, this method was chosen because otherwise the milling guide would have to be removed after each increment in order to measure the increment depth: the inaccuracy involved in repetitive removal-replacement-depth measurement was thought to be larger. It can be deduced that the stress error is inversely proportional to the error in hole depth. Hence an underestimate of the hole depth by 10% results in an overestimate of the stress in that increment by about 10%.

Elastic properties

The magnitudes of the measured stresses depend linearly on the chosen top coat elastic properties E and ν (see Eqs. 5.6 and 5.7). As already mentioned in section 5.4.3, the Young's modulus of a TBC is increased by a heat treatment. However, the data reduction for both the isothermally heated and thermal shock specimens was performed with the same E_{tc} as for the as-sprayed coatings (25 GPa). Hence the reported stresses are probably too small by as much as a factor of two. However, since the same error in E_{tc} is made for all measurements on the isothermally heated and thermal shock specimens, the results can still be compared to indicate a trend.

Summary

Because of the small measured strains (typically 5 to 10 $\mu\epsilon$ per increment), any inaccuracy due to any of the reasons mentioned above can result in large percentage errors in the calculated stresses. This helps to explain most – if not all – of the scatter in some of the measurements.

5.6 Conclusions

Residual stresses in as-sprayed and thermally loaded specimens were measured with the hole-drilling method. The limited number of measurements and the numerous possible experimental errors involved with this technique make it difficult to draw firm conclusions. However, some trends in the residual stresses were observed:

- Low tensile stresses prevailed in the top coat in the as-sprayed state.
- Low compressive stresses prevailed in the top coat in the isothermally heated state. The compressive stresses were close to zero at the coating surface and increased towards the interface. Overall, these stresses decreased with increasing coating thickness.
- After thermal shock the residual stresses at the centre of the flame-covered area were compressive in the 0.3 mm coatings and tensile in the 0.6 and 1.0 mm coatings. The residual stresses 15 mm off-centre from the flame area were close to zero: the sign was tensile for the 0.3 mm coating and compressive for the 0.6 and 1.0 mm coatings.
- The residual stresses were not affected by bond coat preoxidation.

The differences in life and failure mechanisms during furnace testing and burner rig testing between thin and thick TBCs as reported in chapter 3 cannot be explained from the in-plane residual stresses in the as-sprayed state. The explanation must be sought from other stresses (*e.g.* shear and normal stresses or transient stresses) occurring during heating and/or from differences in oxidation behaviour.

The changes in residual stresses after isothermal heating and thermal shock can be explained from the thermal histories and microstructural changes of the specimens, notably vertical cracking and densification.

Owing to numerous possible errors, the hole-drilling method can be applied only to demonstrate the presence of stresses, to indicate the trend of the stress variation with depth, and to provide, at best, an *estimate* of the magnitude of the residual stresses.

6 MODELLING OF THERMAL STRESSES

6.1 Introduction

The life of plasma sprayed TBCs during service or thermal testing is limited. In chapter 3 it was shown that the number of cycles to failure depended strongly on the type of thermal load, the test temperature, the thickness of the top coat and the presence of a preoxidised layer. Generally, failure occurred by complete delamination of the top coat, just above the peaks of the top coat / bond coat interface. Though much experimental research has been carried out (see section 3.1) to assess the lives of TBCs, the exact failure mechanism is still poorly understood.

Over the last 15 years, several FEM-models have been developed to try to determine the failure mechanism (Padovan *et al.*, 1986; Mullen *et al.*, 1987; Chang *et al.*, 1987a&b; Sheets and Kokini, 1991; Petrus and Ferguson, 1997; Tsui *et al.*, 1998; Freborg *et al.*, 1998; Hsueh and Fuller, 2000; Busso *et al.*, 2000). The models attempt to predict the stresses during thermal loading at the top coat / bond coat interface by considering one or more of the factors mentioned in section 3.1. However, a comprehensive model, that includes a realistic simulation of the thermal load *and* stress analysis on both the global (at the level of specimen or gas turbine component) and local (at the level of top coat / bond coat interface undulations) scales is not yet available.

The objective of the work described in this chapter is to develop a model to predict both the temperature and stress profiles in a TBC, on the global and local scales, for different kinds of thermal loads (furnace cycling and burner rig tests) in order to better understand the failure mechanism of TBCs. The experimental results of the furnace and burner rig tests are given in chapter 3.

It must be emphasised that the model's primary goal is to understand the failure mechanism of TBCs. Top coat thickness, the kind of thermal load, top coat / bond coat interface roughness, and the presence of a top coat / bond coat interface oxide layer are important parameters which influence the stresses. The stresses are required in terms of "tensile or compressive", "increasing or decreasing", and order of magnitude rather than absolute values. Therefore the material properties must be the same in all analyses. In order to predict the stresses as accurately as possible, the adopted material properties are as realistic as possible. The microstructure (porosity and microcracks) is represented by the Young's modulus only. However, it should be kept in mind that no plasticity and crack forming (in case the stresses exceed the yield strength or tensile strength respectively) is added to the model. Also, the strongly anisotropic behaviour of plasma sprayed coatings and the effect of a heat treatment (densification) on the material properties are ignored. Finally, it is not the intention to perform a comprehensive parametric study for the material properties.

Section 6.2 provides a detailed description of the computational procedures, geometries and FEM meshes of both the global and local models. The boundary and thermal loading conditions are given in section 6.3. Sections 6.4 – 6.6 present the thermomechanical analysis of the furnace testing, sections 6.7 – 6.10 present the thermal shock and thermal cycling simulations.

6.2 Modelling methodology

An overview of the modelling programme is given in table 6.1. Details of the analysis procedure, model geometries and mesh generation, and the global-local approach will be given in the following sub-sections 6.2.1 – 6.2.4. The material properties are given in sub-section 6.2.5.

Table 6.1 Modelling programme overview

Model simulation		Top coat thickness	GLOBAL		Boundary conditions at global / local interface	LOCAL					
						Idealised		Realistic			
					thermal	stress	thermal	stress			
Furnace		0.3 mm	Thermal	Stress	↓	×	×	×	×		
		1.0 mm						×	×		
Burner rig	Thermal shock	0.3 mm								×	×
		1.0 mm							×	×	
	Thermal cycling	0.3 mm									
		1.0 mm									

6.2.1 Analysis procedure

The model developed describes the thermal loading of a 30 mm diameter disc-shaped Hastelloy-X plate, coated with a 0.1 mm NiCrAlY bond coat and a $\text{ZrO}_2\text{-8wt\%Y}_2\text{O}_3$ ceramic top coat. The thickness of the ceramic coating is 0.3 or 1.0 mm. Three kinds of thermal loads are simulated; (1) the cool down period of furnace tests (remind that failure occurred only during cooling), (2) heating and cooling cycles during burner rig thermal shock, and (3) heating and cooling cycles during burner rig thermal cycling. The general procedure of the model is firstly to determine the global locations of the maximum stresses. Next, a local analysis is performed on the area of interest, incorporating refinements and microstructural details like bond coat roughness and an oxide layer. For the burner rig thermal cycling tests only the global analysis is carried out, for reasons given in section 6.10.

For all analyses it turned out that the radial and tangential stresses are equal except in a small area near the free edge of the disc where the radial stress must reduce to zero. In the following these stresses will be called ‘in-plane’ stresses. The stresses perpendicular to the interface are called ‘normal stresses’.

An essential part of the analysis is to recognise that delamination of a coating can occur by three failure modes:

1. Failure by shear due to high interfacial shear stresses, σ_{xy} .
2. Failure by peel-off due to high normal stresses perpendicular to the interface, σ_x .
3. Failure by local buckling of the top coat owing to high in-plane compressive stresses, σ_y (Evans *et al.*, 1983).

All the stress components will be analysed in order to investigate which failure mode is dominant in the analysed TBC systems.

6.2.2 Geometry and mesh generation

The square specimens used for the experiments are modelled as discs, enabling the three-dimensional configuration to be approximated by a two-dimensional axisymmetric problem, which saves considerable calculation time. The radius of the disc corresponds to the half-width of the furnace test specimens and to the distance from the centre of the flame to the edge of the burner rig specimens, see figure 6.1a. The radius of the top coat surface area heated by the flame (for the burner rig simulations) is 7 mm. Figure 6.1b illustrates the geometry of the modelled specimen. The x-, y- and z-directions correspond to the axial, radial and tangential directions respectively.

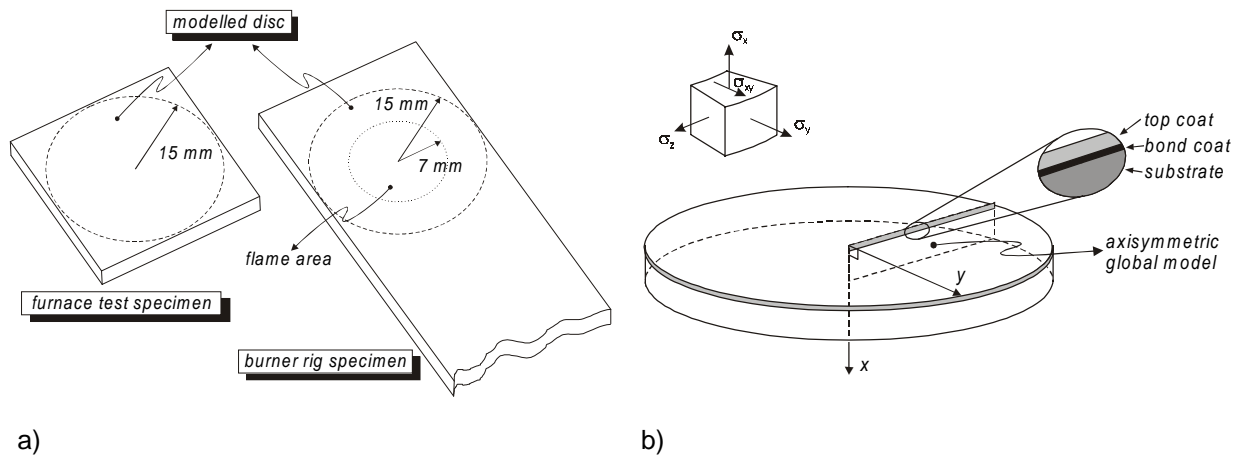


Figure 6.1 Geometry of modelled specimen. a) size and shape of modelled disc with respect to furnace test and burner rig test specimens; b) axisymmetric model to describe disc shaped specimen

The simulations were performed as an uncoupled thermomechanical analysis, using the MARC code, version K7. Pre- and post-processing was done with the MSC/PATRAN program, version 8.5. The meshes of the global and local models consisted of eight-node, isoparametric, arbitrary quadrilateral elements written for axisymmetric applications (MARC type 42 for the thermal analysis, MARC type 28 for the structural analysis). The numbers of nodes and elements in the model are given in table 6.2.

Table 6.2 Numbers of nodes and elements in global and local FEM meshes.

model	global		local			
	flat		idealised		realistic	
interface						
$d_{\text{top coat}}$ [mm]	0.3	1.0	0.3	1.0	0.3	1.0
elements	1800	2850	3270	3837	2112	2784
nodes	5599	8777	9965	11708	6467	8539

6.2.3 Global analysis

Figure 6.2 shows the mesh of the global model. The first step of the analysis required calculation of the temperature profile on the macro scale as a function of time and location. The temperature field was then used as a load for the structural analysis on the macro scale. The output of the model included stress as a function of time, location and direction.

On the axisymmetrical (x-) axis (see figure 6.1) both the heat flux and the displacement must be zero in the radial (y-) direction. To fix the model in space, the

displacement of one node on the x-axis must also be suppressed in the x-direction. The appropriate boundary conditions (BCs) for the thermal analysis depended on the type of thermal load and will be given in section 6.3.

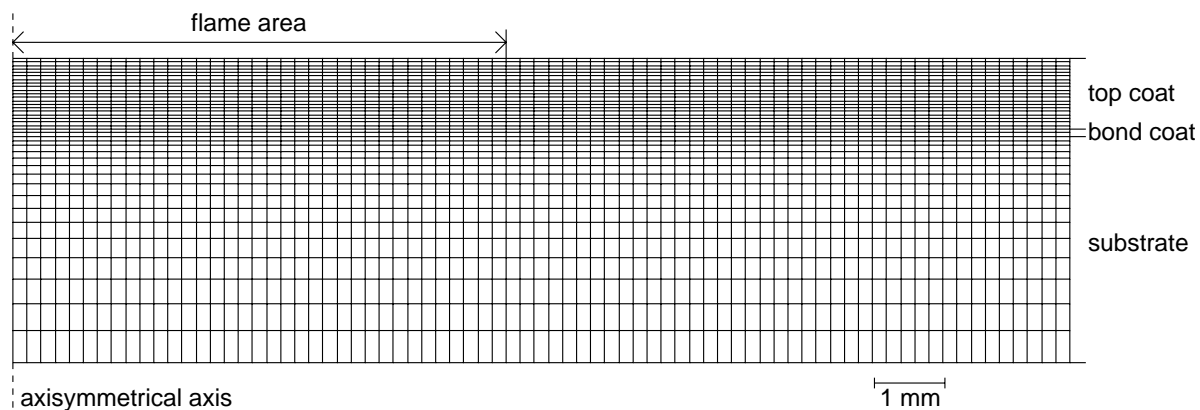


Figure 6.2 Global model mesh with 1 mm top coat

6.2.4 Local analysis

In order to analyse stresses near the top coat / bond coat interface a detailed mesh of this region was made. A small piece with a radial width of 0.6 mm and the same thickness as the global mesh was excerpted from the global model. This local model can be considered as a ring instead of a disc, see figure 6.3. The inner diameter of the ring depends on which part of the global model is analysed with the local model. Next, two fine meshes with bond coat/ceramic interface roughness were generated. In the first mesh the interface was idealised by a sinewave with amplitude of 30 μm and a wavelength of 130 μm . These values were selected based on the measured roughness (Appendix 6A) and microscopic observations. In the second mesh a representative part of a realistic roughness profile was included, see Appendix 6A.

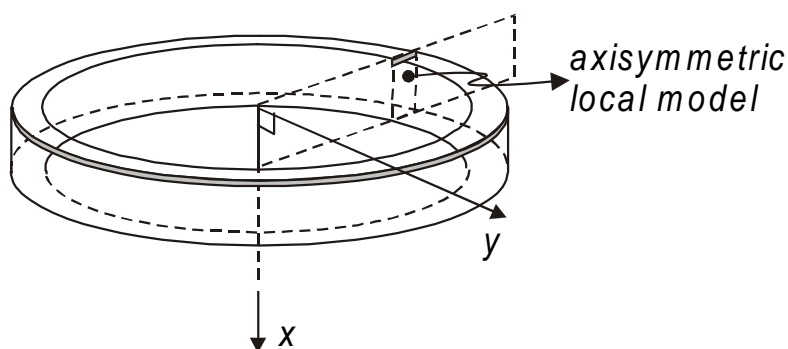


Figure 6.3 Axisymmetric local model to describe ring shaped section of global model (not to scale)

A 5 μm thick layer consisting of very fine elements with a thickness of 1 μm was added to the top coat / bond coat interface of both meshes to enable incorporation of an alumina oxide layer. It should be mentioned that the model does not incorporate the effect of a *growing* oxide, which introduces additional interface stresses (Evans *et al.*, 1983; Tsui *et al.*, 1998; Freborg *et al.*, 1998). Since the effect of the alumina layer on the temperature profile is negligible (see Appendix 6B), all stress analyses with an oxide layer were performed on the basis of temperature analyses without an oxide layer. Details of the idealised interface mesh and realistic interface mesh are shown in figure 6.4.

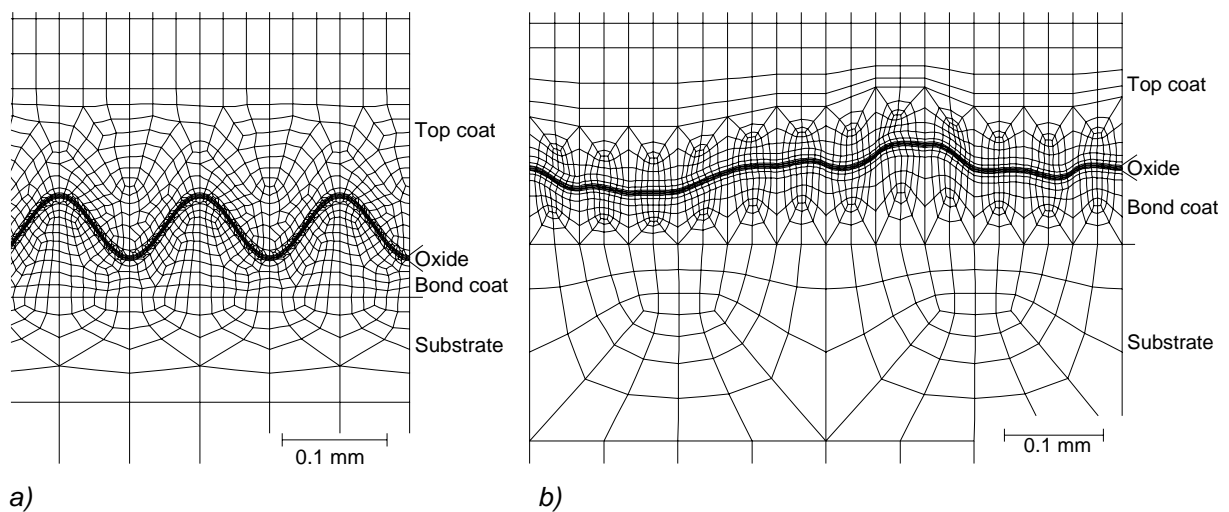


Figure 6.4 Detail of local model mesh with (a) idealised and (b) realistic interface

At the top coat surface and substrate rear side the same boundary conditions applied as in the global model. At the junctions of the global and local models the appropriate time-dependent boundary conditions obtained from the global model must be applied to the nodes of the local model. For the thermal analysis the temperatures were prescribed, and for the stress analysis the axial and radial displacements were prescribed. User subroutines were developed in order to write these values automatically to file during the global analysis, and assign them to the corresponding nodes during the local analysis. The temperature and displacement fields between two nodes or between two neighbouring time steps of the global model were practically linear. Hence for the intermediate nodes or time steps of the local model the values of the BCs were obtained by interpolating. After each analysis the temperatures and displacements at the junctions of the local model were compared with those of the global model in order to verify whether the prescribed boundary conditions were correct.

Table 6.3 Thermophysical and elastic materials properties and creep behaviour used for the FEM analyses

Property	Unit	Top coat	Bond coat ^[1]	Substrate ^[2]	Oxide ^[3]
<i>Thermophysical</i>					
Thermal conductivity	[W m ⁻¹ K ⁻¹]	0.4384+12.78·10 ⁻⁴ T (a)	8.57+0.01143T	3.573+1.99·10 ⁻² T	...
Specific heat	[J kg ⁻¹ K ⁻¹]	566.0+6.123·10 ⁻² T-1.143·10 ⁷ T ⁻² ^[4]	488.9	444.8+15.56e ^(T/416.16)	...
Density	[kg m ⁻³]	5760 ^[1]	6668	8220	3950
CTE	[K ⁻¹]	10.8·10 ⁻⁶ (a)	12.5·10 ⁻⁶	16.3·10 ⁻⁶ (b)	7.9·10 ⁻⁶
<i>Elastic</i>					
Young's modulus	[GPa]	27.6-8.67·10 ⁻³ T (c)	80 (a)	220.0-7.241·10 ⁻² T	387
Poisson's ratio	[-]	0.2 (a)	0.31	0.32	0.3
<i>Creep</i>					
		(d)	(d)	^[2]	
Pre-exponential A	[MPa ⁻ⁿ]	0.066	750000	3.1	...
Stress exponent n	[-]	1.3	3.0	6.4	...
Activation Energy Q	[kJ mol ⁻¹]	156	310	404	...

[1] Tsui and Clyne (1996)

[2] Kattus, (1996)

[3] Evans et. al. (1997)

[4] Schick, (1966)

(a) = average from literature values

(b) = mean value between RT and 900°C

(c) = see text

(d) = NASA data (see text)

6.2.5 Material properties

The substrate, bond coat and top coat were assumed to behave isotropically, homogeneously and linear elastically. The thermophysical and elastic material properties adopted for the FEM analysis are given in table 6.3. These values were taken from the literature, including temperature dependence if available. Where the literature data were in tabular form, they were correlated by, and fitted to, the equations given in table 6.3. Since there is no consensus in the literature about the thermal conductivity, CTE, and Poisson's ratio of the top coat and the Young's modulus of the bond coat, averages from literature values were used. The top coat Young's modulus was assumed to decrease from 25 GPa at room temperature (see chapter 2) to 12 GPa at 1500°C.

For all thermal loads an additional analysis including creep was run. The creep behaviour of the bond coat and top coat materials was derived from NASA data (DeMasi *et al.*, 1989; Brindley and Whittenberger, 1993), while the Hastelloy-X creep data were obtained from an aerospace metal handbook (Kattus, 1996). The strain rate vs. stress data were fitted to a temperature-compensated power law according to the equation:

$$\dot{\varepsilon} = A\sigma^n \exp\left(\frac{-Q}{RT}\right) \quad (6.1)$$

where $\dot{\varepsilon}$ is the strain rate, A the pre-exponential in MPa^{-n} , σ the stress in MPa, n the stress exponent, Q the activation energy in Jmol^{-1} , R the gas constant, and T the absolute temperature. The so-derived A , n and Q for the top coat, bond coat and substrate are also given in table 6.3, while figure 6.5 shows the creep behaviour of the

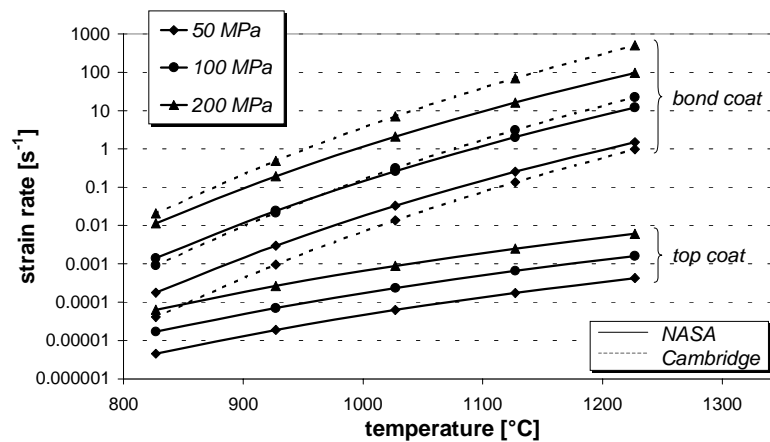


Figure 6.5 Creep behaviour at high temperature of a NiCrAlY bond coat according to NASA data (DeMasi *et al.*, 1989; Brindley and Whittenberger, 1993) and Cambridge data (Tsui *et al.*, 1998) and of a $\text{ZrO}_2\text{-Y}_2\text{O}_3$ top coat according to NASA data.

bond coat and top coat for three stress levels. The creep behaviour of the bond coat according to Cambridge University (Tsui *et al.*, 1998) is also shown in figure 6.5, as a reference. It can be seen that the creep strain rate of the top coat is negligible compared to that of the bond coat.

6.3 Boundary and thermal loading conditions

6.3.1 Furnace simulation

During the furnace simulations the stresses that develop during cool down from an initial temperature (T_{ini}) of 1137°C to room temperature are calculated. It can be assumed that the specimens are stress-free after one hour at 1137°C, see Appendix 6C. Cooling is achieved by way of four boundary conditions (BCs), see figure 6.6a:

BC 1): Radiation from top coat surface to surroundings:

$$q_{rad} = \sigma_{SB} \varepsilon (T_{surf}^4 - T_{\infty}^4) \quad (6.2)$$

where q_{rad} is the radiative heat flow in Wm^{-2} , σ_{SB} the Stefan-Boltzmann constant ($5.67 \cdot 10^{-8} Wm^{-2}K^{-4}$), ε the emissivity (assumed to be 0.75), T_{surf} the top coat surface temperature in K, and T_{∞} the temperature of the surroundings (27°C). Since it is not possible in the MARC code to implement a radiative BC in the form given in Eq. 6.2, this must be converted to a convective expression:

$$\begin{aligned} q_{rad} &= \sigma_{SB} \varepsilon (T_{surf}^3 + T_{surf}^2 T_{\infty} + T_{surf} T_{\infty}^2 + T_{\infty}^3) \cdot (T_{surf} - T_{\infty}) = \\ &= h_{rad} (\sigma_{SB}, \varepsilon, T_{surf}, T_{\infty}) \cdot (T_{surf} - T_{\infty}) \end{aligned} \quad (6.3)$$

where h_{rad} is the 'radiative' heat transfer coefficient, which varies with T_{surf} .

BC 2): Forced convection at top coat surface (fan):

$$q_{conv} = h_{conv} (T_{air} - T_{surf}) \quad (6.4)$$

where q_{conv} is the convective heat flow in Wm^{-2} , h_{conv} the heat transfer coefficient for forced convection (from the experiments it was known that the specimens were cooled to room temperature in 10 minutes: this is achieved by taking $h=100 Wm^{-2}K$) and T_{air} is the temperature of the cooling air (ambient temperature).

BC 3): Radiation from substrate rear side to surroundings: analogue to BC1, only now with T_{surf} as the substrate rear side surface temperature (T_{sub}). Again, it is assumed that $\varepsilon=0.75$.

BC 4): Free convection at substrate rear side:

$$q_{conv,free} = h_{fc} (T_{\infty} - T_{surf}) \quad (6.5)$$

where $q_{conv,free}$ is the convective heat flow in Wm^{-2} , h_{fc} the coefficient of heat transfer for free convection (a value of $15 Wm^{-2}K$ can be adapted, see Appendix 6D) and T_{∞} is the temperature of the surrounding air ($27^{\circ}C$).

No boundary conditions were imposed on the free edge of the specimen because of its relatively small area. In other words, it was assumed that adiabatic conditions occurred at the free edge.

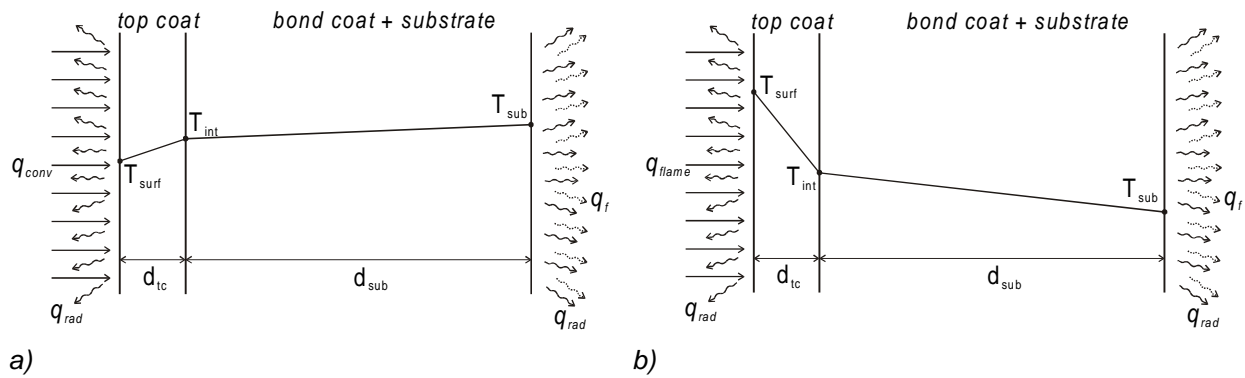


Figure 6.6 Thermal situation in TBC system during (a) cooling in furnace tests and (b) heating in burner rig tests. q_{conv} is the convective heat flow from the fan (solid straight arrows in Fig. a), q_{flame} is the heat input from the flame (solid straight arrows in Fig. b), q_{rad} is the radiative heat flux (solid curved arrows) and q_f is the heat loss due to free convection (dotted curved arrows).

6.3.2 Burner rig simulation

General

In chapter 3 two kinds of burner rig tests were described: thermal shock (short cycles) and thermal cycling (long cycles). The boundary and thermal loading conditions for simulations of both testing methods are the same except for some constants.

Consider figure 6.6b, where the thermal situation during burner rig testing is depicted for an arbitrary temperature profile¹. The radiation and free convection at the substrate rear side and the radiation at the top coat surface are defined in the same way as in the case of furnace testing. The heat input from the flame is modelled as a heat flux by convection (in Wm^{-2}) :

$$q_{flame} = h_{flame} (T_{flame} - T_{surf}) \quad (6.6)$$

¹ Since the bond coat is relatively thin and has material properties close to those of the substrate, the bond coat and substrate are 'lumped' together for the calculations in this section.

where T_{flame} is the flame temperature. The heat transfer coefficient of the flame (h_{flame} in $Wm^{-2}K^{-1}$) is determined semi-empirically. First, the heat flow from the burner to the specimen (q_{in} in Wm^{-2}) is calculated from the steady state temperature profile over the thickness of a coated specimen:

$$q_{in} = \frac{\Delta T}{\sum (d/\lambda)_j} \quad (6.7)$$

where ΔT is the measured temperature difference between T_{surf} and T_{sub} , d is the thickness and λ is the conductivity. The subscript j indicates the top coat or the lumped bond coat and substrate. q_{in} consists of q_{flame} according to Eq. 6.6 minus the radiation to the surroundings q_{rad} :

$$q_{in} = q_{flame} - q_{rad} = h_{flame}(T_{flame} - T_{surf}) - \sigma\epsilon(T_{surf}^4 - T_{\infty}^4) \quad (6.8)$$

Substituting Eq. 6.7 in Eq. 6.8 yields for h_{flame} :

$$h_{flame} = \frac{\Delta T + \sum (d/\lambda)_j \cdot \sigma\epsilon(T_{surf}^4 - T_{\infty}^4)}{\sum (d/\lambda)_j \cdot (T_{flame} - T_{surf})} \quad (6.9)$$

Since λ_{tc} and λ_{sub} are temperature dependent and a temperature gradient is present over both the top coat and substrate, an average conductivity evaluated for the mid-depth temperature of the top coat or substrate must be adopted:

$$\lambda_{tc} = a_{tc} \frac{T_{surf} + T_{int}}{2} + b_{tc} \quad (6.10)$$

and

$$\lambda_{sub} = a_{sub} \frac{T_{sub} + T_{int}}{2} + b_{sub} \quad (6.11)$$

where a and b are the coefficient and constant, respectively, of the linear equations for the conductivities of top coat and substrate (see table 6.3).

To solve h_{flame} the flame temperature must be known. In an attempt to measure T_{flame} one of the most heat resistant thermocouples, Pt-Rh, (melting point about 1800°C) melted. However, at the same position the TBC (melting point 2600°C) did not melt. This led to a value around 2100°C being assumed (see also discussion in sub-section 6.10.1).

The value for h_{flame} according to Eq. 6.9 is only valid at the steady state surface temperature. The dependency of h_{flame} on T_{surf} is analytically determinable from the theory of an impinging jet (Incropera and DeWitt 1990) and is derived in Appendix 6E:

$$h_{flame} = h_{flame,ref} \cdot f(T_{surf}) \quad (6.12)$$

where $h_{flame,ref}$ is the coefficient of heat transfer according to Eq. 6.9 and $f(T_{surf})$ is a third degree polynomial function fitted to calculated data points. Since the steady state surface temperature differs for thermal shock and thermal cycling, the $f(T_{surf})$ values differ also, see figure 6E.1.

Specimen cooling was assumed to occur (as in the tests) over the entire top coat surface. The heat transfer coefficient of the cooling jet ($h_{cool} = 400 \text{ Wm}^{-2}\text{K}^{-1}$) was determined from the calculations by trial and error, knowing that the experimental substrate temperature at the end of the cooling period was about 375°C .

Thermal shock

The heat transfer coefficient h_{flame} for the simulation with a 0.3 mm top coat was calculated with equation 6.9 and using a measured steady state surface temperature. For the 1.0 mm top coats no experimental steady state temperatures were available. However, during the thermal shock experiments of the 1.0 mm TBC systems the distance between the flame and the specimen had to be increased in order to avoid overheating the top coat surface. Hence for the simulation h_{flame} and T_{flame} were adjusted to lower values until the temperatures after the 30 seconds heating period agreed with the experiments.

Table 6.4 Experimental results of burner rig thermal cycling tests

top coat thickness [mm]	$T_{surface}$ [°C]	# cycles to failure	location of failure
0.3	1350	100	flame area
0.6	1400	>250	-
1.0	1400	>250	-
1.0	1505	60	flame area
2.0	1500	3	free edge

Thermal cycling

Burner rig thermal cycling experiments were carried out on specimens with 0.3 mm, 0.6 mm, 1.0 mm and 2.0 mm top coats (chapter 3). The experimental results are summarised in table 6.4. Because of the very short life of the 2.0 mm TBC, an

additional analysis was carried out for a disc with a 2.0 mm top coat² as well as for discs with a 0.3 mm and 1.0 mm top coat.

First, h_{flame} was determined as described above. However, from the thermal analysis it turned out that the predicted steady state temperature differences between top coat surface and substrate rear side were too low. The reason for this is probably that during burner rig tests the specimens were clamped in a water-cooled holder, which resulted in heat loss. Since the distance from the area heated by the flame to the water-cooled specimen holder was large (about 80 mm) compared to the heat-affected zone (25 mm radius) it was initially assumed that this heat flow was negligible. This assumption was valid for thermal shock experiments, where the heating time was short, but for thermal cycling experiments the assumption resulted in a too high substrate temperature.

The additional heat flow can be simulated by an artificially high coefficient of free convection on the rear side of the substrate. To calculate h_{flame} and h_{free} an additional thermal condition must be specified for the rear side of the substrate. By analogy with Eq. 6.8 we define:

$$q_{out} = q_{free} + q_{rad} = h_{free}(T_{sub} - T_{\infty}) + \sigma\epsilon(T_{sub}^4 - T_{\infty}^4) \quad (6.13)$$

Equations 6.7, 6.8, 6.10, 6.11 and 6.13 can then be solved as a set of simultaneous equations using the measured steady state temperature and an assumed flame temperature. It turned out that with the h_{free} according to Eq. 6.13 the heat loss was overestimated, resulting in too low overall temperatures. This can be attributed to the assumption in the one-dimensional analytical model that the *entire* top coat surface is heated, while in the 2½ dimensional numerical model only a part of the surface is heated, resulting in a lower heat input. The correct value of h_{free} was established by iterative comparison of the calculated steady state temperature distribution with the steady state temperatures T_{surf} and T_{sub} measured in the experiments.

Summary

Table 6.5 summarises the measured steady state temperatures of the top coat surface and substrate rear side, the assumed flame temperature, the calculated coefficient of heat transfer for the flame, and the (corrected) coefficient of free convection on the substrate rear side for both the thermal shock and thermal cycling simulations.

² Mesh consists of 2925 elements and 9004 nodes

Table 6.5 Measured steady state surface and substrate temperatures, assumed flame temperature and calculated convection coefficients for a TBC in the burner rig

Simulation top coat thickness [mm]		Thermal shock		Thermal cycling			
		0.3	1.0	0.3	1.0	2.0	
T _{surface}	[°C]	1525	-	1350	1400	1505	1500
T _{substrate}	[°C]	1279	-	1100	975	1000	940
T _{flame}	[°C]	2225	2125	2075	2000	2175	2025
h _{flame}	[Wm ⁻² K ⁻¹]	1812	1750	1694	1607	1780	1600
h _{free}	[Wm ⁻² K ⁻¹]	15*	15*	110	90	125	50

* = according to appendix 6D

6.4 Furnace global analysis

6.4.1 Temperature

Figure 6.7 shows the calculated temperature during the cooling of the top coat surface and substrate rear side for both the 0.3 and the 1.0 mm top coats. Due to forced cooling of the top coat a temperature gradient existed over the specimen thickness (see also figure 6.6a). This temperature gradient was larger for the thicker top coat.

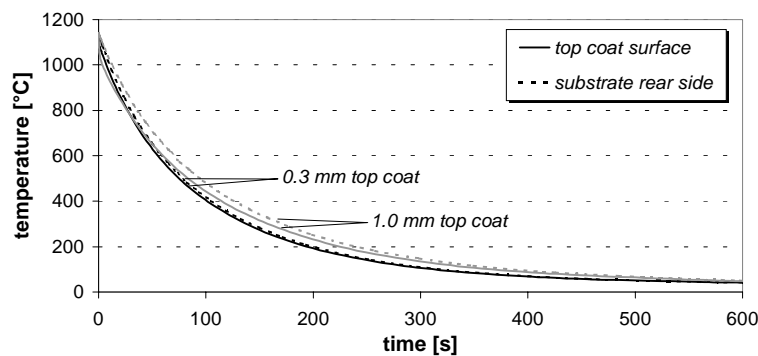


Figure 6.7 Temperature vs. time during cooling after isothermal heating at 1137°C for 0.3 mm and 1.0 mm top coats at the surfaces of the top coat and at the substrate rear side

6.4.2 In-plane stresses

Figure 6.8 shows the in-plane stresses in the centre region of the specimen at the end of the cooling period. Due to bending, the compressive stresses in the top coats increased slightly with depth from the surface, and the stresses in the substrate changed from tensile at the interface with the bond coat to compressive at the rear side. An increase in top coat thickness from 0.3 to 1.0 mm resulted in an overall

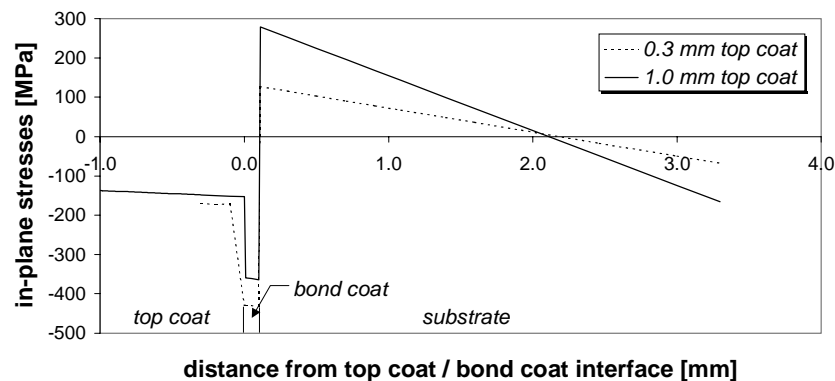


Figure 6.8 Through-thickness in-plane stresses at centre of disc at the end of the cooling period for 0.3 and 1.0 mm top coats

decrease of in-plane stresses in the top coat of about 11%. For the 0.3 mm TBC one analysis was performed allowing all constituents to creep. It turned out that the effect of creep on the in-plane stresses was negligible (results not shown here).

The in-plane stress results cannot explain the difference in life during furnace testing (shorter life for thicker top coat). Indeed, these results suggest the opposite. Hence failure must be caused by other stress components.

6.4.3 Shear and normal stresses

From research on laminated composite materials (Pipes and Pagano, 1970; Whitcomb *et al.*, 1982) and coated structures (Munz and Yang, 1992; Hu *et al.*, 1998), it is known that either a shear stress or a normal tensile stress is responsible for delamination, which occurs at the free edge of the specimen (singular stresses). Figure 6.9 (see colour plates at the end of this chapter) provides a qualitative impression of the shear strains in this region, using a deformed (25 times exaggerated) mesh with a 1.0 mm top coat. The highest shear strains were located in an area just above the top coat / bond coat interface. More comprehensively, figure 6.10 shows the in-plane, normal and shear stresses just (3.5 μm) above the interface for the outer 5 mm of the specimen³. In the main part of the specimen the normal and shear stresses were zero (plane stress) but this situation was disturbed near the free edge. Looking from this free edge, the normal stresses were first compressive but became tensile at only a small distance from the edge. Then a maximum was reached after which the normal stresses diminished to zero. Note that the in-plane and shear stresses are necessarily zero at the free edge. Though the in-plane stresses did decrease (become less

³ As will be discussed in section 6.6.1, the accuracy of the results of the last two elements (14.6 < y < 15 mm) is questionable. This is indicated in figure 6.10 by the 'accuracy border'

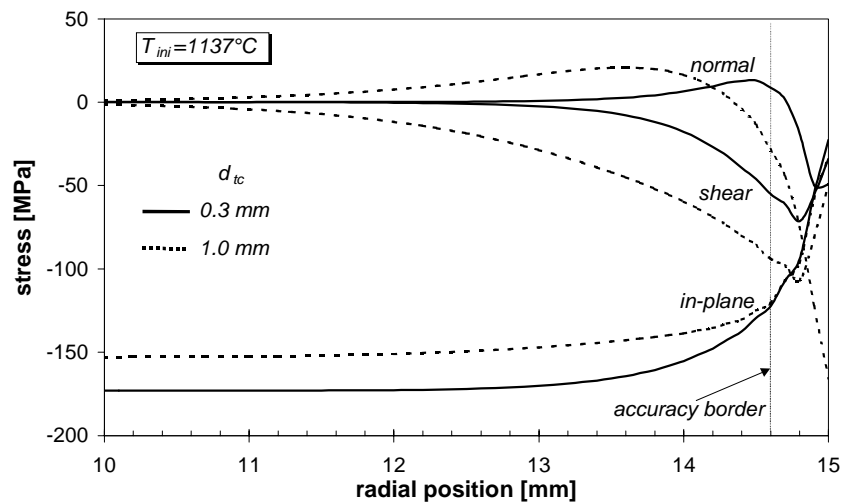


Figure 6.10 In-plane, normal and shear stresses at the end of the cooling period for $10 < y < 15$ mm at $3.5 \mu\text{m}$ above interface for top coat thicknesses (d_{tc}) 0.3 mm and 1.0 mm. $T_{ini}=1137^\circ\text{C}$

compressive) when the coating thickness was increased from 0.3 to 1.0 mm, the normal and shear stresses increased considerably in an absolute sense. Moreover, the distance from the edge across which these stresses applied increased with increasing thickness.

When the specimens for the stress measurements were isothermally heated, it was observed that thick (0.6 and 1.0 mm) TBCs failed after one cycle of $1250^\circ\text{C}/5\text{hr}$, but sustained multiple cycles of $1050^\circ\text{C}/5\text{hr}$. The 0.3 mm TBCs did not fail after both heat treatments. This phenomenon can be studied with the current model by varying the initial temperature (T_{ini}). Figure 6.11 shows the results for the 0.3 and 1.0 mm thick top coats, omitting the results of the last two elements. It is seen that the absolute values of all stress components increase linearly with T_{ini} .

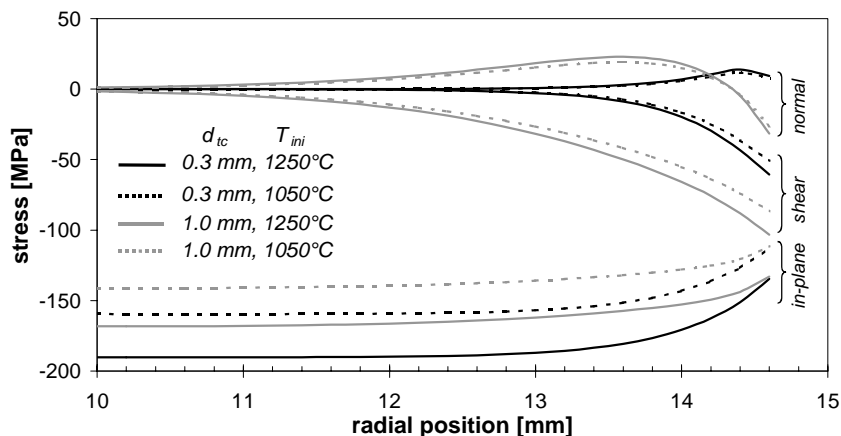


Figure 6.11 In-plane, normal and shear stresses for $10 < y < 15$ mm at $3.5 \mu\text{m}$ above interface for top coat thicknesses (d_{tc}) 0.3 mm and 1.0 mm. $T_{ini}=1050^\circ\text{C}$ and 1250°C . Results of last two elements are omitted owing to lack of accuracy, see figure 6.10 and footnote 3

6.5 Furnace local analysis

6.5.1 Comparison with global analysis

The local model can be validated by comparing its results with those of the global model. Since the stress situation at the free edge is very complicated, a local analysis was first done at the centre of the global model for a 0.3 mm top coat with an idealised interface. At the end of the cooling period the temperatures of the top coat surface and substrate rear side agreed with the temperatures from the global model, and the in-plane stresses in the top coat corresponded exactly with those from the global model (not shown here). These results were very encouraging, and so the in-plane stresses over the specimen thickness in the region near the free edge ($y=14.5$ mm) were also determined. The results from the global and local analyses are compared in figure 6.12. As found before, the agreement was very good, and –as expected– the stresses were disturbed in the vicinity of the interface undulations, especially in the relatively thin bond coat. From the comparisons it was concluded that the local model determines the bulk stresses accurately. Hence the local model is dependable for predicting the stresses near the interface.

6.5.2 Stresses at centre of disc

Table 6.6 gives the local model predictions of the normal and shear stresses just above a peak of the idealised interface (with oxide layer) in the centre of the disc. Since the stresses in the 1.0 mm top coat are *lower* than in the 0.3 mm top coat, this local model result confirms the conclusion from the global model that the relatively

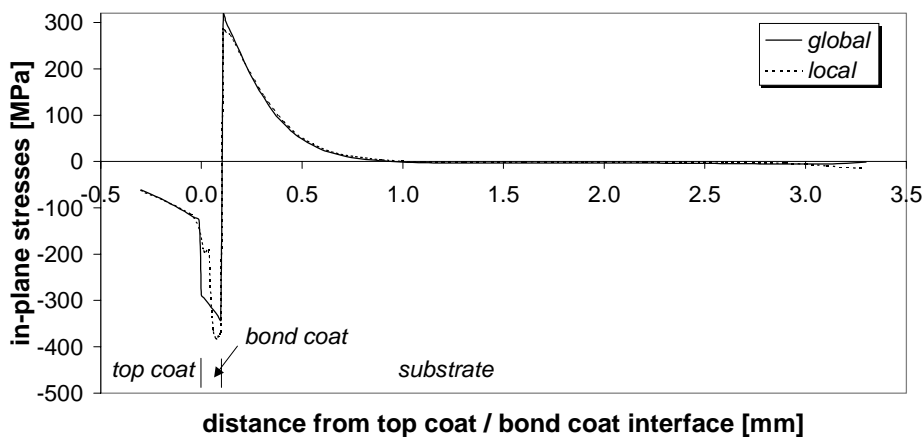


Figure 6.12 Through-thickness in-plane stresses at $y=14.5$ mm for 0.3 mm top coat at the end of the cooling period (furnace simulation) according to the global model and local model with idealised top coat / bond coat interface

short life of the 1.0 mm top coat cannot be explained from the stress situation in the centre of the specimen. Moreover, the normal stresses are compressive, which will not contribute to cracking.

Table 6.6 Normal and shear stresses (furnace simulation) in top coat just above interface peak (idealised interface)

top coat thickness [mm]	σ_x [MPa]	σ_{xy} [MPa]
0.3	-57	27
1.0	-54	23

6.5.3 Stresses near free edge

Figure 6.13 (see colour plates at the end of this chapter) shows contour plots of the shear strains near the free edge of the specimen for a TBC with an oxidised bond

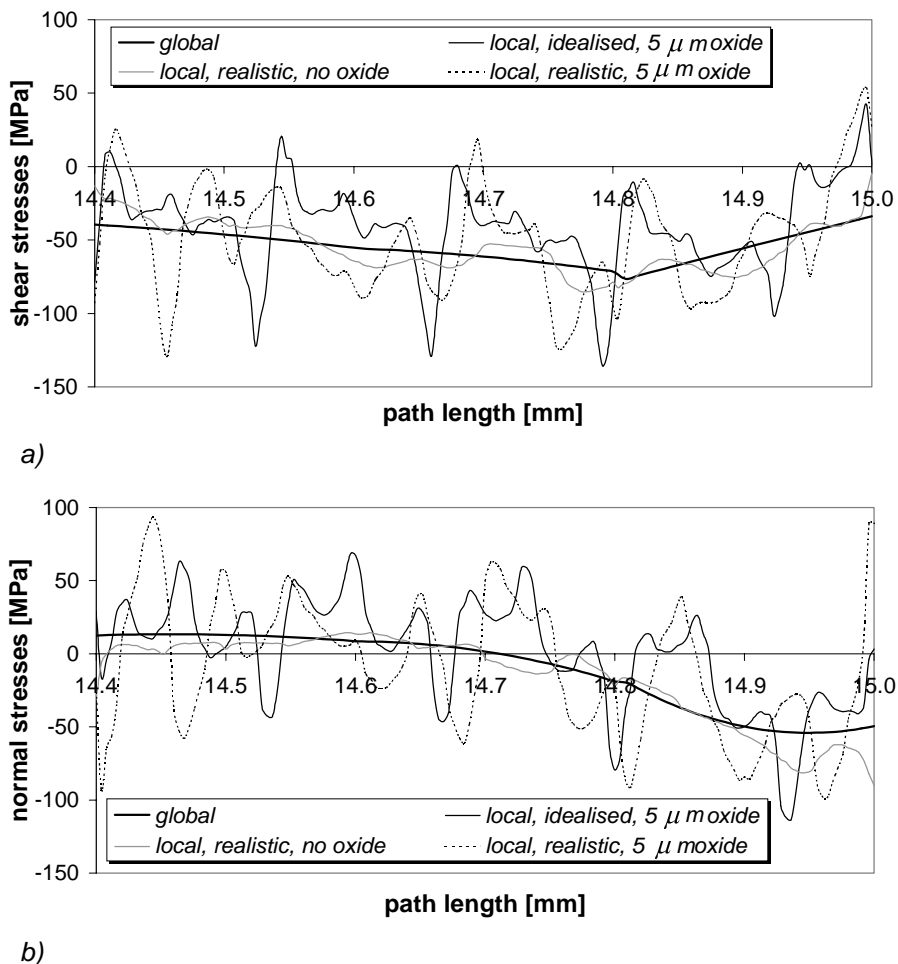


Figure 6.14 Comparison of stresses (furnace simulation) between global model, local model with idealised interface and local model with realistic interface for a 0.3 mm top coat. a) shear stresses, b) normal stresses

coat. In figure 6.13a the interface is idealised by a sinewave and the top coat thickness is 0.3 mm; in figures 6.13b and 6.13c the interface is represented by the selected part of the measured roughness profile, and the top coat thickness is 0.3 mm and 1.0 mm respectively. Figure 6.13 shows that the highest shear strains in the top coat occurred at the interface peaks. In the middle of the realistic interface four bond coat peaks are close together and are situated on a much broader peak. The juxtaposition of these four peaks has resulted in coalescence of the shear stress fields. This effect is enhanced by a thicker top coat: for the 1.0 mm top coat a 0.25 mm wide region of high shear stresses was formed, figure 6.13c.

It is now of interest to compare the normal and shear stresses according to the local model with those from the global model. Figure 6.14 shows this for the shear stresses (a) and normal stresses (b) in a 0.3 mm top coat. Though it is not representative, the results of an analysis without oxide layer are also shown (only for the realistic interface) to demonstrate the effect of such a thin layer. For both stress components, the results obtained by the local model oscillated around the global solution, and the presence of an oxide layer enhanced the effect of the interface roughness (the same was true for an idealised interface). The highest shear stresses were located at the interface peaks, the maximum normal stresses were found on the flanks of the asperities. The amplitudes of the stress peaks depended on the local radius of curvature of the roughness profile.

Figure 6.15 shows the effect of top coat thickness and oxide layer thickness on the shear stress just ($3.5 \mu\text{m}$) above the realistic interface. The roughness profile of the interface is also given (height scale can be found in figure 6A.2). It can be seen that an increase in oxide layer thickness intensified the effect of the interface undulations, *i.e.*

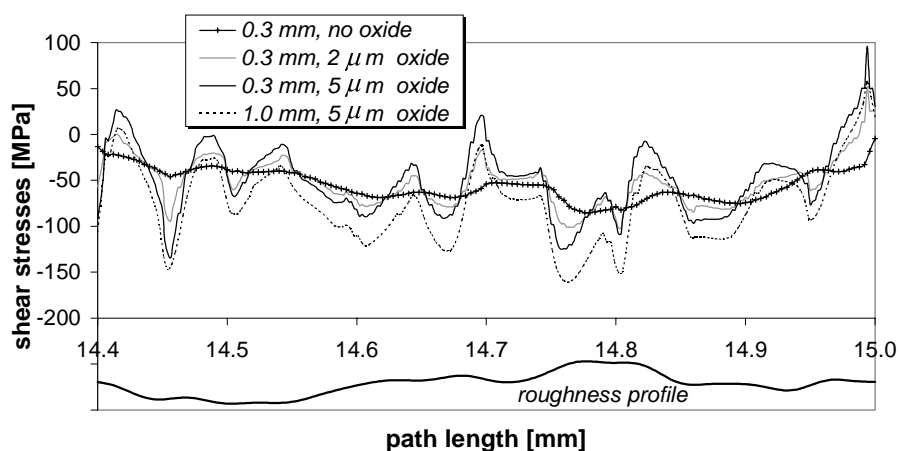


Figure 6.15 Effect of oxide layer thickness and top coat thickness on shear stresses at $3.5 \mu\text{m}$ above interface (furnace simulation)

the amplitudes of the stress peaks became higher. However, although an increase in top coat thickness shifted all stresses more into compression, the amplitudes became smaller. At the peak locations, the maximum compressive shear stresses in a 1.0 mm top coat were on average 40% higher than in a 0.3 mm top coat.

6.6 Discussion of furnace simulation

6.6.1 Global analysis

Validation

The global in-plane stresses can be validated by the analytical model of Clyne and Gill (1996), whereby the resultant stress distribution and curvature owing to a misfit strain is obtained from simple beam bending theory. The stresses in the coating according to this model and according to the numerical model are given in the first two rows of table 6.7 ($T_{ini}=1137^{\circ}\text{C}$). The analytical results agree reasonably well with the numerical results, but show slightly higher absolute values of the stresses. This can be attributed to the fact that the stresses in the analytical model were calculated with the low temperature values for the Young's modulus ($E_{sub}=200$ GPa, $E_{tc}=25$ GPa). However, the stress build-up starts already at high temperatures where the Young's moduli are lower. To compensate for this the analytical calculations were redone with lower moduli. The results of the numerical and analytical models agree very well for $E_{sub}=190$ GPa and $E_{tc}=23.5$ GPa (0.3 mm) or 22.5 GPa (1.0 mm), see first and third rows of table 6.7. Thus it can be concluded that the numerical model predicts the in-plane stresses accurately.

Table 6.7 Comparison of numerical and analytical models for the in-plane stresses [MPa] after cooling from isothermal heating at 1137°C

Model	0.3 mm top coat		1.0 mm top coat	
	surface	interface	surface	interface
numerical	-171	-173	-137	-153
analytical	-182	-183	-153	-166
analytical (corrected)	-171	-172	-139	-150

Effect of coating thickness and initial temperature

The normal and shear stresses near the free edge, which are believed to cause delamination, increase considerably when the top coat thickness is increased from 0.3 to 1.0 mm. The effect of initial temperature on the residual stresses is, within the realistic possibilities of variation, less pronounced than the influence of top coat

thickness. In the elastic analysis the relative change in stress (all components) was found to correlate linearly with the relative change in initial temperature. Thus:

$$\sigma_2 = \sigma_1 \frac{T_{ini,2}}{T_{ini,1}} \quad (6.14)$$

Accuracy

Before discussing the results of the local analysis, the accuracy of the calculated stresses near the free edge according to the global analysis should be evaluated. Owing to stress singularities at the intersection of the interface and the free edge, numerical predictions of the stresses can be very inaccurate. For laminate composite materials Whitcomb *et al.* (1982) compared the finite element predictions for the shear and normal stresses with solutions of other (numerical) methods. They found disagreements in both magnitude *and* sign. After analysis of two well-known edge-stress problems, they concluded that the finite element method appeared to be an accurate and useful technique for analysing the edge stresses in composite laminates, except in the two elements closest to the singularity. For the current global model, this means that the results for $14.6 \leq y \leq 15.0$ should be considered carefully. The normal stress change from tensile to compressive occurred in that unreliable area and the question arises whether the sign close to the free edge is correct (according to Whitcomb *et al.* (1982) it should indeed be compressive). This uncertainty in the global analysis demonstrates clearly the usefulness of a local analysis: owing to the fine mesh of the local model the solution near the free edge can be determined more accurately; moreover, the effect of interface roughness and the presence of an interface oxide layer on the singular stresses can be predicted.

6.6.2 Local analysis

The local analysis demonstrated the effect of an irregular, *i.e.* rough, top coat / bond coat interface and the presence of an interface oxide layer. The normal and shear stresses were amplified at the bond coat asperities⁴, and in the case of a realistic interface a high shear stress region can form just above the roughness peaks. Such stress maxima can be as high as 250% of the average value provided by the global analysis, depending on the morphology of the roughness peak and oxide layer thickness. The differences in maximum stress values between the model with the idealised interface and the model with the realistic interface were small.

⁴ The existence of interface peak shear and normal stresses will be discussed in section 6.10.5

In the outer 0.4 mm of the specimen the local solution varied around the global solution, see figure 6.14. One may assume that the results of the local analysis are accurate except for the outer two elements, *i.e.* the last 15 μm (Whitcomb *et al.*, 1982). This means that the global analysis gave a reasonably accurate prediction of the stresses in the last two elements closest to the singularity.

6.6.3 Summary

In conclusion, high cooling-induced shear and normal stresses develop near the intersection of the top coat / bond coat interface and the free edge during furnace cycling. These stresses increase with initial furnace temperature and top coat thickness. In regions just above the interface roughness peaks the stresses can be 250% higher than those given by the global (average) solution.

Since the solutions of the local model with the idealised interface and the local model with the realistic interface are similar, the modelling of the burner rig tests will be done only with the realistic top coat / bond coat interface.

6.7 Thermal shock global analysis

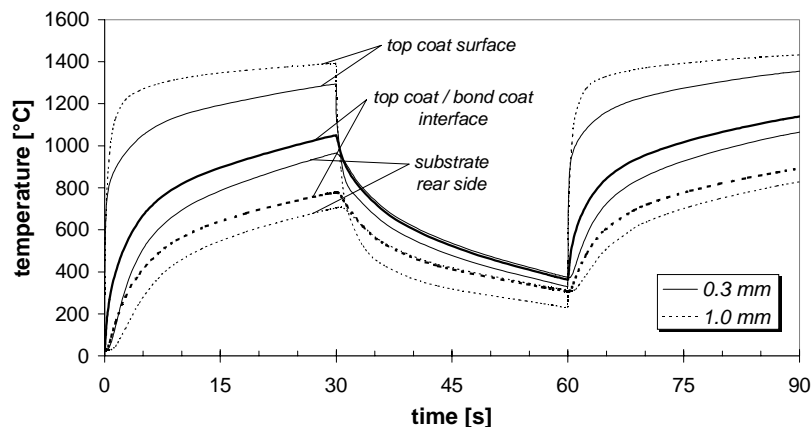
6.7.1 Temperature

Figure 6.16a shows the specimen centre temperature changes at the top coat surface, top coat / bond coat interface, and substrate rear side, for both the 0.3 mm and 1.0 mm TBCs. The temperatures at the end of the heating and cooling periods (after 30 s, 60 s and 90 s) are given in table 6.8.

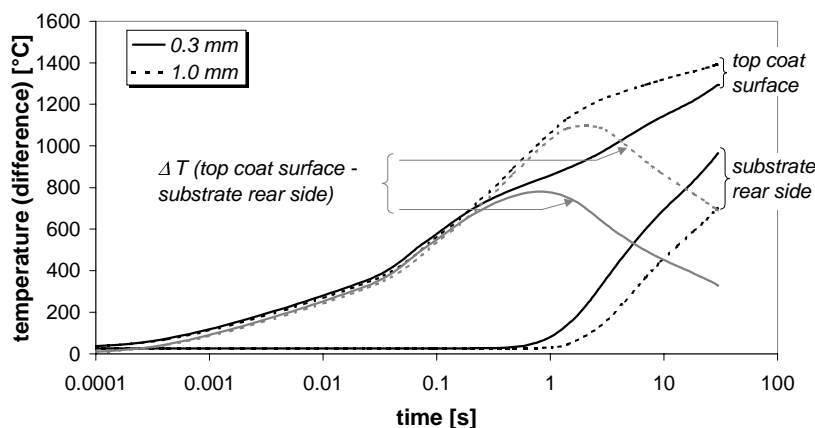
Table 6.8 Temperatures ($^{\circ}\text{C}$) of top coat surface, top coat / bond coat interface and substrate rear side at flame centre during burner rig thermal shock testing at $t=30, 60$ and 90 s, according to the numerical model

time [s]	30		60		90	
	0.3	1.0	0.3	1.0	0.3	1.0
top coat thickness [mm]						
top coat surface	1294	1391	329	233	1354	1433
top coat / bond coat interface	1050	778	362	307	1140	893
substrate rear side	965	704	373	314	1065	829
$\Delta T_{\text{top coat}}$	244	613			214	540
$\Delta T_{\text{specimen}}$	329	687			289	604
$\Delta T_{\text{top coat}}/\Delta T_{\text{specimen}}$	0.74	0.89			0.74	0.89

The initial heating rates, especially of the top coat surface, were high. To better follow these, figure 6.16b shows the temperature change of the top coat surface and substrate rear side during the first heating period on a semi logarithmic plot (top coat / bond coat interface curves have been omitted for clarity). This graph also shows the temperature differences between top coat surface and substrate rear side.



a)



b)

Figure 6.16 Temperature profile during thermal shock for 0.3 and 1.0 mm TBCs. a) at top coat surface, top coat / bond coat interface and substrate rear side for 90 seconds, b) at top coat surface and substrate rear side for first 30 seconds

The difference in start temperature between the first and second heating period was about 300°C for the entire specimen, while the difference in end temperature was only 50°C at the top coat surface and about 100°C at the substrate rear side. This result indicates that the maximum temperatures will converge within a few cycles to values close to those after the second heating period, which was in fact observed during the experiments. The temperature differences between top coat surface and

substrate rear side (Fig. 6.16b) reached a maximum after about 1 second. The relative temperature drops over the coating thickness with respect to those over the specimen thickness, hereafter referred to as *thermal barrier ratio*, at the end of a heating period were high and increased with increasing coating thickness (table 6.8). These ratios were the same after the first and second heating periods and appeared to be reached as early as 10 seconds into each heating period.

6.7.2 In-plane stresses

Figure 6.17a to 6.17d are for 0.3 mm and 1.0 mm top coats, and give the calculated changes with time of the in-plane stresses at the top coat surface and top coat / bond coat interface at three locations: flame centre, flame edge, and specimen free edge.

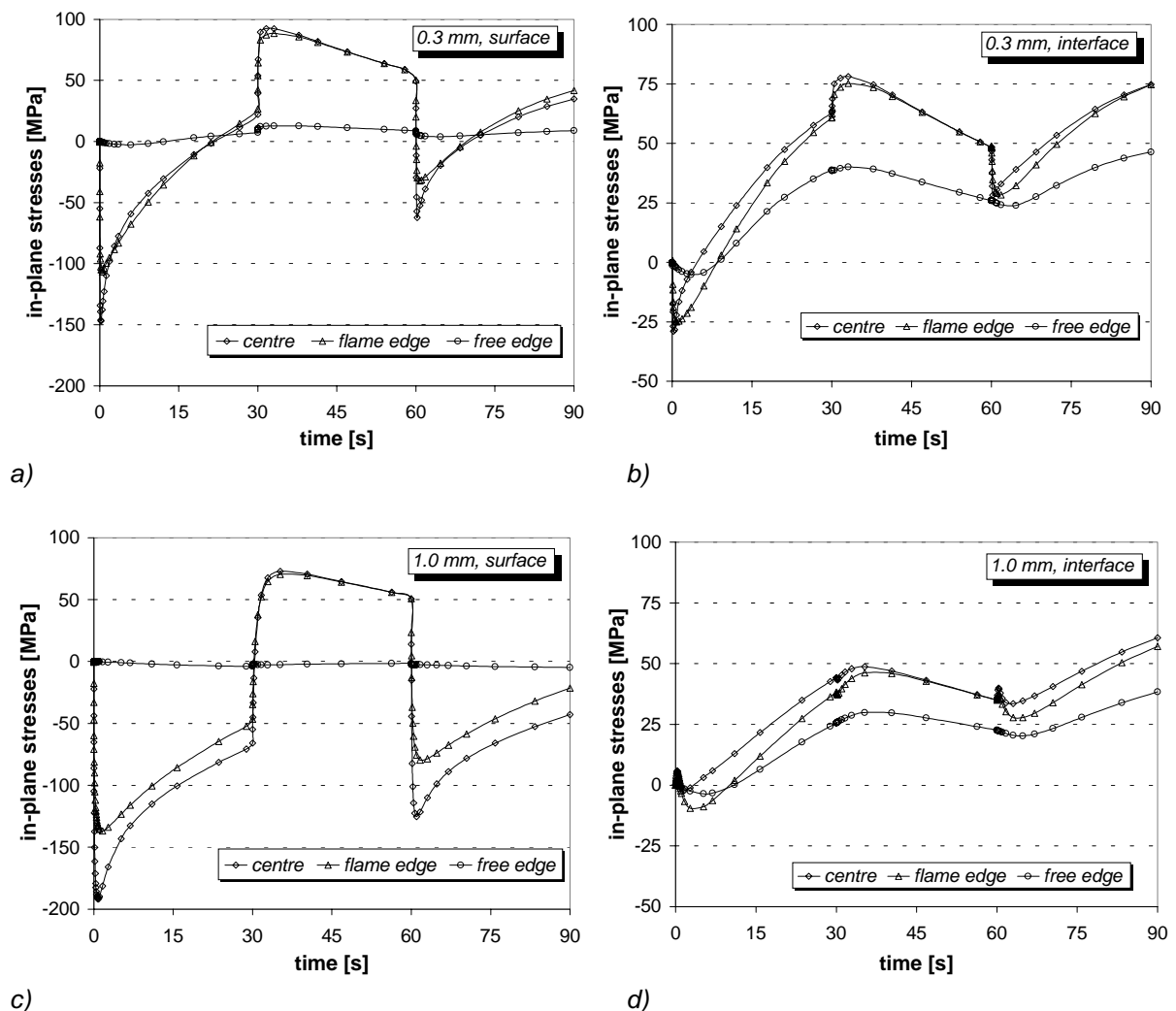


Figure 6.17 Top coat surface and top coat / bond coat interface in-plane stresses during thermal shock at centre of specimen, edge of flame and free edge as functions of time for a,b) 0.3 mm top coat and c,d) 1.0 mm top coat

Top coat surface

High compressive stresses developed in the area heated by the flame, with a maximum after 1 to 2 seconds. The stresses decreased with increasing distance from the (flame) centre. At the end of the heating period the sign of the surface stresses in the flame area depended on the top coat thickness. For a thin coating the stresses were tensile, for a thick coating they were compressive. Outside the flame area the surface stresses were always tensile (not shown in figure 6.17). Near the free edge the surface stresses remained almost zero during the entire heating period. During cooling the surface stresses in the heated part of the coating became tensile due to coating contraction while the underlying material is still hot. After reaching a maximum value, these stresses decreased and would have become zero if the entire specimen had returned to room temperature. Owing to the higher start temperature of the second heating period (see figure 6.16a), the thermal shock effect during the first few seconds was less severe, resulting in lower compressive surface stresses.

Top coat / bond coat interface

The in-plane stresses first became compressive and then tensile, increasing to values of about 30-70 MPa after a heating period. The highest in-plane tensile stresses occurred at the specimen centre, and the tensile stress decreased with increasing distance from the centre. During the cooling period the cold front reached the top coat / bond coat interface after a few seconds. The metallic components then started to contract and the in-plane interface stresses started to decrease. As for the surface stresses, these stresses would have become zero if the entire specimen had returned to room temperature. Owing to the higher start temperature of the second heating period (see figure 6.16a) the relative expansion of the substrate was higher. As a consequence, the initial compressive stresses did not occur, resulting in higher tensile interface stresses at the end of the heating period.

Substrate

As will be shown in section 6.9.2 (thermal cycling, creep), the in-plane stresses in the substrate were compressive and very high (> 500 MPa compressive) during the first 10 seconds of a heating period. The highest compressive stresses occurred in the area just beneath the interface with the bond coat. The stresses diminished in the radial direction and towards the rear side of the substrate. Specimen cooling caused the substrate in-plane stresses to decrease rapidly to almost zero.

Initial stress development

The initial development of the in-plane stresses during heating and cooling is not evident from figure 6.17. However, the stresses in the top coats during the first few seconds are very similar for the thermal shock and thermal cycling simulations and will be shown in more detail in section 6.9.2.

6.7.3 Shear and normal stresses

The shear stresses and normal stresses were almost zero through the entire disc except for two locations: at the flame edge, where a maximum was reached during the early stage of the heating period, and near the free edge of the disc, where a maximum was reached at the end of the heating period. Figure 6.18 shows the maximum values of the shear and normal stresses near the flame edge and the free edge of the disc for both the 0.3 mm and the 1.0 mm top coats. It is seen that both stress components increased with increasing coating thickness.

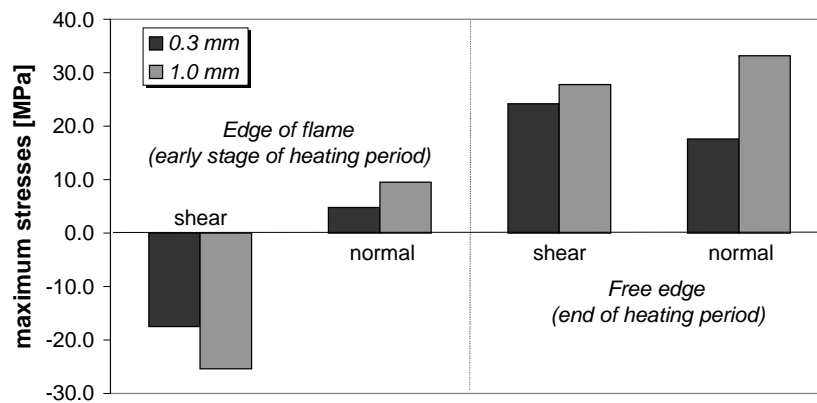


Figure 6.18 Calculated maximum shear and normal stresses during thermal shock testing near edge of flame and free edge in 0.3 mm and 1.0 mm top coats

Flame edge

Figure 6.19 (see colour plates at the end of this chapter) shows, as an example, the shear stresses that developed in a 1.0 mm thick TBC after the first second of the heating period. During the entire heating period shear stresses remained in the top coat but they were very low. A shear stress region equal in magnitude but opposite in sign was present in the substrate.

Two normal stress regions equal in magnitude but opposite in sign developed near the edge of the flame. On the flame-side of the edge the normal stresses were tensile (these stresses are shown in figure 6.18), on the 'cold' side they were compressive. The absolute values of the normal stresses were much lower than those of the shear stresses.

Free edge

As the heat front reached the free edge of the disc, then normal and shear stresses developed in that area. They increased with time to values higher than at the flame edge. An example of a shear stress region near the free edge will be given in section 6.9.3 for the case of burner rig thermal cycling. The absolute values of the shear stresses near the free edge were nearly equal to those near the flame edge (Fig. 6.18).

The normal stresses that developed near the free edge were tensile, and the effect of coating thickness was considerable. The free edge normal stresses were higher than those near the flame edge, see figure 6.18.

6.8 Thermal shock local analysis

6.8.1 Parametric study

First a parametric study was done with a local model (idealised interface, radial width: 0.2 mm) at the centre of the disc. Here the global normal stresses were zero, hence the local normal stresses would be expected to oscillate around zero. Local normal stresses were calculated just above the peaks of the idealised interface. Five cases were run. Firstly, the material properties given in table 6.3 were used, and the small elements allocated to the oxide layer were given bond coat properties (reference analysis). The four following cases examined the influences of the bond coat Young's modulus (100% increase), the bond coat CTE (30% increase), the top coat Young's modulus (100% increase), and the presence of a 5 μm thick oxide (Al_2O_3) layer between the top coat and the bond coat.

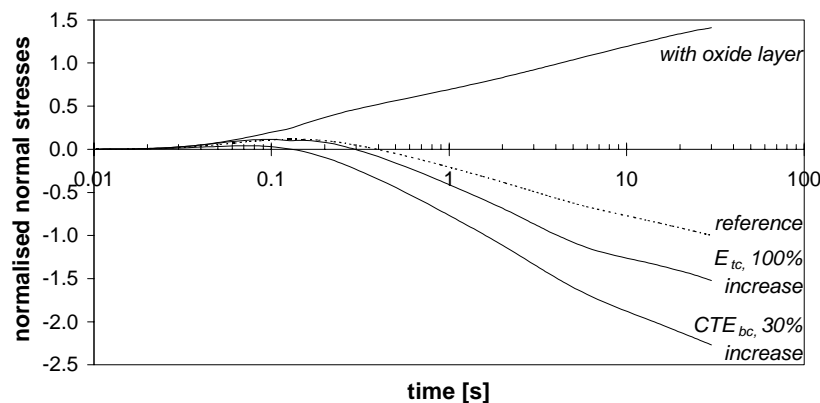


Figure 6.20 Effect of oxide layer, top coat Young's modulus (E_{tc}) and bond coat Coefficient of Thermal Expansion (CTE) on normal stresses in the top coat near an interface peak that is at the centre of the flame area during the first heating period.

Figure 6.20 gives the results of the parametric study. The normal stresses are normalised with respect to the reference analysis compressive stress at 30 seconds heating. When the Young's modulus of the top coat was increased by 100%, the stresses increased about 50%. (N.B.: the effect of a change in bond coat Young's modulus, not shown in figure 6.20, was negligible.) The influence of the bond coat CTE was considerable: a CTE increase of 30% resulted in a stress increase of more than 100%. Be that as it may, the most remarkable result was obtained when a 5 μm thick oxide layer between the top coat and the bond coat was modelled: figure 6.20 shows that in this case the stresses near the interface peak reversed, becoming completely tensile with an absolute value about 1.5 times greater.

6.8.2 Stresses near flame edge

Since delamination occurred generally in the area covered by the flame (chapter 3), the remainder of this section deals only with the stresses at the flame edge. This means that the left-hand side y-coordinate of the local model equals 6.7 mm, and the right-hand side y-coordinate 7.3 mm. Figure 6.21 shows the change in time of the normal and shear stresses in a 0.3 mm top coat just above the large peak of the realistic interface at 0.42 mm from the left-hand side (global coordinate: 7.12 mm). The effect of an oxide layer is also shown. The maximum shear and normal stresses occurred at the end of the heating period, in contrast to the global solution where a maximum occurred during the early stages of heating (see section 6.7.3). As before, the presence of an oxide layer reversed the sign of the normal stress, but now the absolute value was about 4 to 5 times greater. The shear stresses remained compressive and were increased 3 times by the oxide layer. These are obviously very important effects.

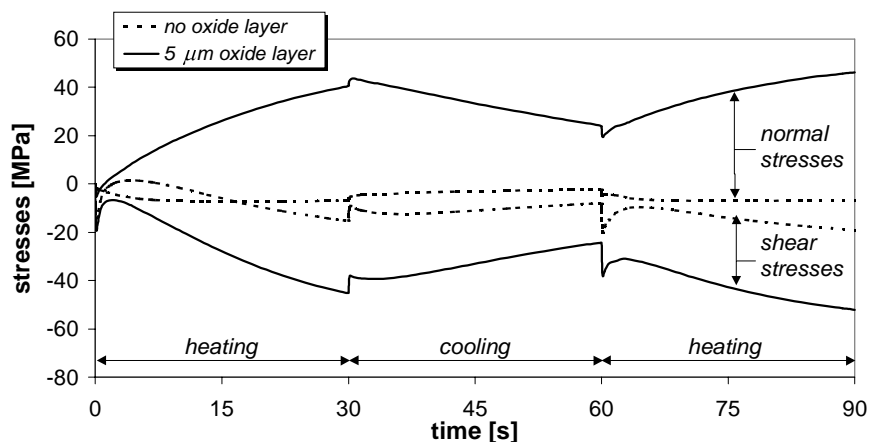


Figure 6.21 Effect of oxide layer on normal and shear stresses in a 0.3 mm top coat near peak of realistic top coat / bond coat interface at $y=7.12$ mm (see text)

Figure 6.22 (see colour plates at the end of this chapter) gives an impression of the in-plane (a), normal (b) and shear (c) stresses at the flame edge after the second heating period in a 0.3 mm top coat with an oxidised bond coat. The bulk in-plane stresses, which agreed with the results of the global analysis, were disturbed in the vicinity of the interface where stress peaks occurred on the flanks of the top coat / bond coat interface undulations. At the tops of these undulations high tensile normal stresses developed and at a position between the flanks and the tops the shear stresses reached a maximum.

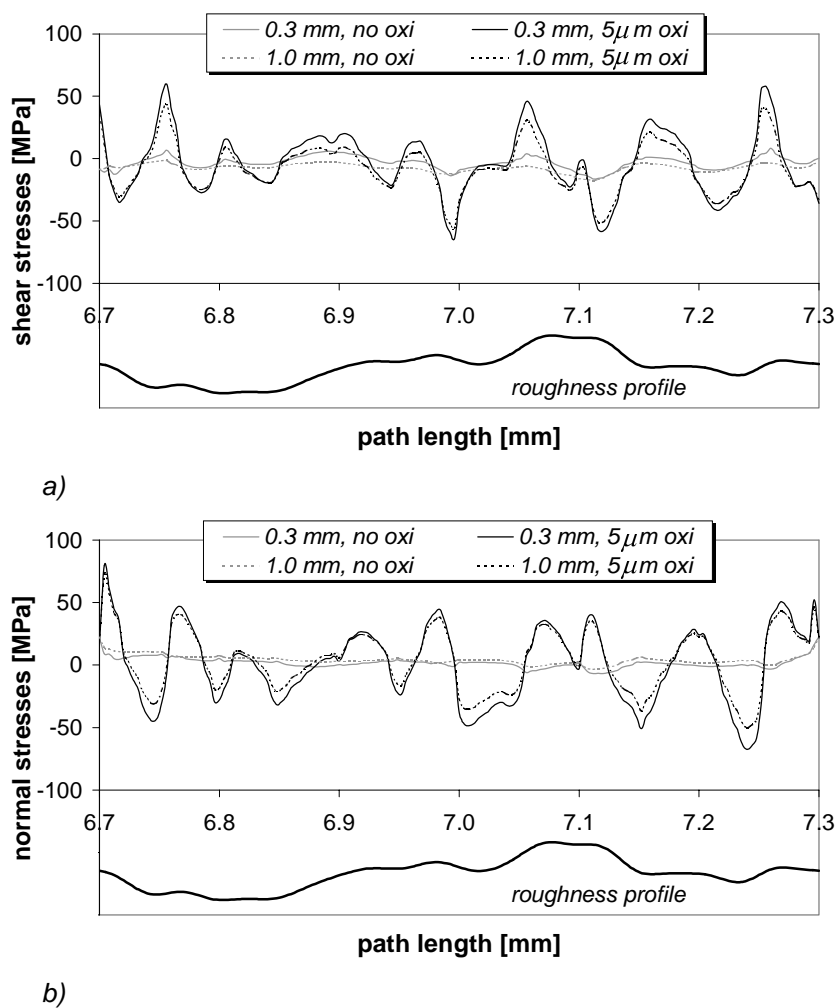


Figure 6.23 Effect of oxide layer and top coat thickness on (a) shear and (b) normal stresses near flame edge ($6.7 < y < 7.3$ mm) after second heating period of burner rig testing at $3.5 \mu\text{m}$ above realistic interface

Figure 6.23 shows the shear and normal stresses along a path just ($3.5 \mu\text{m}$) above the interface, illustrating the effect of an oxide layer and top coat thickness. Again it is clear that the presence of an oxide layer had a very large effect on the peak stresses.

However, an increase in top coat thickness resulted in a slight decrease in peak stresses.

6.9 Thermal cycling global analysis

6.9.1 Temperature

Figure 6.24 (see colour plates at the end of this chapter) gives the steady state temperature distribution for a disc with a 1.0 mm top coat. At the flame area a steep temperature gradient existed over the coating, illustrating its thermal barrier function. At the free edge of the specimen the temperature of the top coat was almost equal to but lower than that of the substrate.

Figure 6.25 shows the transient heating behaviour of the TBC system for thin (0.3 mm) and thick (2.0 mm) top coats, whereby the temperatures for the top coat surface and substrate rear side are given for the first 1000 seconds. The curves shown are taken from the centre of the flame and at the free edge of the disc. The temperature difference over the thickness at the centre of the disc (ΔT) is also given. The maximum ΔT , which occurred after 0.5 to 4 seconds depending on the coating thickness, coincided with the start of heating of the substrate, and it can be seen that from that moment the heating rate of the top coat surface diminished. After reaching a maximum, ΔT decreased to a much lower and steady state value. During the following cooling period (not shown in figure 6.25) the temperature of the entire disc dropped to values of about 250°C. The transient heating behaviour of the TBC system with a 1.0 mm top coat was similar to those shown in figure 6.25.

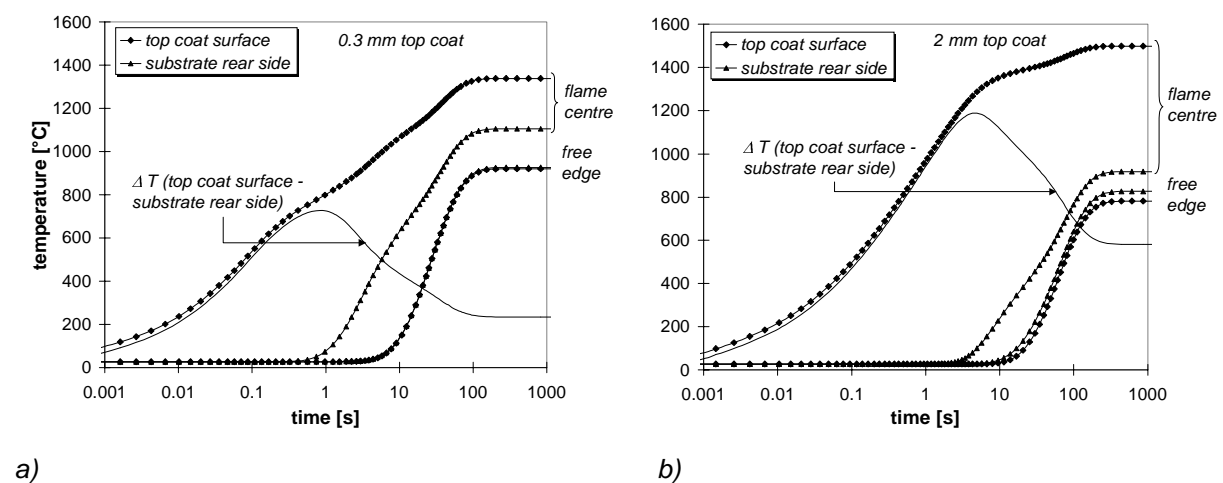


Figure 6.25 Calculated temperature profile in (a) 0.3 and (b) 2.0 mm top coat during first 1000 seconds of burner rig thermal cycling heating period. The temperature difference between the top coat surface and substrate rear side is given by ΔT

The steady state temperatures of the top coat surface, top coat / bond coat interface and substrate rear side are listed in table 6.9 for all analyses. The thermal barrier ratios of the 0.3 mm and 1.0 mm TBCs equalled those found for the thermal shock simulations (*cf.* table 6.8).

Table 6.9 Steady state temperatures (°C) of top coat surface, top coat / bond coat interface and substrate rear side at flame centre during burner rig thermal cycling of 0.3 mm, 1.0 mm and 2.0 mm top coats, according to the numerical model

top coat thickness [mm]	0.3	1.0	2.0
top coat surface	1339	1406	1506
top coat / bond coat interface	1169	1014	955
substrate rear side	1105	965	990
$\Delta T_{\text{top coat}}$	170	392	456
$\Delta T_{\text{specimen}}$	234	441	516
$\Delta T_{\text{top coat}} / \Delta T_{\text{specimen}}$	0.73	0.89	0.88

6.9.2 In-plane stresses

Heating

As an example, figure 6.26 gives the in-plane stresses for the 1.0 mm TBC ($T_{\text{surf}}=1500^{\circ}\text{C}$) at the top coat surface and at the top coat / bond coat interface during the first 1000 sec. of the heating period and at three locations: the flame centre, the flame edge and at the free edge of the specimen. The time is plotted on a logarithmic scale so that the initial stress development at the top coat surface can be followed.

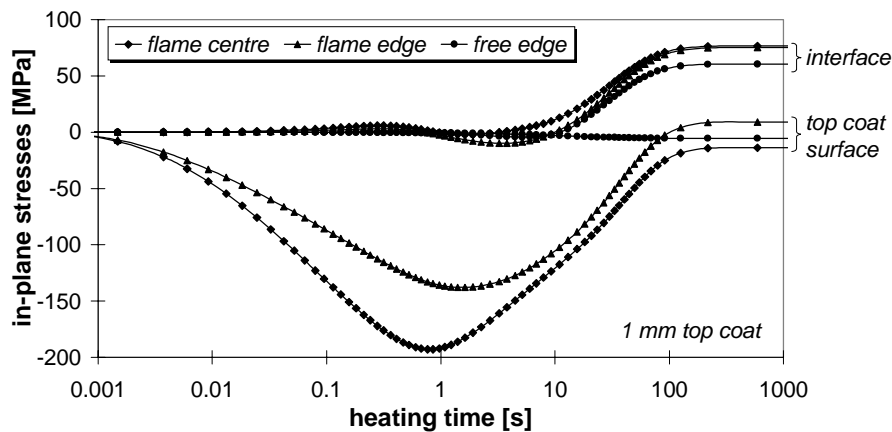


Figure 6.26 In-plane stresses in 1.0 mm top coat during first 1000 seconds of burner rig thermal cycling heating period

The in-plane stresses in the top coat appeared to change with time in a similar way as during thermal shock, and the order of magnitude of the in-plane stresses also agreed. However, during thermal cycling a steady state was reached and from figure 6.26 it is seen that the steady state stresses were higher (less compressive, or even tensile, and more tensile) than the stresses after 30 seconds. Table 6.10 lists the maximum in-plane surface stresses and steady state in-plane surface and interface stresses at the flame centre for the 0.3, 1.0 and 2.0 mm top coats. From table 6.10 it is seen that the maximum compressive stress at the top coat surface was lower for the 0.3 mm top coat than for the 1.0 and 2.0 mm top coats. Also, the steady state surface stresses were tensile in the 0.3 mm top coat but compressive in the 1.0 and 2.0 mm top coats, and decreased with decreasing heat input (compare the stresses in the 1.0 mm top coat for $T_{\text{surf}}=1400^{\circ}\text{C}$ and $T_{\text{surf}}=1500^{\circ}\text{C}$). At the top coat / bond coat interface the steady state in-plane stresses were always tensile for any position, owing to expansion of the underlying metallic bond coat and substrate. Also, the interface steady state stresses decreased with increasing top coat thickness.

Table 6.10 Maximum in-plane surface stresses and steady state in-plane surface and interface stresses in 0.3, 1.0 and 2.0 mm top coats at centre of flame area during thermal cycling. The time at which maximum surface stress occurred is also given. The top coat surface temperature in the second column is the steady state test temperature.

d_{tc} [mm]	T_{surf} [$^{\circ}\text{C}$]	maximum stress [MPa]		steady state stresses [MPa]	
		surface	time [s]	interface	surface
0.3	1350	-139	0.25	85	52
1.0	1400	-183	0.85	77	-5
1.0	1500	-193	0.90	77	-14
2.0	1500	-188	1.65	75	-38

Cooling

Figure 6.27 shows the in-plane stresses during cooling from $T_{\text{surf}}=1500^{\circ}\text{C}$ for the 1.0 mm TBC. Note that the stress curves in figure 6.27 are a continuation of those in figure 6.26. The surface stresses for the formerly flame heated part of the coating first became tensile due to contraction while the underlying material was still hot. When the cold front reached the interface after a few seconds, the metallic components started to contract and all the tensile in-plane stresses in the coating (both at the surface and at the interface) started to decrease. All the stresses would have been zero if the entire specimen had returned to room temperature.

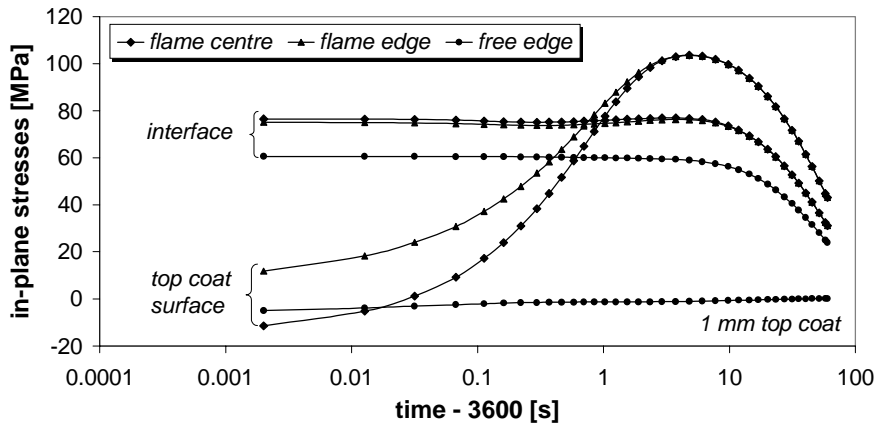


Figure 6.27 In-plane stresses in 1.0 mm top coat during burner rig thermal cycling cooling period

Creep

For the 0.3 mm TBC one stress analysis was performed with all constituents being allowed to creep. Figure 6.28 shows the results for the first 200 seconds of (a) a heating period and (b) during cooling. As mentioned in section 6.7.2, the compressive stresses in the substrate are very high during the early stages of heating irrespective of whether creep is allowed or not. Figure 6.28a shows that within three minutes of heating the stresses in all constituents were diminished by creep to almost zero. As a consequence, larger stresses were present in the specimen after the cooling period (Fig. 6.28b) and residual stresses would have been present if the specimen had returned to room temperature (for the elastic analysis all stresses would be zero). It also becomes clear from figure 6.28a that during thermal shock (30 sec heating period) the effect of creep is negligible.

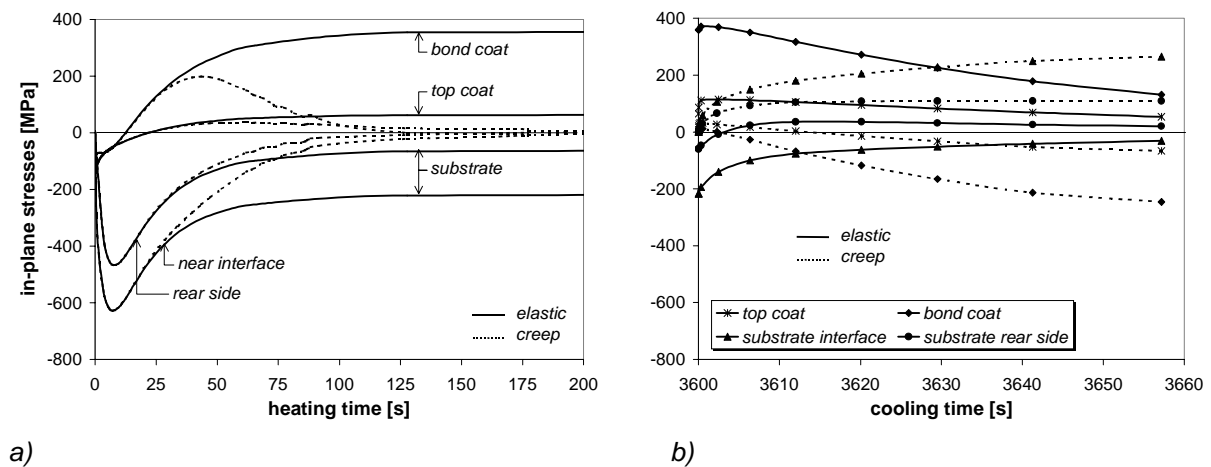


Figure 6.28 Effect of creep on in-plane stresses in substrate, bond coat and a 0.3 mm top coat during burner rig thermal cycling. a) first 200 sec. of heating; b) 60 sec. cooling period

6.9.3 Shear and normal stresses

The development of the shear and normal stresses during the transient heating period was the same as described for the thermal shock simulations (see section 6.7.3). However, during steady state heating high shear and normal stresses developed at the free edge of the disc. Figure 6.29 (see colour plates at the end of this chapter) shows the steady state shear stresses in a specimen with a 1.0 mm top coat. The shear stresses at the flame edge are still present but lower than during the beginning of the heating period (compare with figure 6.19), while at the free edge the shear stresses have reached a constant (maximum) level.

Figure 6.30 shows the maximum values of the shear stresses and normal stresses at the flame edge (beginning of heating period) and at the free edge (steady state heating) for the 0.3, 1.0 and 2.0 mm top coats. It is seen that the stresses at the flame edge are much lower than at the free edge. In more detail:

- *Flame edge*

The exact combined effect of heat flux and coating thickness on the shear stresses at the flame edge cannot yet be given from the present results. However, the shear stresses increased with increasing heat flux (compare the different temperature simulations for the 1.0 mm top coat); and the normal stresses appeared to increase with both the heat flux and the coating thickness.

- *Free edge*

At the free edge both the shear and the normal stresses increase with increasing coating thickness. The effect of the heat flux is negligible, at least for the two simulations with a 1.0 mm top coat.

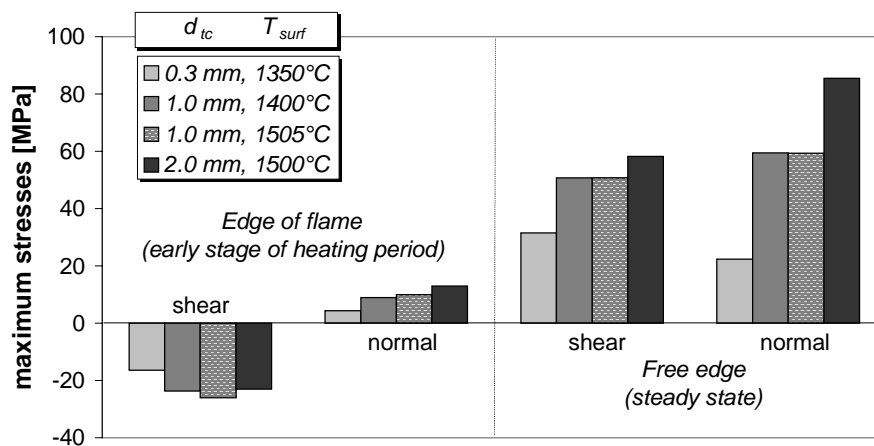


Figure 6.30 Calculated maximum shear and normal stresses during thermal cycling near edge of flame and free edge in 0.3 mm, 1.0 mm and 2.0 mm top coats

6.10 Discussion of burner rig simulations

6.10.1 Thermal analysis

The choice of T_{flame} would seem to be arbitrary, since for the same heat input it is coupled to h_{flame} (see Eq. 6.6). However, this relationship is not linear. For example, when during thermal shock simulation for the 0.3 mm top coat T_{flame} is 1800°C instead of 2225°C, h_{flame} approaches 5000 Wm⁻²K⁻¹. On the other hand, if T_{flame} is 2600°C, h_{flame} decreases by only a few hundred Wm⁻²K⁻¹ compared to the value obtained for $T_{\text{flame}}=2225^\circ\text{C}$. A high value of h_{flame} results in a very high initial heating rate of the top coat, which is undesirable. By running a few analyses with different combinations of T_{flame} and h_{flame} and comparing the results with the experiments, the T_{flame} and h_{flame} values given in table 6.5 appeared to give the best results. This is illustrated in figure 6.31 for a 0.3 mm TBC system, where the substrate rear side temperature change during the second heating cycle is compared with a measured temperature change. Both changes are scaled to $T_{(t=0)}$ to eliminate small differences in absolute temperature. It can be seen that model and experiment practically coincide. The initial heating rate for the model is slightly higher, but the maximum temperature difference during heating is less than 8%, which is acceptable.

If the heat transfer coefficient and temperature of the flame are determined empirically from the heat balance at the top coat surface, and a realistic value is assumed for the coefficient of free convection at the substrate rear side, the consequence is that the experimental heat losses via the specimen holder are ignored. Using the values obtained in this way for the numerical analysis, a too low temperature drop over the specimen is predicted. The error involved is acceptable

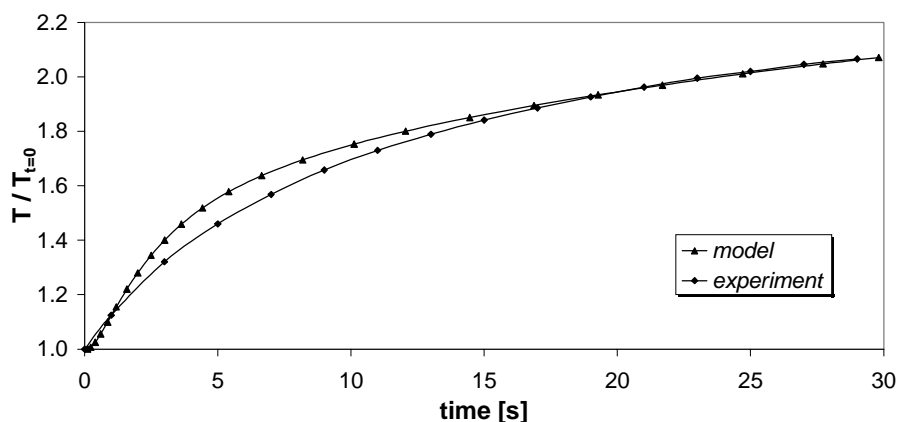


Figure 6.31 Comparison of measured substrate rear side temperature during burner rig experiments and predicted substrate rear side temperature according to model (second heating period) for a 0.3 mm TBC. Temperatures are scaled to $T_{t=0}$.

for the thermal shock simulations, but too large for the thermal cycling simulations. To solve this discrepancy the heat loss was simulated by an artificially high free convection at the substrate rear side, which resulted in good agreement between model and experiment.

The temperature drop through the top coat is an important parameter for designers of gas turbine components. This temperature drop can be expressed relative to the total temperature drop over the specimen thickness: the thermal barrier ratio. For the thermal shock simulation the thermal barrier ratio after about 10 seconds remained constant for the rest of the heating period. This constant ratio increased with increasing coating thickness. The same constant ratios per coating thickness were found during the thermal cycling simulations for the steady state temperature profile. This indicates that the thermal barrier ratio is independent of the heat input.

Finally, before discussing the results of the burner rig stress simulations it should be kept in mind that if the top coat thickness is changed the temperature distribution also changes. An increase in top coat thickness resulted most often in an increase in surface temperature, even though the total heat flux was similar or lower.

6.10.2 Global in-plane stresses

The in-plane stresses that developed during the heating period of the thermal shock analyses were similar to those that developed during the first 30 seconds of the thermal cycling analyses. Therefore, these analyses are discussed together in this subsection.

The initial compressive in-plane surface stresses in the flame area develop due to expansion of the outer coating material while the surrounding material is still cold. The peaks of these in-plane stresses occurred just before the peaks of the maximum difference in temperature and coincide with the start of bond coat heating. From that moment the bond coat and substrate expand, and as a consequence the compressive stresses in the top coat decrease.

For the thick TBCs the in-plane surface stresses in the flame area during heating were always compressive. For a thin coating these stresses changed from compressive at the beginning of the heating period to tensile at its end. This is explained by the difference in temperature drop through the top coat for the two coating thicknesses: for a thick TBC this temperature drop is large resulting in a relatively cold substrate. As a consequence, the substrate expansion will be less than

the top coat expansion, resulting in top coat compressive stresses during the entire heating period. For a thin TBC the temperature drop through the top coat is lower. In the beginning of the heating period the substrate is still relatively cold resulting in top coat *compressive* stresses. However, halfway during the heating period the substrate temperature is increased to such an extent that the substrate expansion exceeds the top coat expansion, resulting in top coat *tensile* stresses.

Except for the initial phase of the first thermal shock heating cycle, the top coat/ bond coat interface stresses are always tensile and increase with time. This can be explained by expansion of the underlying metallic bond coat and substrate. This expansion is larger than that of the top coat.

Thermal shock vs. thermal cycling

During thermal cycling the steady state period causes the in-plane stresses to increase to a higher level compared to the stresses after 30 seconds, *i.e.* tensile stresses will become more tensile and compressive stresses less compressive or even tensile.

Effect of creep

When a thermally cycled specimen is allowed to creep (see figure 6.28) the in-plane stresses at the end of the heating period are completely relaxed, resulting in residual stresses after cooling. This will affect the stresses in the following heating period. However, since those stresses will relax again, the effect of the residual stresses will be seen only at the beginning of the heating period.

6.10.3 Global shear and normal stresses

As for the in-plane stresses, the shear and normal stresses that developed during the heating period of the thermal shock analyses were similar to those that developed during the first 30 seconds of the thermal cycling analyses. Therefore, these analyses are discussed together in this section.

The global shear and normal stresses near the flame edge were relatively low and showed a maximum within the first few seconds of the heating period. When the heat front reached the free edge of the disc, then shear and normal stresses started to develop there, but these stresses were still low after 30 seconds (see figure 6.18). The low shear and normal stresses near the flame edge are surprising since delamination normally occurs in this area. It was therefore hoped and expected that failure could be explained with the aid of the local analysis, see section 6.10.4 and chapter 7.

The largest difference between thermal shock and thermal cycling is that during the steady state period of thermal cycling high shear and normal stresses developed near the free edge of the specimen, compare figures 6.18 and 6.30. These free edge shear and normal stresses increased considerably with increasing top coat thickness at the same test temperature (compare the results of the 1.0 and 2.0 mm top coat at 1500°C in figure 6.30) and were independent of the heat input (compare the results of the 1.0 mm top coat at 1400°C and 1500°C in figure 6.30).

6.10.4 Local stresses

Thermal shock

Near the flame edge the maximum *local* shear and normal stresses at the top coat / bond coat interface peaks (end of heating period) did not coincide with the maximum *global shear and normal stresses* (beginning of heating period). However, the *global in-plane* interface stresses were also at a maximum at the end of the heating period, and it can hence be concluded that the *local shear and normal* stresses are initiated by these *global in-plane* interface stresses. Since the radial variation of the global interface in-plane stresses in the flame area is very small, it may be assumed that the local solution applies for the entire flame area. From the foregoing it is clear that in contrast to furnace simulations – where at the free edge of the disc high *local* and *global* shear and normal stresses coincided (see section 6.5) – the maximum *local* shear and normal stresses near the flame edge during burner rig testing occurred when the *global* shear and normal stresses were low.

Thermal cycling

Though local analyses were not done for the thermal cycling simulations, it may be expected that near the flame edge the local thermal cycling solution is similar to the local thermal shock solution. Also, near the free edge of the disc the effect of top coat / bond coat interface roughness and the presence of an oxide layer are expected to have the same effect as seen during furnace simulations, *i.e.* a variation of the shear and normal stresses around the average global solution.

6.10.5 Final remarks about local stress distribution

An important difference between the local stress distributions of a furnace simulation and a thermal shock simulation is that in the furnace simulation local stresses vary around a high mean value, and in the thermal shock simulation local stresses vary

around practically zero (compare figures 6.14 and 6.23). Hence when no oxide layer is present at the top coat / bond coat interface (low deviation of local stresses from the mean value), the local shear and normal stresses during furnace testing are still at a high level, while the local shear and normal stresses during thermal shock are almost zero. This explains also the apparent paradox that for the furnace simulations the local maximum stresses *increased*, and for the burner rig simulations they *decreased* with increasing top coat thickness: on the one hand, for both simulations the variation of the local stresses around the mean stress value decreased with increasing top coat thickness owing to the decrease in global in-plane stresses with increasing top coat thickness. On the other hand, during the furnace simulations the global shear and normal stresses (*i.e.* local stress mean value) increased (became more compressive) with increasing top coat thickness, while during thermal shock simulations the global shear and normal stresses remained practically zero.

One might doubt the existence of local normal and shear stresses at an top coat / bond coat interface roughness peak (these stresses being caused by in-plane coating stresses). Evans *et al.* (1983) has shown that normal stresses most probably do occur at these peaks. However, because an explicit analytical solution is unavailable or unfeasible for the entire profile of the interface, Evans *et al.* (1983) formulated a model of the local situation at an interface roughness peak whereby the interface shear stresses were required to be zero. This restriction is unrealistic and contradicted by the present work.

6.11 Conclusions

The relative temperature drop through the coating with respect to that through the specimen (thermal barrier ratio) reaches a constant value after about 10 seconds of heating, and remains constant during the rest of the heating period, including steady state. The thermal barrier ratio increases with increasing coating thickness, but is virtually independent of the heat input.

Using an artificially high coefficient of free convection at the substrate rear side can simulate the experimental heat losses via the specimen holder during burner rig tests.

The global model provides useful information about the locations of highly stressed areas. This may sometimes be sufficient to understand the failure behaviour of TBCs (see also chapter 7).

The local model provides additional information about the effects of top coat / bond coat interface roughness and the presence of an interface oxidation layer, especially with respect to the shear and normal stresses:

- Interface roughness results in small variations of the shear and normal stresses around the global solution.
- During the heating period of the burner rig simulations the normal stresses at the roughness peaks are compressive, which cannot explain delamination.
- An oxide layer between the top coat and bond coat has two very important effects near and at the top coat / bond coat interface:
 - the shear and normal stresses show very large variations around the global solution stresses
 - the normal stresses at the interface peaks during the heating period of the burner rig simulations become reversed in sign from compressive to tensile. This can explain delamination (see also chapter 7).

The modelling work presented in this chapter contributed to a better understanding of the thermal stresses during different kinds of thermal loads. In the following chapter the experimental and theoretical results will be discussed together in order to provide a comprehensive explanation of the observed failure modes described in chapter 3.

Appendix 6A Bond coat roughness

Measurements

The bond coat roughness was measured using a Mitutoya SurfTest profilometer. 2560 data points were measured over a length of 6.4 mm with a cut-off length of 800µm. A first degree polynomial function was fitted through the data and subsequently subtracted from the profile to remove a possible skewness trend and to obtain a nominal profile. Figure 6A1 shows a filtered roughness profile.

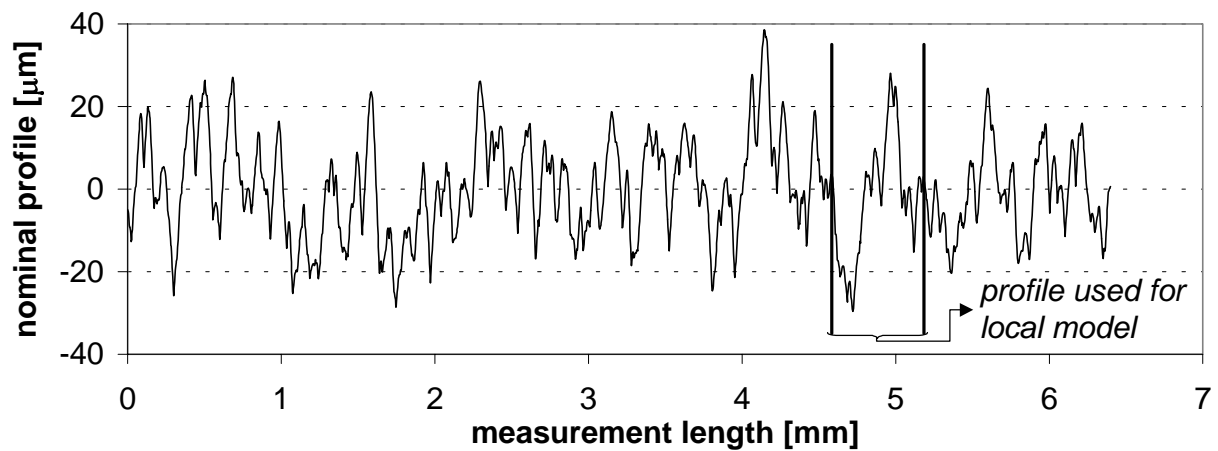


Figure 6A.1 Nominal roughness profile of plasma sprayed bond coat

From the measured nominal profiles two roughness parameters, R_A and R_P , were determined. R_A is the arithmetic average roughness value, determined from deviations about the centre line taken over the evaluation length l_m .

$$R_A = \frac{1}{l_m} \int_0^{l_m} |z(x)| dx = \frac{1}{n} \sum_{i=1}^n |z_i| \tag{6A.1}$$

R_P is the maximum peak-to-centre-line distance over the evaluation length l_m . This parameter can be used as the amplitude of the sinewave interface in the idealised local model. The average roughness values of 15 measurements (random locations) are given in table 6A.1. There was no effect of measuring direction.

Table 6A.1 Average values of R_A and R_P in microns

R_A	8.0 ± 0.7
R_P	29.3 ± 5.4

The R_A value of the bond coat is relatively low. Zhangxiong and Knight (1999) measured the bond coat roughness for several industrial thermal spray processes and found for an LPPS bond coat $R_A \approx 20 \mu\text{m}$ and for an HVOF bond coat $R_A \approx 7 \mu\text{m}$. Haynes *et al.* (2000) found for an APS Ni22Cr10Al1.0Y bond coat $R_A = 10.6 \mu\text{m}$ and for a VPS Ni22Cr10Al1.0Y bond coat $R_A = 11.8 \mu\text{m}$.

The roughness of a coating decreases with increasing degree of particle flattening. Good flattening is obtained for high particle velocities and /or when the particles are homogeneously heated to the melting point. Apparently, the plasma spray process applied during the present project results in the same degree of flattening as an industrial HVOF process.

Top coat / bond coat interface used for local model

For the local model with a realistic interface a representative 0.6 mm was taken from the nominal roughness profile, see figure 6A.1. Since the mesh resolution of the local model is limited to a few micrometers, very small details of the profile were filtered out by taking the 200 most powerful signals by Fourier transformation. The obtained profile used for the FEM analysis is given in figure 6A.2. This figure also shows the sinewave used for the idealised local model.

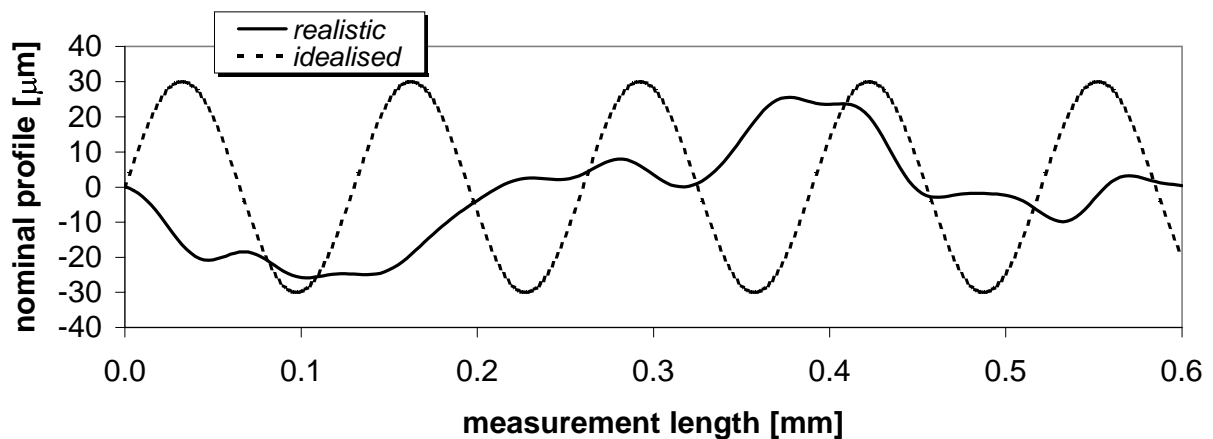


Figure 6A.2 Part of the roughness profile used as the interface for the realistic local model (solid line) and sinewave used as the interface for the idealised local model (dotted line)

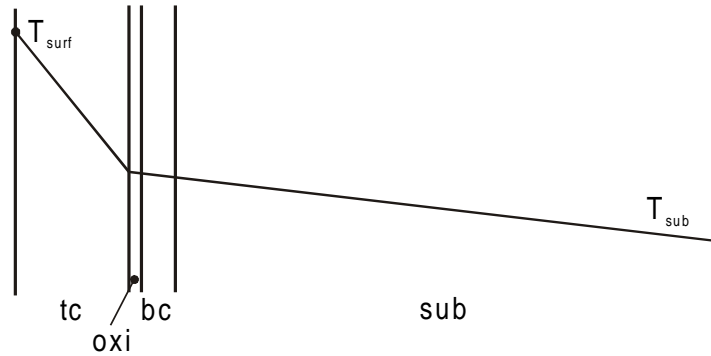
Appendix 6B Effect of oxide layer on temperature profile


Figure 6B.1 Composite wall for one-dimensional heat transfer (not to scale)

Consider figure 6B.1 where a one-dimensional heat flow through a composite wall consisting of a top coat (tc), an oxide layer (oxi), a bond coat (bc) and a substrate (sub) is shown. The steady state heat transfer rate for this system may be expressed as:

$$q = \frac{T_{surf} - T_{sub}}{\left(\frac{d}{\lambda}\right)_{tc} + \left(\frac{d}{\lambda}\right)_{oxi} + \left(\frac{d}{\lambda}\right)_{bc} + \left(\frac{d}{\lambda}\right)_{sub}} \quad (6B.1)$$

where T_{surf} and T_{sub} are the top coat surface and substrate rear side temperature respectively, d is the thickness of an element and λ is the thermal conductivity. The substrate rear side temperature can be determined from:

$$T_{sub} = T_{surf} - q \cdot \left[\left(\frac{d}{\lambda}\right)_{tc} + \left(\frac{d}{\lambda}\right)_{oxi} + \left(\frac{d}{\lambda}\right)_{bc} + \left(\frac{d}{\lambda}\right)_{sub} \right] \quad (6B.2)$$

Hence, the temperature difference for T_{sub} due to the oxide layer is given by:

$$\Delta T_{sub} = -q \cdot \left(\frac{d}{\lambda}\right)_{oxi} \quad (6B.3)$$

For $q \approx 1 \cdot 10^6 \text{ Wm}^{-2}$ (typical value for burner rig used), $d_{oxi} = 5 \mu\text{m}$ and $\lambda_{oxi} = 2.0 \text{ Wm}^{-1}\text{K}^{-1}$, Eq. 6B.3 gives $\Delta T_{sub} = -2.5 \text{ K}$. Since T_{sub} is typically about 1300K, this is a relative change of only 0.2%. It is therefore concluded that the influence of an oxide layer on the temperature profile is negligible.

Appendix 6C Creep of a coated bar

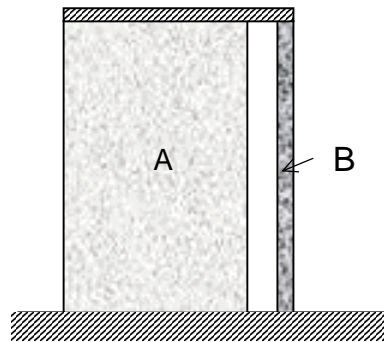


Figure 6C.1 Two-bar model

The creep behaviour of a coated bar can be simulated with a simple two-bar finite element model based on Embley and Kallianpur (1986). Consider figure 6C.1 where the ends of two bars are connected resulting in constrained thermal expansion when the system is heated to 1137°C. The relaxation of the thermal expansion mismatch stresses can be determined by allowing both materials to creep. Bar A represents Hastelloy-X with a thickness of 3.2 mm, bar B represents a ZrO_2 - Y_2O_3 top coat with a thickness of 0.3 or 1.0 mm. Creep behaviour was defined using the temperature dependent power-law creep model given in Equation 6.1. Material properties and creep constants are listed in table 6.3. The in-plane stress developments in the top coat and substrate at 1137°C for the 0.3 and 1.0 mm top coat is given in figure 6C.2. It is seen that the stresses diminish to zero within one hour.

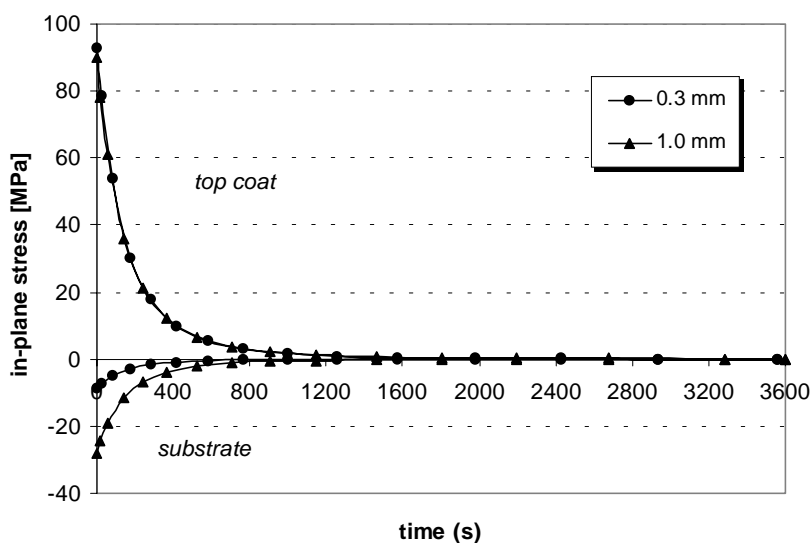


Figure 6C.2 Stress relaxation in substrate and top coat at 1137°C

Appendix 6D Heat transfer coefficient for free convection

The coefficient of heat transfer for free convection from a vertical plate, h_{fc} , is given by (Incropera and DeWitt, 1990):

$$h_{fc} = \frac{Nu \cdot \lambda}{L} \quad (6D.1)$$

where λ is the thermal conductivity of air, L is the characteristic length ($L = 30$ mm) and Nu is the Nusselt number, which is approximated by:

$$Nu = C \cdot Ra_L^n \quad (6D.2)$$

where $C=0.59$ and $n=0.25$ for laminar flows, or $C=0.10$ and $n=0.33$ for turbulent flows, and Ra_L is the Rayleigh number, defined as:

$$Ra_L = \frac{g\beta(T_{surf} - T_{\infty})L^3}{\mu\alpha} \quad (6D.3)$$

where g is the acceleration due to gravity, β is the volumetric thermal expansion coefficient, μ is the viscosity of air, α is the diffusivity of air, T_{surf} is the surface temperature and T_{∞} is the temperature of the surroundings. The air properties μ , λ and α are evaluated at the film temperature, $(T_{surf} + T_{\infty})/2$ and β can be approximated by $1/T_f$.

The transition from laminar to turbulent flow occurs at $Ra_L=10^9$. For the present case $Ra_L \approx 10^5$, and so $C=0.59$ and $n=0.25$. With air properties from Incropera and DeWitt (1990) the course of h_{fc} as a function of the surface temperature is presented in figure 6D.1. The high temperature value for h_{fc} ($15 \text{ Wm}^{-2}\text{K}^{-1}$) is adopted for the entire temperature range.

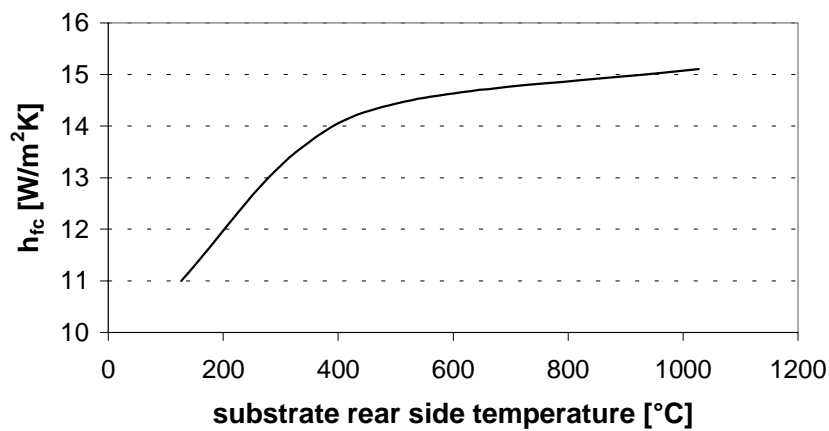


Figure 6D.1 Heat transfer coefficient for free convection as a function of the substrate rear side temperature

Appendix 6E Heat transfer coefficient for impinging jet

For an impinging jet, the coefficient of heat transfer, h , is given by (Incropera and DeWitt, 1990):

$$h = \frac{Nu\lambda}{D_h} \quad (6E.1)$$

where D_h is the hydraulic diameter of the nozzle, λ is the gas conductivity and Nu the Nusselt number which can be determined from:

$$\frac{Nu}{Pr^{0.42}} = G \cdot F(Re) \quad (6E.2)$$

where Pr is the Prandtl number, G is a geometric function and

$$F = 2 Re^{1/2} (1 + 0.005 Re^{0.55})^{1/2} \quad (6E.3)$$

Re is the Reynolds number and is given by:

$$Re = \frac{V_e D_h \rho}{\mu} \quad (6E.4)$$

where V_e is the gas velocity at the nozzle exit, ρ is the gas density and μ is the gas viscosity. D_h , G and V_e are independent of the temperature, and Pr is nearly constant over the temperature range. Consequently, the effect of the temperature on the heat transfer coefficient can be determined by the following correlation:

$$h \propto \lambda \cdot Nu \propto \lambda \left[\sqrt{Re} + \sqrt{0.005} \cdot Re^{0.775} \right] \propto \lambda \left[\sqrt{\frac{C_1 \rho}{\mu}} + \sqrt{0.005} \cdot \left(\frac{C_1 \rho}{\mu} \right)^{0.775} \right] \quad (6E.5)$$

where $C_1 = V_e \cdot D_h \sim 0.25 \text{ m}^2/\text{s}$ (estimated).

The properties in Eq 6E.5 are evaluated for air at the film temperature, $(T_{\text{surf}} + T_{\text{flame}})/2$, with $T_{\text{flame}} = 2200^\circ\text{C}$. For the thermal shock and thermal cycling simulations the reference surface temperatures at which h_{flame} is determined are 1500°C and 1300°C respectively. The relative change in h_{flame} with respect to the coefficient of heat transfer at the steady state surface temperature ($h_{T\text{-ref}}$) is shown in figure 6E.1 as a function of the top coat surface temperature.

The curves are third degree polynomial functions fitted to the data points, and are given by:

$$f = 4.966835 \cdot 10^{-11} T^3 - 9.281396 \cdot 10^{-8} T^2 + 5.833688 \cdot 10^{-5} T + 0.9056204 \tag{6E.6}$$

for thermal shock, and:

$$f = 1.021407 \cdot 10^{-10} T^3 - 2.6669 \cdot 10^{-7} T^2 + 2.290901 \cdot 10^{-4} T + 0.8994668 \tag{6E.7}$$

for thermal cycling.

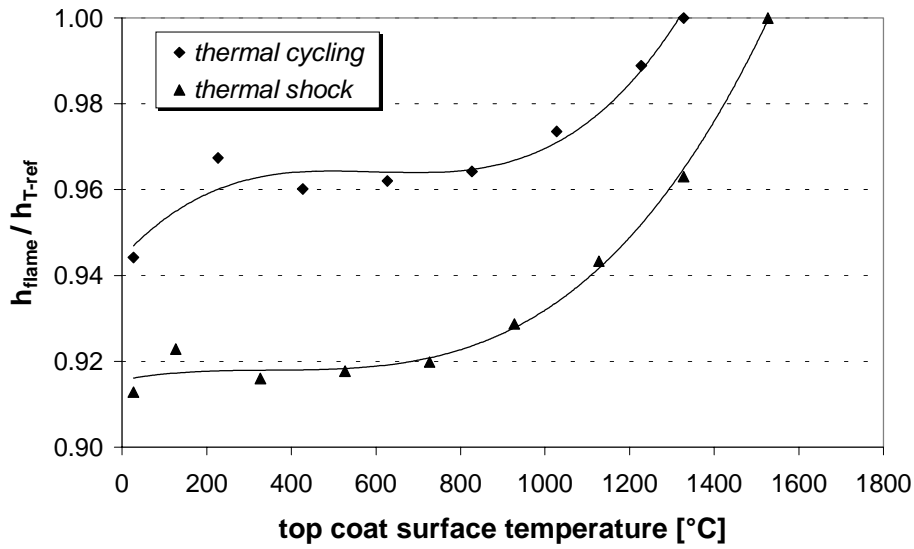


Figure 6E.1 Relative change in the coefficient of heat transfer for the flame as a function of the top coat surface temperature

Colour Plates for Figures 6.9, 6.13, 6.19, 6.22, 6.24, 6.29

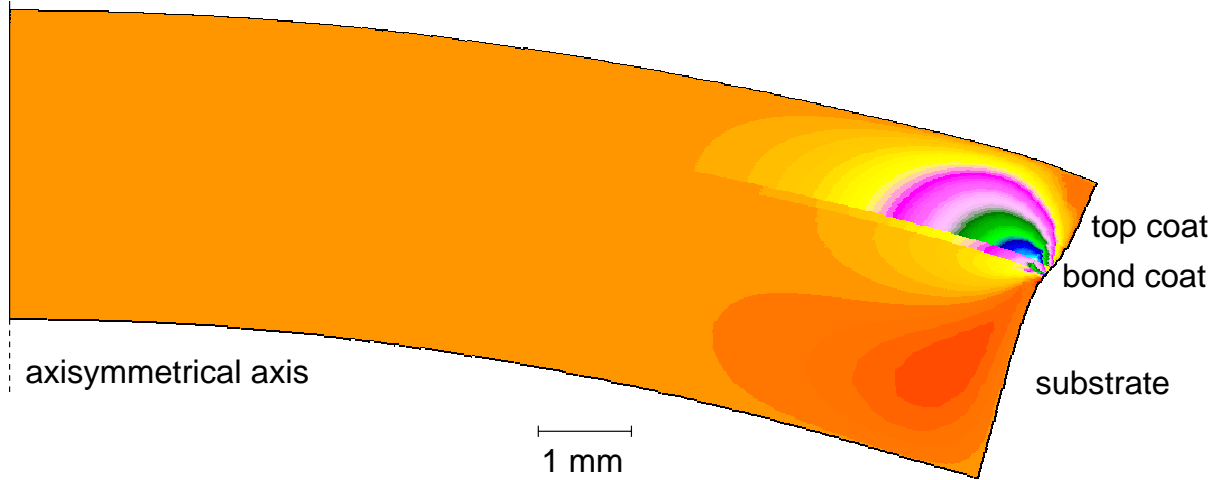


Figure 6.9 Contour plot of shear strains in a 1.0 mm top coat specimen near edge of disc at the end of the cooling period (furnace simulation), shown on a deformed (25 times exaggerated) mesh

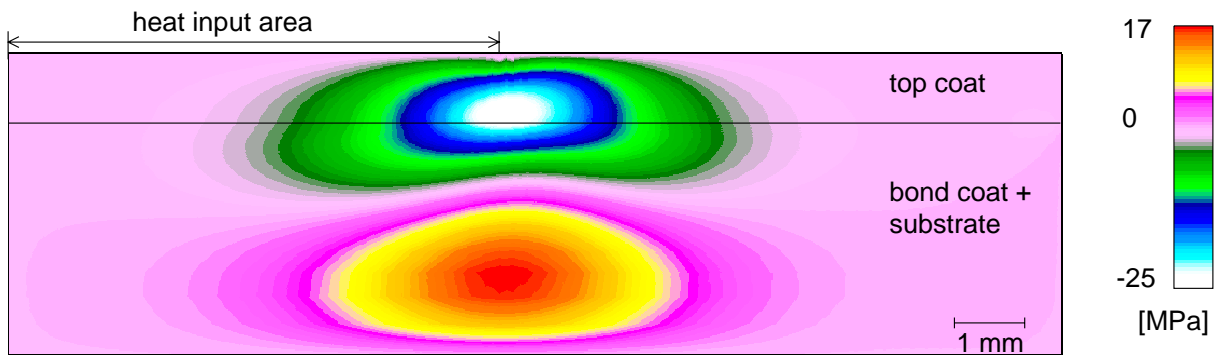


Figure 6.19 Contour plot of shear stresses during burner rig testing after 1 second in a disc with a 1.0 mm top coat

Colour Plates for Figures 6.9, 6.13, 6.19, 6.22, 6.24, 6.29

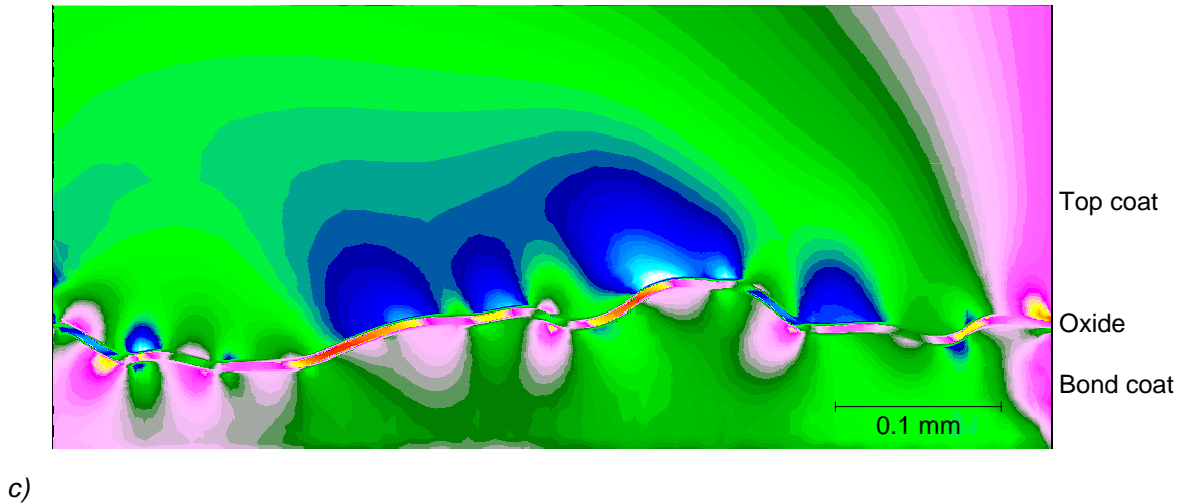
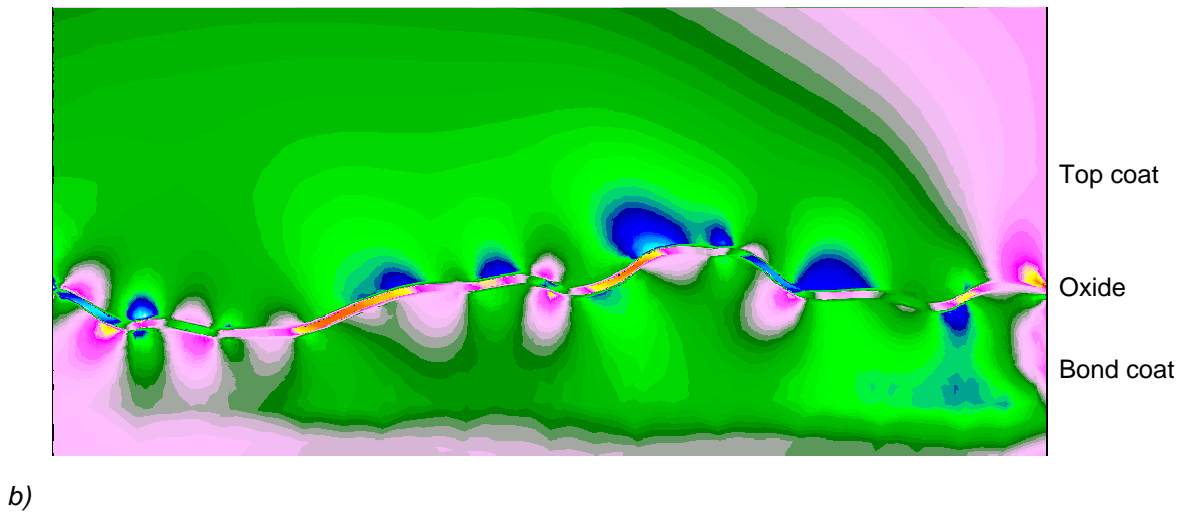
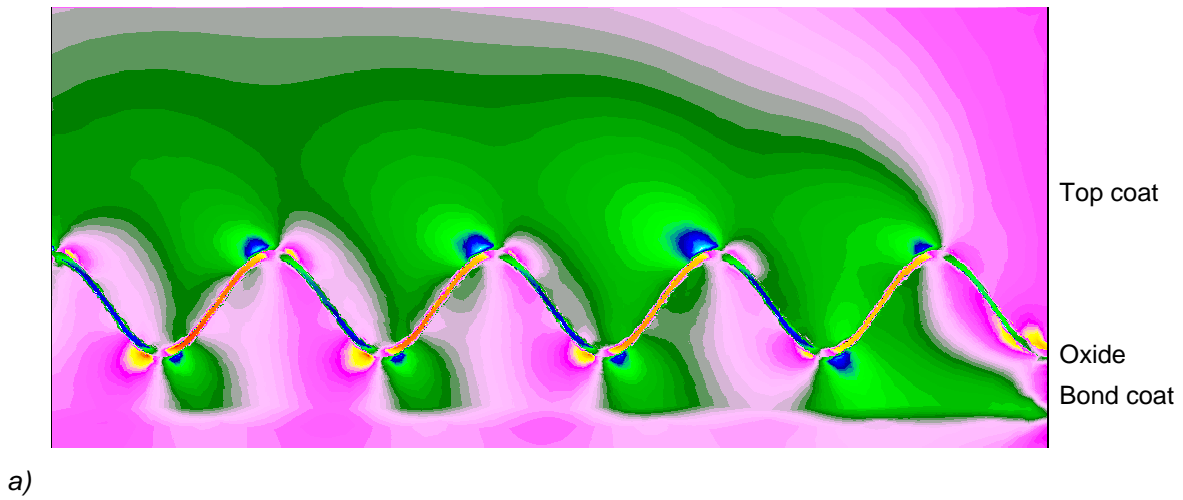


Figure 6.13 Contour plots of shear strains near free edge (furnace simulation) for (a) idealised interface with 0.3 mm top coat, (b) realistic interface with 0.3 mm top coat, and (c) realistic interface with 1.0 mm top coat. The free edge is located at the right-hand side of the plots.

Colour Plates for Figures 6.9, 6.13, 6.19, 6.22, 6.24, 6.29

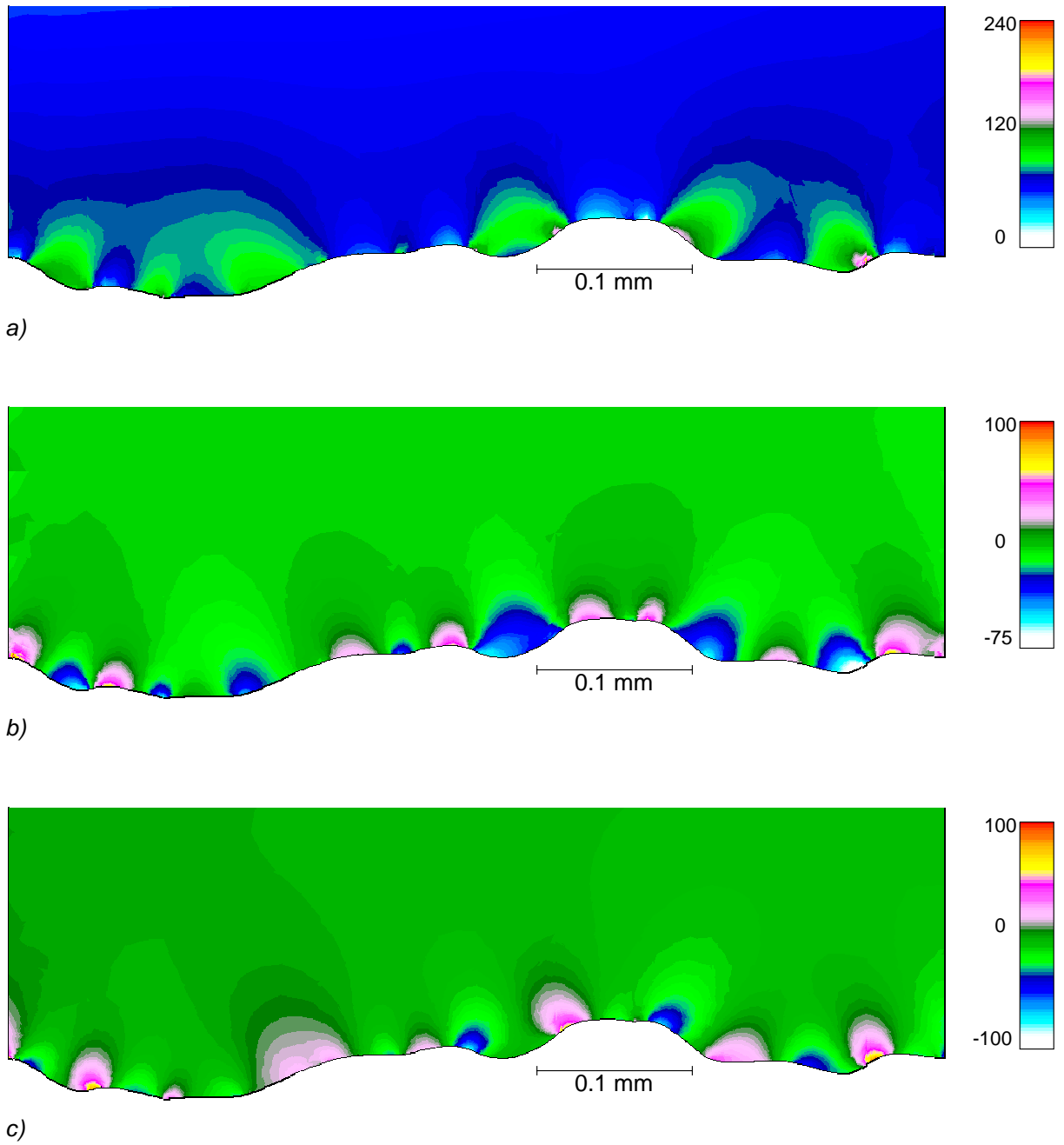


Figure 6.22 Contour plots of (a) in-plane, (b) normal and (c) shear stresses (MPa) near flame edge ($6.7 < y < 7.3$ mm) after second heating period of burner rig thermal shock testing in a 0.3 mm top coat with a $5 \mu\text{m}$ oxide layer at the top coat / bond coat interface

Colour Plates for Figures 6.9, 6.13, 6.19, 6.22, 6.24, 6.29

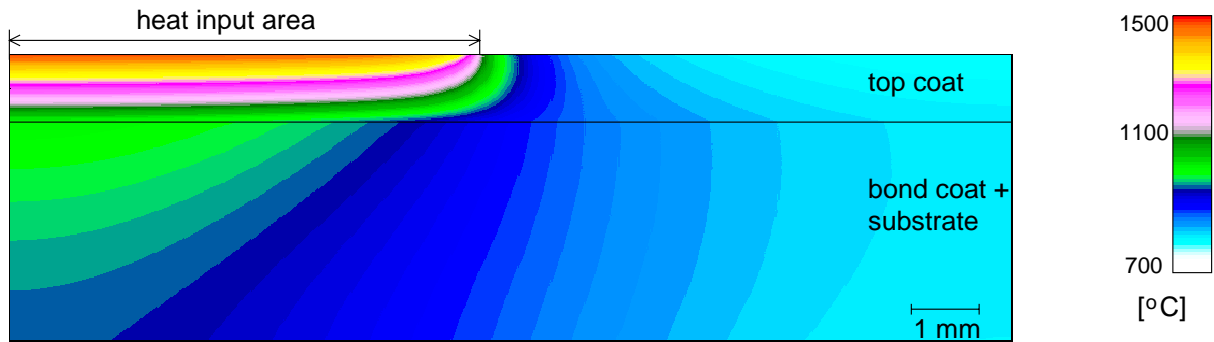


Figure 6.24 Contour plot of steady state temperature distribution ($^{\circ}\text{C}$) during burner rig thermal cycling for a disc with a 1.0 mm top coat

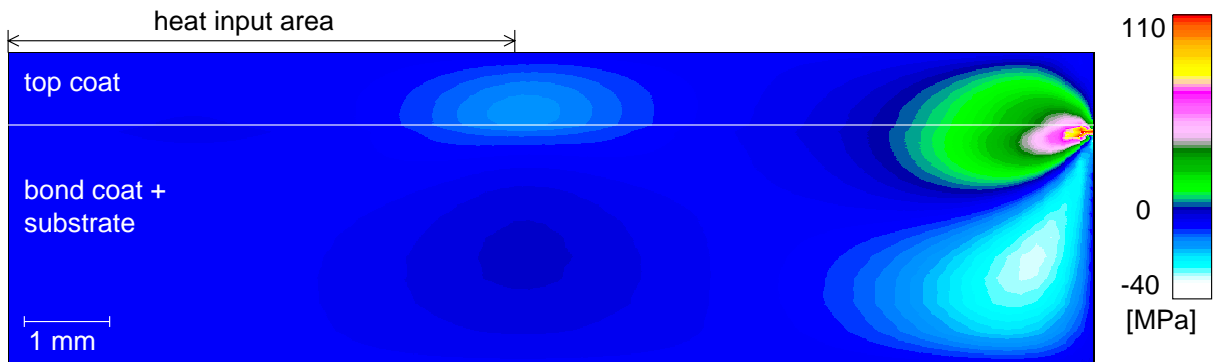


Figure 6.29 Contour plot of steady state shear stresses during burner rig thermal cycling for a disc with a 1.0 mm top coat

7 DISCUSSION

7.1 Introduction

The foregoing chapters have presented an experimental and theoretical study of thermal testing of TBCs. In chapter 3 it was shown that the number of cycles to failure and the failure modes depend strongly on the type of test (furnace or burner rig), the test temperature and the top coat thickness. In chapter 4 and chapter 5 it was demonstrated that substantial changes in (microstructural) properties and residual stresses take place during a heat treatment. In chapter 6 the locations and order of magnitude of the stresses that develop during furnace and burner rig testing were predicted, and it was shown that interface roughness and the presence of an interface oxide layer had considerable effects on the local stress distribution.

In this chapter the experimental and theoretical results will be discussed together in order to provide a comprehensive explanation of the observed failure modes, summarised in tables 3.3 and 3.4.

7.2 Furnace testing

7.2.1 Residual stresses

Since it can be assumed that a TBC is stress-free at high temperatures, numerical analysis of the cooling period during furnace testing (section 6.4-6.6) predicts the residual stresses at room temperature. Though the numerical model agreed with an analytical model (see section 6.6.1, table 6.7), there was a large discrepancy with the experimental results. The measured in-plane residual stresses after a heat treatment never exceeded -50 MPa (section 5.4), while the numerical model predicted stresses between -150 and -200 MPa, depending on top coat thickness and test temperature. Obviously, there must be some stress relaxation in practise. Microcracking is unlikely

under compressive conditions, and creep can also be excluded since the time at high temperature during cooling is too short. Two mechanisms remain to explain the large difference between model and experimental residual stresses:

1. Vertical cracks or segmentation cracks formed during heating (see also section 7.2.2). These will result in a lower effective Young's modulus and hence in a different response of the top coat during hole drilling compared to an uncracked TBC.
2. Inelastic deformation of the top coat. According to DeMasi-Marcin *et al.* (1990), who conducted uniaxial tensile tests in the plane of the coating, substantial reversed inelastic deformation at ambient and elevated temperatures can occur. They attributed this deformation to the accumulation of discrete discontinuous displacements across adjacent shear loaded surfaces in the interpenetrating and mechanically interlocked microcracked structure.

It would appear that these two mechanisms greatly reduce the residual stresses, to values smaller than one-third of the theoretical value.

In chapter 5 it was shown that residual stresses after a heat treatment decreased with increasing coating thickness (fig. 5.9). This agrees with model predictions made in chapter 6. However, the model also predicted about the same difference in residual stresses when decreasing the isothermally heating temperature from 1250°C to 1050°C, while the measurements showed a minor effect of the isothermally heating temperature on the residual stresses (fig. 5.6). Apparently, the change in residual stresses due to a change in isothermal heating temperature is annulled by the stress relaxation mechanisms discussed above, while the change in residual stress due to a change in thickness is still present after stress relaxation.

7.2.2 Failure modes

Vertical cracking

After furnace testing thick TBCs showed segmentation cracks and thin TBCs showed some vertical cracks. These types of cracks can be explained only from tensile in-plane stresses, which occur only during the first heating cycle, see figure 7.1. Hence vertical (segmentation) cracks must have been formed during the first heating cycle.

Though in-plane stresses decrease with increasing top coat thickness (see section 6.4) segmentation cracking occurred for thick TBCs and not for thin TBCs. Apparently, the driving force for cracking (the strain energy before cracking minus the surface energy after cracking) increases with increasing top coat thickness.

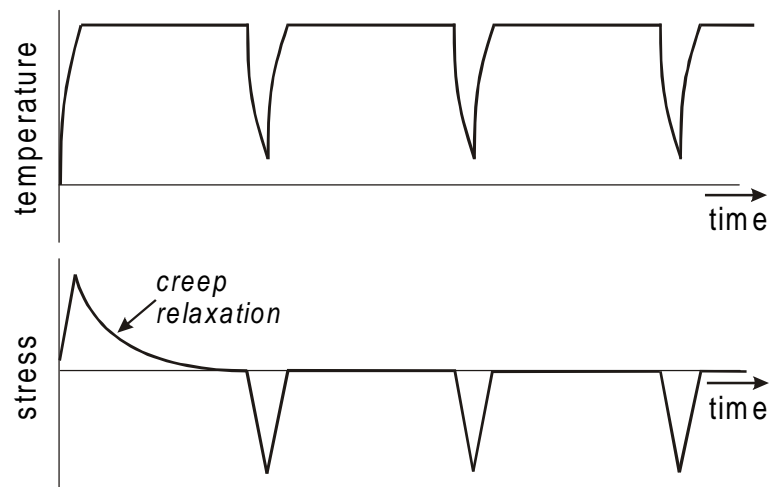


Figure 7.1 Schematic temperature and stress profiles during furnace testing. The tensile stresses in the first heating cycle relax by creep.

Delamination

During furnace testing delamination always occurred during cooling, starting from the free edges. From the results of the global analysis it was learned that high shear and normal stresses develop near the free edge (sub-section 6.4.3). Moreover, owing to the top coat / bond coat interface roughness and the presence of an interface oxide layer, these stresses could be amplified by 250% (sub-section 6.5.3). However, the global normal stresses near the free edge are compressive, and will most likely not contribute to delamination. It is therefore concluded that delamination during furnace testing is predominantly due to cooling-induced shear stresses near the intersection of the top coat/ bond coat interface and the free edge. Once a free edge crack has formed the coating material just above the crack is no longer attached to the bond coat and will therefore bend more away from the underlying material. It is suggested that this facilitates vertical cracking near the crack tip, which results in the typical nibbling-off effect. It must be mentioned that delamination occurs after a large number of cycles, indicating thermal fatigue. The actual shear stresses must be below a critical value that would cause delamination after one cycle. We will come back to this in sub-section 7.2.3.

Away from the free edge there are shear stresses at the interface peaks, see table 6.6, but they are much lower than the shear stresses near the free edge. The stresses at interface peaks will not cause delamination, but together with the stresses caused by a growing oxide layer (Tsui *et al.*, 1998), they are believed to attribute to the forming of interface cracks (see *e.g.* figure 3.18) by fatigue.

7.2.3 Effect of top coat thickness and test temperature

Top coat thickness

Increased top coat thickness increases the shear stresses near the free edge, which explains the short lives of thick TBCs. Failure of the 1.0 mm TBC at 1250°C after one cycle tested suggests that the critical shear stress for delamination is about 110 MPa (see figure 6.11). Assuming that this value is independent of the coating thickness Eq 6.14 shows that a 0.3 mm TBC (65 MPa at $T_{ini}=1050^{\circ}\text{C}$, see fig. 6.11) should delaminate after one cycle at $T_{ini}=1750^{\circ}\text{C}$ (ignoring the effect of the increased oxidation rate at this temperature, see below). This is far beyond the application temperature.

The failure modes of the thick and thin TBCs differed. For thick TBCs segmentation cracking was followed by *complete* delamination instead of nibbling-off. This may be explained by the following mechanism. After segmentation cracking the top coat is divided into small islands with an average diameter of 3 mm (see figure 3.14). At the intersections of the edges of these islands and the top coat / bond coat interface a singular stress situation occurs similar to that near the free edge of the specimen. Hence the shear stresses close to the interface but away from the free edge will be much higher than in a TBC without segmentation cracking, and delamination proceeds easily along the interface.

Test temperature

According to the numerical analysis, cooling stresses that develop in the furnace tested specimens correlate linearly with the temperature drop (Eq. 6.14). This explains the following experimental observations:

- Failure of the ITC furnace tested specimens during the 4-hour stay at room temperature. This failure can be attributed to the increase in stresses due to the extra cooling from 200°C to ambient temperature.
- The number of 1-hour cycles to failure for the 0.3 mm TBCs during the NLR furnace tests at 1100°C was lower than those during the ITC furnace tests at 1137°C (220 vs. 310). This can be attributed to the larger temperature change during NLR furnace testing (1100°C–25°C=1075°C) compared to ITC furnace testing (1137°C–200°C=937°C), resulting in higher thermal stresses.

Changing the test temperature (T_{ini}) alters both the cooling stresses and the oxidation rate of the bond coat. Consequently, the change in number of cycles to failure due to a change in T_{ini} cannot be estimated from the change in stresses only. Failure of the thick TBCs tested at 1250°C after one cycle will hence be due not only to the increase

in shear stresses near the free edge (see figure 6.11) but also the higher oxidation rate, with correspondingly higher oxide-layer-growth-stresses (Evans *et al.*, 1983; Tsui *et al.*, 1998; Freborg *et al.*, 1998). Similarly, the non-failure of the NLR furnace tested specimens at 1000°C after 2000 cycles is due not only to the lower shear stresses near the free edge but also the lower oxidation rate.

It should be remembered that this interaction between thermal stresses and oxidation and its effect on TBC life also finds expression when the cycle length is changed, see the discussion in section 3.6.1.

7.3 Burner rig testing

7.3.1 Temperature profile

The predicted change in substrate temperature at the centre of the specimen agreed well with the measured change in temperature, see figure 6.31. The predicted radial temperature profile at the substrate rear side at the end of the heating period (not shown in chapter 6) also agreed well with the measured profile shown in figure 3.7. Moreover, the suggestion from chapter 3 (sub-section 3.6.2) that the radial temperature drop at the top coat surface is much larger than that at the substrate rear side is confirmed by the model, as is clearly visible in figure 6.24. Remember, however, that top coat densification at 15 mm off-centre was observed for thick TBCs and not for 0.3 mm TBCs (see sub-section 5.4.3), so the actual radial top coat temperature drop may be lower than the predictions for thick TBCs.

It is concluded that the semi-empirical approach, given in sub-section 6.3.2, to determine the heat transfer from the flame to the specimen is a relatively easy and dependable engineering solution.

7.3.2 Failure by delamination

Globally the observed failure modes during the present investigation can be described as follows (section 3.5):

Thermal shock tests

- thin top coats delaminated generally in the flame area (exceptions in failure mechanisms will be discussed separately in sub-section 7.3.3 for convenience)
- intermediate and thick top coats did not fail within a specified large number of cycles.

Thermal cycling tests

- thin top coats delaminated in the flame area
- intermediate top coats did not fail but could show segmentation cracking
- thick top coats failed by edge to flame area delamination.

These failure modes can be explained with the help of the numerical analyses presented in chapter 6:

Thermal shock

From the global solution it might be expected that delamination would occur at a free edge instead of in the flame area, since the shear stresses near free edges are larger than those at the flame edge. However, firstly the shear stresses near a free edge are probably still too low to cause delamination (<30 MPa, see figure 6.18). Secondly, bond coat oxidation in the flame area causes extra stresses due to the growing oxide¹ and also high shear and normal stresses at the top coat / bond coat interface peaks (see section 6.8.2). Therefore:

- thin TBCs show flame area delamination because the bond coat is oxidised in the flame area but not at the edge of the specimen
- intermediate and thick coatings show longer life than thin coatings because little or no oxidation of the bond coat occurs.

Thermal cycling

- thin TBCs showed flame area delamination owing to bond coat oxidation (same reasoning as for thermal shock)
- thick top coats failed by edge-to-flame-area delamination, which can be attributed to shear and normal stresses near the free edge. These free edge stresses are much higher than those for thin TBCs and for TBCs subjected to burner rig thermal shock tests, see figures 6.18 and 6.30. Since the bond coat is not oxidised, the stresses in the flame area are too low to cause local failure.

Hence the negative effect of bond coat oxidation decreases with increasing top coat thickness, and the thermal stresses increase with increasing top coat thickness. (Note that the thermal stresses are not necessarily stresses at the free edge; for the 1.0 mm TBCs segmentation cracking occurred in the flame area, resulting in flame area delamination for the specimen tested at $T_{\text{surf}}=1500^{\circ}\text{C}$.) These opposing effects of top

¹ The effect of a growing oxide was not modelled, but it is known that an oxide growing between top coat and bond coat causes stresses in the interface region (Evans *et al.*, 1983; Tsui *et al.*, 1998; Freborg *et al.*, 1998).

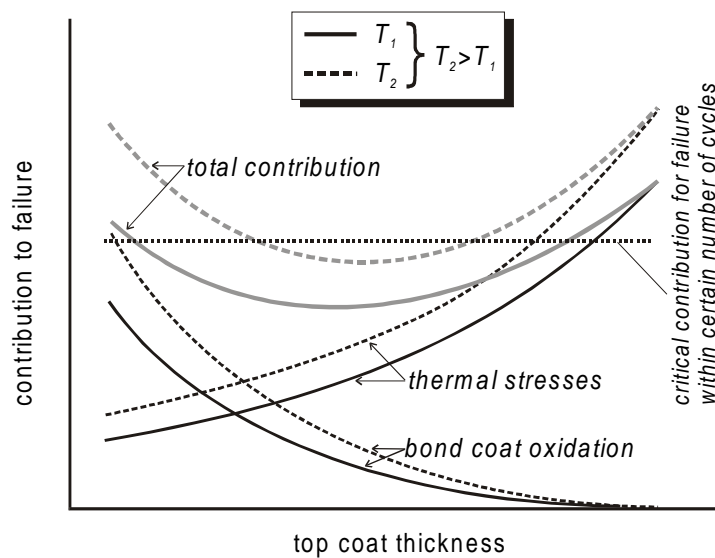


Figure 7.2 Schematic representation of effect of top coat thickness on the life of TBCs during burner rig thermal cycling, in terms of thermal stresses and bond coat oxidation and their contributions to failure

coat thickness result in the observed optimum coating thickness (see sub-section 3.6.2), as shown schematically in figure 7.2. This figure also shows the effect of test temperature, thereby explaining why a 1 mm TBC did not fail at 1400°C but did fail at 1500°C.

7.3.3 Other failure modes

- Severe metallic component degradation and specimen bending occurred during burner rig thermal shock at $T_{\text{surf}}=1350^{\circ}\text{C}$, but not during burner rig thermal cycling at this temperature (sub-section 3.5.2). In chapter 6 it was shown that though the surface temperatures are the same, the heat input is higher for the thermal shock tests. This resulted in a higher bond coat temperature and higher stresses throughout the entire component. In addition, the number of cycles during thermal shock was higher, resulting in more thermal fatigue.
- Surface spalling occurred in 0.3 mm TBCs at $T_{\text{surf}}=1400^{\circ}\text{C}$ (fig. 3.20). Figure 6.17 shows that the compressive in-plane surface stresses, which are most likely responsible for surface spalling since they cause local buckling in areas with horizontal cracks, are higher for the 1.0 mm TBC than for the 0.3 mm TBC. However, surface spalling did not occur for the 1.0 mm TBC, not even at $T_{\text{surf}}=1475^{\circ}\text{C}$. Hence this type of failure must be attributed to poor splat adhesion in the 0.3 mm TBCs sprayed under the ‘excessive energy’ plasma conditions, as discussed in sub-section 3.6.2.

- Vertical cracks occurred in the top coat outside the flame area. These cracks are caused by in-plane stresses in that region which are always tensile through the entire coating, irrespective of the thickness, see sub-section 6.7.2.
- The calculated large compressive in-plane stresses in the substrate (see figure 6.28a) exceeded the yield strength of Hastelloy-X (Kattus, 1996), and it would be expected that the substrate would plastically deform. This was indeed observed for some specimens tested with the burner rig (see sub-section 3.5.2). These specimens were bent and the substrate thickness had increased in the flame area.

7.4 Effect of preoxidation

In section 3.4, it was shown that the effect of bond coat preoxidation on the life of a TBC depended on the type of thermal test and top coat thickness:

- positive effect for the furnace and burner rig thermal cycling tests of 0.3 mm TBC
- practically no effect for the burner rig thermal shock tests of 0.3 mm TBC
- negative effect for the burner rig thermal shock tests of 0.6 mm TBC. Failure mode changes from flame area delamination to edge-to-flame-area delamination.

The contribution of preoxidation to the life of TBCs is ambiguous. On the one hand, it prevents oxide growth stresses that occur predominantly during the early stages of oxidation. On the other hand, the high interface stresses due to an oxide layer (see local analyses, chapter 6) are present during thermal testing from the first cycle onwards. In addition, preoxidation resulted in decreased adhesion strength (see section 4.4), which might indicate a lower critical stress to failure. This negative contribution to life increased with increasing top coat thickness. Thus whether or not preoxidation has a positive effect on TBC life depends on the relative contribution of these three factors. This is shown in figure 7.3. It should be remembered that bond coat preoxidation had no effect on the residual stresses (section 5.4, fig. 5.10), and so this possible effect on TBC life may be discounted.

Furnace testing

- 0.3 mm: an oxidation layer is always present from the first cooling cycle (formed during the 1-hour stay at high temperature). Thus besides the lower adhesion strength (negative contribution) there is a large positive contribution of preoxidation because it hinders oxide growth and the accompanying stresses. Adding the two contributions results in a large positive effect of preoxidation.

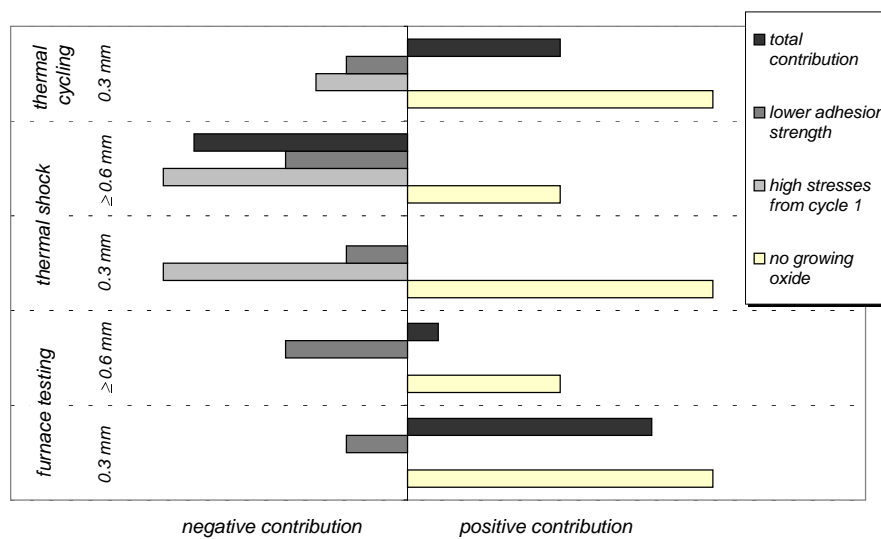


Figure 7.3 Schematic effect of bond coat preoxidation on the life of TBCs

- 0.6 mm and thicker: the stresses that cause delamination are so high anyway that the positive contribution of hindering oxide growth is relatively low. Combined with the lower adhesion strength this results in only a small beneficial effect of preoxidation.

Burner rig, thermal shock

- 0.3 mm: the positive contribution of hindering oxide growth stresses appears to counterbalance the negative contributions of lower adhesion strength and increased stresses from the first cycle onwards.
- 0.6 mm and thicker: The positive contribution of hindering oxide growth stresses is less pronounced than that for the 0.3 mm TBCs, since the oxidation rate is lower because of the increased top coat thickness. Also, there is a negative contribution of increased stresses from the first cycle onwards, both in the flame area *and* near the free edge (stresses near free edges increase with increasing coating thickness, see figure 6.18). Combined with the lower adhesion strength the total contribution of preoxidation to TBC life is negative.

Burner rig, thermal cycling

Compared to the thermal shock tests a relatively small number of cycles suffer the negative contribution of increased stresses from the first cycle onwards², while the

² Suppose that for the non-preoxidised TBCs an oxide layer causing significantly higher local stresses is present after 5 h at high temperature for both types of tests, meaning for thermal cycling 5 cycles and for thermal shock about 900 cycles (based on 20 sec oxidation per cycle). This means that respectively 5% (100 cycles to failure) and 25% (3600 cycles to failure) of the cycles suffer higher local stresses where the TBC is preoxidised.

positive contribution of hindering oxide growth stresses is similar. Hence the total contribution of preoxidation to TBC life will be intermediate to those for furnace testing and thermal shock, *i.e.* moderately positive.

7.5 A remark about top coat thickness

From the foregoing discussions it is clear that thick TBCs perform relatively poorly during furnace testing and burner rig thermal cycling. Since the latter is believed to be the most realistic thermal test (see chapter 3) it might be concluded that thick TBCs are not suitable for use in gas turbines. However, failure of thick TBCs occurred *always* at the specimen free edge because of high singular stresses at the intersection of the free edge and the top coat / bond coat interface. Moreover, from the thermal shock and thermal cycling tests of 0.6 mm and 1.0 mm TBCs at 1400°C it appears that thick TBCs exhibited excellent thermal strain tolerance, owing to the dense network of microcracks and the segmentation cracks formed during the first heating cycle, see the discussion in sub-section 3.6.5. It is therefore concluded that the thick TBCs in the present research would most probably perform well on gas turbine components provided there are no free edges. This could be experimentally verified by subjecting a TBC coated cylindrical specimen to a burner rig thermal cycling test, whereby the specimen is long enough that the flame area is localised and well away from the cylinder ends (no free edge effect).

It must be mentioned that the numerical analyses in chapter 6 demonstrated that for gas turbine component with a free edge (also: cooling holes!) the practical thickness of TBCs will be limited: beyond a certain thickness the singular free edge stresses become too high and will lead to premature or immediate failure of the coating.

7.6 Fracture mechanics

Since thermally sprayed TBCs contain microcracks, which are also present along the interface, a fracture mechanics approach might be adopted to assess the coating strengths. To do so, the stresses at which delamination occurs can be related to a critical value of the strain energy release rate, G , which is a parameter that can be assumed to control fracture (Brown *et al.*, 1988; Evans *et al.*, 1990; Dal Maschio *et al.*, 1994; Howard *et al.*, 1994; Clyne and Gill, 1996; Kokini *et al.*, 1997).

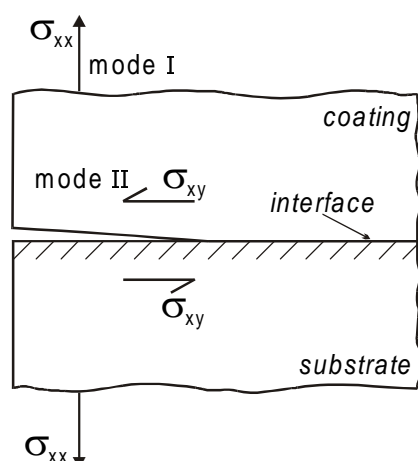


Figure 7.4 Mixture of deformation modes at a bimaterial interface crack. They are referred to as opening mode (I), where the two crack surfaces are pulled apart, and shearing mode (II), where the two crack surfaces slide over each other along the crack line.

However, application of fracture mechanics to failure of TBCs is fraught with problems, even when considering an immediate static failure, let alone cycle-dependent failure. One of the most complicating factors is that the (residual) stress field at the crack tip results in mixed mode loading: besides pure crack opening (mode I), a substantial shear component (mode II) is present at the crack tip (figure 7.4), which makes data interpretation very difficult (Brown *et al.*, 1988; Charalambides *et al.*, 1992; Howard *et al.*, 1994; Clyne and Gill, 1996).

It is beyond the scope of this thesis to give an extensive treatment of the strain energy release rate in general, or its use for coated systems in particular³. Instead, some basic features of fracture mechanics applied to coated materials will be given.

In the simplest case of a thin coating with in-plane stresses only, the strain energy release rate is the stored elastic strain energy per unit interfacial area (Clyne and Gill, 1996), given by:

$$G = \frac{\sigma_c^2 d_c}{2E_c} \left(1 + \frac{d_c}{d_s} \cdot \frac{E_c}{E_s} \right) \quad (7.1)$$

where σ_c is the (residual) in-plane stress in the coating; d_c and d_s the coating and substrate thickness; and E_c and E_s the coating and substrate Young's modulus. Eq. 7.1 can be used to estimate the critical strain energy release rate of the interface, G_{ic} , which is also called the interfacial fracture energy or the interfacial toughness. If the delamination stress in the coating is known, G_{ic} is simply equal to the value of G at this point.

³ For a basic treatment of the concepts of fracture mechanics the reader is referred to the textbook of Ewalds and Wanhill (1984). Recent work on the strain energy release rate during interfacial debonding of thermally sprayed coatings is reviewed by Clyne and Gill (1996).

However, as mentioned above, stresses affect the actual strain energy release rate in a more complicated way than suggested by Eq. 7.1. Calculations based on the in-plane stresses may not be sufficient for estimation of the interfacial toughness. For example, high shear and normal stresses are present near the intersection of the interface with a free edge of a specimen, while the in-plane stresses are lower than those away from the free edge (see chapter 6). This stress distribution can strongly affect the crack initiation and propagation behaviour.

It should be mentioned that the fracture mechanics approach for coating delamination is applied especially for *global* stress solutions and for model systems with *flat* interfaces (Howard *et al.*, 1994). In contrast, the model presented in chapter 6 focussed on the *local* stress distribution near a *rough* interface, which is realistic and for which no fracture mechanics solutions are available (to the author's knowledge).

7.7 Use and further development of the present model

The model presented in chapter 6 predicts only the elastic thermal stresses whereby the microstructure (porosity and microcracks) is represented only by the room temperature as-sprayed value of the Young's modulus. The usefulness of this model is that failure of TBCs can be understood phenomenologically, rather than that failure can be predicted in terms of number of cycles. Thus the model can be used to qualitatively determine (predict) the effect of test method, test temperature or coating thickness for a TBC.

To compare different types of TBCs one would have to use failure criteria parameters like fatigue crack initiation resistance, strain tolerance and fatigue crack growth resistance, *i.e.* including a fracture mechanics approach. Also, to assess TBC lives the model would have to be supported by an extensive experimental programme. Still further development of the model should include anisotropic material properties, an explicit representation of porosity and (micro) cracks, changes in material properties owing to sintering and degradation, creep, plasticity of metallic components, oxide layer growth, and realistic (gas turbine component) geometries: all in all, a formidable problem.

8 CONCLUSIONS AND RECOMMENDATIONS

8.1 General conclusions

Thermal Barrier Coatings (TBCs) consist of a heat-resistant ceramic top coat and a metallic bond coat. The bond coat's main purpose is to attach the top coat to the substrate, but the bond coat also prevents or delays oxidation of the substrate. Unfortunately, a major life-limiting weakness of TBCs is oxidation of the bond coat itself; the other major problem is their susceptibility to damage by thermally-induced stresses.

The mechanisms of damage and ultimate failure of TBCs are difficult to determine. The objective of the present work, reported in this thesis, has been to use a combination of experiments and theoretical modelling to improve the understanding of TBC damage accumulation and failure.

From the discussion in chapter 7 on the experiments and modelling the following general conclusions are drawn:

1. Failure of a TBC during furnace testing is caused by the high shear stresses near the intersection of the top coat / bond coat interface and a free edge of the specimen. Local analysis is not required for understanding failure.
2. Failure of a TBC during burner rig thermal shock testing is caused by a combination of bond coat oxidation in the flame area and the high normal and shear stresses close to the interface roughness peaks. A local analysis is necessary to understand failure.
3. Failure of thin TBCs during burner rig thermal cycling is caused by the same mechanism as during thermal shock testing (flame area delamination due to

oxidation). Failure of thick TBCs is caused by the same mechanism as during furnace testing (normal and shear stresses near the intersection of the top coat / bond coat interface and a free edge of the specimen). In the latter case local analysis is not required for understanding failure.

4. Preoxidation has a beneficial effect for test methods with long heating cycles. This result, from chapter 3, is explained in chapter 7 using a rationale which contains several competing factors that affect the contribution of preoxidation to TBC life.
5. Thick TBCs exhibited excellent thermal strain tolerance, owing to the dense network of microcracks after deposition and the segmentation cracks formed during the first few heating cycles. However, for gas turbine components with free edges the practical thickness of TBCs will be limited: beyond a certain thickness the singular free edge stresses become too high and will lead to failure of the coating.

8.2 Detailed conclusions

Chapter 2

Several TBCs were applied by Air Plasma Spraying (APS) to Hastelloy X substrates with NiCrAlY bond coats. The main process variables were the top coat thickness and bond coat condition (as-sprayed or preoxidised) before applying the top coat. These are important for the experiments and modelling dealt with in chapters 3-6. The secondary process variables were optimisation of the spraying parameters and comparison of 'mild' and 'excessively energetic' plasma spraying conditions. From this the following conclusions are drawn:

6. The deposition efficiency appears to be a good measure of spraying parameters optimisation.
7. The 'mild' plasma spraying conditions resulted in dense microcracked TBCs that can be applied in thicknesses up to 2 mm.

Chapter 3

The TBCs were subjected to three types of thermal tests: isothermal furnace tests, short cycle (thermal shock) burner rig tests, and long cycle burner rig tests. The results were the number of thermal cycles to failure and a phenomenological

description of failure as function of the type of test, the top coat thickness, and bond coat condition before applying the top coat. The following conclusions are drawn:

8. Failure of a TBC under realistic testing conditions must be due to an interaction between thermal stresses and bond coat oxidation. For example, thick TBCs perform excellently during burner rig thermal shock tests and poorly during furnace tests. For the most generally realistic test, burner rig thermal cycling, there seems to be an optimum coating thickness.
9. Good thermal shock resistance can be obtained from a high microcrack density in the top coat, provided that good particle adhesion exists. This was achieved with the mild spraying conditions during the present research. However, during testing vertical cracking or segmentation cracking occurs (especially in the thick TBCs), which also contributes to good thermal shock resistance.
10. Thick TBCs always fail by delamination starting from a free edge. This indicates that specimen geometry also plays an important part in the failure mode.
11. Empirical testing, no matter how realistic, is insufficient for understanding the observed failure mechanisms and the effects of coating thickness and pre-oxidation on these mechanisms. Thus the changes in the TBC systems, including bond coat oxidation, should be investigated, and also the stresses that develop during thermal testing should be quantitatively predicted.

Chapter 4

In addition to thermal testing, several properties were determined for both the as-sprayed and thermally tested TBCs. These properties included coating hardness, erosion resistance, bond strength and phase composition. Also, the influence of heat treatment on the bond coat composition was determined. The following conclusions are drawn:

12. Sintering occurred during isothermal heating of the TBCs and resulted in microstructural changes. In general, the porosity decreased and sealing of flaws occurred. In consequence the microhardness, erosion resistance and top coat bond strength increased.
13. Surface spalling of the top coat during burner rig testing with a coating surface temperature of 1400°C is not caused by the tetragonal to monoclinic phase transformation.

14. Aluminium depletion of the bond coat occurred during furnace testing of TBCs with 0.3 mm thick top coat.

Chapter 5

Residual stresses in as-sprayed and thermally tested coatings were measured using the hole-drilling method. Despite the difficulties involved in this technique some trends may be concluded:

15. Low tensile stresses prevailed in the top coat in the as-sprayed state.
16. Low compressive stresses prevailed in the top coat in the isothermally heated state. The compressive stresses were close to zero at the coating surface and increased towards the interface. Overall, these stresses decreased with increasing coating thickness.
17. After thermal shock the residual stresses at the centre of the flame-covered area were compressive in the 0.3 mm coatings and tensile in the 0.6 and 1.0 mm coatings. The residual stresses 15 mm off-centre from the flame area were close to zero: the sign was tensile for the 0.3 mm coating and compressive for the 0.6 and 1.0 mm coatings.
18. The residual stresses were not affected by bond coat preoxidation.

Furthermore, in relation to the results reported in chapters 3 and 4 the following additional conclusions can be drawn:

19. The differences in life and failure mechanisms during furnace testing and burner rig testing between thin and thick TBCs as reported in chapter 3 cannot be explained from the in-plane residual stresses in the as-sprayed state. The explanation must be sought from other stresses (*e.g.* shear and normal stresses or transient stresses) occurring during heating and/or from differences in oxidation behaviour.
20. The changes in residual stresses after isothermal heating and thermal shock can be explained from the thermal histories and microstructural changes of the specimens, notably vertical cracking and densification.

Chapter 6

The theoretical modelling used the Finite Element Method (FEM) to simulate the three types of thermal testing. The so-called global-local approach was used. First, overall temperature and stress distributions in the TBCs were obtained, as functions of the type of test. From this global model the following conclusions are drawn:

21. The relative temperature drop through the coating with respect to that through the specimen (thermal barrier ratio) reaches a constant value after about 10 seconds of heating, and remains constant during the rest of the heating period, including steady state. The thermal barrier ratio increases with increasing coating thickness, but is virtually independent of the heat input.
22. Using an artificially high coefficient of free convection at the substrate rear side can simulate the experimental heat losses via the specimen holder during burner rig tests.
23. The global model provides useful information about the locations of highly stressed areas.

Next, the interesting areas were subjected to local and more refined FEM modelling. The local model provided additional information about the effects of bond coat roughness and the presence of an interface oxidation layer, especially with respect to the shear and normal stresses. The following conclusions are drawn:

24. Interface roughness results in small variations of the shear and normal stresses around the global solution.
25. During the heating period of the burner rig simulations the normal stresses at the roughness peaks are compressive, which cannot explain delamination.
26. An oxide layer between the top coat and bond coat has two very important effects near and at the top coat / bond coat interface:
 - the shear and normal stresses show very large variations around the global solution stresses
 - the normal stresses at the interface peaks during the heating period of the burner rig simulations become reversed in sign from compressive to tensile.

8.3 Recommendations

The model presented in this thesis has contributed to a better understanding of the failure mechanisms of plasma sprayed TBCs. Logically, the next steps should be to provide the capabilities of comparing different types of TBCs and assessing TBC lives. To achieve these capabilities requires further development of the model, for which the following suggestions are given:

1. Incorporation of failure criteria parameters like fatigue initiation resistance, strain tolerance and fatigue crack growth resistance. The latter implies use of a fracture mechanics approach.
2. Inclusion of anisotropic material properties, an explicit representation of porosity and (micro) cracks, changes in material properties owing to sintering and degradation, creep, plasticity of metallic components, and oxide layer growth.

The model would have to be supported by an extensive experimental programme:

3. The changes in material properties and behaviour owing to a heat treatment should be investigated thoroughly.
4. A large number of long-cycle burner rig tests should be done, not only on flat specimens but also on specimens with realistic (gas turbine component) geometries.
5. It should be investigated how the formation of oxides other than Al_2O_3 enhances TBC failure.

Finally, more attention should be paid to thick TBCs:

6. The behaviour of thick TBCs should be investigated both experimentally and numerically using specimens without free edges and specimens with realistic (gas turbine component) geometries.

REFERENCES

- Ajovalasit, A., 1979, "Measurement of Residual Stresses by the Hole-Drilling Method: Influence of Hole Eccentricity," *J. of Strain Analysis*, Vol. 14(4), pp. 171-178
- Alaya, M., Grathwohl, G., and Musil, J., 1994, "A Comparison of Thermal Cycling and Oxidation Behaviour of Graded and Duplex ZrO₂ Thermal Barrier Coatings," Presented at: *3th Int. Symp. on Functional Gradient Materials FGM '94*, October 10-12, Lausanne, Switzerland
- Allen, A.J., Long, G.G., Wallace, J., Ilavsky, J., Berndt, C.C., and Herman, H., 1999, "Microstructural Changes in YSZ Deposits During Annealing," *Proc. United Thermal Spray Conference '99*, Eds. E. Lugscheider and P.A. Kammer, ASM International, Materials Park, OH, USA, pp. 228-233
- ASTM C633-79, 1982, "Standard Method of Test for Adhesion or Cohesive Strength of Flame Sprayed Coatings," *1982 Annual Book of ASTM Standards*, Part 17, American Society for Testing and Materials, Philadelphia, PA, USA, pp. 636- 642
- ASTM, 1992, "Determining Residual Stresses by the Hole-Drilling Strain-Gage Method," *ASTM Standard E837-92*, American Society for Testing and Materials, Philadelphia, PA, USA
- Bartuli, C., Bertamini, L., Matera, S., and Sturlese, S., 1995, "Investigation of the Formation of an Amorphous Film at the ZrO₂-Y₂O₃/NiCoCrAlY Interface of Thermal Barrier Coatings Produced by Plasma Spraying," *Mater. Sci. Eng.*, Vol. A199, pp. 229-237
- Bengtsson, P., and Persson, C., 1997, "Modelled and Measured Residual Stresses in Plasma Sprayed Thermal Barrier Coatings," *Surf. Coat. Technol.*, Vol. 92, pp. 78-86
- Bengtsson, P., Ericsson, T., and Wigren, J., 1998, "Thermal Shock Testing of Burner Cans Coated with Thick Thermal Barrier Coating," *J. Thermal Spray Technol.*, Vol. 7, pp. 340-348
- Bose, S., and DeMasi-Marcin, J.T., 1997, "Thermal Barrier Coating Experience in Gas Turbine Engines at Pratt & Whitney," *J. Thermal Spray Technol.*, Vol. 6(1), pp. 99-104
- Brandon, J.R., and Taylor, R., 1991, "Phase Stability of Zirconia-Based Thermal Barrier Coatings. Part I. Zirconia-Yttria Alloys," *Surf. Coat. Technol.*, Vol. 46, pp. 75-90
- Brindley, W.J., 1997, "Properties of Plasma-Sprayed Bond Coats," *J Thermal Spray Technology*, Vol. 6(1), pp. 85-90
- Brindley, W.J., and Miller, R.A., 1990, "Thermal Barrier Coatings Life and Isothermal Oxidation of Low-Pressure Plasma-Sprayed Bond Coat Alloys," *Surf. Coat. Technol.*, Vol. 43/44, pp. 446-457
- Brindley, W.J., and Miller, R.A., 1998, "Improved Bond Coat Layers for Thermal Barrier Coatings," *NASA Tech Briefs*, NASA, Cleveland, OH, USA, pp. 63-65
- Brindley, W.J., and Whittenberger, J.D., 1993, "Stress Relaxation of Low Pressure Plasma-Sprayed NiCrAlY Alloys," *Materials Science and Engineering*, Vol. A163, pp. 33-41
- Brown, S.D., Chapman, B.A., and Wirtz, G.P., 1988, "Fracture Kinetics and the Mechanical Measurement of Adherence," *Proc. Nat. Thermal Spray Conf.*, Cincinnati, OH, USA, pp. 147-157

- Busso, E.P., Lin, Y, Sakurai, S, and Nakayama, M., 2000, "A Mechanistic Study of Oxidation-Induced Degradation in a Plasma-Sprayed Thermal Barrier Coating System. Part I: Model Formulation," *Acta Mater.* (in press)
- Chang, G.C., Phucharoen, W., and Miller, R.A., 1987a, "Behavior of Thermal Barrier Coatings for Advanced Gas Turbine Blades," *Surf. Coat. Technol.*, Vol. 30, pp. 13-28
- Chang, G.C., Phucharoen, W., and Miller, R.A., 1987b, "Finite Element Thermal Stress Solutions for Thermal Barrier Coatings," *Surf. Coat. Technol.*, Vol. 32, pp. 307-325
- Charalambides, M., Kinloch, A.J., Wang, Y., and Williams J.G., 1992, "On the Analysis of Mixed-Mode Failure," *Int. J. Fract.*, Vol. 54, pp. 269-291
- Choules, B.D., Kokini, K., and Taylor, T.A., 1998, "Thermal Fracture of Thermal Barrier Coatings in a High Heat Flux Environment," *Surf. Coat. Technol.*, Vol. 106, pp. 23-29
- Claussen, N., Rühle, M., and Heuer, A.H. (Eds.), 1984, "Science and Technology of Zirconia II," *Advances in Ceramics*, Vol. 12, The American Ceramic Society, Columbus, OH, USA (Proc. 2nd Int. Conf. Science and Technology of Zirconia, Stuttgart, Germany, June 21-23, 1983)
- Clyne, T.W., and Gill, S.C., 1996, "Residual Stresses in Thermal Spray Coatings and their Effect on Interfacial Adhesion: A Review of Recent Work," *J. Thermal Spray Technol.*, Vol. 5 (4), pp. 401-418
- Dal Maschio, R., Sglavo, V.M., Mattivi, L., Bertamini, L., and Sturlese, S., 1994, "Indentation Method for Fracture Resistance Determination of Metal/Ceramic Interfaces in Thick TBCs," *J. Thermal Spray Technol.*, Vol. 3(1), pp.51-56
- Das, D.K., and Sivakumar, R., 1990, "Modelling of the Temperature and the Velocity of Ceramic Powder Particles in a Plasma Flame-II. Zirconia," *Acta Metall. Mater.*, Vol. 38, No. 11, pp. 2193-2198
- DeMasi, J.T., Ortiz, M., Sheffler, K.D., 1989, *Thermal Barrier Coating Life Prediction Model Development, Phase I Final Report*, NASA CR-182230, NASA, Cleveland, OH, USA
- DeMasi-Marcin, J.T., Sheffler, K.D., and Bose, S., 1990, "Mechanisms of Degradation and Failure in a Plasma-Deposited Thermal Barrier Coating," *J. Eng. Gas Turbines and Power*, Vol. 112, pp. 521-526
- Diessen, van, S.L.M., 1998, *Mechanical Measuring Method for Plasma Sprayed Particle Velocities*, Master's Thesis, WOC/GTS/98-001, Eindhoven University of Technology, The Netherlands (in Dutch)
- Dolhof, V., Musil, J., Cepera, M., and Zeman, J, 1995, "Stress Analysis of Thermal Sprayed Coatings Using a Semi-Destructive Hole-Drilling Strain Gauge Method," *Proc. 8th National Thermal Spray Conference*, Houston, TX, USA, pp. 445-449
- Duan, K., Funke, C., and Steinbrech, R.W., 1997, "Elastic/Plastic Properties of Thermal Barrier Coatings," *Proc. 5th European Conference on Advanced Materials and Processes and Applications*, Vol. 3: *Surface Engineering and Functional Materials*, Eds. L.A.J.L. Sarton and H.B. Zeedijk, Netherlands Society for Materials Science, Zwijndrecht, The Netherlands, pp. 381-384
- Dykhuisen, R.C., 1994, "Review of Impact and Solidification of Molten Thermal Spray Droplets," *J. Thermal Spray Technol.*, Vol. 3(4), pp. 351-361

- Eaton, H.E., and Novak, R.C., 1987a, "Particulate Erosion of Plasma-Sprayed Porous Ceramic," *Surf. Coat. Technol.*, Vol. 30, pp. 41-50
- Eaton, H.E., and Novak, R.C., 1987b, "Sintering Studies of Plasma Sprayed Zirconia," *Surf. Coat. Technol.*, Vol. 32, pp. 227-236
- Eigenmann, B., Scholtes, B., and Macherauch, E., 1989, "Grundlagen und Anwendung der Röntgenographischen Spannungsermittlung an Keramiken und Metall-Keramik-Verbundwerkstoffen," *Mat.-wiss. und Werkstofftech.*, Vol. 20, pp. 314-325 (in German)
- Elsing, R., Knotek, O., and Balting, U., 1990, "Calculation of Residual Thermal Stresses in Plasma-Sprayed Coatings," *Surf. Coat. Technol.*, Vol. 43-44, pp. 416-425
- Embley, G.T., and Kallianpur, V.V., 1986, "Long-Term Creep Response of Gas Turbine Bucket Alloys," *Proc. EPRI Workshop on Life Prediction of High Temperature Gas Turbine Materials*, Eds. V. Weiss and W.T. Bakker, Electric Power Research Institute, Palo Alto, CA, USA, pp. 5.1-5.27
- Evans, A.G., Crumley, G.B., and Demaray, R.E., 1983, "On the Mechanical Behavior of Brittle Coatings and Layers," *Oxid. Met.*, Vol. 20, pp. 193-216
- Evans, A.G., Rühle, M., Dalgleish, B.J., and Charalambides, P.G., 1990, "The Fracture Energy of Bimaterial Interfaces," *Mater. Sci. Eng.*, Vol. A126, pp. 53-64
- Evans, H.E., Strawbridge, A., Carolan, RA, Ponton, C.B., 1997, "Creep Effects on the Spallation of an Alumina Layer From a NiCrAlY Coating," *Mat. Sci. Eng.*, A225, pp. 1-8
- Ewalds, H.L., and Wanhill, R.J.H., 1984, *Fracture Mechanics*, Edward Arnold Ltd, London, UK / Delftse Uitgevers Maatschappij b.v., Delft, The Netherlands
- Fauchais, P., Vardelle, M., Vardelle, A., and Coudert, J.F., 1989, "Plasma Spraying of Ceramic Particles in Argon-Hydrogen D.C. Plasma Jets: Modeling and Measurements of Particles in Flight Correlation with Thermophysical Properties of Sprayed Layers," *Met. Trans. B*, Vol. 20B, pp. 263-276
- Freborg, A.M., Ferguson, B.L., Brindley W.J., and Petrus, G.J., 1998, "Modeling Oxidation Induced Stresses in Thermal Barrier Coatings," *Mat. Science Eng.*, Vol. A245, pp. 182-190
- Goward, G.W., 1998, "Progress in Coatings for Gas Turbine Airfoils," *Surf. Coat. Technol.*, Vol. 108-109, pp. 73-79
- Greving, D.J., Rybicki, E.F., and Shadley, J.R., 1994, "Through-Thickness Residual Stress Evaluations for Several Industrial Thermal Spray Coatings Using a Modified Layer-Removal Method," *J. Thermal Spray Technol.*, Vol. 3, pp. 379-388
- Grünling, H.W., and Mannsmann, W., 1993, "Plasma Sprayed Thermal Barrier Coatings for Industrial Gas Turbines: Morphology, Processing and Properties," *Journal de Physique IV*, Vol. 3, pp. 903-912
- Harmsworth, P.D., and Stevens, R., 1992, "Microstructure of Zirconia-Yttria Plasma-Sprayed Thermal Barrier Coatings," *J. Mat. Sci.*, Vol. 27, pp. 616-624
- Harrison, R.W., and Karnitz, M.A., 1999, "Advanced Turbine Systems Program Materials/Manufacturing Technology Needs," *Proc. Materials Solutions '98*, Eds. P.J. Maziasz *et al.*, ASM International, Materials Park, OH, USA, pp. 13-25

- Haubold *et al.* 1998, "Comparison of Thermal Cycling Experiments on Thick Thermal Barrier Coatings," *Proc. 15th Int. Thermal Spraying Conference*, Ed. C. Coddet, ASM International, Materials Park, OH, USA, pp. 1617-1622
- Haynes, J.A., Ferber, M.K., Porter, W.D., and Rigney, E.D., 1999, "Mechanical Properties and Fracture Behavior of Interfacial Alumina Scales on Plasma-Sprayed Thermal Barrier Coatings," *Materials at High Temperatures*, Vol. 16(2), pp. 49-69
- Haynes, J.A., Ferber, M.K., and Porter, W.D., 2000, "Thermal Cycling Behavior of Plasma-Sprayed Thermal Barrier Coatings with Various MCrAlX Bond Coats," *J. Thermal Spray Technol.*, Vol. 9(1), pp. 38-48
- Hobbs, M.K., and Reiter, H., 1988, "Residual Stresses in ZrO₂-8%Y₂O₃ Plasma Sprayed Thermal Barrier Coatings," *Surf. Coat. Technol.*, Vol. 34, pp. 33-42
- Hoel, R.H., Pantucek, P., and Kvernes, I., 1991, "Plasma Sprayed ZrO₂ Thick Thermal Barrier Coatings," *Mat. Manufact. Processes*, Vol. 6, pp. 117-124
- Houben, J.M., 1976, "Some Remarks on Plasma Spraying Powder Injection Techniques," *Proc. 8th Int. Thermal Spray Conference*, Miami Beach, FL, USA
- Houben, J.M., 1980, "Remarks Concerning a Rational Plasma for Thermal Spraying," *Proc. 9th Int. Thermal Spraying Conference*, The Hague, The Netherlands, 19-23 May, pp. 143-154
- Houben, J.M., 1988, *Relationship Between the Adhesion of Plasma Sprayed Coatings to the Process Parameters Size, Velocity and Heat Content of the Spray Particles*, Ph.D. Thesis, Eindhoven University of Technology, Eindhoven, The Netherlands
- Howard, S.J., Tsui, Y.C., and Clyne, T.W., 1994, "The Effect of Residual Stresses on the Debonding of Coatings, Part I: A Model for Delamination at a Bimaterial Interface," *Acta Metall. Mater.*, Vol. 42, pp. 2823-2836
- Hsueh, C.H., and Fuller Jr., E.R., 2000, "Residual Stresses in Thermal Barrier Coatings: Effects of Interface Asperity Curvature/Height and Oxide Thickness," *Mat. Science Eng.*, Vol. A283, pp. 46-55
- Hu, S.Y., Li, Y.L., Munz, D., and Yang, Y.Y., 1998, "Thermal Stresses in Coated Structures," *Surf. Coat. Technol.*, Vol. 99(1-2), pp. 125-131
- Ibégazène, H., Alperine, S., and Diot, C., 1993, "Microstructure of Yttria Stabilized Zirconia-Hafnia Plasma Sprayed Thermal Barrier Coatings," *J. Physique IV*, Vol. 3, pp. 1013-1016
- Ilavsky, J., Long, G.G., Allen, A.J., and Berndt, C.C., 1999, "Evolution of the Void Structure in Plasma-Sprayed YSZ Deposits During Heating," *Mat. Science Eng.*, Vol. A272, pp. 215-221
- Incropera, F.P., and DeWitt, D.P., 1990, *Fundamentals of Heat and Mass Transfer*, 3rd ed., John Wiley & Sons, New York, NY, USA
- Itoh, A., Hirata, M., and Ayagaki, M., 1993, "Effects of Substrate Temperature During Spraying on the Properties of Sprayed Coatings (I)," *Proc. 5th Nat. Thermal Spray Conf.*, Anaheim, CA, USA, pp. 593-600
- Janos, B.Z., Lugscheider, E., and Remer, P., 1999, "Effect of Thermal Aging on the Erosion Resistance of Air Plasma Sprayed Zirconia Thermal Barrier Coatings," *Surf. Coat. Technol.*, Vol. 113, pp. 278-285

- Jordan, D.W., and Faber, K.T., 1993, "X-ray Residual Stress Analysis of a Ceramic Thermal Barrier Coating Undergoing Thermal Cycling," *Thin Solid Films*, Vol. 235, pp. 137-141
- Joshi, S.V., and Srivastava, M.P., 1993, "On the Thermal Cycling Life of Plasma-Sprayed Yttria-Stabilized Zirconia Coatings," *Surf. Coat. Technol.*, Vol. 56, pp. 215-224
- Joshi, S.V., and Srivastava, M.P., 1995, "Lifetime Determining Factors During Thermal Cycling of Zirconia Based Thermal Barrier Coatings," *Surf. Eng.*, Vol. 11(3), pp. 233-239
- Kattus, J.R., 1996, in *Aerospace Structural Metals Handbook, Vol 4*, Eds. F.B. William, H. Mindlin and C.Y. Ho, CINDAS/USAF CRDA Handbooks Operation, West Lafayette, USA, code 4112, p 1-23
- Kaysser, W.A., Peters, M., Fritscher, K., and Schulz, U., 1998, "Processing, Characterisation and Testing of EB-PVD Thermal Barrier Coatings," in: *Thermal Barrier Coatings*, AGARD-R-823, paper 9
- Khor, K.A., Gu, Y.W., and Dong, Z.L., 1998, "Plasma Spraying of Functionally Graded ZrO₂/NiCoCrAlY Coating System Using Composite Powders," *Proc. 15th Int. Thermal Spray Conf.*, Ed. C. Coddet, ASM International, Materials Park, OH, USA, pp. 1543-1548
- Kim, Y.C., Terasaki, T., and North, T.H., 1992, "A Method of Measuring the Through-Thickness Residual Stress in a Thermally-Sprayed Coating," *Thermal Spray Coatings: Properties, Processes and Applications*, Ed. T.F. Bernecki, ASM International, Materials Park, OH, USA, pp. 221-227
- Kingswell, R., Scott, K.T., and Sørensen, B., 1991, "Measurement of Residual Stress in Plasma Sprayed Ceramic Coatings," *Proc. 2nd Plasma-Technik Symp.*, Eds. S. Blum-Sandmeier, H. Eschnauer, P. Huber and A.R. Nicoll, Plasma-Technik, Wohlen, Switzerland, pp. 377-388
- Knight, R., and Smith, R.W., 1993, "Residual Stress in Thermally Sprayed Coatings," *Proc. 5th National Thermal Spray Conference*, Ed. C.C. Berndt, ASM International, Materials Park, OH, USA, pp. 607-612
- Kokini, K., Choules, B.D., and Takeuchi, Y.R., 1997, "Thermal Fracture Mechanisms in Ceramic Thermal Barrier Coatings," *J. of Thermal Spray Technol.*, Vol. 6(1), pp. 43-49
- Koolloos, M.F.J., 1996, *Measurement of Residual Stresses in Plasma Sprayed Thermal Barrier Coatings: a Preliminary Study*, Progress Report, WOC/GTS/96-010, Eindhoven University of Technology, The Netherlands
- Koolloos, M.F.J., Liempd, van G.G., and Houben, J.M., 1998, "Effect of Local Thermal Shock Load on Plasma Sprayed Thermal Barrier Coatings," *Surf. Eng.*, Vol. 14(2), pp. 144-148
- Koolloos, M.F.J., and Houben, J.M., 2000, "Behavior of Plasma Sprayed TBCs During Thermal Cycling and the Effect of a Pre-Oxidized NiCrAlY Bond Coat," *J. Thermal Spray Technol.*, Vol. 9(1), pp. 49-58
- Koolloos, M.F.J., and Houben, J.M., 2000, "Residual Stresses in As-Sprayed and Heat Treated TBCs; Measurements and FEM-Calculations," *Materials Science Forum*, Vols. 347-349, Eds. A.J. Böttger, R. Delhez and E.J. Mittemeijer, pp. 465-470
- Kuroda, S., Fukushima, T., and Kitahara, S., 1988, "Simultaneous Measurement of Coating Thickness and Deposition Stress During Thermal Spraying," *Thin Solid Films*, Vol. 164, pp. 157-163

- Kuroda, S., and Clyne, T.W., 1991, "The Quenching Stress in Thermally Sprayed Coatings", *Thin Solid Films*, Vol. 200, pp. 49-66
- Lee, J.D., Ra, H.Y., Hong, K.T., and Hur, S.K., 1992, "Analysis of Deposition Phenomena and Residual Stress in Plasma Spray Coatings," *Surf. Coat. Technol.*, Vol. 56, pp. 27-37
- Lelait, L., Alpérine, S., Diot, C., and Mévrel, M., 1989, "Thermal Barrier Coatings: Microstructural Investigations after Annealing," *Mater. Sci. Eng.*, Vol. A121, pp. 475-482
- Levit, M., Grimberg, I., and Weiss, B.Z., 1994, "Residual Micro- and Macro stresses in the Plasma-Sprayed Zirconia-Based TBCs," *Materials Letters*, Vol. 19, pp. 48-52
- Lih, W., Chang, E., Wu, B.C., and Chao, C.H., 1991, "Effects of Bond Coat Preoxidation on the Properties of ZrO₂-8wt.%Y₂O₃/Ni-22Cr-10Al-1Y Thermal-Barrier Coatings," *Oxid. Met.*, Vol 36, pp. 221-238
- Lin, C.K., and Berndt, C.C., 1994, "Measurement and Analysis of Adhesion Strength for Thermally Sprayed Coatings," *J. Thermal Spray Technol.*, Vol. 3(1), pp. 75-104
- Lugscheider, E., Barimani, C., Eckert, P., and Eritt, U., 1996, "Modeling of the APS Plasma Spray Process," *Computational Materials Science*, Vol. 7, pp. 109-114
- Matejicek, J., Sampath, S., Brand, P.C., and Prask, H.J., 1999, "Quenching, Thermal and Residual Stress in Plasma Sprayed Deposits: NiCrAlY and YSZ Coatings," *Acta Mater.*, Vol. 47(2), pp. 607-617
- McDonald, G., and Hendricks, R.C., 1980, "Effect of Thermal Cycling on ZrO₂-Y₂O₃ Thermal Barrier Coatings," *Thin Solid Films*, Vol. 73, pp. 491-496
- McPherson, R., 1981, "The relationship Between the Mechanism of Formation, Microstructure and Properties of Plasma Sprayed Coatings," *Thin Solid Films*, Vol. 83, pp. 297-310
- Measurements Group, 1993, "Measurement of Residual Stresses by the Hole-Drilling Strain Gage Method," *Tech Note TN-503-4*, Measurements Group, Inc., Raleigh, NC, USA
- Meier, S.M., and Gupta, D.K., 1994, "The Evolution of Thermal Barrier Coatings in Gas Turbine Engine Applications," *J. Eng. Gas Turbines Power*, Vol. 116, pp. 250-257
- Miller, R.A., 1987, "Current Status of Thermal Barrier Coatings: an Overview," *Surf. Coat. Technol.*, Vol. 30, pp. 1-11
- Miller, R.A., 1997, "Thermal Barrier Coatings for Aircraft Engines: History and Directions," *J. Thermal Spray Technol.*, Vol. 6(1), pp. 35-42
- Miller, R.A. and Lowell, C.E., 1982, "Failure Mechanisms of Thermal Barrier Coatings Exposed to Elevated Temperatures," *Thin Solid Films*, Vol. 95, pp. 265-273
- Miller, R.A., and Berndt, C.C., 1984, "Performance of Thermal Barrier Coatings in High Heat Flux Environments," *Thin Solid Films*, Vol 119, pp. 195-202
- Miller, R.A., Smialek, J.L., and Garlick, R.G., 1981, "Phase Stability in Plasma Sprayed Partially Stabilized Zirconia-Yttria," *Science and Technology of Zirconia, Advances in Ceramics*, Vol. 3, Eds. A.H. Heuer and L.W. Hobbs, The American Ceramic Society, Westerville, OH, USA, pp. 241-253
- Morrell, P., and Rickerby, D.S., 1998, "Advantages/Disadvantages of Various TBC Systems as Perceived by the Engine Manufacturer," *Thermal Barrier Coatings*, AGARD-R-823, paper 20

- Mullen, R.L., Hendricks, R.C., and McDonald, G., 1987, "Interface Roughness Effect on Stresses in Ceramic Coatings," *Ceram. Eng. Sci. Proc.*, Vol. 8, pp. 559-571
- Munz, D., and Yang, Y.Y., 1992, "Stress Singularities at the Interface in Bonded Dissimilar Materials under Mechanical and Thermal Loading," *J. Appl. Mech.*, Vol. 59, pp. 857-861
- Musil, J., Alaya, M., and Oberacker, R., 1995, "Thermal Cycling, Oxidation Behaviour and Mechanical Properties of Graded and Duplex PSZ TBC Coatings," presented at: *12th Int. Symp. Plasma Chemistry*, Minneapolis, MN, USA
- Nickola, W.E., 1986, "Practical Subsurface Residual Stress Evaluation by the Hole-Drilling Method," *Proc. Spring Conference on Experimental Mechanics*, Society for Experimental Mechanics, Bethel, CT, USA, pp. 47-58
- Nissley, D.M., 1997, "Thermal Barrier Coating Life Modeling in Aircraft Gas Turbine Engines," *J. Thermal Spray Technol.*, Vol. 6(1), pp. 91-98
- Noyan, J.C., and Cohen, J.B., 1987, *Residual Stress: Measurement by Diffraction and Interpretation*, Springer Verlag, New York, NY, USA
- Ostojic, P., and Berndt, C.C., 1988, "The Variability in Strength of Thermally Sprayed Coatings," *Surf. Coat. Technol.*, Vol. 34, pp. 43-50
- Padovan, J., Dougherty, D., and Hendricks, B., 1986, "Inelastic High-Temperature Thermomechanical Response of Ceramic Coated Gas Turbine Seals," *J. Thermal Stresses*, Vol. 9, pp. 31-43
- Pantucek, P., Lugscheider, E., and Müller, U., 1991, "Influence of Surface Temperature During Plasma Spraying on Residual Stresses in TBC's," *Proc. 2nd Plasma Technik Symp.*, Eds. S. Blüm-Sandmeier, H. Eschnauer, P. Huber, and A.R. Nicoll, Plasma-Technik, Wohlen, Switzerland, pp. 143-150
- Petrus, G.J., and Ferguson, B.L., 1997, "A Software Tool to Design Thermal Barrier Coatings: A Technical Note," *J. Thermal Spray Technol.*, Vol. 6(1), pp. 29-34
- Pina, J., Dias, A., and Lebrun, J.L., 1999, "Mechanical Stiffness of Thermally Sprayed Coatings and Elastic Constants for Stress Evaluation by X-Ray Diffraction," *Mat. Sci. Eng.*, Vol. A267, pp. 130-144
- Pipes, R.B., and Pagano, N.J., 1970, "Interlaminar Stresses in Composite Laminates Under Uniform Axial Extension," *J. Composite Materials*, Vol. 4, pp. 538-548
- Rabiei, A., and Evans, A.G., 2000, "Failure Mechanisms Associated with the Thermally Grown Oxide in Plasma-Sprayed Thermal Barrier Coatings," *Acta Mater.*, Vol. 48, pp. 3963-3976
- Rettig, U., Bast, U., Steiner, D., and Oechsner, M., 1999, "Characterization of fatigue Mechanisms of Thermal Barrier Coatings by a Novel Laser-Based Test," *J. Eng. Gas Turbines and Power*, Vol. 121, pp. 259-264
- Roode, van, M., and Beardsley, B., 1988, "Porosity Determination of Thermal Barrier Coatings," ASME paper 88-GT-278 presented at: *Gas Turbine and Aeroengine Congress*, Amsterdam, The Netherlands
- SAE, 1965, "Methods of Residual Stress Measurements," *Handbook Supplement J936*, Society of Automotive Engineers Inc., Warrendale, PA, USA

- Sandifer, J.P., and Bowie, G.E., 1978, "Residual Stress by Blind-Hole Method with Off-Center Hole," *Experimental Mechanics*, Vol. 18, pp.173-179
- Sasaki, K., Kishida, M., and Itoh, T., 1997, "The Accuracy of Residual Stress Measurements by the Hole-Drilling Method," *Experimental Mechanics*, Vol. 37, pp. 250-257
- Scardi, P., Leoni, M., and Bertamini, L., 1995, "Influence of Phase Stability on the Residual Stress in Partially Stabilized Zirconia TBC Produced by Plasma Spray," *Surf. Coat. Technol.*, Vol. 76-77, pp. 106-112
- Scardi, P., Leoni, M., Bertamini, L., and Marchese, M., 1996, "Residual Stress in Plasma Sprayed Y_2O_3 -PSZ Coatings on Piston Heads," *Surf. Coat. Technol.*, Vol. 86-87, pp. 109-115
- Schajer, G.S., 1988, "Measurement of Non-Uniform Residual Stresses Using the Hole Drilling Method," *J. Eng. Mat. Tech.*, Vol. 110(4), Part I: pp. 338-343, Part II: pp. 344-349
- Schajer, G.S., and Altus, E., 1996, "Stress Calculation Error Analysis for Incremental Hole-Drilling Residual Stress Measurements," *J. Eng. Mat. Tech.*, Vol. 118, pp.120-126
- Schick, H.L., 1966, *Thermodynamics of Certain Refractory Compounds*, Vol. 1, Academic Press, New York and London, p 2.266
- Scott, H.G., 1975, "Phase Relationships in the Zirconia-Yttria System," *J. Mater. Sci.*, Vol. 10, pp. 1527-1535
- Shadley, J.R., Rybicki, E.F., and Shealy, W.S., 1987, "Application Guidelines for the Parting Out Step in a Through Thickness Residual Stress Measurement Procedure," *Strain*, Vol. 23, pp. 157-166
- Sheets, B.E., and Kokini, K., 1991, "Thermal Stresses under Engine Heat Flux: 1. Ceramic Coatings on Metal Substrate," *Proc. 14th Annual Energy Sources Technol. Conf. and Exhibition*, American Society of Mechanical Engineers, pp. 257-261
- Shillington, E.A.G., and Clarke, D.R., 1999, "Spalling Failure of a Thermal Barrier Coating Associated with Aluminum Depletion in the Bond Coat," *Acta Mater.*, Vol. 47(4), pp. 1297-1305
- Siebert, B., Funke, C., Vaßen, R., and Stöver, D., 1999, "Changes in Porosity and Young's Modulus Due to Sintering of Plasma Sprayed Thermal Barrier Coatings," *J. Mat. Proc. Technol.*, Vol. 92-93, pp. 217-223
- Sobolev, V.V., Guilemany, J.M., Nutting, J., and Miquel, J.R., 1997, "Development of Substrate-Coating Adhesion in Thermal Spraying," *Int. Mat. Reviews*, Vol. 42(3), pp. 117-136
- Stecura, S., 1978, *Effects of Compositional Changes on the Performance of a Thermal Barrier Coating System*, NASA TM-78976, NASA, Cleveland, OH, USA
- Steffens, H.D., and Fischer, U., 1988, "Correlation Between Microstructure and Physical Properties of Plasma Sprayed Zirconia Coatings," *Proc. National Thermal Spray Conference*, 24-27 Oct, Cincinnati, OH, USA, pp. 167-173
- Steffens, H.D., Wielage, B., and Drozak, J., 1991, "Interface Phenomena and Bonding Mechanism of Thermally Sprayed Metal and Ceramic Composites," *Surf. Coat. Technol.*, Vol. 45, pp. 299-308
- Strangman, T.E., 1982, *Columnar Grain Ceramic Thermal Barrier Coatings*, U.S. Patent No. 4,321,311

- Stringer, J., 1999, "The Role of the Coating and Superalloy System in Enabling Advanced Land-Based Combustion Turbine Development," *Proc. Materials Solutions '98*, Eds. P.J. Maziasz *et al.*, ASM International, Materials Park, OH, USA, pp. 3-12
- Sturlese, S., and Bertamini, L., 1994, "Segmented Thermal Barrier Coatings on Turbine Blades and Diesel Engine Components," *Materials for Advanced Power Engineering, Part I*, Eds. D. Coutouradis *et al.*, Kluwer Academic Publishers, Dordrecht/Boston/London, pp. 705-716
- Sun, J.H., Chang, E., Wu, B.C., and Tsai, C.H., 1993, "The Properties and Performance of (ZrO₂-8wt%Y₂O₃) / (Chemically Vapour-Deposited Al₂O₃) / (Ni-22wt%Cr-10wt%Al-1wt%Y) Thermal Barrier Coatings," *Surf. Coat. Technol.*, Vol. 58, pp. 93-99
- Takeuchi, S., Ito, M., and Takeda, K., 1990, "Modelling of Residual Stress in Plasma-Sprayed Coatings: Effect of Substrate Temperature," *Surf. Coat. Technol.*, Vol. 43-44, pp. 426-435
- Taylor, T.A., Appleby, D.L., Weatherill, A.E., and Griffiths, J., 1990, "Plasma-Sprayed Ytria-Stabilized Zirconia Coatings: Structure-Property Relationships," *Surf. Coat. Technol.*, Vol. 43/44, pp. 470-480
- Te Raa, G., 1996, *Personal Communication*, Philips CMTI, Eindhoven, The Netherlands
- Thompson, J.A., and Clyne, T.W., 1999, "The Stiffness of Plasma Sprayed Zirconia Top Coats in TBCs," *Proc. UTSC '99*, Eds. E. Lugscheider and P.A. Kammer, pp. 835-840
- Thornton, J., Ryan, N., and Stocks, G., 1994, "The Production of Stresses in Thermal Barrier Systems by High Temperature Oxidation," *Proc. 7th National Thermal Spray Conference*, Boston, MA, USA, pp. 633-638
- Tsai, H.L., and Tsai, P.C., 1995, "Performance of Laser-Glazed Plasma-Sprayed (ZrO₂-12wt% Y₂O₃) / (Ni-22wt%Cr-10wt%Al-1wt%Y) Thermal Barrier Coatings," *Surf. Coat. Technol.*, Vol. 71, pp. 53-59
- Tsui, Y.C., and Clyne, T.W., 1996, "Adhesion of Thermal Barrier Coating Systems and Incorporation of an Oxidation Barrier Layer," in: *Thermal Spray: Practical Solutions for Engineering Problems*, Ed. C.C. Berndt, ASM International, Materials Park, OH, USA, pp. 275-284
- Tsui, Y.C., Reed, R.C., and Clyne, T.W., 1998, "On the Change in Stress State Associated with Bond Coat Oxidation During Heat Treatment of a Thermal Barrier Coating System," *Proc. 1st United Thermal Spray Conference*, Ed. C.C. Berndt, ASM International, Materials Park, OH, USA, pp. 267-276
- Usmani, S., and Sampath, S., 1996, "Erosion Studies on Duplex and Graded Ceramic Overlay Coatings," *JOM*, Vol. 48(11), pp. 51-54
- VanValzah, J.R., and Eaton, H.E., 1991, "Cooling Rate Effects on the Tetragonal to Monoclinic Phase Transformation in Aged Plasma-Sprayed Ytria Partially Stabilized Zirconia," *Surf. Coat. Technol.*, Vol. 46, pp. 289-300
- Vardelle, M., Vardelle, A., and Fauchais, P., 1993, Spray Parameters and Particle Behavior Relationships During Plasma Spraying, *J. Thermal Spray Technol.*, Vol. 2, pp. 79-92
- Verbeek, A.T.J., 1992, *Plasma Sprayed Thermal Barrier Coatings: Production, Characterization and Testing*, Ph.D. Thesis, Eindhoven University of Technology, Eindhoven, The Netherlands

- Watson, J.W., and Levine, S.R., 1984, "Deposition Stress Effects on the Life of Thermal Barrier Coatings in Burner Rigs," *Thin Solid Films*, Vol. 119, pp. 185-193
- Wesling, K.F., Socie, D.F., and Beardsley, B., 1994, "Fatigue of Thermal Barrier Coatings," *J. Am. Ceram. Soc.*, Vol. 77(7), pp. 1863-1868
- Whitcomb, J.D., Raju, I.S., and Goree, J.G., 1982, "Reliability of the Finite Element Method for Calculating Free Edge Stresses in Composite Laminates," *Computers and Structures*, Vol. 15(1), pp. 23-37
- Wigren, J. *et al.*, 1996a, "Process and In-Service Residual Stresses in Thermal Barrier Systems," *Thermal Spray: Practical Solutions for Engineering Problems*, Ed. C.C. Berndt, ASM International, Materials Park, OH, USA, pp. 847-854
- Wigren, J., de Vries, J.F., and Greving, D., 1996b, "Effects of Powder Morphology, Microstructure, and Residual Stresses on Thermal Barrier Coating Thermal Shock Performance," *Thermal Spray: Practical Solutions for Engineering Problems*, Ed. C.C. Berndt, ASM International, Materials Park, OH, USA, pp. 855-861
- Wigren, J., and Pejryd, L., 1998, "Thermal Barrier Coatings – Why, How, Where and Where To," *Proc. 15th Int. Thermal Spraying Conference*, Ed. C. Coddet, ASM International, Materials Park, OH, USA, pp. 1617-1622
- Williams, J.C., 1994, "The development of Advanced Gas Turbines: The Technical and Economic Environment," *Materials for Advanced Power Engineering Part II*, Eds. D. Coutsouradis *et al.*, Kluwer Academic Publishers, Dordrecht/Boston/London, pp. 1831-1846
- Wu, B.C., Chang, E., Chang, S.F., and Tu, D., 1989, "Degradation Mechanisms of ZrO₂-8wt%Y₂O₃/Ni-22Cr-10Al-1Y Thermal Barrier Coatings," *J. Am. Ceram. Soc.*, Vol. 72(2), pp. 212-218
- Zhangxiong, D., and Knight, R., 1999, "Factors influencing the surface roughness of TBC bond coats," *Proc. United Thermal Spray Conference '99*, Eds. E. Lugscheider and P.A. Kammer, ASM International, Materials Park, OH, USA, pp. 825-829
- Zhu, D., and Miller, R.A., 1997, "Investigation of Thermal Fatigue Behavior of Thermal Barrier Coating Systems," *Surf. Coat. Technol.*, Vol. 94-95, pp. 94-101

ACKNOWLEDGEMENTS

After four years of research at Eindhoven University of Technology I had the opportunity to start working at the National Aerospace Laboratory, NLR. The experimental research was finished and the modelling work could be carried out at the NLR. And the writing part.....I would do it in the evenings and week-ends. Some people, who probably didn't know me as well as they thought, didn't expect I would finish the job. Two years later I write these last words for my thesis: hence, though I now know I underestimated the writing part, I have finished the work. However, this thesis couldn't have been completed without the support of many persons, a few of whom I would like to mention.

First I would like to thank my first promotor, prof.dr.ir. M.J.W. Schouten, for reviewing the manuscript but especially for the confidence he showed in me during the last two years.

Secondly, I would like to thank my co-promotor dr.ir. J.M. Houben for teaching me the principles of plasma spraying and for allowing me to embark on a new course from a process technological approach to a more or less descriptive modelling approach.

Furthermore I am much obliged to the other members of the main promotion committee, prof.dr. R. Metselaar and prof.dr. E. Lugscheider for the time they spent reviewing and improving this thesis. Also I would like to thank prof.dr.ir. A. de Boer, prof.dr.ir. S. van der Zwaag and dr. R.J.H. Wanhill for completing the board of promotion.

I am especially grateful to some colleagues from the NLR, Structures and Materials Division. Russell Wanhill voluntarily reviewed the entire manuscript very thoroughly, and prevented me from writing 'Dunglish'. Russell, thank you very much. I enjoyed our (scientific) discussions and learned a lot from you. Harold Ottens and Henk-Jan ten Hoeve enabled me to finish this thesis, and I thank them for their confidence in a successful result.

Then there are all the people who assisted me technically, and to whom I am most indebted. From the section Thermal Spraying: Gijs van Liempd for the assistance during the many plasma spray sessions and the microstructural investigations, and for his constant presence and support; Piet de Waal and Ben Lamers for their technical assistance; Stefan van Diessen (former student) for the particle velocity measurements. Furthermore: Hans Heijligers from the department of Chemical Engineering and Chemistry, Eindhoven University of Technology, for

the chemical and phase analyses; Gerard te Raa from Philips CMTI, Eindhoven, for the porosity measurements and the many discussions about the coating microstructure and spraying technology; Leon Laas from ECN, Petten, for the porosity measurements; Giel Marijnissen from the Interturbine Coating Centre, Lomm, for the ITC furnace tests; Jos Boogers from the NLR, Marknesse, for the NLR furnace tests; the Materials Science section from Twente University, Department Mechanical Engineering, for the X-ray diffraction stress measurements; Henk Slot and Cor Lossi from TNO Institute of Industrial Technology for making the hole-drilling device available and the erosion tests, respectively; the personal of the Materials Laboratory at the NLR for the many 'last minute' microstructural photographs; Rob Hagmeijer, Andre de Boer (both former NLR colleagues but currently employed at Twente University), Tiedo Tinga, Joost van Rijn and Carel Lof (NLR, Structures and Materials Division) for the suggestions and fruitful discussions during the development of the numerical model.

In addition, I wish to express my thanks to my family and friends for their support and encouragement, especially Kees Hendriks for the interesting and engaging discussions during our four years of sharing in office.

And last, but definitely not least: Yvette, you were indispensable. You supported and motivated me when necessary, believed in me unconditionally, and showed a lot of patience, especially during the last two years. Thank you for everything!

CURRICULUM VITAE

Martijn Koolloos was born on January 20th, 1970 in Heerenveen, The Netherlands. He completed his high school (VWO) education in 1988 at the “Rijkscholen-gemeenschap” in Heerenveen. The same year he began studying Mechanical Engineering at Twente University in Enschede. In August 1994 he graduated under the supervision of prof. ir. P. Jongenburger of the Materials Science section. The subject of his Master’s thesis was the effect of carbide stability on the sensitivity for Nelson-hydrogen attack in low-alloyed Mo steels. The research was carried out at TNO Institute of Industrial Technology.

In October 1994 he began his PhD research at Eindhoven University of Technology, Department of Mechanical Engineering, section Thermal Spraying. Most of the practical work described in this thesis was done during the first four years. In December 1998 he started working at the National Aerospace Laboratory, NLR, where he developed the FE-model presented in this thesis.

Martijn Koolloos is currently affiliated with the Structures and Materials Division of the National Aerospace Laboratory, NLR (Marknesse, The Netherlands)

STELLINGEN

behorende bij het proefschrift

Behaviour of Low Porosity Microcracked Thermal Barrier Coatings under Thermal Loading

Martijn Koolloos

1. In tegenstelling tot wat Wigren *et al.* (1996) beweren kan een netwerk van microscheurtjes wel degelijk bijdragen tot een hoge thermische schok weerstand.
 - Wigren, J., de Vries, J.F., and Greving, D., 1996, "Effects of Powder Morphology, Microstructure, and Residual Stresses on Thermal Barrier Coating Thermal Shock Performance," *Thermal Spray: Practical Solutions for Engineering Problems*, ASM International, Materials Park, OH, USA, pp. 855-861
 - dit proefschrift, hoofdstuk 3
2. De levensduur van TBCs is sterk afhankelijk van de testmethode en -condities en zal dus per toepassing geëvalueerd moeten worden.
 - dit proefschrift, hoofdstuk 3
3. De eigenschappen van een TBC veranderen na een verblijf op hoge temperatuur dermate dat het vrijwel geen relevantie heeft de top coat te karakteriseren in de *as-sprayed* toestand.
 - dit proefschrift, hoofdstuk 4 en 5
4. Bij toepassing in gasturbines zal de dikte van TBCs gelimiteerd blijven.
 - dit proefschrift, hoofdstuk 6 en 7
5. Hoewel brosse breuk in vele gevallen een zeer ongewenst verschijnsel is, is het voor de beschaving van de mens onmisbaar geweest.
6. Omdat iedereen modelresultaten gelooft, behalve de maker van het model, en niemand experimentele resultaten gelooft, behalve de experimentator, is het raadzaam model en experiment te combineren.

7. Een vers afgestudeerde dient bij zijn keuze voor een AiO-plaats zich te realiseren dat het onderwerp van het onderzoek van ondergeschikt belang is ten opzichte van de reputatie en het succes van de onderzoeksgroep.
 - prof.dr.ir. B.H. Kolster, 1994, personal communication
8. De grote gelijkens die de vorm van de plattegrond van de stad Eindhoven vertoont met de morfologie van een *single splat* maakt het logisch dat het onderzoek naar thermisch spuiten daar plaats vindt.
9. Gezien de gang van zaken bij de beursgang en ondergang van World Online zou de directie er beter aan hebben gedaan een Nederlandse naamvoering te hanteren: “De wereld aan het lijntje”.
10. Het feit dat de oudste vorm van RSI schrijfkrimp onder kloosterlingen is, onderstreept dat het schrijven van een proefschrift monnikenwerk is.

